EUROPEAN MECHANICAL SCIENCE

E-ISSN: 2587-1110

2024 | vol. 8(3)

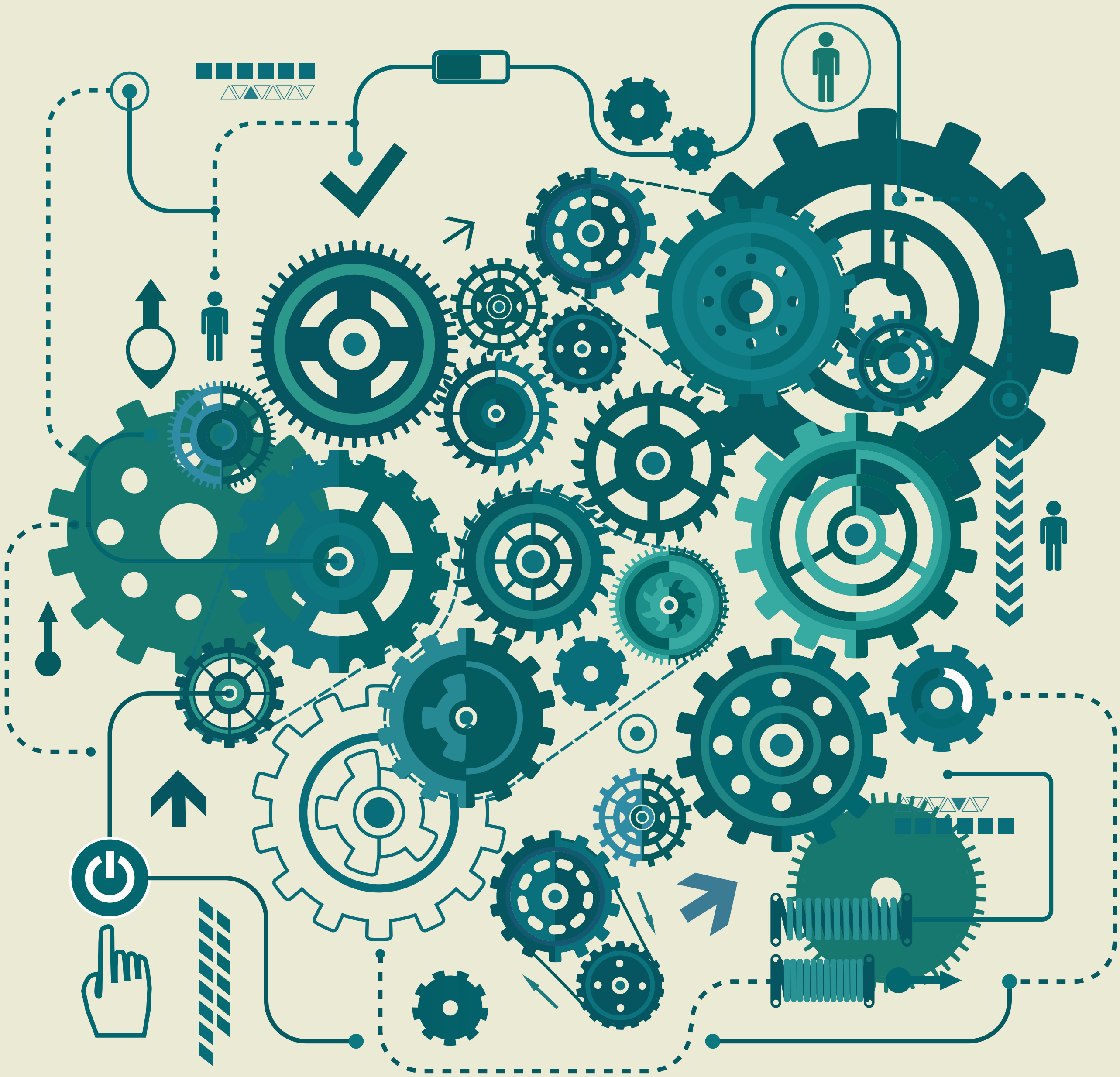

https://dergipark.org.tr/ems

EUROPEAN
MECHANICAL
SCIENCE
e-ISSN: 2587-1110

Editorial Board

European Mechanical Science 2024, 8(3)

Editor in Chief

Mustafa Ozcanli
Automotive Engineering, Cukurova University, Türkiye
Email: ozcanli@cu.edu.tr, Orcid: https://orcid.org/0000-0001-6088-2912

Editors

Zoran Lulic
Faculty of Mechanical Engineering and Naval Architecture, University of Zagreb, Croatia
Email: zoran.lulic@fsb.hr, Orcid: https://orcid.org/0000-0003-3489-2281

Sandra Paszkiewicz
West Pomeranian University of Technology, Poland
Email: spaszkiewicz@zut.edu.pl, Orcid: https://orcid.org/0000-0001-7487-9220

Iva Petrikova
Applied Mechanics, Technical University of Liberec, Czech Republic
Email: Iva.Petrikova@tul.cz, Orcid: https://orcid.org/0000-0002-9472-5066

Iulian Antoniac
Materials Science and Engineering, University Politecnica of Bucharest, Romania
Email: antoniac.iulian@gmail.com, https://orcid.org/0000-0003-0112-3494

Umut Atakan Gurkan
Department of Mechanical and Aerospace Engineering, Case School of Engineering, USA
Email: umut@case.edu, Orcid: https://orcid.org/0000-0002-0331-9960

Tomeh Elias
Vehicles and Engines, Technical University of Liberec, Czech Republic
Email: elias.tomeh@tul.cz

Ahmet Çalık
Mechanical Engineering, Burdur Mehmet Akif Ersoy University, Türkiye
Email: acalik@merhmetakif.edu.tr, Orcid: https://orcid.org/0000-0001-7425-4546

Aleksandra Borsukiewicz
West Pomeranian University of Technology, Poland
Email: aborsukiewicz@zut.edu.pl

Murat Demiral
College of Engineering and Technology, American University of the Middle East, Kuwait,
Email: murat.demiral@aum.edu.kw, https://orcid.org/0000-0002-7206-1713

Elżbieta Piesowicz
West Pomeranian University of Technology, Poland
Email: Elzbieta.Senderek@zut.edu.pl

Technical Editors

Ali Cem Yakaryılmaz
Automotive Engineering, Cukurova University, Türkiye,
Email: acyakaryilmaz@cu.edu.tr

Berkay Karaçor
Automotive Engineering, Cukurova University, Türkiye
Email: bkaracor@cu.edu.tr

Language Editorial Board

Yonca Özkan
School of Foreign Languages, Cukurova University,Turkey, Email: yoncaca@cu.edu.tr

Ayşe Fırat Dalak Ataözü
School of Foreign Languages, Cukurova University,Turkey, Email: aataozu@cu.edu.tr

Indexed / Abstracted in:

TR-Dizin, Scilit, EXALY Full-Text Search Engine, Index Copernicus, Root Indexing, Google Scholar, Harvard, journaltocs, Sobiad, Fatcat, Cite Factor, WorldCat, Freien Universität Berlin, Crossref, DTU Findit, The Open Ukrainian Citation Index (OUCI), Paperity Open Science, Asian Science Citation Index

Aims and Scopes

European Mechanical Science (EMS) is an international, peer reviewed journal which publishes full length original research papers, reviews related to all areas of Mechanical Engineering such as: Solid Mechanics, Materials Engineering, Automotive Engineering, Fluid Mechanics, Thermal Engineering, Engine and Power Engineering, Dynamics & Control, Robotics & Mechatronics, Transportation Engineering, Computational Mechanics, Design, Systems, Manufacturing, BioMedical Engineering; Process Engineering, Aerospace Engineering. No charges are required from the Authors to publish the articles.EMS is a quarterly published journal operating an online submission and peer review system. It allows authors to submit articles online and track their progress via its web interface.

https://dergipark.org.tr/ems

Contents

– *Research Articles*

– *Review Articles*

EUROPEAN MECHANICAL SCIENCE

Research Article

e-ISSN: 2587-1110

The effect of niobium carbide coating on wear behavior of grey cast iron via thermo-reactive diffusion process

Rifat Yakut[1*]

[1]Department of Energy Systems Engineering, Batman University, Batman, Türkiye

Orcid: R. Yakut (0000-0003-0059-3785)

Abstract: Wear is the limit for grey cast iron (GCI), which is utilized extensively in today's industries. Coating the surface of a material can enhance its ability to withstand wear. In this study, thermo-reactive diffusion (TRD) process was used to coat the surface of grey cast iron with niobium carbide (NbC). The coatings were applied for 2, 4 and 6 hours at 950^{0}C and 1050^{0}C. The coated samples were subjected to metallographic examination to investigate the microstructure of the coating zone. For this purpose, optical microscopy examinations were carried out. Microhardness tests were carried out to assess the mechanical properties of the samples. The coated surfaces were analyzed using energy-dispersive X-ray spectrometry (EDS), X-ray diffraction (XRD), and scanning electron microscopy (SEM). Wear tests were carried out on the coated surfaces to measure the volumetric wear loss, the wear rate and the changes in the coefficient of friction. Coating thickness rose as furnace waiting time increased, according to optical microstructures of coated surfaces. The hardness of the coated surfaces increased with a longer coating duration. Depending on the duration and temperature of the coating process, the layer thickness ranged from 6 to 52 μm. The lowest microhardness and the highest microhardness values of the coatings were determined at 950^{0}C for 2 hours and at 950^{0}C for 6 hours, respectively. Compared to the uncoated samples, the coated samples had a 6-9 times higher hardness value. In the abrasion tests, the loss of wear volume increased with increase in load.

Keywords: Thermo-Reactive Diffusion (TRD); Grey Cast Iron (GCI); Niobium Carbide (NbC); Sliding wear

1. Introduction

The use of cast iron is widespread in many industries. Meltability, strength and ductility are fundamental properties of this material. At heavy loads, it is utilized to replace steel castings. [1]. Chemically speaking, cast iron is a ferrous metal with more than 2% carbon content. It is an iron-carbon-silicon alloy containing about 1-3% silicon and 2-4% carbon. Cast iron contains elements such as phosphorus, manganese, sulfur, carbon and silicon [2]. Cast iron is a ternary Fe-C-Si alloy with small amounts of S and P [3, 4]. GCI is often used in engineering applications due to its features of vibration damping, machinability, and high thermal conductivity [5]. Due to its versatility, excellent castability, low cost (20-40% cheaper than steel) and strong mechanical properties, GCI is used in various industrial applications. The structure of GCI is influenced by its chemical composition, inoculants and cooling conditions [6-9]. Graphite flakes, which give them solid lubrication properties, are placed on the contact surfaces of GCI [10].

The hardness of the material, the high surface quality and the wear resistance ensure a long service life. In industrial settings, surface treatment processes are crucial for extending the life of mechanical components and tools [11]. Carbide and nitride coatings are utilized in various tribological applications, such as tools, mechanical components, and molds for processing metals, plastics, and glass. Traditionally, two different techniques have been used: physical vapor deposition (PVD) and chemical vapor deposition (CVD). However, these techniques have disadvantages such as plant invest-

*Corresponding author:
Email: rifat.yakut@batman.edu.tr

Cite this article as:
Yakut, R. (2024). The effect of niobium carbide coating on wear behavior of grey cast iron via thermo-reactive diffusion process. *European Mechanical Science*, *8*(3): 115-124. https://doi.org/10.26701/ems.1467274

History dates:
Received: 09.04.2024, ***Revision Request***: 25.04.2024, ***Last Revision Received***: 24.05.2024, ***Accepted***: 22.06.2024

ment cost, vacuum or highly controlled atmosphere [12, 13]. Moreover, CVD process produces highly toxic gases [14]. Carbide coatings are highly resistant to wear and corrosion. Therefore, they are of great industrial interest. One successful method for forming these coatings is TRD method [15]. TRD is a thermochemical process that forms dense and compact ceramic coatings on a substrate, especially steel [16-22]. The TRD method has many advantages compared to other coating processes, for example, being relatively simple, inexpensive [23], and environmentally friendly [24]. It produces consistent coatings with excellent adhesion, abrasion resistance and low friction. [16]. In TRD, elements form carbides in the salt and react with carbon atoms in the substrate. This produces an effective carbide coating that forms on the substrate surface. Niobium carbide, chromium carbide and vanadium carbide are the most commonly used single-carbide coatings [24]. Vanadium carbide (VC) and niobium carbide (NbC) are transition metal carbides. They have a wide range of industrial applications due to their high melting point, hardness, and thermal conductivity [25-27]. The layers formed by NbC coating have high microhardness [28], toughness and Young's modulus. This property is desirable for applications requiring high wear resistance. Moreover, this material is suitable for applications that require high temperatures, as its melting point is 3873.8°C [29]. The TRD technique is a high-temperature-resistant coating process that operates at temperatures between 800 and 1250°C [30]. Using a thermochemical process, a carbide-forming agent is deposited on the material's surface (Cr, V, Ti). Then a reaction occurs between the carbon decayed from the substrate to the surface and the carbide-forming agent [31-34]. This TRD technique was developed and patented by Toyota Motor Corp. in Japan [35-38]. Cai and Xu. [39] coated NbC on GCI using the in situ reaction (ISR) technique at 1085°C for 10, 20 and 30 minutes. In their study, it was discovered that the niobium carbide coating exhibited a lower wear rate, a higher load-carrying capacity, and excellent resistance to wear and corrosion.

Wear is a major problem in today's industry. Wearing is an unwanted deformation of materials caused by the mechanical actions of particles being removed from their surface [40]. Wearing causes deterioration, increased maintenance costs, pollution, energy costs and possibly accidents [41]. Corrosion and wear-resistant coatings are often required for mechanical components, such as tools that shape and machine workpieces. Selecting a suitable coating method can lead to significant performance improvements [42]. Mariani et al. [43] studied the formation of NbC and VC coatings (produced by TRD process) on Austempered Ductile Iron (ADI) specimens and their effects on the wear properties of the coatings. At 1000°C for 2 hours, they used molten salt baths containing sodium borate, aluminum, and a ferroalloy (Fe-V or Fe-Nb). As the high TRD temperature is responsible for the austenitisation of the sample, austenitisation in a further molten salt bath at 300°C occurred immediately after the TRD bath. Compared to the substrate, the coated parts were harder and more wear-resistant after these processes. The austempering process, on the other hand, increased the hardness further. The carbide coatings produced have a much higher wear performance (5-35 times) than the substrate. Soltani et al. [44] coated low-alloyed special tool steel (AISI L2) with NbC using the TRD process. The process took place in a sealed container containing a mixture of ferro niobium, ammonium chloride, and aluminum oxide powder at temperatures of 900, 950, 1000, and 1050°C over a period of 2, 4, 6, and 8 hours. Depending on the thickness of the coatings, the ratio of powders was optimized. After the TRD procedure, the samples were cooled in the air. This process resulted in NbC coatings of AISI L2 steel having a hardness of 2500±200 HV.

GCI, widely used in industry, is subject to wear. The surface hardening of GCI can increase the wear resistance. For this purpose, it is necessary to obtain a coating that effectively prevents wear and reduces the coefficient of friction. Therefore, GCI is coated, thus its surface hardness is increased. In this study, the surface of GCI was coated with NbC using TRD process. Coatings were performed for 2, 4 and 6 hours at 950°C and 1050°C. The microstructure of the coated samples was examined at the coating zone. Tests were then carried out using a reciprocal wear tester to investigate the wear behavior of the coated samples. Testing was conducted with a 6 mm Al_2O_3 ball at a 10 cm/s sliding speed, 8.5 mm sliding length, and 500 m total sliding distance, with loads of 10N and 15N, respectively. This study aims to improve the hardness and shear wear properties of coated surfaces by using the TRD process.

2. Materials and Methods

2.1. Preparation of Sample Materials

The substrate material used was GCI with a chemical composition of 3.30C-2.70Si-0.65Mn-0.016P-0.08S-0.28Cr-0.12Cu-0.001Al-0.025Ti (wt%) and equilibrium Fe. The GCI samples used as substrate material were cut with a precision metallographic cutter for microstructural analysis. All surfaces of the cut specimens were finally polished with 1200 mesh sandpaper. The polished samples were cleaned with alcohol before TRD process. For the coating process, Ferro Nb powder (45%), alumina (45%) and ammonium chloride (10%) were weighed with a precision balance and then mixed. Ferro niobium (FeNb) powder with a chemical composition of 65Nb-0.10C-2.5Si-0.05S-0.1P-1.5Al (wt%) was used in equal weight for each experiment. Melting point, purity, density, and size were 1530-1580°C, 99.5%, 8.1 g/cm^3 and 43 µm, respectively. This powder material was purchased from BC Technology (Türkiye). All surfaces of the GCI specimens used as the substrate materials were polished, cleaned and placed in a stainless steel crucible with the coating powder mixture. The crucible was then tightly sealed. Preparation of the crucibles was followed by coating at 950°C and 1050°C using the TRD process. After the process, the crucibles, which were removed from the furnace, were rapidly cooled with water, then the mouth of each crucible was opened, and the samples were quickly removed and cooled in water.

2.2. Sample characterization

The samples coated in accordance with the TRD method were molded using the cold molding technique. They were sanded through coarse and fine stages until the base material was reached. The ground specimens were polished with 3 and 1-micron diamond solutions. They were etched with a 5% Nital solution. Thus, the coating layer and layer-substrate material interface cross-sections were prepared for optical microscopy and SEM. The inverted metal microscope Nikon MA 100 and the image analysis system, Clemex, were used for the optical microscopy. EDS and XRD analyses were performed on the coated surfaces, along with SEM analysis.

In this study, microhardness measurements were performed on samples prepared for optical microscopy, such as coating cross-section and the substrate material near the interface. The hardness measurements on the samples used in the experiments were performed with the Future Tech FM -700 Vickers hardness tester. The parameters used for the microhardness measurements were 50 gf load and 10 seconds duration.

Sliding wear tests were performed according to ASTM G99. All abrasion tests were carried out with a reciprocating abrasion tester under normal atmospheric conditions (25 ± 1 °C and 60 ± 2% humidity) in a dry environment. The abrasive used was a 6mm diameter Al_2O_3 ball. The wear tests were carried out under 10N and 15N loads. The sliding speed was 10 cm/s, the sliding length was 8.5 mm, and the total sliding distance was 500 m. Friction coefficients were recorded during the test. The sliding wear was carried out on a different area of the specimen each time. The wear marks never overlapped. After the abrasion tests, the appearance of the abrasion marks was examined via SEM.

3. Results and Discussion

3.1. Microhardness test results

For the measurements at 950°C, the average hardness values were found to be 1943 HV for 2-hour coating, 2231 HV for 4-hour coating and 2551 HV for 6-hour coating. Hardness measurements at 1050°C were recorded as average hardness values of 2259 HV in 2-hour coating, an average of 2448 HV in 4-hour coating and an average of 2364 HV in 6-hour coating. At the end of the hardness measurements, it was found that the highest average value for the coating was measured at 950°C for 6 hours. The lowest average value was obtained for the coating held at 950°C for 2 hours. It was established that as the coating time increased, the hardness values increased. The hard NbC phase and the microstructure greatly influenced the hardness of the coating [39]. The results of the hardness measurements for NbC-coated samples are shown in ▶**Table 1** for various temperatures and dwell times.

Soares et al. [41] treated two ductile cast irons (with and without copper addition) in a salt bath of borax, Ferro niobium (16 wt%) and aluminum (3 wt%) at 1000 °C for 4 hours. The hardness measurements they carried out on the samples produced using the TRD process yielded NbC coatings with a hardness of more than 2000 HV. Mariani et al. [45] subjected GCI samples to two thermo-reactive niobizing processes as a substrate material. Iron-niobium powders, NH_4Cl, and Al_2O_3 were used for the first process, which took 2 hours at 900°C. In the second process of the TRD method, a liquid molten bath consisting of sodium borate and iron niobium was used for 2 hours at 900°C. After the surface coating process with NbC, the hardness measurement value was obtained as 2000 HV. When similar studies are examined, it is seen that the microhardness values obtained in this study and shown in ▶**Table 1** are compatible with those of other studies.

Table 1. Average values of microhardness of NbC-coated samples

Coating Temperature (°C)	Coating Time (hour)	Coating Thickness (μm)	Microhardness (HV)	
			Coating Layer	Substrate Material (Grey Cast Iron)
950	2	11± 2	1943 ± 182	290± 83
950	4	14± 2	2231 ± 63	
950	6	16± 3	2551 ± 129	
1050	2	7± 1	2259 ± 187	
1050	4	14± 2	2448 ± 49	
1050	6	41± 9	2364 ± 90	

3.2. Wear Test Results

In this study, the development of wear was continuously analyzed. The highest coefficient of friction was observed at a load value of 10N at 1050°C for 6 hours, while the lowest coefficient of friction was observed at a load value of 10N at 950°C for 2 hours, considering the changes in the coefficient of friction of the samples in **▶Figure 1**. The applied load and the reinforcement ratios are shown in **▶Table 2**. The maximum wear volume loss was found to be 6.97×10^{-2} mm^3 at a load of 15 N on the grey cast iron surface used as the substrate material. The maximum wear volume loss was 2.29×10^{-2} mm^3 at 2 hours and 15 N load for 2 hours, 4 hours and 6 hours at 950°C. The lowest wear volume loss at 950°C was 1.84×10^{-2} mm^3 at 6 hours and 10 N load. The highest wear volume loss for 2 h, 4 h and 6 h at 1050°C was 2.66×10^{-2} mm^3 for 6 h and 15 N load. The lowest wear volume loss at 1050°C was 1.54×10^{-2} mm^3 at 2 hours and 10 N load. When analyzing the wear volume loss (**▶Figure 2**), it was found that the wear volume loss increased with increasing load when the temperature and waiting time were kept constant. In addition, an increase in the coefficient of friction with increasing load was also observed at constant temperature and waiting time. It can be said that the wear rate (**▶Figure 3**) also generally increases with increasing load when the temperature and dwell time are kept constant. More severe wear conditions can be attributed to the increase in wear loss of the specimens with applied load and sliding speed. The tendency to crack due to dissolution at the interfaces between graphite and matrix leads to a significantly higher wear loss due to the crumbling of the material. The changing slope of the wear loss versus load graphs (**▶Figure 2**) shows that the mechanism of working wear is changing. For example, a low inclination corresponds to light wear, while a high inclination indicates heavy wear [46]. GCI's wear rate increased with increasing load during wear tests [10]. However, when the surface of the GCI was coated with NbC using TRD method and the temperatures and waiting times were kept constant, it was observed that the wear rate values (**▶Figure 3**) decreased with increasing load. This situation can be explained by the fact that the hardness of the coating surface increases with increasing temperature and waiting time. The hardness of materials is a decisive factor influencing wear properties [38, 47]. As the material's hardness increases, the wear rate decreases as it becomes more difficult to remove particles from the surface. Factors that influence wear resistance include microstructure, surface hardness, modulus of elasticity, size and distribution of hard particles [47]. In the dry sliding test, the contact area between the coating and the counterpart was reduced compared to the substrate. This led to a reduction in the coefficient of friction due to the harder NbC phase and the fine microstructure in the coating [39, 48, 49].

3.3. Optical and SEM/EDS/XRD Results

The substrate material was coated with NbC using the TRD technique for 2 hours, 4 hours and 6 hours. Optical microstructures were examined to analyze the coating layer, and SEM examinations were carried out after wear tests. When investigating the optical microstructures of NbC coatings held at 950 °C for 2 hours, 4 hours and 6 hours, it was found that the coating thickness increased as a function of the holding time in the oven. It was determined that the coating time is a determining parameter in coating thickness. Optical microstructure views are given in **▶Figure 4**. Depending on the deposition time and temperature, NbC layers with a thickness of 6 to 52 μm formed on the substrate.

Table 2. Values of the volume loss, wear rate, and coefficient of friction for the samples

Coating Temperature (°C)	Coating Time (Hours)	Load (N)	Volume Loss ($\times 10^{-2}$ mm^3)	Wear Rate ($\times 10^{-6}$ mm^3/Nm)	Coefficient of Friction (COF)
Substrate Material (Grey Cast Iron)	-	10	6.62	13.25	0.511
	-	15	6.97	9.30	0.445
950	2	10	1.95	3.91	0.249
950	2	15	2.29	3.05	0.342
950	4	10	1.90	3.79	0.373
950	4	15	2.11	2.81	0.392
950	6	10	1.84	3.69	0.404
950	6	15	2.06	2.75	0.423
1050	2	10	1.54	3.08	0.518
1050	2	15	2.39	3.18	0.601
1050	4	10	1.89	3.79	0.434
1050	4	15	2.09	2.78	0.455
1050	6	10	2.23	4.45	0.630
1050	6	15	2.66	3.55	0.529

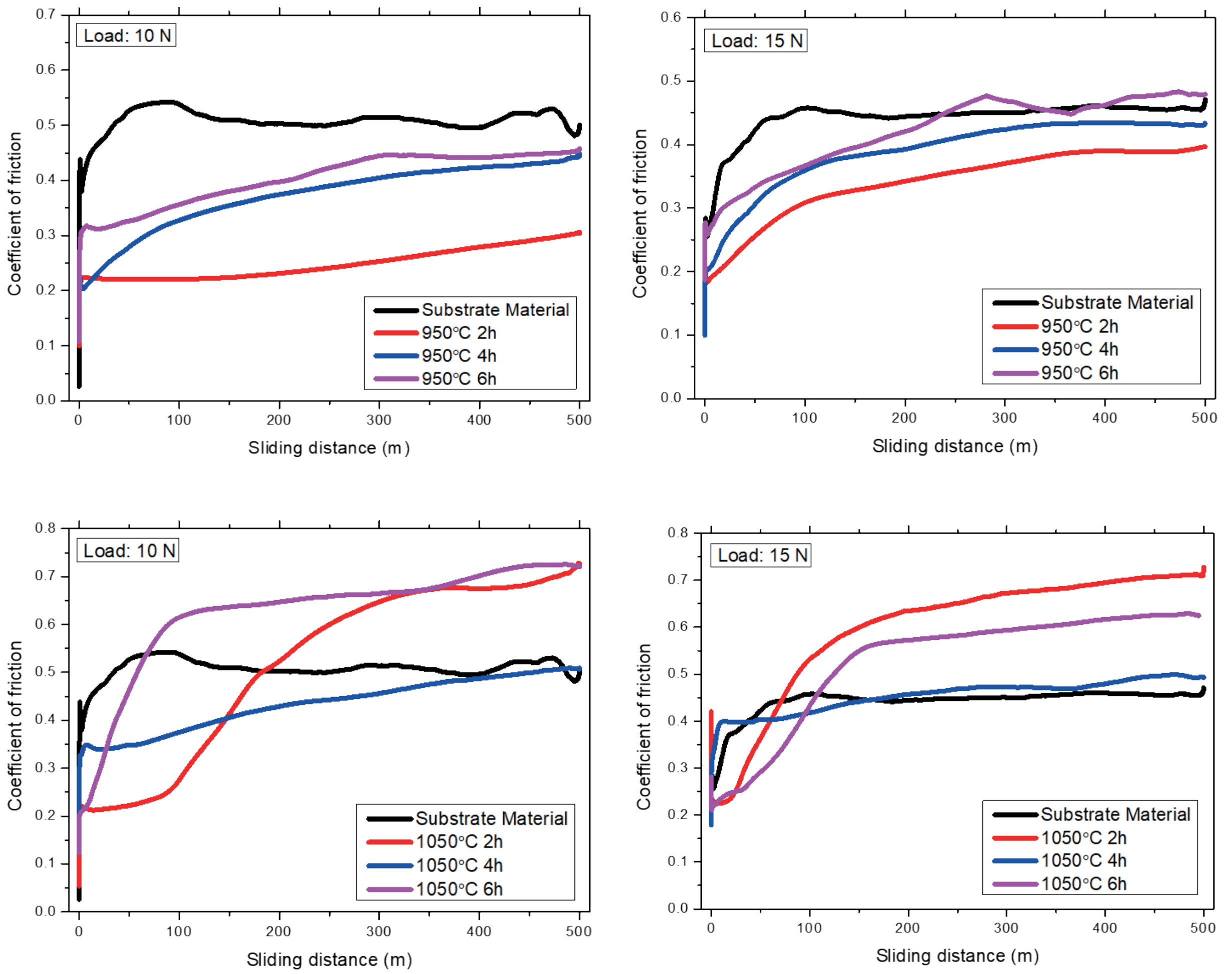

Figure 1. Comparison of friction coefficients at 10 N and 15 N loads

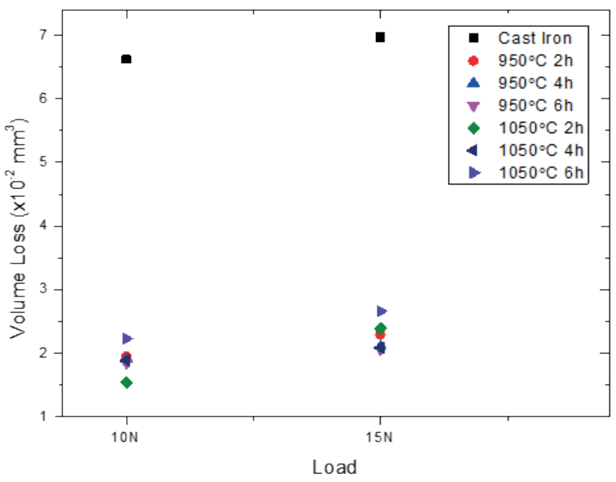

Figure 2. Wear volume loss measurement values

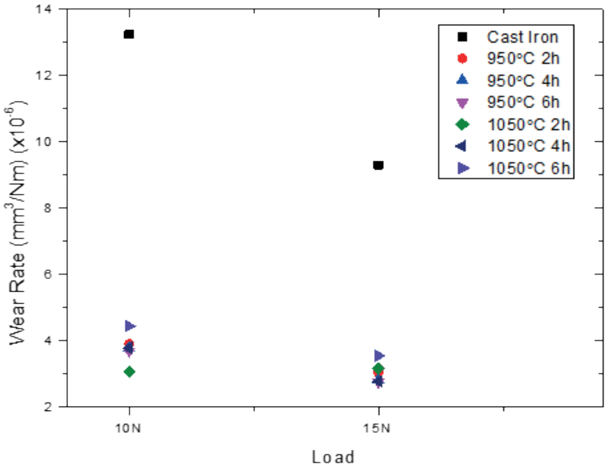

Figure 3. Wear rate measurement values

Element diffusion analysis mainly focuses on C and Nb atoms. Nb atoms can diffuse into the substrate and form a layer of solid solution on its surface. The nucleation of NbC begins at the dislocations or grain boundaries on the substrate's surface. The crystal nucleus grows and expands to form a thin, continuous layer of NbC [50]. Niobium carbide's structure is a face-centered cubic (FCC) lattice. The niobium atoms are located in the FCC phase, and the carbon atoms are in the intermediate areas, resulting in a subtly defined crystalline material [15]. The grain size is significantly influenced by the concentration of C atoms [51]. In this study, NbC

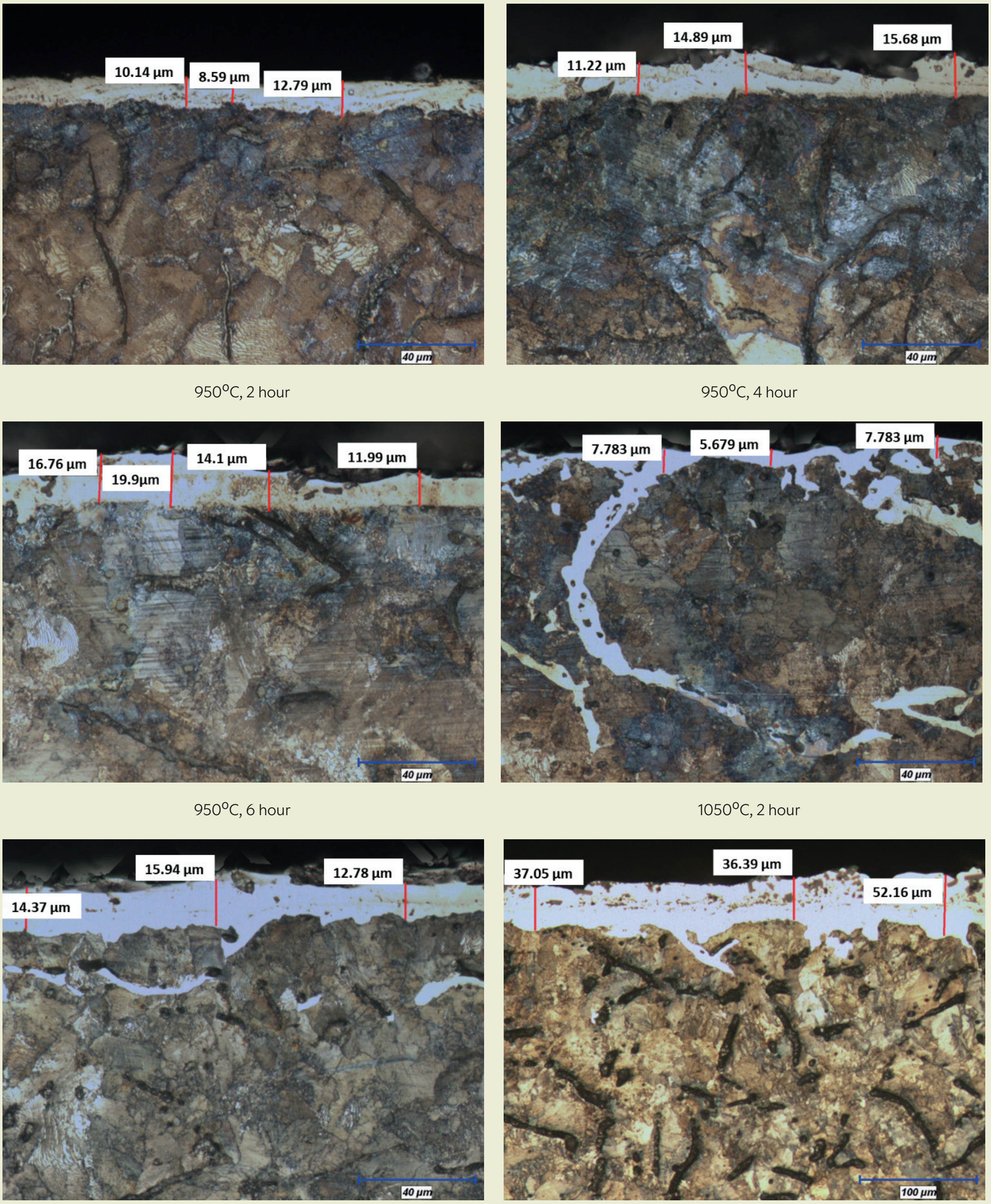

950°C, 2 hour

950°C, 4 hour

950°C, 6 hour

1050°C, 2 hour

1050°C, 4 hour

1050°C, 6 hour

Figure 4. Optical microstructure views

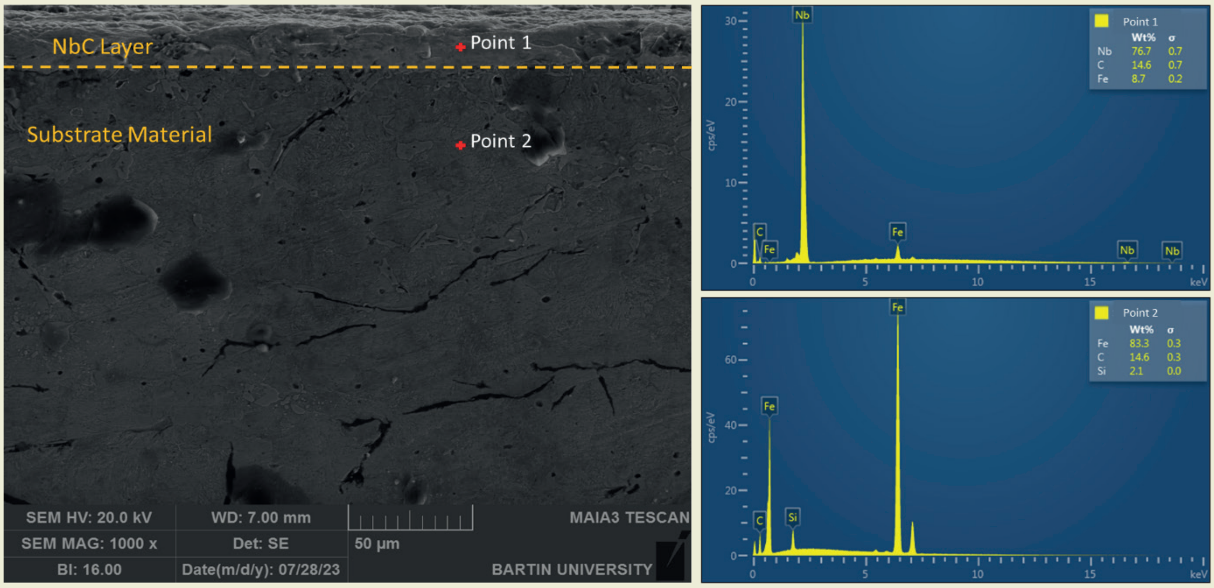

Figure 5. EDS image of NbC coated specimens at 950°C for 6 hours

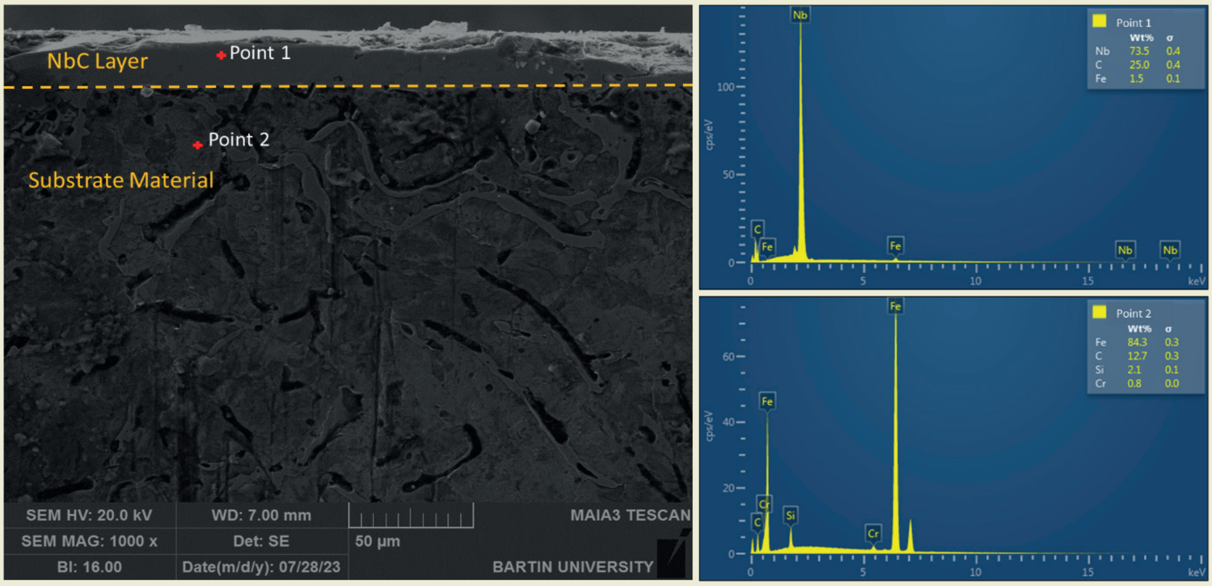

Figure 6. EDS image of NbC coated specimens at 1050°C for 4 hours

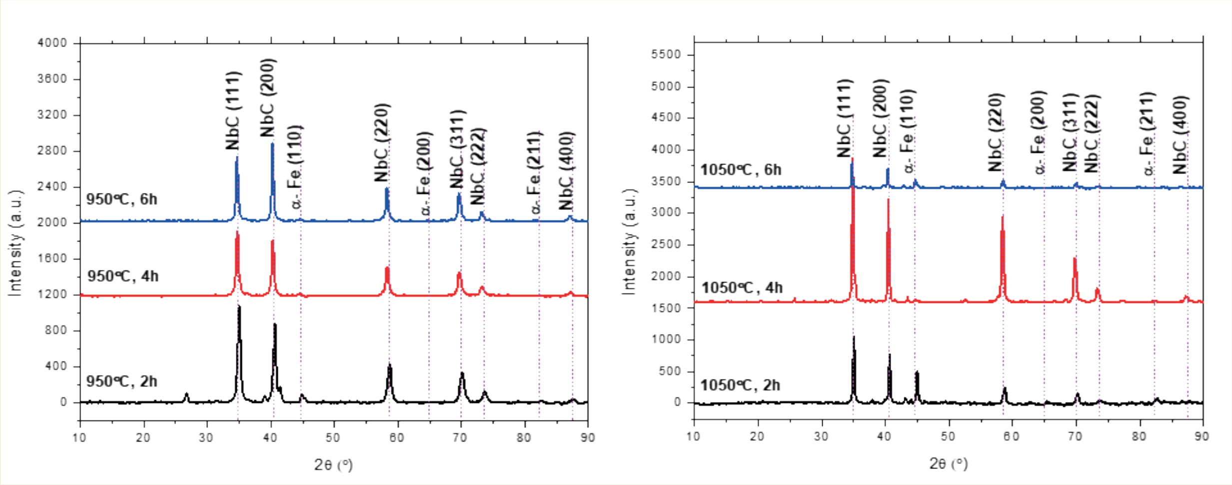

Figure 7. XRD analysis results of NbC-coated samples

extended due to the high diffusion speed of the grain boundaries and the graphite carbon density.

NbC was coated on grey cast iron by TRD method at 950 and 1050°C for 2, 4 and 6 hours. When EDS image (**▶Figure 5**) of NbC coated samples at 950°C for 6 hours was analyzed, wt% Nb: 76.7, C: 14.6, Fe: 8.7 in spectrum 37 (Point 1) and wt% Fe: 83.3, C: 14.6, Si: 2.1 in spectrum 39 (Point 2) were found. When EDS image (**▶Figure 6**) of NbC coated samples, which were kept at 1050°C for 4 hours, was analyzed, wt% Nb:73.5, C:25.0, Fe:1.5 in spectrum 10 (Point 1) and wt% Fe:84.3, C:12.7, Si: 2.1, Cr:0.8 in spectrum 12 (Point 2) were found.

When the results of the XRD analysis of the NbC-coated samples are examined in **▶Figure 7**, it can be seen that the NbC phase has been formed as the dominant phase on the surface of all the samples. Soares et al. [41] coated spheroidal graphite iron surfaces with NbC using TRD. The XRD analysis conducted on the coating layer revealed that it was made up solely of NbC phase. OrjuelaG et al. [30] coated AISI 1045 steel surfaces with NbC using TRD method. XRD analysis of the coating layer showed that NbC phase was the main phase, while the other phase was α-Fe.

After the sliding wear test under dry sliding conditions were conducted, the sample surfaces were analyzed using the TESCAN MAIA3 XMU scanning electron microscope (SEM) (**▶Figure 8**). When the sample coated at 1050°C for 2 hours was subjected to an abrasion test at 15 N load, the abrasion marks were clearly visible. As the applied load increases, so does the contact pressure [52]. Due to the high hardness of the coated parts, no damage to the wear surfaces due to particle breakage was observed. However, the coated samples showed higher wear resistance. As a result, fewer particles broke off the coated surfaces and smoother surfaces were achieved.

4. Conclusions

The surface of the grey cast iron was coated with NbC using the Thermo-reactive diffusion technique (TRD). The coating process was carried out at 950°C and 1050°C for 2, 4 and 6 hours. The microstructure of the coated samples was analyzed in the area of the coating. Tests were then carried out using a reciprocating wear tester to investigate the wear behavior of the coated samples. The wear tests were carried out under 10N and 15N loads. The results obtained in the study are given below:

- When examining the optical microstructures of 2, 4 and 6 NbC layers, it was found that the layer thicknesses increased with the waiting time in the furnace.

- NbC layers with a thickness of 6 to 52 μm were formed on the substrate, depending on the coating time and temperature. Hardness measurements showed the coating's highest value at 950°C for 6 hours and the lowest value at 950°C for 2 hours.

- The substrate material showed the highest volumetric wear loss at a load of 15 N, while the sample coated for 2 hours at 1050°C showed the lowest volumetric wear loss at a load of 10 N.

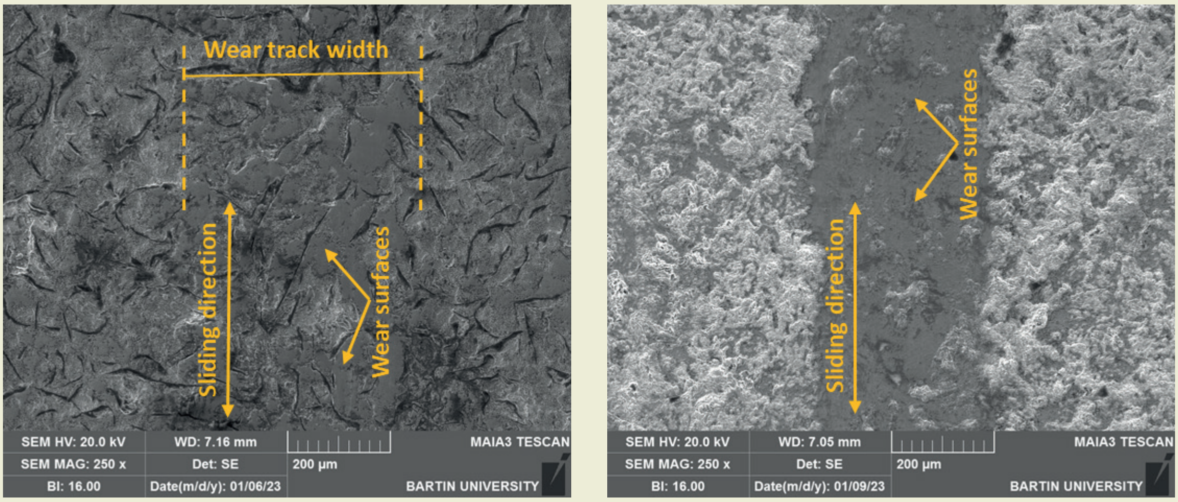

950°C, 2 hour, 15N

1050°C, 2 hour, 15N

Figure 8. SEM images after sliding wear tests

- The highest wear rate occurred at a load of 10 N on the substrate material, while the lowest wear rate occurred at a load of 15 N on the sample coated at 950°C for 6 hours.

Research Ethics

Ethical approval not required.

Author Contributions

The author(s) accept full responsibility for the content of this article and have approved its submission.

Competing Interests

The author(s) declare that there are no competing interests.

Research Funding

Not reported.

Data Availability

Not applicable.

Peer-review

Externally peer-reviewed.

References

[1] Tokova, O., & Savchenko, Y. (2019). Modelling of dependence of mechanical properties of cast iron on chemical composition of raw materials. In *2019 IEEE 14th International Conference on Computer Sciences and Information Technologies (CSIT)* (pp. 179-182). IEEE. https://doi.org/10.1109/stc-csit.2019.8929865

[2] Yakut, R., & Çiftçi, Ö. (2023). Investigation of the microstructure, hardness, and compressive properties of TaC-reinforced lamellar graphite cast irons. *European Mechanical Science, 7*(2), 56-62. https://doi.org/10.26701/ems.1213039

[3] Nam, J., Lee, S., & Lee, S. (2023). Guaranteed soundness of heavy section spheroidal graphite cast iron based on a reliable C and Si ranges design. *Metals and Materials International, 29*(8), 2151-2158. https://doi.org/10.1007/s12540-022-01377-4

[4] Lima, F. F. O., Bauri, L. F., Pereira, H. B., & Azevedo, C. R. F. (2020). Effect of the cooling rate on the tensile strength of pearlitic lamellar graphite cast iron. *International Journal of Cast Metals Research, 33*(4-5), 201-217. https://doi.org/10.1080/13640461.2020.1822573

[5] Diószegi, A., Svidró, P., Elmquist, L., & Dugic, I. (2016). Defect formation mechanisms in lamellar graphite iron related to the casting geometry. *International Journal of Cast Metals Research, 29*(5), 279-285. https://doi.org/10.1080/13640461.2016.1211579

[6] Collini, L., Nicoletto, G., & Konečná, R. (2008). Microstructure and mechanical properties of pearlitic gray cast iron. *Materials Science and Engineering: A, 488*(1-2), 529-539. https://doi.org/10.1016/j.msea.2007.11.070

[7] Bartocha, D., Janerka, K., & Suchoń, J. (2005). Charge materials and technology of melt and structure of gray cast iron. *Journal of Materials Processing Technology, 162-163*, 465-470. https://doi.org/10.1016/j.jmatprotec.2005.02.050

[8] Xu, W., Ferry, M., & Wang, Y. (2005). Influence of alloying elements on as-cast microstructure and strength of gray iron. *Materials Science and Engineering: A, 390*(1-2), 326-333. https://doi.org/10.1016/j.msea.2004.08.030

[9] Hemanth, J., & Rao, K. S. (1999). Effect of cooling rate on eutectic cell count, grain size, microstructure, and ultimate tensile strength of hypoeutectic cast iron. *Journal of Materials Engineering and Performance, 8*(4), 417-423. https://doi.org/10.1361/105994999770346701

[10] Prasad, B. K. (2005). Sliding wear response of a zinc-based alloy and its composite and comparison with a gray cast iron: Influence of external lubrication and microstructural features. *Materials Science and Engineering: A, 392*(1-2), 427-439. https://doi.org/10.1016/j.msea.2004.10.031

[11] Fesahat, M., Soltanieh, M., & Eivani, A. R. (2016). Effect of plasma nitriding on nanostructure of TRD coating. *Surface Engineering, 32*(8), 547-553. https://doi.org/10.1179/1743294415Y.0000000094

[12] Biesuz, M., & Sglavo, V. M. (2016). Chromium and vanadium carbide and nitride coatings obtained by TRD techniques on UNI 42CrMoS4 (AISI 4140) steel. *Surface and Coatings Technology, 286*, 319-326. https://doi.org/10.1016/j.surfcoat.2015.12.063

[13] Fan, X. S., Yang, Z. G., Zhang, C., Zhang, Y. D., & Che, H. Q. (2010). Evaluation of vanadium carbide coatings on AISI H13 obtained by thermo-reactive deposition/diffusion technique. *Surface and Coatings Technology, 205*(2), 641-646. https://doi.org/10.1016/j.surfcoat.2010.07.065

[14] Najari, M. R., Sajjadi, S. A., & Ganji, O. (2022). Microstructural evolution and wear properties of chromium carbide coating formed by thermo-reactive diffusion (TRD) process on a cold-work tool steel. *Results in Surfaces and Interfaces, 8*, 100059. https://doi.org/10.1016/j.rsurfi.2022.100059

[15] Ghadi, A., Ebrahimnezhad-Khaljiri, H., & Gholizadeh, R. (2023). A comprehensive review on the carbide-base coatings produced by thermo-reactive diffusion: Microstructure and properties viewpoints. *Journal of Alloys and Compounds, 967*, 171839. https://doi.org/10.1016/j.jallcom.2023.171839

[16] Ganji, O., Sajjadi, S. A., Yang, Z., Mirjalili, M., & Najari, M. R. (2020). On the formation and properties of chromium carbide and vanadium carbide coatings produced on W1 tool steel through thermal reactive diffusion (TRD). *Ceramics International, 46*(16), 25320-25329. https://doi.org/10.1016/j.ceramint.2020.06.326

[17] Strahin, B. L., Shreeram, D. D., & Doll, G. L. (2017). Properties and tribological performance of vanadium carbide coatings on AISI 52100 steel deposited by thermo-reactive diffusion. *JOM, 69*(7), 1160-1164. https://doi.org/10.1007/s11837-017-2370-2

[18] Arai, T. (2015). The thermo-reactive deposition and diffusion process for coating steels to improve wear resistance. In *Thermochemical Surface Engineering of Steels* (pp. 703-735). https://doi.org/10.1533/9780857096524.5.703

[19] Khalaj, G., Nazari, A., Khoie, S. M. M., & Khalaj, M. J., Pouraliakbar, H. (2013). Chromium carbonitride coating produced on DIN 1.2210 steel by thermo-reactive deposition technique: Thermodynamics, kinetics and modeling. *Surface and Coatings Technology, 225*, 1-10. https://doi.org/10.1016/j.surfcoat.2013.02.030

[20] Khalaj, G., & Pouraliakbar, H. (2014). Computer-aided modeling for predicting layer thickness of a duplex treated ceramic coating on tool steels. *Ceramics International, 40*(4), 5515-5522. https://doi.org/10.1016/j.ceramint.2013.10.141

[21] Khalaj, G. (2012). Artificial neural network to predict the effects of coating parameters on layer thickness of chromium carbonitride coating on pre-nitrided steels. *Neural Computing and Applications, 23*(3-4), 779-786. https://doi.org/10.1007/s00521-012-0994-2

[22] Pouraliakbar, H., Khalaj, G., Gomidželović, L., Khalaj, M. J., & Nazerfakhari, M. (2015). Duplex ceramic coating produced by low temperature thermo-reactive deposition and diffusion on the cold work tool steel substrate: Thermodynamics, kinetics and modeling. *Ceramics International, 41*(8), 9350-9360. https://doi.org/10.1016/j.ceramint.2015.03.306

[23] Amaya, A., Piamba, O., & Olaya, J. (2018). Improvement of corrosion resistance for gray cast iron in palm biodiesel application using thermoreactive diffusion niobium carbide (NbC) coating. *Coatings, 8*(6), 216. https://doi.org/10.3390/coatings8060216

[24] Jin, W., Meng, Q., Niu, L., Li, C., & Wang, H. (2017). Properties of the functionally gradient chromium-niobium carbide coating obtained by thermo-reactive deposition technique. *Key Engineering Materials, 753*, 129-133. https://doi.org/10.4028/www.scientific.net/kem.753.129

[25] Triani, R. M., Mariani, F., De Assis Gomes, L. F., De Oliveira, P. G., Totten, G. E., & Casteletti, L. C. (2019). Improvement of the tribological characteristics of AISI 8620, 8640 and 52100 steels through thermo-reactive treatments. *Lubricants, 7*(8), 63. https://doi.org/10.3390/lubricants7080063

[26] Cuppari, M. G., & Santos, S. F. (2016). Physical properties of the NbC carbide. *Metals, 6*(10), 250. https://doi.org/10.3390/met6100250

[27] Johansson, L. I. (1995). Electronic and structural properties of transition-metal carbide and nitride surfaces. *Surface Science Reports, 21*(5-6), 177-250. https://doi.org/10.1016/0167-5729(94)00005-0

[28] Yingpeng, L., Wang, K., Fu, H., Bin, Z., & Zhang, J. (2023). Wear resistance of in situ NbC-reinforced laser cladding Ni45 coatings. *Lubricants, 11*(8), 316. https://doi.org/10.3390/lubricants11080316

[29] De Oliveira, P. G., Triani, R. M., Filho, A. I., Neto, A. L., Totten, G. E., & Casteletti, L. C. (2021). Production of niobium carbide layers on high-strength bainitic steels by thermo-chemical treatment of TRD followed by austempering. *Steel Research International, 93*(1), 2100352. https://doi.org/10.1002/srin.202100352

[30] Orjuela-G, A., Rincon, R., & Olaya, J. J. (2014). Corrosion resistance of niobium carbide coatings produced on AISI 1045 steel via thermo-reactive diffusion deposition. *Surface & Coatings Technology, 259*, 667-675. https://doi.org/10.1016/j.surfcoat.2014.10.012

[31] Aghaie-Khafri, M., & Fazlalipour, F. (2008). Kinetics of V(N,C) coating produced by a duplex surface treatment. *Surface and Coatings Technology, 202*(17), 4107-4113. https://doi.org/10.1016/j.surfcoat.2008.02.027

[32] Taktak, S., & Ulu, S. (2010). Wear behaviour of TRD carbide coatings at elevated temperatures. *Industrial Lubrication and Tribology, 62*(1), 37-45. https://doi.org/10.1108/00368791011012452

[33] King, P., Reynoldson, R. W., Brownrigg, A., & Long, J. A. (2004). Cr(N,C) diffusion coating formation on pre-nitrocarburised H13 tool steel. *Surface and Coatings Technology, 179*(1), 18-26. https://doi.org/10.1016/s0257-8972(03)00791-6

[34] Ozdemir, O., Sen, S., & Sen, U. (2007). Formation of chromium nitride layers on AISI 1010 steel by nitro-chromizing treatment. *Vacuum, 81*(5), 567-570. https://doi.org/10.1016/j.vacuum.2006.07.002

[35] Castillejo, F. E., Marulanda, D. M., Olaya, J. J., & Alfonso, J. E. (2014). Wear and corrosion resistance of niobium–chromium carbide coatings on AISI D2 produced through TRD. *Surface and Coatings Technology, 254*, 104-111. https://doi.org/10.1016/j.surfcoat.2014.05.069

[36] Wu, Z., Qing, H., Guo, H., & Chen, Y. (2021). Growth and mechanical properties of Nb-Cr carbide coatings on graphite by TRD technique. *International Journal of Refractory Metals and Hard Materials, 101*, 105660. https://doi.org/10.1016/j.ijrmhm.2021.105660

[37] Günen, A., Kalkandelen, M., Gök, M. S., Kanca, E., Kurt, B., Karakaş, M. S., Karahan, İ. H., & Çetin, M. (2020). Characteristics and high temperature wear behavior of chrome vanadium carbide composite coatings produced by thermo-reactive diffusion. *Surface and Coatings Technology, 402*, 126402. https://doi.org/10.1016/j.surfcoat.2020.126402

[38] Kurt, B., Küçük, Y., & Gök, M. S. (2014). Microabrasion wear behavior of VC and CrC coatings deposited by thermoreactive diffusion technique. *Tribology Transactions, 57*(2), 345-352. https://doi.org/10.1080/10402004.2014.880538

[39] Cai, X., & Xu, Y. (2017). Microstructure, friction and wear of NBC coatings on a Fe substrate fabricated via an in situ reaction. *Surface and Coatings Technology, 322*, 202-210. https://doi.org/10.1016/j.surfcoat.2017.05.046

[40] Yakut, R., & Çiftçi, Ö. (2022). The effects of reinforcement with TaC on the microstructure and wear properties of lamellar graphite cast irons. *European Journal of Technique, 12*(1), 77-81. https://doi.org/10.36222/ejt.1088994

[41] Soares, C., Mariani, F. E., Casteletti, L. C., Lombardi, A. N., & Totten, G. E. (2017). Characterization of niobium carbide layers produced in ductile cast iron using Thermo-Reactive treatments. *Materials Performance and Characterization, 6*(4), 607-616. https://doi.org/10.1520/mpc20160093

[42] Wei, C.-Y., & Chen, F.-S. (2005). Characterization on multi-layer fabricated by TRD and plasma nitriding. *Materials Chemistry and Physics, 90*(1), 178-184. https://doi.org/10.1016/j.matchemphys.2004.10.008

[43] Mariani, F. E., Lombardi, A. N., & Casteletti, L. C. (2022). Tribological evaluation of NbC and VC layers produced by thermo-reactive diffusion treatment in ductile cast irons with varying composition. *Journal of Materials Engineering and Performance, 32*(12), 5421-5434. https://doi.org/10.1007/s11665-022-07495-9

[44] Soltani, R., Sohi, M. H., Ansari, M., Haghighi, A., Ghasemi, H. M., & Haftlang, F. (2017). Evaluation of niobium carbide coatings produced on AISI L2 steel via thermo-reactive diffusion technique. *Vacuum, 146*, 44-51. https://doi.org/10.1016/j.vacuum.2017.09.023

[45] Mariani, F., Rêgo, G. C., Bonella, P. G., Neto, A. L., Totten, G. E., & Casteletti, L. C. (2020). Wear resistance of niobium carbide layers produced on gray cast iron by thermoreactive treatments. *Journal of Materials Engineering and Performance, 29*(6), 3516-3522. https://doi.org/10.1007/s11665-020-04645-9

[46] Prasad, B. K. (2011). Sliding wear response of a grey cast iron: Effects of some experimental parameters. *Tribology International, 44*(5), 660-667. https://doi.org/10.1016/j.triboint.2011.01.006

[47] Arabi Jeshvaghani, R., Shamanian, M., & Jaberzadeh, M. (2011). Enhancement of wear resistance of ductile iron surface alloyed by stellite 6. *Materials & Design, 32*(4), 2028-2033. https://doi.org/10.1016/j.matdes.2010.11.060

[48] Zhang, L., Sun, D., & Yu, H. (2008). Effect of niobium on the microstructure and wear resistance of iron-based alloy coating produced by plasma cladding. *Materials Science and Engineering: A, 490*(1-2), 57-61. https://doi.org/10.1016/j.msea.2008.02.041

[49] Mishra, R., Basu, B., & Balasubramaniam, R. (2004). Effect of grain size on the tribological behavior of nanocrystalline nickel. *Materials Science and Engineering: A, 373*(1-2), 370-373. https://doi.org/10.1016/j.msea.2003.09.107

[50] Cai, X., Xu, Y., Zhao, N., Zhong, L., Zhao, Z., & Wang, J. (2016). Investigation of the adhesion strength and deformation behavior of in situ fabricated NBC coatings by scratch testing. *Surface and Coatings Technology, 299*, 135-142. https://doi.org/10.1016/j.surfcoat.2016.05.004

[51] Cai, X., Xu, Y., Liu, M., Zhong, L., & Bai, F. (2017). Preparation of a gradient nanostructured surface TaC layer-reinforced Fe substrate by in situ reaction. *Journal of Alloys and Compounds, 712*, 204-212. https://doi.org/10.1016/j.jallcom.2017.04.081

[52] Tasyurek, M., & Duzcukoglu, H. (2021). Improving the wear behavior of epoxy resin with boron carbide reinforcement. *Iranian Polymer Journal, 31*(2), 169-184. https://doi.org/10.1007/s13726-021-00987-w

EUROPEAN
MECHANICAL
SCIENCE

Research Article

e-ISSN: 2587-1110

Comparison of the impact of R449-A and R290 on refrigerated display cabinets using life-cycle climate performance method

Havva Demirpolat[1*], Süleyman Erten[2], Şafak Ataş[3], Mustafa Aktaş[4], Mehmet Özkaymak[3]

[1] Selçuk University,Faculty of Technology, Mechanical Engineering, Konya, Türkiye
[2] Nurdil Technical Refrigeration, Ankara, Türkiye
[3] KarabükUniversity, Energy Systems Engineering, Karabük, Türkiye
[4] Gazi University, Energy Systems Engineering, Ankara, Türkiye

Orcid: H.Demirpolat (0000-0002-2981-9867), S.Erten(0000-0002-7811-6148), Ş.Ataş(0000-0003-4124-8929), M.Aktaş(0000-0003-1187-5120), M.Özkaymak(0000-0002-4575-8988)

Abstract: Due to the high energy consumption of refrigerated display cabinets used in supermarkets, a life cycle cooling performance analysis to increase energy efficiency and reduce environmental impacts is the main subject of this study. It also emphasizes the need for cabinets that consume less energy and provide environmentally friendly working conditions. The Life Cycle Climate Performance (LCCP) of the two refrigerants R290 and R449-A was evaluated using measured data to compare the environmental impact of the refrigerants over the entire fluid and equipment life cycle, including energy consumption. Both vapor-compressed cooling cycles were thermodynamically modeled with the parameters taken from the experiments and the efficiency of system was calculated by using the EES software. The results show that the cabinet using R290 has lower compressor power utilization. The COP of the R290 system increased by 13% compared to the R449A system. The total daily energy consumption was also significantly lower for the R290 system. The energy efficiency index provides a standardized metric that can be used to compare the performance of different cooling systems. In this study, the energy efficiency index value was 17.3 points lower for the R290 system, indicating higher energy efficiency. The energy classes are "E" for the R449-A system and "C" for the R290 system, with the R290 system two classes higher in terms of energy class labeling. The EEI value of the system with R290 refrigerant has been reduced by 33% in comparison with the system with R449A refrigerant. The system using R290 refrigerant achieved a 33% reduction in energy consumption compared to the system using R449A refrigerant. The study also assessed the life cycle climate performance of the two systems. It was found that the R449-A system emits 19032.45 kg CO2e more over its lifetime compared to the R290 system. This was attributed to the relatively high global warming potential and energy consumption of R449-A refrigerant. However, when considering safety (flammability), it was concluded that R-449A has a lower environmental impact than R-290.

Keywords: LCCP; R449-A; R290; RDC.

1. Introduction

Commercial refrigerated display cabinets (RDCs) preserve and display food products by extending their shelf life. RDCs are in constant use 24 hours a day, and this continuous operation accounts for approximately 60% of the total energy consumption of supermarkets and food retail stores [1]. This energy-intensive situation in the commercial refrigeration system leads to the production of greenhouse gases (GHGs) with a global warming impact, directly based on the leakage of hydro-

Corresponding author:
Email: hdemirpolatl@selcuk.edu.tr

Cite this article as:
Demirpolat, H., Erten, S., Ataş, Ş., Aktaş, M., Özkaymak, M. (2024). Comparison of the impact of R449-A and R290 on refrigerated display cabinets using life-cycle climate performance method. *European Mechanical Science*, *8*(3): 125-136. https://doi.org/10.26701/ems.1493164

History dates:
Received: 30.05.2024, ***Revision Request***: 05.06.2024, ***Last Revision Received***: 22.06.2024, ***Accepted***: 23.06.2024

fluorocarbons (HFC) gases with high global warming potential (GWP) and indirect CO2 emissions from high electricity consumption [2]. The share of the refrigeration system in the total energy consumption is 15% and this is responsible for 1% of the CO_2 emissions in the world [3]. The increasing demand for fresh food with a growing population makes it inevitable that the consumption of electricity and the contribution of F-gases to global warming will increase many times over in the coming decades. Chlorofluorocarbons (CFCs) were banned by the Montreal Protocol (signed in 1987) and were replaced by hydrochlorofluorocarbons (HCFCs) and then by HFCs [4]. In contrast to CFCs, HFCs have a negligible ODP but a high GWP. Therefore, the contribution of HFCs to global warming is estimated to be in the range of 0.3°C to 0.5°C by 2100 [5]. According to Koronaki et al. [6] HFC's contribute significantly to the greenhouse effect, especially in large commercial refrigeration systems, where they leak around 11 per cent per year. Therefore, the revised F-Gas Regulation entered into force on 1 January 2015 to control fluorinated greenhouse gas emissions with zero ODP and low GWP. However, commercial refrigeration systems are still generally designed to use HFC refrigerants [7]. In recent years, hydrofluoroolefins (HFOs) synthetic refrigerants have been offered as an alternative 4th generation refrigerant to HFCs with low GWP (<1) and ODP (=0) value [8]. Also, hydrocarbon natural refrigerants are generally considered an alternative as they have thermodynamic properties with low GWP and zero ODP. R290 and R600a are generally accepted as alternative hydrocarbon natural refrigerants due to compatibility with current equipment and cooling installation in commercial refrigerators and freezers [9]. HC refrigerants and their mixtures are not only a good option with low GWP values for the environment but also show superior performance in terms of energy efficiency [10]. But hydrocarbon refrigerant charges have been limited for flammability concerns with safety precautions in commercial refrigeration systems [11]. The amount of hydrocarbon refrigerant in heat exchangers where the liquid phase is the majority in refrigeration systems is a key design consideration [12]. Therefore, the volume of heat exchanger must be decreased to improve the heat transfer coefficient (HTC) for lower coolant flow rate. In recent years, many researchers have investigated the use of microchannels to improve heat transfer in refrigeration systems using natural refrigerants [13-15]. Over the past few years, refrigeration manufacturers have focused on specialty blend gases that have low environmental impact, high energy and thermal performance, and low flammability risk. This is due to the flammability properties and the restrictions on the gas charge rate. HFC/HFO mixtures have been the preferred choice in vapor compression systems due to their higher efficiency and low GWP. Replacement of HFC/HFO/HC/R744 refrigerant blends with high GWP R134a, R404A and R410A refrigerants in terms of energy performance was evaluated by Aricapa et al. [7]. While R442A, R449-A and R407H stand out in terms of energy efficiency in conversion, R455A and R465A showed the maximum COP decrease. The use of the mixed gas refrigerant R449-A instead of the high GWP refrigerant R404A in supermarket RDCs was suggested by Mahnatch et al [16]. The mass percentages of R449-A refrigerant have been reported as 24.3%/24.7%/25.7%/25.3% because of blending R32/R125/R134a/R1234yf refrigerants. R449-A is a non-flammable and ODP-free refrigerant, according to Ghanbarpour et al. [17] Compared to R404A, which has a higher critical temperature and pressure than R449-A, the energy required for compression is reduced. In addition, the GWP of R449-A is approximately three times lower than that of R404A. Llopis et al. [18] predicted that lower GWP HFC/HFO mixture refrigerants (e.g. R448A, R449-A, R455A or R454C) as alternatives to R404A and R507 refrigerants could make the largest contribution to reducing emissions in commercial refrigeration by 2030.

Different techniques have been developed to evaluate the environmental impacts of refrigeration systems on global warming by leaking refrigerant and high energy consumption. Global warming potential (GWP) is a widely used measure of the greenhouse effect of refrigerants. The lower the GWP, the less the substance contributes to global warming [19]. GWP is the index used to compare the global warming effect of emitting a greenhouse gas with the effect of emitting a similar amount of CO_2, which is estimated over a given time horizon. An indicator called Total Equivalent Warming Impact (TEWI) is used to assess the environmental impact of systems or processes that use energy, in addition to the direct impact of the refrigerant [20]. For low GWP refrigerants, the direct effect is quite small compared to the indirect effect. Therefore, the performance of energy consumption data based on TEWI will greatly influence the outcome of a refrigerant comparison [21]. The TEWI metric, unlike the GWP, is an indicator that includes emissions associated with energy production but does not include all relevant indirect emissions associated with the refrigerant life cycle, such as emissions associated with transport and production of the system and refrigerant. An approach that holistically evaluates the environmental impact of different refrigerants and assesses lifecycle climate performance together with environmental impact is LCCP. This tool is used to evaluate the GWP effects of the analyzed refrigerating system in terms of direct and indirect carbon emissions as total CO2eq throughout the entire life cycle [22]. A standardized approach to the use of LCCP and comprehensible data sources for all aspects of the calculation is proposed by Troch et al [23]. It was recommended that the data sources be used for the calculation of averages of all LCCP inputs. An open source and modular solution for LCCP based analysis of vapour compression refrigeration systems was presented by Beshr et al. [24] evaluated the refrigeration systems of a supermarket using low GWP refrigerants using a method based on LCCPs. It was found that the use of low GWP refrigerants resulted in a significant reduction in the impact on the uncertainty of the total emissions of the system, with a reduction in the direct emission value. The most environmentally friendly refrigerants were identified as R1270, R290 and R152a in the LCCP assessment, which evaluates the entire life of the refrigerant with a holistic approach that measures its impact on system emissions. Another LCCP-based analysis was carried out by Lee et al. [25] for different vapor compression cycles (VCC) using low GWP refrigerants. With the R290 refrigerant, they observed a significant reduction in the LCCP value of about 15.1%. In heat pump applications using R290 refrigerant, total CO_2 emissions were reduced by approximately 22.3%. A LCCP-based model of refrigeration and heating systems has been investigated by Choi et al. [26] in South Korean weather conditions. The LCCP-based assessment method was reviewed and applications for identifying refrigerants to replace high GWP refrigerants were documented by Wan et al. [27]. Using the developed LCCP method, Choi et al. [28] investigated the environmental impact of household refrigerators. The results showed that system performance and manufacturing emissions are the dominant factors influencing lifecycle emissions. They found that by selecting aluminum material in the condenser in a well-insulated refrigeration system with the binary cycle option, CO_2 emissions can be reduced by up to 25%. Li et. al. [29] focused on food transport refrigeration systems and conducted a life cycle climate performance study. They found that replacing R404A refrigerant with R452A, which has a lower global warming potential, could reduce emissions in the food transport refrigeration system by 5-15%. They also found that reducing the ambient temperature from 32°C to 15.5°C could reduce emissions by up to 60% for fresh produce and up to 39% for frozen produce. In addition, the study highlighted that reducing the refrigerant leakage rate from 25% to 10% could result in emissions reductions of 13% for fresh products and 4% for frozen products. Regulations are constantly being updated to reduce the use of high GWP refrigerants, promote the use of refrigerants with a lower environmental footprint, increase the energy efficiency and performance of cooling systems and ensure the implementation of eco-design requirements throughout the lifecycle of cooling equipment [30]. Eco-design has become a key issue in the development of refrigeration systems with the adoption of EU Regulation 2019/2019 and EU Regulation 2016/2281, which set eco-design requirements and frameworks for energy-related products, including refrigeration systems, to achieve low lifetime emissions and low energy consumption targets for both commercial and domestic applications [31]. To comply with these regulations and meet the new technological challenges, research and development efforts are required to identify innovative solutions that ensure high performance, low energy consumption, and the use of alternative fluids with limited environmental impact. This includes considering all life cycle phases, not just the use phase, in the design and development of refrigeration systems. In the literature review, there are many studies on LCCP assessment methodologies. However, the life cycle emission assessments of RDC systems are limited in scope. In this study, an experimental environmental assessment was carried out on the energy consumption and refrigerant-related emissions of RDCs. The environmental impacts of the refrigerants R449-A and R290 were compared using LCCP. In addition, an energy label classification was performed for RDCs using two different refrigerants. An analysis of the lifecycle climate performance of commercial RDCs and information on the reduction of CO_2 emissions over a 10-year operating life because of this performance analysis is presented in this study.

2. Materials and Methods

2.1. LCCP Calculation

LCCP is a calculation methodology developed to determine the lifecycle environmental impact of refrigeration and air conditioning systems operating with a stationary vapor compression cycle powered by the local electrical grid. LCCP calculations are made in units of CO_{2e} or CO_{2eq}/kWh, consisting of direct emissions (refrigerant leaks) and indirect emissions (energy consumption for manufacturing). LCCP concept is illustrated in ▶**Figure 1**. Direct emissions are affected by refrigerant emissions and atmospheric degradation, while indirect emissions are affected by energy consumption, emissions from production, material, and refrigerant recycling.

LCCP, which consists of two emission values, can be calculated as in Eq. (1).

$$\text{LCCP} = \text{Direct Emissions} + \text{Indirect Emissions} \qquad (1)$$

Annual leaks, catastrophic leaks and leaks resulting from disposal of the unit constitute the direct emission value throughout refrigeration's life cycle. Direct Emissions (DE) account for the refrigerant leakage over the course of the lifetime of unit and calculated by the following [32]:

$$\text{Direct Emissions} = C \times (L \times ALR + EOL) \times (GWP + Adp.GWP) \qquad (2)$$

Here, the charge amount of the refrigerant is C (kg); L is an average lifetime of component (year); ALR is the annual leak rate (%); EOL is the end-of-life refrigerant leakage (%); GWP is Global Warming Potential (kgCO_{2e}/kg); Adp.GWP is the atmospheric degradation product of the refrigerant (kgCO_{2e}/kg) GWP.

Indirect emissions contain emissions due to energy consumption in operation, manufacturing emissions

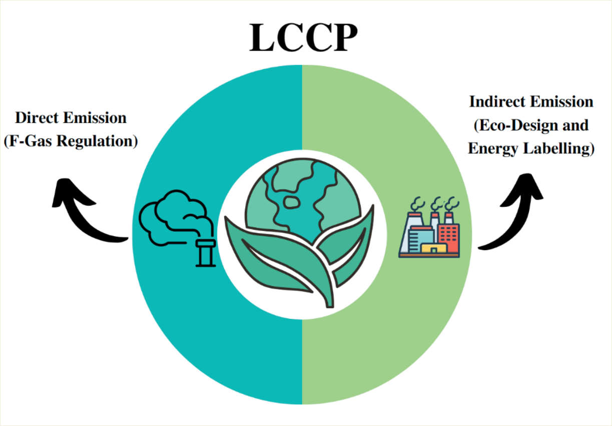

Figure 1. LCCP graphical representation

and emissions from unit disposal. Indirect emissions are consisted of the use of the unit over its lifetime and account for the following [32]:

$$\begin{aligned}\text{Indirect Emissions} = {} & L \times AEC \times EM \\ & + \sum (m \times MP) \\ & + \sum (MR \times RM) \\ & + C \times (1 + L \times ALR) \times RFM \\ & + C \times (1 - EOL) \times RFD \end{aligned} \quad (3)$$

AEC is Annual Energy Consumption (kWh); EM is the electricity generation emission ($kgCO_{2e}/kWh$); m is the mass of RDC (kg); MP is the material production emission ($kgCO_{2e}/kg$); MR is the mass of recycled material (kg); RM is the recycled material ($kgCO_{2e}/kg$); RFM is the refrigerant manufacturing emissions ($kgCO_{2e}/kg$); RFD is the refrigerant disposal emissions in ($kgCO_{2e}/kg$). Values of parameters were taken based on the guideline for LCCPM[32]. Mechanical vapor compression system is used in refrigerated display cabinets. Approximately 80-95% of the LCCP emissions of the mechanical vapor compression systems used consist of indirect emissions. The GWP values of the refrigerants analyzed in the experiment are given in ▶**Table 1**. The ODP and GWP values of the refrigerants R449-A and R290 are shown in ▶**Table 1**. The R290 refrigerant is more environmentally friendly than R449-A based on these values.

Table 1. GWP values for refrigerants

Refrigerant	Class	ODP	GWP	Adp.GWP
R449-A	A1	0	1397	-
R290	A3	0	3	-

Emissions from material production have been calculated considering the International Refrigeration Institute (IIR) standard. In addition, production emission values of these materials are given in IIR standard (released 2015)[32]. CO_2 emission values per unit area, expressed in [$kgCO_{2e}/m2$], can be calculated using the average coefficient per electricity consumption (ACPEC) as follow:

$$CO_2\ emission = \frac{ACPEC \times TEC}{TDA} \quad (4)$$

2.2. Experimental analysis

In this study, two different low GWP refrigerants R449-A and R290 were analyzed in commercial open-type RDCs designed with the same VCC system. Total display area (TDA) of RDC is $4.3m^2$ and there are 5-piece shelves and a pan at the bottom of the cabinet designed seen in ▶**Figure 2**. Experiments were conducted under EN ISO 23953-2:2015 (298.15K, 60% relative humidity) test room conditions. The mixed refrigerant R449-A was used in the first experimental cooling cycle while R290 natural refrigerant was used as the second refrigeration circuit. The designed systems were tested under 0.1-0.2m/s airflow velocity conditions for 24 hours. During the test activities, M-Pack temperatures, temperature, and pressure values of the refrigeration system equipment (compressor, condenser, and evaporator), energy consumptions of compressor and other components were measured from certain points. The test room measurement instruments are specified in ▶**Table 2** as part of the EN ISO 23953-2:2015 standard. The prototype of the open type RDC is given in ▶**Figure**

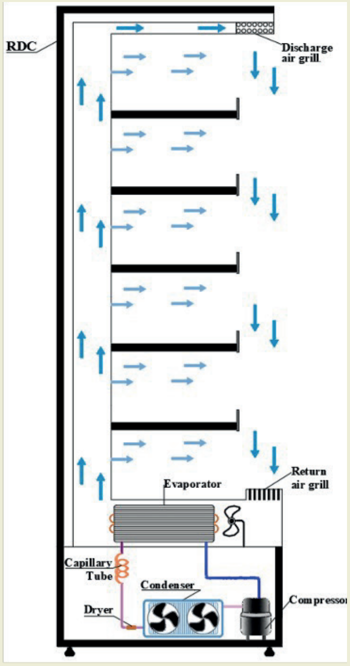

Figure 2. Schematic of ORDC

3. RDC systems were designed to operate with R449-A refrigerant and R290 refrigerant. Both mechanical vapor compression refrigeration cycles consist of two compressors, two condensers, two capillary tubes and an evaporator with five fans given in **▶Figure 4**. While 1400g(2x700 g) of R449-A refrigerant was charged to the cooling system, this amount was 300g(2x150 g) for R290. The experimental conditions were set at a condenser temperature of 45°C and an evaporator temperature of -10°C, which are close to the practical operating conditions. The climate class of the test room is 3, the dry bulb temperature is 298.15K±1K, the relative humidity is 60±5%, and the air velocity varies between 0.1-0.2 m/s. EKM (electro-commutated) type condenser and evaporator fan, piston hermetic type compressor, microchannel condenser and copper tube aluminum fin evaporator were used in the Refrigerated Display Cabinet.

Table 2. Specifications of measurement instruments

Measuring device	Measuring range	Accuracy
Refrigerant flow meter	0–1000kg/h	±0.1%
Energy meter	0–16 A	±0.2%
T-type thermocouple	233.15–473.15 K	±0.1%
Thermohygrometer	0–100%RH 273.15–312.15 K	±1.5% ±0.03%
Digital manifold gauge	223.15–423.15 K 1– 0 bar	±0.1% ±0.01%
Anemometer	0–2 m/s	±0.01%
Low-pressure transmitter	0.5–8 bar	±0.01%
High-pressure transmitter	0–30 bar	±0.1%

The probes measuring the refrigerant temperatures input and output the evaporator, the refrigerant temperatures entering and leaving the condenser, the low and high pressures of the refrigerant input and output the compressor, the measurement of the air temperatures entering the air-on grille of the refrigerant and output the air-off honeycomb, the energy consumption of the refrigerant, the refrigerant flow measurement tests are carried out. The properties and precisions of the measurement instruments are given in **▶Table 2**.

The data obtained because of the experiments were found using measuring devices in accordance with the standard. Uncertainty analysis is important to find the uncertainty of measurement and to make precise measurement. They are errors caused by test conditions, measuring devices, ambient conditions, reading and measuring points. For this reason, uncertainty analysis is important in finding accurate results by reaching the desired experimental standards. The total uncertainty is calculated with the Equation 5-6.

$$W_R = \left[\left(\frac{\partial R}{\partial x_1} w_1 \right)^2 + \left(\frac{\partial R}{\partial x_2} w_2 \right)^2 + \cdots + \left(\frac{\partial R}{\partial x_n} w_n \right)^2 \right]^{1/2} \quad (5)$$

$$wn = \sqrt{(A_1)^2 + (A_2)^2 + \cdots + (B_n)^2} \quad (6)$$

Where n is the number of parameters, Wn is measured uncertainty of each parameter, WR is total uncertainty, wn denotes the uncertainty of each independent parameter (A and B) measured.

Figure 3. The prototype of ORDC and M-packages

2.3. Theoretical Analysis

RDCs run with mechanical vapor compression refrigeration cycle. A schematic diagram is illustrated in ▶**Figure 4**. Energy conservation equation is utilized to calculate the total energy consumption in Eq.7.

$$E_T = E_{fans}t_{fans} + E_{compressor}t_{compressor} + E_{defrost}t_{defrost} + E_{other}t_{other} \tag{7}$$

The power consumption of the compressor is calculated as:

$$\dot{W}_c = \dot{m}\left(h_2 - h_1\right) \tag{8}$$

Where, h_1 is the enthalpy of the compressor input and h_2 is the enthalpy of the compressor output.

The capacity of evaporator is:

$$\dot{Q}e = \dot{m}\left(h_1 - h_4\right) \tag{9}$$

Here, h_4 is evaporator inlet enthalpy and h_1 is evaporator outlet enthalpy.

The COP of the RDC system is calculated by combining the refrigeration loads and power of compressor as below:

$$COP = \frac{\dot{Q}_e}{\dot{W}_{comp}} \tag{10}$$

The energy efficiency index (EEI) value can be calculated with European Union regulation of (EU) 2017/1369:

$$EEI = \frac{AE}{SAE} \tag{11}$$

Annual energy consumption, expressed in kW/h, can be calculated as follows:

$$AE = 365 \times E_{daily} \tag{12}$$

Edaily is energy consumption of the RDC over 24 hours, expressed in kWh/24h.

$$E_{daily} = \left[\left(\dot{W}_{comp}t_{comp}\right) + \left(\dot{W}_{ef}t_{ef}\right) + \left(\dot{W}_{cf}t_{cf}\right) + \left(\dot{W}_{h}t_{h}\right) + \left(\dot{W}_{l}t_{l}\right)\right] \tag{13}$$

SAE as a reference value can be calculated as below:

$$SAE = \left(M + N \times Y\right) \times 365 \times C \times P \tag{14}$$

The values of M, N, P and C are given in ▶**Table 3**. These parameters are specified with (EU)2017/1369 regulation for M1 temperature class experiment condition in vertical combined supermarket refrigerator cabinets. Y, expresses in m^2, is the sum of the total display area.

3. Results and Discussions

This study evaluated the R449-A and R290 refrigerants energy efficiency and environmental performance in the same designed RDC system. Both low GWP refrigerants were compared with thermodynamically and LCCP analysis methods in accordance with EN ISO 23953-2:2015 standard under M1 medium temperature test conditions. M1 package temperature class and test room climate class 3, as described in ISO 23953-2, for a 10-year service life in an open commercial refrigeration display cabinet. This choice is consistent with previous studies on the same scope [33-35]. Theoret-

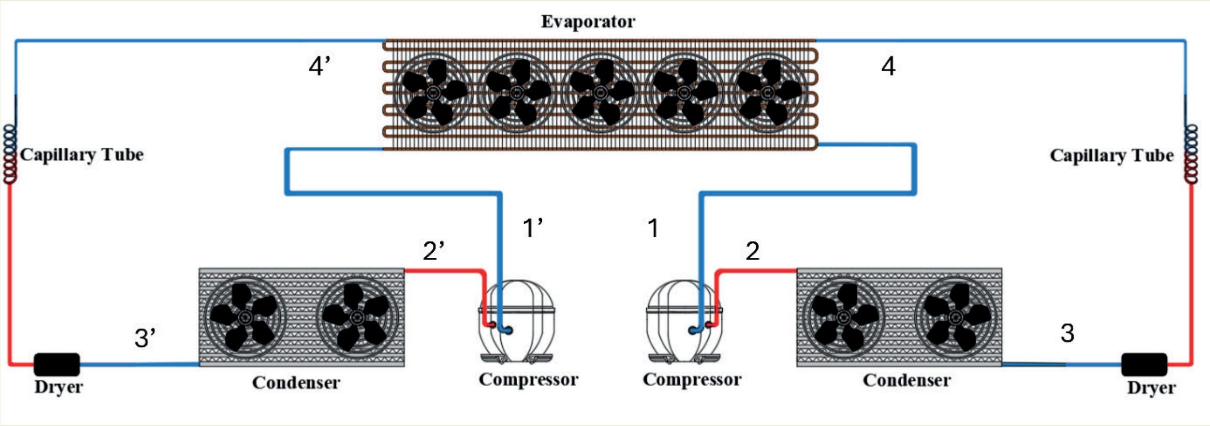

Figure 4. Schematic of the mechanical vapor compression refrigeration system

Table 3. M1 Temperature class vertical RDC coefficient values

Coefficient	Value
M	9.1
N	9.1
P	1.1
C	1.15

ical and experimental results were presented in this section. The evaporator inlet temperature (EIT) and evaporator outlet temperature (EOT) values for open-type RDCs used R449-A and R290 refrigerants. Open-type RDCs according to EN ISO 23953-2:2015 within the test period, firstly 12h switched on lighting, without the night-covers secondly 12h with the night-covers and the cabinet lighting switched off. The total uncertainty value was calculated as 2.3312% Therefore, this value is at an acceptable level and the measurements made in the study can be considered reliable. The low-temperature source value was T_L=263.15K and the high-temperature value was T_H=318.15K during the experiment. Carnot coefficient of performance value was determined as $\mathbf{COP_{carnot}} = \mathbf{4.8}$. Moreover, the compressor power of the RDC system for R449-A and R290 refrigerants were recorded as $\dot{\mathbf{W}}_{\mathbf{comp}} = \mathbf{1640W}$ and $\dot{\mathbf{W}}_{\mathbf{comp}} = \mathbf{1448W}$, respectively. Due to several factors, including the more efficient thermodynamic properties of the R290 refrigerant, compressor run time and power consumption were lower than expected [36]. The reduction in the time required for the delivery of cooled air further reduces energy consumption and the overall energy efficiency index. The cooling capacity was $\dot{\mathbf{Q}}_{\mathbf{e}} = \mathbf{3145}$ W for refrigerant RDC systems. COP value was 1.92 for R449-A refrigerant while it was 2.17 for low GWP natural refrigerant R290. The COP value of the system operating with R290 was obtained as 11.5% higher than R449-A refrigerant used system. As a result of lower compressor power requirements in the same cooling process, the COP has been significantly improved when R290 is used. Furthermore, the second law efficiencies of R449-A and R290 were calculated as 40% and 45.2%, respectively. Because of the same reason as in the COP calculations, the second law efficiency of the R290 system is improved by 5.2% as compared to R449-A system. The inlet and outlet temperatures of the evaporator are given in ▶**Figure 5**, for both refrigerants R449-A and R290. The difference between the inlet and outlet temperatures of R290 used case is less than in the case used R449-A refrigerant. Evaporator inlet and outlet temperatures differed by 4°, and a 3% increase was measured with R449-A refrigerant. The difference between the evaporator inlet and outlet temperatures decreases at night when the covers are closed. The evaporator inlet temperature is about 1 degree less where R449-A refrigerant was used in night period. Daily energy consumption in the R449-A refrigerant case was 31.55kW/day, while in the R290 case, it was 21kW/day. This illustrates the impact of the reduced compressor on cycle time savings [36]. In this case, daily energy saving was 10.55kW/day. Similarly, annual consumptions (AE) were 11515.75kW/year and

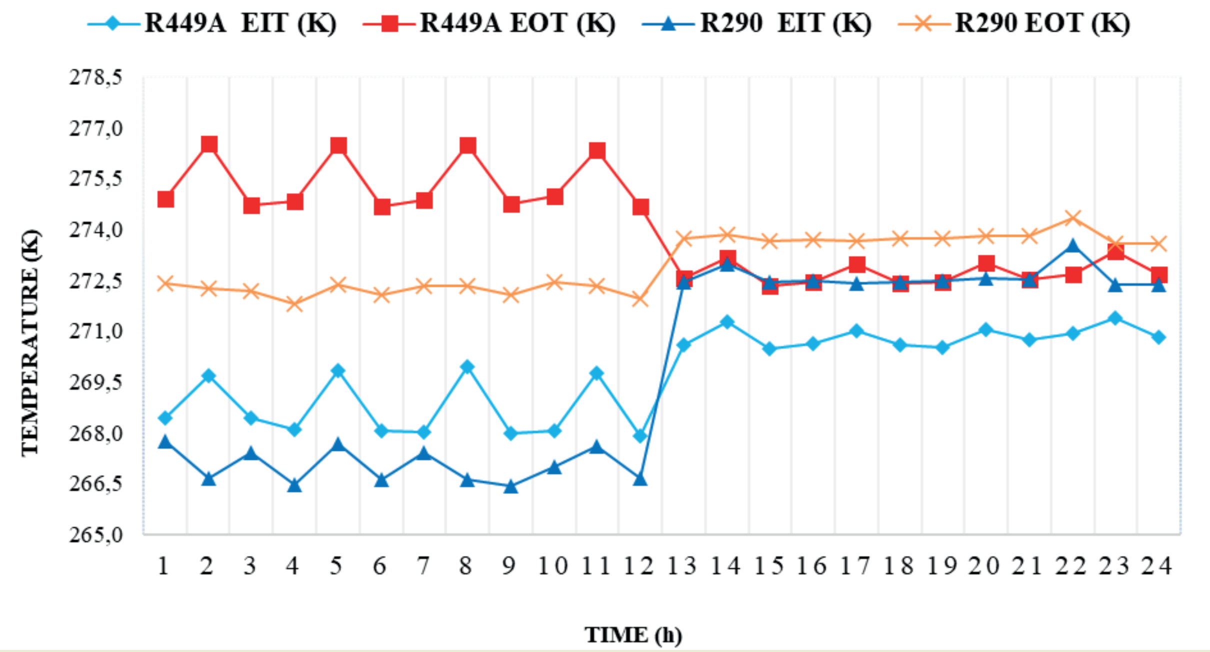

Figure 5. Evaporator inlet-outlet temperature graph

7665kWh/year for R449-A and R290 refrigerant systems, respectively. In this way, annual energy saving was calculated as 3850.75 kWh/year. The SAE value of the experimental setup was calculated as 22269kWh/year for all compartments with the same temperature class commercial refrigerator.

The temperature of the refrigerant input and output of the condenser is given in ▶**Figure 6**. When the R449-A refrigerant enters and exits the condenser compared with the R290 refrigerant, there is a difference in temperatures. While the condenser inlet temperature drop was measured at 6%, the outlet temperature difference was measured at 2%. One of the most important reasons for this difference is the use of R290, a natural refrigerant with low ODP and GWP values and high heat transfer potential. LCCP evaluation of the two refrigerant systems was also performed in this study and the results were summarized.

The summary of the evaluations is presented in ▶**Figure 7**. In addition, the emission values obtained from the LCCP analysis are given in ▶**Table 4**. The total lifetime CO_2 emission in the R449-A system was determined as 61853.93 $kgCO_{2e}$ and the total lifetime CO_2 emission in the case of R290 was determined as 42821.48 $kgCO_{2e}$. Therefore, the use of R449-A as the refrigerant results in 19032.45 kg CO_{2e} more emissions to the environment over the lifetime of the system.

The excess CO_2 emissions observed in the R449-A system come mainly from both direct and indirect emissions. In the direct emissions, due to the annual refrigerant leakage and end-of-life (EOL) refrigerant leakage, the total emission was calculated as 3716.02 $kgCO_{2e}$ for the R449-A system. 3520.44 $kgCO_{2e}$ of this value comes from the annual refrigerant leakage, whereas annual refrigerant leakage emission was calculated as 1.71 $kgCO_{2e}$ in the R290 system. Due to the high GWP value of R449-A, the direct emission values were higher compared to the R290 system. Nevertheless, the major difference between the two cases comes from indirect emission, 61852.22 $kgCO_{2e}$ in total was estimated in the R449-A system and 42819.77 $kgCO_{2e}$ in total was estimated for the R290 system. The difference between the two systems in the indirect emissions is due to the high annual energy consumption observed in the R449-A system. Since the equipment is the same for both systems, emissions due to equipment manufacturing and equipment EOL are the same for this type of RDC. Due to unavailable refrigerant manufacturing emission data for R449-A, the emission due to refrigerant manufacturing for R449-A was neglected, whereas this value was calculated as 0.04 $kgCO_{2e}$ for the R290 system. EEI values were calculated as 51.7 for R449-A refrigerant system and 34.4 for R290 refrigerant system consequently. By evaluating the EEI, RDCs can be identified the energy-efficient features. According to the EEI value of 51.7 the energy class “E” was found for R449-A refrigerant system whereas R290 system was in the energy class of “C” with 34.4 EEI value. Energy efficiency can be significantly improved when R290 is used as the refrigerant. When these rates are considered, the system using R290 refrigerant has 11.5% higher COP value, 33% lower energy consumption, 33 % lower EEI value compared to the system using R449-A refrigerant, in this case, the energy label class is higher in higher levels.

The emission values obtained from the LCCP analysis are given in ▶**Table 4**. The total lifetime CO_2 emission in the R449A system was determined as 61853.93 $kgCO_{2e}$ and the total lifetime CO_2 emission in the case of R290 was determined as 42821.48 $kgCO_{2e.}$ Therefore, the use of R449A as the refrigerant results in 19032.45 kg CO_{2e} more emissions to the environment over the lifetime of

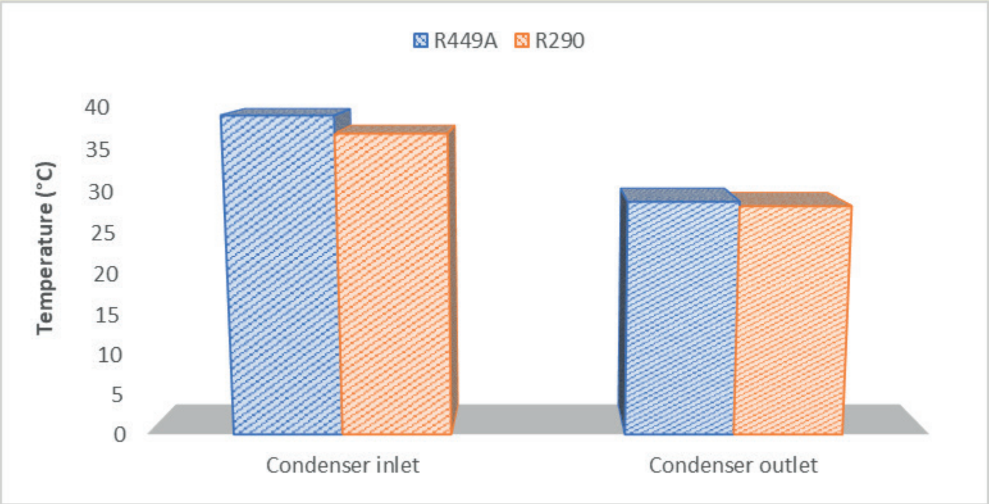

Figure 6. Condenser inlet and outlet temperature graph

Table 4. LCCP results of R449-A and R290 systems

LCCP Results	R449-A	R290
Total Lifetime Emission (kgCO_{2e})	61853.93	42821.48
Total DE (kgCO_{2e})	3716.02	1.71
Annual Refrigerant Leakage (kgCO_{2e})	3520.44	1.62
EOL Refrigerant Leakage (kgCO_{2e})	195.58	0.09
Adp. GWP (kgCO_{2e})	-	-
Total IE (kgCO_{2e})	61852.22	42819.77
Equipment Mfg (kgCO_{2e})	1599.30	1599.30
Equipment EOL (kgCO_{2e})	25.29	25.29
Refrigerant Mfg (kgCO_{2e})	-	0.04
CO_2 emission per m2(kg CO_{2e}/m^2)	3.28	2.18

the system. These results come from the total energy consumption of 11515.75kWh/year and 7.665kWh/year for R449-A and R290, respectively. Transcribing the energy consumption to the total life of 10 years of the RDCs, LCCP evaluation indicates that an additional 19032.49 kgCO_{2e} will be released to the atmosphere in the case of R449-A.

4. Conclusions

Theoretical and experimental analyses of an open RDC system with two working refrigerants (R449-A and R290) were performed in this study. An environmental impact assessment was performed by calculating EEI and using the LCCP method based on energy consumption measurements. Analysis results are presented below:

- With the use of R290 refrigerant, a reduction in compressor power of approximately 200W can contribute to energy efficiency by providing a significant reduction in electricity consumption. Thus, the lower energy consumed in the compression process enabled the performance of RDC with R290 refrigerant to be 11.5% higher.

- It was determined that the annual energy consumption of the R290 system for the same cooling area was 3850.75kWh/year lower than the R449-A system.

- It was possible to reduce the amount of daily CO_2 emissions related to RDCs' daily energy consumption thanks to the use of R290 refrigerant.

- With R449-A refrigerant, the EEI value was increased from 34.4 to 51.7. As a result, the energy

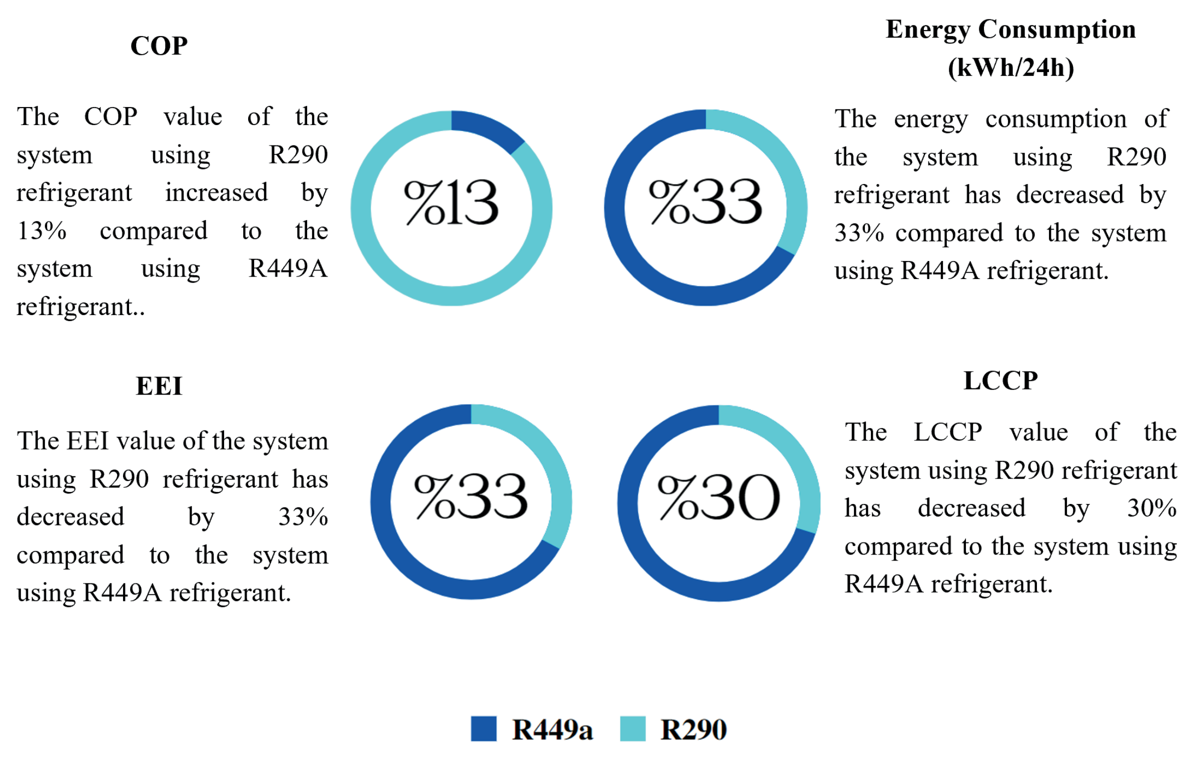

COP

The COP value of the system using R290 refrigerant increased by 13% compared to the system using R449A refrigerant..

Energy Consumption (kWh/24h)

The energy consumption of the system using R290 refrigerant has decreased by 33% compared to the system using R449A refrigerant.

EEI

The EEI value of the system using R290 refrigerant has decreased by 33% compared to the system using R449A refrigerant.

LCCP

The LCCP value of the system using R290 refrigerant has decreased by 30% compared to the system using R449A refrigerant.

Figure 7. COP, EEI, energy consumption, LCCP rates

https://doi.org/10.26701/ems.1493164

class of RDC in the same area using R449-A refrigerant was E, while the C energy class was determined for R290. Due to the considerably less energy consumption by R290 working refrigerant, the energy class of the system was two classes higher.

- LCCP evaluation of both systems was performed. Quantitatively, the main difference comes from both direct and indirect emissions. Due to the high GWP value of R449-A, the direct emission for the R449-A system was calculated as 3716.02 $kgCO_{2e}$, while this value was only 1.71 $kgCO_{2e}$ in the R290 system. In indirect emission results, the main and almost only difference comes from the annual energy consumption.
- The results show that the R449-A system releases 30% more kg CO_{2e} into the environment over the lifetime of the system.
- Due to high energy consumption of R449-A, emissions were 61852.22 $kgCO_{2e}$ whereas indirect emission of R290 system was calculated as 42819.77 $kgCO_{2e}$.
- The system using R290 refrigerant used 78% less refrigerant compared to the system using R449-A refrigerant.
- The system using R290 refrigerant shows superior performance compared to the system using R449A refrigerant, with a 13% increase in COP, a 33% reduction in EEI and energy consumption, and a 30% reduction in LCCP.
- Thanks to the new generation refrigerant with zero ODP and low GWP, the impact of RDCs on global warming can be reduced.

As a result of the calculation of indirect emissions and direct emissions, it has been observed that indirect emissions are higher. In indirect emissions, it is foreseen that it will be beneficial to reduce the effect of emissions released to nature due to the energy used to produce the refrigerant. It can also be proposed to reduce the energy consumed for the production, assembly, and transport of systems/components, as well as to reduce emissions from the energy consumption required for the recovery of the refrigerant/system.

Future studies will use a machine learning model to develop sustainable design and manufacturing processes for energy-intensive commercial refrigeration. This approach will address the challenges of the experimental investigation of different conditions in the field and in test chambers, which are often costly and time consuming. Our aim is to streamline these processes, making them more efficient and effective by machine learning.

Nomenclature

ACPEC	Average coefficient per electricity consumption
RDC	Refrigerated Display Cabinet
GWP	Global Warming Potential
GWPadp	Adaptive Global Warming Potential
CFD	Computational Fluid Dynamics
DAG	Discharge Air Grille
DE	Direct Emissions
IE	Indirect Emissions
RAG	Return Air Grille
COP	Coefficient of Performance
EEI	Energy Efficiency Index
AE	Annual Energy Consumption Amount
SAE	Reference Value of the Annual Energy Consumption Amount
LCCP	Life Cycle Climate Performance
EOL	End of Life
ODP	Ozone Depletion Potential
TDA	Total Display Area
TEC	Total Energy Consumption (kWh)
E	Energy (kWh)
Q	Rate of Heat Transfer (kW)
W	Power (kW)
T	Temperature (K)
η	Second Law Efficiency (%)
mr	Mass of Refrigerant (kg)

Subscripts

max	maximum
comp	compressor
T	total
def	defrost
e	evaporator
r	refrigerant

Acknowledgments

We would like to thank Nurdil Refrigeration Inc. for their contributions to this study.

Research Ethics

Ethical approval not required.

Author Contributions

Conceptualization: [Havva Demirpolat]
Methodology: [Süleyman Erten]
Formal Analysis: [Süleyman Erten]
Investigation: [Havva Demirpolat]

Resources: [Mehmet Özkaymak]
Data Curation: [Şafak Ataş]
Writing - Original Draft Preparation: [Mehmet Özkaymak]
Writing - Review & Editing: [Havva Demirpolat]
Visualization: [Şafak Ataş]
Supervision: [Süleyman Erten]
Project Administration: [Mustafa Aktaş]
Funding Acquisition: [Süleyman Ert

Competing Interests

The authors declare that there is no conflict of interest regarding the publication of this paper.

Research Funding

Not reported.

Data Availability

Not applicable.

Peer-review

Externally peer-reviewed.

References

[1] Rivers, N. (2005). Management of energy usage in a supermarket refrigeration systems. The Institute of Refrigeration.

[2] James, S., & James, C. (2010). The food cold-chain and climate change. *Food Research International, 43*(7), 1944-1956. https://doi.org/10.1016/j.foodres.2010.02.001

[3] Tassou, S., Ge, Y., Hadawey, A., & Marriott, D. (2011). Energy consumption and conservation in food retailing. *Applied Thermal Engineering, 31*(2-3), 147-156. https://doi.org/10.1016/j.applthermaleng.2010.08.023

[4] Benhadid-Dib, S., & Benzaoui, A. (2012). Refrigerants and their Environmental Impact Substitution of Hydro Chlorofluorocarbon HCFC and HFC Hydro Fluorocarbon. Search for an Adequate Refrigerant. *Energy Procedia, 18*, 807-816. https://doi.org/10.1016/j.egypro.2012.05.096

[5] Velders, G. J., Fahey, D. W., Daniel, J. S., Andersen, S. O., & McFarland, M. (2015). Future atmospheric abundances and climate forcings from scenarios of global and regional hydrofluorocarbon (HFC) emissions. *Atmospheric Environment, 123*, 200-209. https://doi.org/10.1016/j.atmosenv.2015.10.071

[6] Koronaki, I., Cowan, D., Maidment, G., Beerman, K., Schreurs, M., Kaar, K., Chaer, I., Gontarz, G., Christodoulaki, R., & Cazauran, X. (2012). Refrigerant emissions and leakage prevention across Europe–Results from the RealSkillsEurope project. *Energy, 45*(1), 71-80. https://doi.org/10.1016/j.energy.2012.05.040

[7] Heredia-Aricapa, Y., Belman-Flores, J., Mota-Babiloni, A., Serrano-Arellano, J., & García-Pabón, J. J. (2020). Overview of low GWP mixtures for the replacement of HFC refrigerants: R134a, R404A and R410A. *International Journal of Refrigeration, 111*, 113-123. https://doi.org/10.1016/j.ijrefrig.2019.11.012

[8] Ciconkov, R. (2018). Refrigerants: There is still no vision for sustainable solutions. *International Journal of Refrigeration, 86*, 441-448. https://doi.org/10.1016/j.ijrefrig.2017.12.006

[9] Lommers, C., Airah, F., & Ashrae, M. (2003). Air conditioning and refrigeration industry refrigerant selection guide. Report AIRAH.

[10] Sruthi Emani, M., & Kumar Mandal, B. (2018). The use of natural refrigerants in refrigeration and air conditioning systems: A review. *IOP Conference Series: Materials Science and Engineering, 377*, 012084. https://doi.org/10.1088/1757-899X/377/1/012064

[11] Ardhapurkar, P., Sridharan, A., & Atrey, M. (2014). Experimental investigation on temperature profile and pressure drop in two-phase heat exchanger for mixed refrigerant Joule–Thomson cryocooler. *Applied Thermal Engineering, 66*(1-2), 94-103. https://doi.org/10.1016/j.applthermaleng.2014.01.067

[12] Palm, B. (2008). Hydrocarbons as refrigerants in small heat pump and refrigeration systems–a review. *International Journal of Refrigeration, 31*(4), 552-563. https://doi.org/10.1016/j.ijrefrig.2007.11.016

[13] Ramesh, K. N., Sharma, T. K., & Rao, G. A. P. (2021). Latest advancements in heat transfer enhancement in the micro-channel heat sinks: A review. *Archives of Computational Methods in Engineering, 28*, 3135-3165. https://doi.org/10.1007/s11831-020-09495-1

[14] Xia, L., & Chan, Y. (2015). Investigation of the enhancement effect of heat transfer using micro channel. *Energy Procedia, 75*, 912-918. https://doi.org/10.1016/j.egypro.2015.07.234

[15] Spizzichino, M., Sinibaldi, G., & Romano, G. (2020). Experimental investigation on fluid mechanics of micro-channel heat transfer devices. *Experimental Thermal and Fluid Science, 118*, 110141. https://doi.org/10.1016/j.expthermflusci.2020.110141

[16] Makhnatch, P., & Khodabandeh, R. (2014). The role of environmental metrics (GWP, TEWI, LCCP) in the selection of low GWP refrigerant. *Energy Procedia, 61*, 2460-2463. https://doi.org/10.1016/j.egypro.2014.12.023

[17] Ghanbarpour, M., Mota-Babiloni, A., Makhnatch, P., Badran, B. E., Rogstam, J., & Khodabandeh, R. (2021). ANN modeling to analyze the R404A replacement with the low GWP alternative R449A in an indirect supermarket refrigeration system. *Applied Sciences, 11*(23), 11333. https://doi.org/10.3390/app112311333

[18] Llopis, R., Calleja-Anta, D., Sánchez, D., Nebot-Andrés, L., Catalán-Gil, J., & Cabello, R. (2019). R-454C, R-459B, R-457A and R-455A as low-GWP replacements of R-404A: Experimental evaluation and optimization. *International Journal of Refrigeration, 106*, 133-143. https://doi.org/10.1016/j.ijrefrig.2019.06.013

[19] Makhnatch, P., Mota-Babiloni, A., Rogstam, J., & Khodabandeh, R. (2017). Retrofit of lower GWP alternative R449A into an existing R404A indirect supermarket refrigeration system. *International Journal of Refrigeration, 76*, 184-192. https://doi.org/10.1016/j.ijrefrig.2017.02.009

[20] Ceglia, F., Marrasso, E., Roselli, C., & Sasso, M. (2021). An innovative environmental parameter: Expanded total equivalent warming impact. *International Journal of Refrigeration, 131*, 980-989. https://doi.org/10.1016/j.ijrefrig.2021.08.019

[21] Mota-Babiloni, A., Navarro-Esbrí, J., Barragán-Cervera, Á., Molés, F., & Peris, B. (2015). Analysis based on EU Regulation No 517/2014 of new HFC/HFO mixtures as alternatives of high GWP refrigerants in refrigeration and HVAC systems. *International Journal of Refrigeration, 52*, 21-31. https://doi.org/10.1016/j.ijrefrig.2014.12.021

[22] Fabris, F., Fabrizio, M., Marinetti, S., Rossetti, A., & Minetto, S. (2024). Evaluation of the carbon footprint of HFC and natural refrigerant transport refrigeration units from a life-cycle perspective. *International Journal of Refrigeration, 159*, 17-27. https://doi.org/10.1016/j.ijrefrig.2023.12.018

[23] Troch, S. Lee, H. Hwang, Y. & Radermacher, R. (2016). Harmonization of Life Cycle Climate Performance (LCCP) Methodology. International Refrigeration and Air Conditioning Conference. Paper 1724. http://docs.lib.purdue.edu/iracc/1724

[24] Beshr, M., Aute, V., Sharma, V., Abdelaziz, O., Fricke, B., & Radermacher, R. (2015). A comparative study on the environmental impact of supermarket refrigeration systems using low GWP refrigerants. *International Journal of Refrigeration, 56*, 154-164. https://doi.org/10.1016/j.ijrefrig.2015.03.025

[25] Lee, H., Troch, S., Hwang, Y., & Radermacher, R. (2016). LCCP evaluation on various vapor compression cycle options and low GWP refrigerants. *International Journal of Refrigeration, 70*, 128-137. https://doi.org/10.1016/j.ijrefrig.2016.07.003

[26] Choi, S., Jung, Y., Kim, Y., Lee, H., & Hwang, Y. (2021). Environmental effect evaluation of refrigerator cycle with life cycle climate performance. *International Journal of Refrigeration, 122*, 134-146. https://doi.org/10.1016/j.ijrefrig.2020.10.032

[27] Wan, H., Cao, T., Hwang, Y., Radermacher, R., Andersen, S. O., & Chin, S. (2021). A comprehensive review of life cycle climate performance (LCCP) for air conditioning systems. *International Journal of Refrigeration, 130*, 187-198. https://doi.org/10.1016/j.ijrefrig.2021.06.026

[28] Choi, S., Oh, J., Hwang, Y., & Lee, H. (2017). Life cycle climate performance evaluation (LCCP) on cooling and heating systems in South Korea. *Applied Thermal Engineering, 120*, 88-98. https://doi.org/10.1016/j.applthermaleng.2017.03.105

[29] Li, G. (2017). Comprehensive investigation of transport refrigeration life cycle climate performance. *Sustainable Energy Technologies and Assessments, 21*, 33-49. https://doi.org/10.1016/j.seta.2017.04.002

[30] Mota-Babiloni, A., Barbosa Jr, J. R., Makhnatch, P., & Lozano, J. A. (2020). Assessment of the utilization of equivalent warming impact metrics in refrigeration, air conditioning and heat pump systems. *Renewable and Sustainable Energy Reviews, 129*, 109929. https://doi.org/10.1016/j.rser.2020.109929

[31] Rossi, M., Favi, C., Germani, M., & Omicioli, M. (2021). Comparative life cycle assessment of refrigeration systems for food cooling: Eco-design actions towards machines with natural refrigerants. International Journal of Sustainable Engineering, 14(6), 1623-1646. https://doi.org/10.1080/19397038.2021.1970274

[32] Hwang, Y., Ferreira, C., & Piao, C. (2015). Guideline for life cycle climate performance. *International Institute of Refrigeration, Paris.*

[33] Tsamos, K. M., Mroue, H., Sun, J., Tassou, S. A., Nicholls, N., & Smith, G. (2019). Energy savings potential in using cold-shelves innovation for multi-deck open front refrigerated cabinets. *Energy Procedia, 161*, 292-299. https://doi.org/10.1016/j.egypro.2019.02.094

[34] Öder, M., Demirpolat, H., Erdoğmuş, F. N., & Erten, S. (2022). Development of deflector structure and effects on performance: Refrigerated display cabinet application. *The European Journal of Research and Development, 2*(4), 155-168.

[35] Geilinger, E., Janssen, M., Pedersen, P. H., Huggins, P., & Bush, E. (2017). Best available technology of plug-in refrigerated cabinets, beverage coolers and ice cream freezers and the challenges of measuring and comparing energy efficiency. *The Carbon Trust, Topten International Services.*

[36] Bulk, A., Faramarzi, R., Shoukas, G., Ghatpande, O., & Labarge, S. (2022). Performance assessment of high-efficiency refrigerated display cases with low-GWP refrigerants. *The Carbon Trust, Topten International Services.*

EUROPEAN MECHANICAL SCIENCE

Research Article

e-ISSN: 2587-1110

Response of PLA material to 3D printing speeds: A comprehensive examination on mechanical properties and production quality

Fuat Kartal[1*], **Arslan Kaptan**[2]

[1]Kastamonu University, Engineering and Architecture Faculty, Mechanical Engineering Department, Türkiye
[2]Sivas Cumhuriyet University, Sivas Technical Sciences Vocational School, Motor Vehicles and Transportation Technologies Department, Türkiye

Orcid: F. Kartal (0000-0002-2567-9705), A. Kaptan (0000-0002-2431-9329)

Abstract: This study investigates the impact of printing speed on the mechanical properties of parts produced through the fused deposition modeling (FDM) method using a three-dimensional (3D) printer. Tensile test specimens, fabricated with Polylactic Acid (PLA) material on an Ender 3 S1 3D printer, were subjected to varying printing speeds from 15 mm/s to 105 mm/s in 15 mm/s increments, maintaining a 100% infill rate. Detailed measurements of sample masses, hardness values, and surface roughness were conducted to assess the potential effects of printing speed on PLA's mechanical properties. Porosity values were also calculated to evaluate internal structure homogeneity and void ratios. The results indicate that an increase in printing speed leads to a substantial reduction in production time. For instance, at a speed of 15 mm/s, the printing time was 119 minutes, decreasing to 15 minutes at 105 mm/s. As speed increased, there was a tendency for a decrease in sample masses, with a notable 12% reduction from 8.21 grams at 15 mm/s to 7.21 grams at 105 mm/s. While lower speeds (15 and 30 mm/s) exhibited higher Shore D hardness values, an overall decrease in hardness was observed with increasing speed. Surface roughness showed a proportional increase with printing speed; for example, at 0° angle, the roughness value increased from 0.8 at 15 mm/s to 1.9 at 105 mm/s. Moreover, tensile strength values decreased with higher printing speeds. For samples printed at 15 mm/s, the tensile strength was 60 MPa, decreasing to 44 MPa at 105 mm/s, representing a 27% reduction. These numerical findings underscore the significant influence of 3D printing speed on both production efficiency and the mechanical properties of the printed material.

Keywords: Additive manufacturing, three dimensional printing, polylactic acid, printing speed, mechanical properties, surface roughness.

1. Introduction

3D printing technology is a rapidly advancing method of production focused on prototypes, widely utilized in various industrial and academic fields. Among the fundamental advantages of this technology are the ease of producing complex geometries, rapid prototyping, and flexibility in production processes. The variety of materials used in 3D printing processes and the characteristics of these materials have a significant impact on the functionality and durability of printed objects. Among these materials, poly-lactic acid (PLA) is preferred due to its biocompatibility, ease of processing, and eco-friendliness. Printing speed is a factor that directly influences production time and efficiency, but it can also have important effects on the fundamental mechanical properties of the material, such as strength, hardness, surface roughness, and porosity [1-3].

PLA stands out as a widely utilized material in the

*Corresponding author:
Email: fkartal@kastamonu.edu.tr

Cite this article as:
Kartal, F., Kaptan, A. (2024). Response of PLA material to 3D printing speeds: A comprehensive examination on mechanical properties and production quality. *European Mechanical Science, 8*(3): 137-144. https://doi.org/10.26701/ems.1395362

History dates:
Received: 24.11.2023, *Revision Request*: 05.01.2024, *Last Revision Received*: 24.01.2024, *Accepted*: 01.02.2024

realm of 3D printing. Its popularity is attributed to its biodegradability, ease of use, and versatility. As a dominant player in the 3D printing materials landscape, PLA's mechanical properties are of paramount importance for ensuring the reliability and functionality of printed objects.

A review of the literature reveals that some researchers have examined the effects of 3D printing process parameters on the mechanical properties and mass of PLA parts [3,4], the impact of different printing angles and speeds [5], lattice structures [6], printing speed, and extrusion temperature on mechanical properties [7], as well as their effects on strength and fatigue behavior [8]. Others have investigated the effects of process parameters and processing time on mechanical behaviors [9], hardness values [10], energy consumption [11], surface quality, and wear resistance [12]. Recent studies have delved into the intricate relationship between printing speed and the mechanical properties of PLA-printed objects. The printing speed is a critical parameter that can significantly influence the final product's strength, durability, and overall performance. Various studies have shed light on the subtle effects of varying printing speeds on the mechanical properties of PLA [13-20].

However, considering the parameters in the 3D printing process, the effects of factors such as printing speed on the mechanical properties of materials like PLA have not yet been fully understood.

Understanding how printing speed impacts layer adhesion, porosity, and overall structural integrity is imperative for optimizing 3D printing processes. These recent studies emphasize the need to consider printing speed as a crucial variable in the quest for enhancing the mechanical properties of PLA-printed objects. By incorporating these findings into the broader discourse on PLA, we can further refine our approach to 3D printing with PLA, ensuring that the mechanical performance aligns with the diverse applications and expectations within the ever-evolving field of additive manufacturing.

This study aims to examine how PLA material responds at different speeds (15, 30, 45, 60, 75, 90, and 105 mm/s) during the 3D printing process and determine the effects of these speeds on the material's mechanical properties. The research was conducted on tensile test specimens prepared using an Ender 3 S1 3D printer, and the samples' masses, hardness values, surface roughness, and porosity rates were measured. These results provide valuable information about the material's production quality and mechanical properties. It is believed that this information can contribute to the wider application of 3D printing technology. This study aims to shed light on the development of 3D printing technology and better material selection and parameter adjustment choices.

Table 1. Physical and mechanical properties of Microzey PLA Pro filament.

Properties	Units	Values
Diameter	mm	1.75
Color		White
Density	g/cm^3	1.25
Bed Temperature	°C	60-80
Printing Temperature	°C	190-210
Elasticity Modules	MPa	1500
Tensile Strength	MPa	50 ~ 60
Elongation at Break	%	7

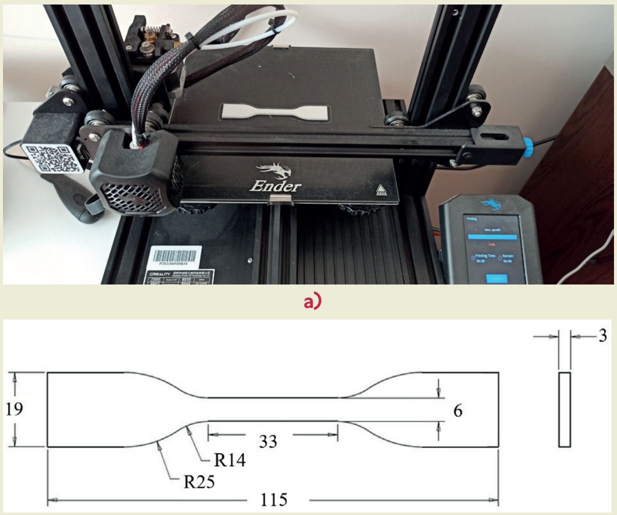
a)

b)

Figure 1. (a) Production of test specimens using the Creality Ender 3 S1 3D printer. (b) Dimensions of samples according to ASTM D638-14/Type IV standard.

2. Material and Method

2.1. Study Process and Used Equipment

In this research, the "Creality Ender 3 S1" 3D printer, known for its precision printing potential and high-resolution production capability as shown in **▶Figure 1**.a, was used. In this study, PLA Pro filaments obtained from Microzey Limited were used. **▶Table 1** below shows some physical and mechanical properties of PLA filaments according to the supplier's information. Tensile test specimens were produced according to the dimensions specified in ASTM D638-14/Type IV standard, which is commonly preferred in the literature and depicted in **▶Figure 1**.b. The printing parameters during this production process are listed in **▶Table 2**. SolidWorks CAD software, known for its precision and

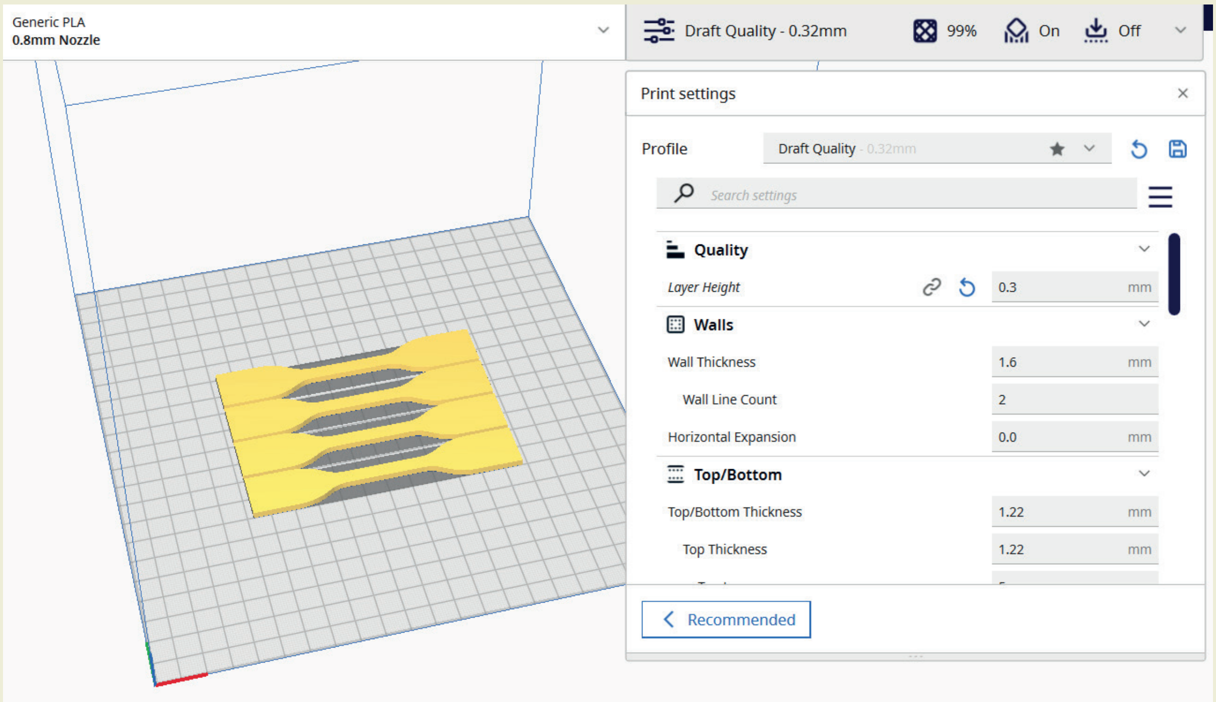
Generic PLA
0.8mm Nozzle

Draft Quality - 0.32mm

Print settings

Profile: Draft Quality - 0.32mm

Quality
Layer Height: 0.3 mm

Walls
Wall Thickness: 1.6 mm
Wall Line Count: 2
Horizontal Expansion: 0.0 mm

Top/Bottom
Top/Bottom Thickness: 1.22 mm
Top Thickness: 1.22 mm

Figure 2. Model placement and printing parameter selection in the Cura slicing software.

detailed design capabilities in industry standards, was used during the 3D design process of the specimens.

2.2. G-Code Generation

To convert the created designs into formats compatible with the 3D printer, Ultimaker's Cura software, as shown in ▶**Figure 2**, was used. Cura is popular for its ability to slice 3D objects and convert them into G-code. The model was transferred to the Cura slicing program, and the printing parameters given in ▶**Table 2** were selected before sending it to the 3D printer for printing.

2.3. Printing Process

In this study, samples were produced at varying printing speeds within the range of 15-105 mm/s. Six different samples were prepared for each speed increment, resulting in a total of 42 samples. The primary material used in the production of the samples was "Mikrozey PLA Pro," commercially sourced. The melting and printing temperatures of the filaments were adjusted as shown in ▶**Table 2**, according to the manufacturer's recommendations. Additionally, a magnetic feature Table named polyetherimide was used during 3D printing to ensure the initial layer of the samples adhered fully and smoothly to the printing surface.

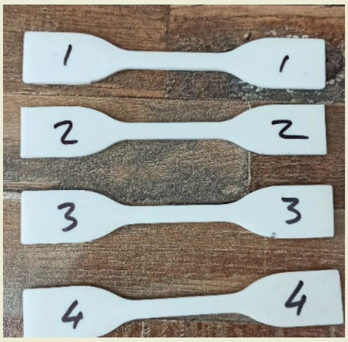

Figure 3. Tensile test specimens.

Table 2. 3D printing settings and parameters.

Parameters	Units	Value
Nozzle Temperature	°C	220
Bed Temperature	°C	60
Nozzle Diameter	mm	0.8
Layer Thickness	mm	0.3
Wall Thickness	mm	1.6
Top/Bottom Thickness	mm	1.22
Infill Density	%	100
Infill Pattern		Lines

2.4. Tests and Analyses

Some of the printed samples can be seen in ▶**Figure 3**. Mass measurements of the prepared samples were conducted using an A&D Ej-303 precision balance, hardness tests were performed using a Pepisky portable 0-100 HD Shore D device, and surface roughness measurements were taken using a Mitutoyo Surfest SJ-310 device. Furthermore, after the tensile tests, the fractured surfaces of the samples were thoroughly examined using a scanning electron microscope (SEM) to better understand how the printing process at different speeds affected the material's internal structure. SEM utilized in this study was the FEI Quanta FEG 250 model. Additionally, the Universal mechanical testing machine employed for mechanical testing was the Shimadzu Autograph AGS-X model. The Shore D hardness test was employed to assess the hardness of three different hard thermoplastic materials, following the guidelines outlined in ISO 7619-1:2010. The dimensions of the test specimens and the testing procedure adhered to the standards specified in ASTM D 2240-05.

3. Results and Discussions

This study produced tensile test samples using the Ender 3 S1 3D printer with PLA material having a 1.25 g/mm^3 density at 7 different printing speeds (15, 30, 45, 60, 75, 90, and 105 mm/s). The results obtained are presented in ▶**Table 3**. As the printing speed increased, there was a tendency for a decrease in mass and lattice volume, an increase in void volume, and porosity rates. As seen in ▶**Figure 4**.a, for example, the printing time at a speed of 15 mm/s was 119 minutes, but when the printing speed was increased by 6 times (105 mm/s), it decreased to 15 minutes, which is an 8-fold decrease. On the other hand, as shown in ▶**Figure 4**.b, when the printing speed was increased from 15 mm/s to 105 mm/s, the sample masses decreased from 8.21 grams to 7.21 grams, resulting in a 12% mass reduction. This is also confirmed by the porosity calculations shown in ▶**Table 3**.

The porosity percentage in the printed samples, depending on the printing speed, was calculated as follows [9]:

ϕ: Porosity percentage
V_{void}: Volume of voids inside the 3D printed product
V_{total}: Designed total volume of the 3D model
V_{solid}: Volume of solid material in the 3D printed product
$m_{product}$: Mass of the 3D printed product
$\rho_{filament}$: Density of the filament material

The porosity percentage has been calculated using Equation 1.

$$\phi = \frac{V_{void}}{V_{total}} \cdot 100 \tag{1}$$

The void volume has been calculated using Equation 2.

$$V_{void} = V_{total} - V_{solid} \tag{2}$$

The solid volume has been calculated from the mass using Equation 3.

$$V_{solid} = \frac{m_{product}}{\rho_{filament}} \tag{3}$$

As the printing speed increases, challenges in filament feeding accuracy and stability are expected to arise, potentially leading to insufficient filament feeding and a reduction in product mass [21,22]. ▶**Table 3** illustrates a notable increase in porosity rate from 7.02% at 15 mm/s to 15.96% at 105 mm/s, suggesting that higher speeds may result in irregular extrusion and deficiencies or voids in printed samples. High printing speeds could also contribute to issues such as inadequate filament heating, poor adhesion, and irregular layer bonding [23]. Therefore, a comprehensive evaluation of printer settings and filament characteristics is crucial to determine the optimal printing speed for achieving the best results [24].

In summary, the study conducted with the Ender 3 S1 3D printer highlights the significant impact of printing speed on both product quality and duration. This information can serve as a valuable guide for optimizing 3D printing processes to enhance efficiency and results [24-26].

However, it is essential to acknowledge that while this study provides valuable insights, further research and experimentation are necessary to fully comprehend the intricate relationship between printing speed and the mechanical properties of 3D printed objects. Delving deeper into these complexities will contribute to a more nuanced understanding, facilitating the optimization of 3D printing processes for superior and efficient results.

▶**Figure 4**.a illustrates the relationship between print speed (mm/s) and mass (g). According to the graph, as the print speed increases, the mass decreases. This implies a negative correlation between print speed and mass. The data on the graph represent masses ranging from 7.0 g to 8.4 g for print speeds varying between 15 mm/s and 105 mm/s. The graph comprises seven data points, denoted by blue dots. The blue line connecting these data points depicts the trend between print speed and mass. ▶**Figure 4**.b depicts the relationship between print speed (mm/s) and print duration (minutes). According to the graph, as print speed increases, the print duration decreases. This implies that higher speeds result in faster printing times. The graph consists of seven data points, marked with red dots. The red line connecting these data points illustrates that as print speed increases, the print duration rapidly decreases, but the rate of decrease slows down after approximately 60 mm/s.

▶**Figure 5** illustrates the relationship between print

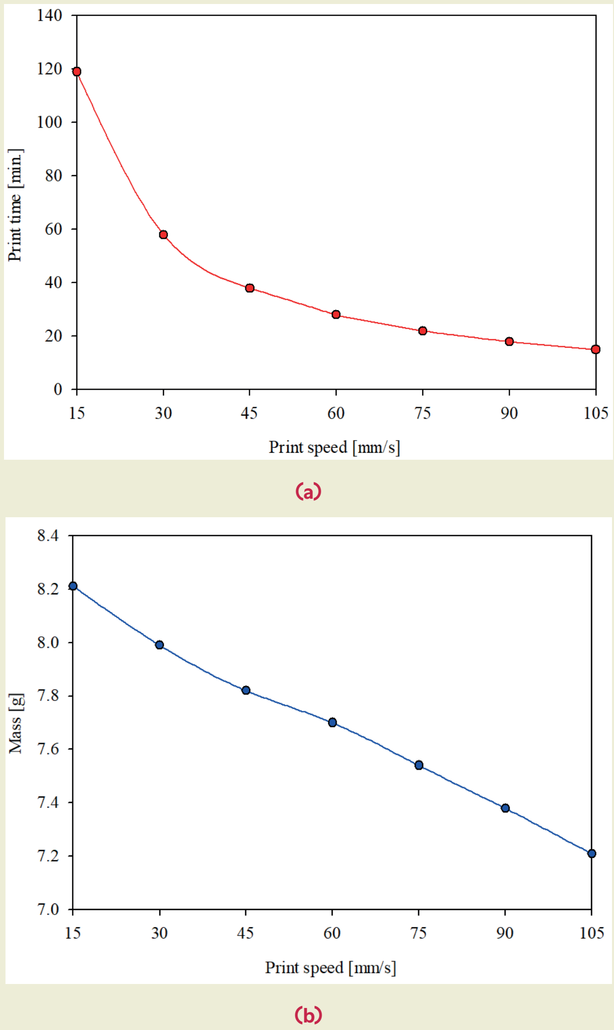

(a)

(b)

Figure 4. PLA tensile test samples produced at different printing speeds (a) Printing times and (b) Average mass values.

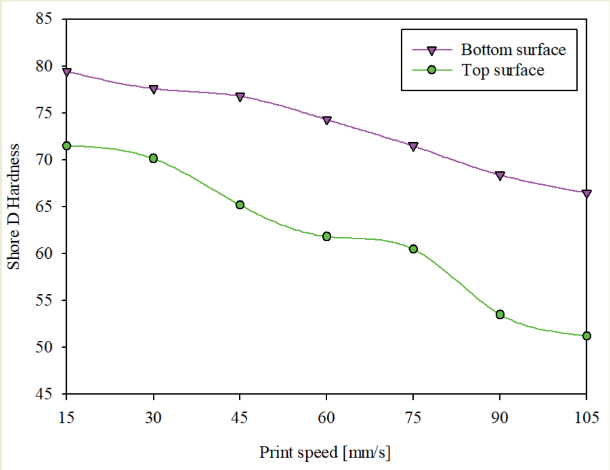

Figure 5. Shore D hardness values of test samples.

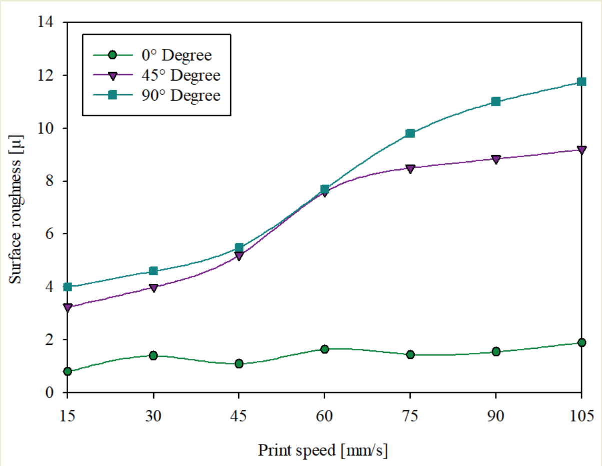

Figure 6. The variation in surface roughness values with respect to printing speed.

speed (mm/s) and Shore D Hardness. According to the graph, as the print speed increases, Shore D Hardness decreases for both the upper and bottom surfaces, with a more pronounced effect on the top surface. The graph comprises seven data points, divided into two groups: “Top Surface” (marked with green circles) and “Bottom Surface” (marked with purple triangles). Both groups indicate a decrease in Shore D Hardness as print speed increases.

▶**Figure 6** depicts the relationship between print speed (mm/s) and surface roughness (μ). According to the graph, as the print speed increases, surface roughness also increases for three different orientation angles (0°, 45°, and 90°). The 0° orientation shows the highest increase in surface roughness with increasing print speed. The graph consists of seven data points, divided into three groups: “0° Angle” (green), “45° Angle” (purple), and “90° Angle” (blue). All three groups indicate an increase in surface roughness as print speed increases.

During the printing process of the samples, a denser infill pattern is used to enhance adhesion to the printing bed. As a result, ▶**Figure 5** illustrates that the bottom surfaces of the samples exhibit higher Shore D hardness values than the top surfaces. On the other hand, an increase in printing speed leads to a decrease in hardness values for both the top and bottom surfaces. It can be inferred that the printing speed can be selected based on the desired hardness value.

It can be observed, as depicted in ▶**Figure 6**, that an increase in printing speed tends to elevate surface roughness. In this context, roughness values were measured at 0°, 45°, and 90° angles. Relatively lower roughness values were obtained in the 0° measurements, while higher values were observed at 45° and 90° measurements.

▶**Figure 7** illustrates the relationship between print speed (mm/s) and tensile strength (MPa). According to the graph, as the print speed increases, tensile strength decreases. This implies that higher speeds result in

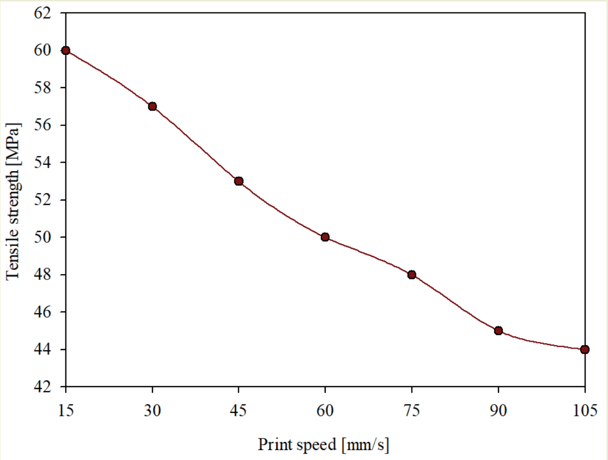

Figure 7. Variation in tensile strength values with printing speed.

materials with lower tensile strength. The graph comprises seven data points, marked with red dots. The red line connecting these data points indicates that as print speed increases, tensile strength decreases. According to the Figure, the samples printed at a speed of 15 mm/s achieved a tensile strength of 60 MPa, whereas those printed at 105 mm/s exhibited a tensile strength of 44 MPa. Thus, it has been determined that there is a 27% reduction in tensile strength.

Within the domain of Fused Deposition Modeling printing, the significance of layer adhesion cannot be overstated. Inadequate adhesion between layers may lead to delamination, posing a threat to the mechanical strength of the printed object. SEM images become invaluable in this context, offering a detailed visual inspection of layer adhesion. Through the analysis of SEM images, one can glean insights into optimizing critical printing parameters, including temperature and speed, to achieve the pinnacle of layer adhesion and overall mechanical integrity.

This meticulous examination of porosity and layer adhesion through SEM analysis stands as a transformative approach in advancing the quality and performance of 3D-printed objects. The works of researchers such as Abeykoon et al. (2020), Dudek (2013), Gordeev et al. (2018), Popescu et al. (2018), Sandhu et al. (2019), Shen et al. (2018), Sood et al. (2012), and Wickramasinghe et al. (2020) underscore the importance of leveraging SEM insights to enhance the understanding and optimization of porosity and layer adhesion in the 3D printing landscape [13-20]. Printing speed is a critical factor that directly influences the quality of a 3D-printed object. Higher printing speeds can lead to increased porosity due to reduced precision in layer deposition and inadequate layer bonding. ▶**Figure 8**.a shows SEM images of samples printed at 15 mm/s, ▶**Figure 8**.b at 30 mm/s, and ▶**Figure 8**.c at 105 mm/s. It can be observed that as printing speed increases, layer thicknesses become more pronounced. Filament strands are distinguishable at a printing speed of 105 mm/s, and the gaps between them are visibly apparent. This condition can weaken strength performance on one hand and lead to worsened surface roughness on the other.

In conclusion, SEM images demonstrate that layers printed at higher speeds exhibit more irregularities and voids than those printed at lower speeds. Conversely, while consuming more time, slower printing speeds contribute to better layer adhesion and lower porosity, resulting in a stronger and more reliable final product.

4. Conclusions

This study examines the impact of printing speed on the mechanical properties of materials, particularly using PLA material, in the rapidly evolving field of 3D printing technology. Using an Ender 3 S1 3D printer, tensile test samples were prepared at different speeds (15, 30, 45, 60, 75, 90, and 105 mm/s), and their tensile strengths, masses, hardness values, surface roughness, and porosity values were measured. As a result, this study has revealed that 3D printing parameters, especially printing speed, can play a decisive role in the material's mechanical properties. The acceleration of

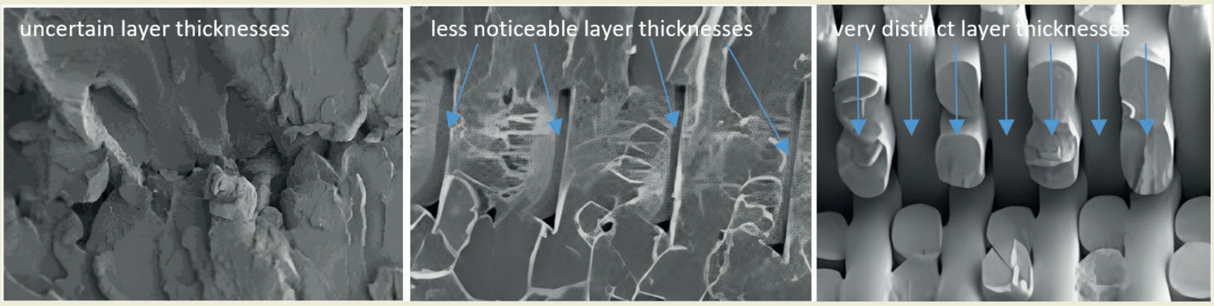

a) (b) (c)

Figure 8. SEM images of fracture surfaces (200x) at different printing speeds: (a) 15 mm/s, (b) 30 mm/s, and (c) 105 mm/s.

printing speeds, while potentially enhancing efficiency, introduces challenges such as reduced material mass, heightened porosity, and compromised structural integrity. This phenomenon may be attributed to insufficient filament feeding during extrusion, resulting in adverse consequences, particularly for applications prioritizing durability and structural robustness. Elevated printing speeds correlate with diminished hardness and tensile strength, potentially stemming from irregular layer assembly and increased porosity. Weak inter-layer adhesion contributes to decreased material strength and the potential formation of a more brittle structure, a concern for load-bearing applications. The escalation of surface roughness at higher speeds not only impacts aesthetic quality but also raises concerns for precision-critical applications. SEM analysis offers microscopic insights into factors like layer adhesion and porosity, emphasizing the negative implications of increased porosity on the structural integrity of objects printed at higher speeds. This finding underscores the importance of considering these factors, particularly in applications requiring mechanical strength and precision. The study results can be summarized as follows:

- As printing speed increases, printing time significantly decreases. For example, at a speed of 15 mm/s, the printing time is reduced from 119 minutes to 15 minutes at a speed of 105 mm/s. During this process, the average mass decreases from 8.21 grams at 15 mm/s to 7.21 grams at 105 mm/s, representing an approximate 12% decrease (Figure 4).

- Changes in Shore D hardness values of the samples were observed as printing speed increased. Higher hardness values were measured at low speeds (15 and 30 mm/s), while an overall decrease in hardness values was observed as speed increased. This indicates that rapid printing conditions can negatively affect material hardness (Figure 5).

- Surface roughness increased directly with printing speed. For example, the roughness value at 0° angle at a speed of 15 mm/s was 0.8, while this value increased to 1.9 at 105 mm/s. This trend indicates a decrease in surface quality at high speeds (Figure 6).

- Tensile strength values decreased as printing speed increased, indicating a rapid decrease in the structural integrity and strength of the material. The tensile strength, which was 60 MPa at a speed of 15 mm/s, decreased to 44 MPa at 105 mm/s, representing an approximate 27% decrease (Figure 7).

- The increase in printing speed adversely affects the ergonomics and mechanical properties of the part. On the other hand, reducing the printing speed significantly increases the printing time. The optimal choice can be made here according to the conflicting goals based on the expected qualities of the final product.

These numerical results demonstrate that the impact of 3D printing on mechanical properties is complex and multifaceted. It is understood that high speeds negatively affect the material's mechanical properties and surface quality, while lower speeds improve these outputs. This information shows that 3D printing parameters, especially speed settings, can significantly influence the outcome of the printing process.

Acknowledgments

We would like to thank Kastamonu University Scientific Research Coordinatorship for supporting this study with project number KÜBAP-01/2023-18.

Research Ethics

Ethical approval not required.

Author Contributions

The author(s) accept full responsibility for the content of this article and have approved its submission.

Competing Interests

There is no conflict of interest. The funders had no role in the design of the study; in the collection, analyses, or interpretation of data; in the writing of the manuscript, or in the decision to publish the results.

Research Funding

Not reported.

Data Availability

Not applicable.

Peer-review

Externally peer-reviewed.

References

[1] Zhu, Y., Gao, Y., Jiang, J., Gu, H., Lv, S., Ni, H., Wang, X., & Jia, C. (2019, November 1). Study on effects of FDM 3D printing parameters on mechanical properties of polylactic acid. *IOP Conference Series: Materials Science and Engineering, 688*(3), 033026-033026. https://doi.org/10.1088/1757-899X/688/3/033026

[2] Wang, X. C., Wei, J., Yi, X. B., Zhang, J., Shang, K., & Wang, Q. (2014, September 1). 3D printing technology and the adaptability of printing material. *Applied Mechanics and Materials, 633-634*, 569-573. https://doi.org/10.4028/www.scientific.net/amm.633-634.569

[3] Afonso, J. A., Alves, J. L., Caldas, G., Gouveia, B. P., Santana, L., & Belinha, J. (2021). Influence of 3D printing process parameters on the mechanical properties and mass of PLA parts and predictive models. *Rapid Prototyping Journal, 27*(3), 487-495. https://doi.org/10.1108/RPJ-03-2020-0043

[4] Lanzotti, A., Grasso, M., Staiano, G., & Martorelli, M. (2015). The impact of process parameters on mechanical properties of parts fabricated in PLA with an open-source 3-D printer. *Rapid Prototyping Journal, 21*(5), 604-617. https://doi.org/10.1108/RPJ-09-2014-0135

[5] Khosravani, M. R., Berto, F., Ayatollahi, M. R., & Reinicke, T. (2022). Characterization of 3D-printed PLA parts with different raster orientations and printing speeds. *Scientific Reports, 12*(1), 1016. https://doi.org/10.1038/s41598-022-05005-4

[6] Tang, C., Liu, J., Yang, Y., Liu, Y., Jiang, S., & Hao, W. (2020). Effect of process parameters on mechanical properties of 3D printed PLA lattice structures. *Composites Part C: Open Access, 3*, 100076. https://doi.org/10.1016/j.jcomc.2020.100076

[7] Ansari, A. A., & Kamil, M. (2021). Effect of print speed and extrusion temperature on properties of 3D printed PLA using fused deposition modeling process. *Materials Today: Proceedings, 45*, 5462-5468. https://doi.org/10.1016/j.matpr.2021.02.137

[8] El Magri, A., Vanaei, S., Shirinbayan, M., Vaudreuil, S., & Tcharkhtchi, A. (2021). An investigation to study the effect of process parameters on the strength and fatigue behavior of 3D-printed PLA-graphene. *Polymers, 13*(19), 3218. https://doi.org/10.3390/polym13193218

[9] Kamer, M. S., Temiz, Ş., Yaykaşlı, H., Kaya, A., & Akay, O. (2022). Comparison of mechanical properties of tensile test specimens produced with ABS and PLA material at different printing speeds in 3D printer. *Journal of the Faculty of Engineering and Architecture of Gazi University, 37*(3), 1197-1211.

[10] Maguluri, N., Suresh, G., & Guntur, S. R. (2022, July). Effect of printing parameters on the hardness of 3D printed poly-lactic acid parts using DOE approach. In *IOP Conference Series: Materials Science and Engineering* (Vol. 1248, No. 1, p. 012004). IOP Publishing. https://doi.org/10.1088/1757-899X/1248/1/012004

[11] Vidakis, N., Petousis, M., Karapidakis, E., Mountakis, N., David, C., & Sagris, D. (2023). Energy consumption versus strength in MEX 3D printing of polylactic acid. *Advances in Industrial and Manufacturing Engineering, 6*, 100119. https://doi.org/10.1016/j.aime.2023.100119

[12] Portoacă, A. I., Ripeanu, R. G., Diniță, A., & Tănase, M. (2023). Optimization of 3D printing parameters for enhanced surface quality and wear resistance. *Polymers, 15*(16), 3419. https://doi.org/10.3390/polym15163419

[13] Abeykoon, C., Abeykoon, C., & Fernando, A. (2020, September 1). Optimization of fused deposition modeling parameters for improved PLA and ABS 3D printed structures. *International Journal of Lightweight Materials and Manufacture, 3*(3), 284-297. https://doi.org/10.1016/j.ijlmm.2020.03.003

[14] Dudek, P. (2013, December 1). FDM 3D printing technology in manufacturing composite elements. *Archives of Metallurgy and Materials, 58*(4), 1415-1418. https://doi.org/10.2478/amm-2013-0186

[15] Gordeev, E. G., Galushko, A. S., & Ananikov, V. P. (2018, June 7). Improvement of quality of 3D printed objects by elimination of microscopic structural defects in fused deposition modeling. *PLOS ONE, 13*(6), e0198370-e0198370. https://doi.org/10.1371/journal.pone.0198370

[16] Popescu, D., Zapciu, A., Amza, C. G., Baciu, F., & Marinescu, R. (2018, August 1). FDM process parameters influence over the mechanical properties of polymer specimens: A review. *Polymer Testing, 69*, 157-166. https://doi.org/10.1016/j.polymertesting.2018.05.020

[17] Sandhu, K., Singh, S., & Prakash, C. (2019, October 1). Analysis of angular shrinkage of fused filament fabricated poly-lactic-acid prints and its relationship with other process parameters. *IOP Conference Series: Materials Science and Engineering, 561*(1), 012058-012058. https://doi.org/10.1088/1757-899X/561/1/012058

[18] Shen, Z., Hua, H., Yang, S., & Zhang, Y. (2018, November 6). Effect of fabrication parameters and material features on tensile strength of FDM built parts. *IOP Conference Series: Materials Science and Engineering, 423*, 012050-012050. https://doi.org/10.1088/1757-899X/423/1/012050

[19] Sood, A. K., Ohdar, R., & Mahapatra, S. S. (2012, January 1). Experimental investigation and empirical modelling of FDM process for compressive strength improvement. *Journal of Advanced Research, 3*(1), 81-90. https://doi.org/10.1016/j.jare.2011.05.001

[20] Wickramasinghe, S., Do, T., & Tran, P. (2020, July 10). FDM-based 3D printing of polymer and associated composite: A review on mechanical properties, defects and treatments. *Polymers, 12*(7), 1529-1529. https://doi.org/10.3390/polym12071529

[21] Pan, A. Q., Huang, Z. F., Guo, R., & Li, J. (2015, October 1). Effect of FDM process on adhesive strength of polylactic acid (PLA) filament. *Key Engineering Materials, 667*, 181-186. https://doi.org/10.4028/www.scientific.net/kem.667.181

[22] Liu, W., Zhou, J., Ma, Y., Wang, J., & Xu, J. (2017, December 1). Fabrication of PLA filaments and its printable performance. *IOP Conference Series: Materials Science and Engineering, 275*, 012033-012033. https://doi.org/10.1088/1757-899X/275/1/012033

[23] Li, J., Li, H. B., Dong, J., Wang, T. Y., & Zhang, H. T. (2018, February 1). The investigation of the effect caused by deposition velocity on bonding degree within the structure of FDM. *Key Engineering Materials, 764*, 142-155. https://doi.org/10.4028/www.scientific.net/kem.764.142

[24] Wu, J. (2018, August 3). Study on optimization of 3D printing parameters. *IOP Conference Series: Materials Science and Engineering, 392*, 062050-062050. https://doi.org/10.1088/1757-899X/392/6/062050

[25] Santana, L., Ahrens, C. H., Netto, A. D. C. S., & Bonin, C. (2017, June 20). Evaluating the deposition quality of parts produced by an open-source 3D printer. *Rapid Prototyping Journal, 23*(4), 796-803. https://doi.org/10.1108/RPJ-05-2016-0078

[26] Giri, J., Patil, A., & Prabhu, H. (2018, September 8). The effect of various parameters on the nozzle diameter and 3D printed product in fused deposition modelling: An approach. In S. K. S. Yadav & A. K. Yadav (Eds.), *Lecture Notes in Networks and Systems* (pp. 839-847). Springer. https://doi.org/10.1007/978-981-13-1217-5_83

EUROPEAN MECHANICAL SCIENCE

Research Article

e-ISSN: 2587-1110

The effect of rolling direction and strain rates on the tensile properties of AA2024-T3 aluminum alloy

Mehmet Fatih Demirdogen[1], **Suleyman Kilic**[2*]

[1]Petlas Tire Industry and Trade Company, Kırşehir, Türkiye
[2]Kırşehir Ahi Evran Üniversity, Faculty of Engineering and Architecture, Kırşehir, Türkiye

Orcid: M. F. Demirdogen (0000-0002-0545-3733), S. Kilic (0000-0002-1681-9403)

Abstract: The AA2024-T3 alloy is a lightweight and durable material commonly used in the aerospace industry. This study investigates the impact of the rolling direction (RD) and strain rates on the alloy's tensile properties. Tensile tests have been performed on samples oriented parallel and transverse to the rolling direction at varying strain rates (5, 25, and 125 mm/min). Samples parallel to the rolling direction have exhibited higher strength compared to those in the transverse direction (TD). At a strain rate of 5 mm/min, the maximum tensile strength in RD samples has been 530.72 MPa, while in TD samples, it has been 505.76 MPa. At 25 mm/min, the tensile strength has been 498.31 MPa in RD and 482.91 MPa in TD. At 125 mm/min, the tensile strength has been 508.52 MPa in RD and 480.36 MPa in TD. The increase in strain rate has had a complex effect on the mechanical properties. The total elongation values have also varied with strain rate, with the highest total elongation observed at 5 mm/min (0.168) in both RD and TD directions. These findings have highlighted the significant impact of the rolling direction and strain rate on the mechanical properties of the AA2024-T3 alloy, which should be considered in design and manufacturing processes.

Keywords: AA2024, rolling direction, strain rate, formability.

1. Introduction

In many industrial sectors, including energy, machinery, transportation, and aerospace, shaped semi-finished products are commonly used. Material selection for these products is based on the required mechanical properties, and the production method is also a crucial factor. Rolling is a significant plastic shaping method that alters the crystal structure of the material, resulting in anisotropic properties. Anisotropic behavior refers to the phenomenon where materials exhibit different mechanical properties in different directions. This behavior affects the mechanical properties of the material [1-5]. The strain rate used in production processes is another parameter that significantly affects the mechanical properties [6-10]. Strain rate also causes changes in dislocation movements, leading to variations in strength levels. The heat generated during deformation also affects dislocation movements.

The rolling process is known to have a variable effect on the mechanical behaviors of materials [11-15]. In particular, this impact on tensile properties is a critical factor in the development of materials' anisotropic characteristics. In this regard, research has shown that the direction of rolling alters the material's fundamental mechanical properties, such as microstructure, strength, modulus of elasticity, and fracture toughness. Goli and Jamaati [16] investigated the effect of the deformation path applied during the cold rolling process on the microstructure and mechanical properties of the AA2024 aluminum alloy. They emphasized that the average grain size decreased due to dynamic recrystallization in samples that underwent cross rolling. Pang et al. [17] examined the anisotropy

*Corresponding author:
Email: suleymankilic@gmail.com

Cite this article as:
Demirdogen, M., Kilic, S. (2024). The effect of rolling direction and strain rates on the tensile properties of AA2024-T3 aluminum alloy. *European Mechanical Science, 8*(3): 145-152. https://doi.org/10.26701/ems.1486134

History dates:
Received: 18.05.2024, *Revision Request*: 05.06.2024, *Last Revision Received*: 28.06.2024, *Accepted*: 28.06.2024

of the cold-rolled AA2024-T3 aluminum alloy using a laser imaging sensor. Furthermore, they demonstrated that the Yld2004-18p model accurately represents the anisotropic behavior of AA2024-T3 in finite element analyses. Aghabalaeivahid and Shalvandi [18] developed a microstructure-based crystal plasticity model to model the anisotropic plasticity and yield behavior of the AA2024-T3 aluminum alloy. In their work, they mentioned that crystal plasticity modeling based on the actual microstructure could be a useful tool in understanding and predicting the anisotropic behavior of the AA2024-T3 aluminum alloy. Anijdan et al. [19] demonstrated that the combination of cold rolling and suitable aging heat treatment alters the mechanical properties and microstructure of the AA2024 aluminum alloy. It has been stated that cold rolling, double-stage aging, and over-aging treatments have significant effects on the strength of the AA2024 aluminum alloy [20]. These processes lead to changes in the alloy's mechanical properties and microstructure. It has been observed that the mechanical properties of aged samples significantly improve with the correct application of cold deformation. In a study on the microstructure of the AA2024 aluminum alloy in a semi-solid state [21], the impact of rolling and extrusion processes on microstructural conditioning and change has been examined. The results of the study provide important insights into the formability of the alloy in its semi-solid state. It is said that the higher the deformation rate, the smaller the initial particle size, and a 30% thickness reduction is sufficient to achieve a fine distribution of Al-α particles. In tensile tests conducted in three different rolling directions on the AA2024-T351 aluminum alloy, it has been indicated that samples rolled perpendicular to the rolling direction exhibit higher yield strength and ductility characteristics. These characteristics are significantly better compared to those rolled in the thickness direction [22]. The importance of anisotropy in accurately predicting the deformation behavior of materials has been emphasized. In a study that examined the effect of rolling direction on the AA5083 aluminum alloy [23], it has been shown that the process has a significant effect on the tensile properties of the samples. Furthermore, it has been highlighted that when the directional angle increases, tensile strength increases and modulus of elasticity decreases. In a study investigating the effect of cold rolling and subsequent heat treatments on the microstructure and mechanical properties of the AA5052 aluminum alloy [24], it has been shown that an increasing rolling rate elongates the grains of the alloy, and it enhances its strength but reduces its ductility. It has been shown that the AA7050-T7451 alloy exhibits specific internal structural features after rolling, which affects the material's strength properties [25]. The sample to be perpendicular to the rolling direction has achieved the highest tensile strength, whereas the lowest has been obtained in the thickness direction. Rout [11] investigated the effect of different rolling directions on the microstructure and tensile properties of 304 austenitic stainless steel. It has been shown that cross rolling (CR) and reverse rolling (RR) processes have significant impacts on tensile properties. Medjahed et al. [13] studied the effects of different rolling directions (0°, 45°, and 90°) on the microstructure, strength, and anisotropy properties of the Al-Cu-Li-Mg-X alloy. Different rolling directions have been shown to lead to distinctive microstructures that affect the properties.

Another parameter that affects mechanical properties is the strain rate. It is known that the strain rate affects the tensile and fracture strength of the alloy [26, 27]. Understanding these effects is important in determining the production method. Wen et al. [28] have investigated the effects of deformation parameters (strain rate and temperature) on the hot tensile deformation and fracture behaviors of a high-strength steel. Their work has shown that the hot tensile behavior of the material is largely influenced by the relationship between damage formation, hardening, and dynamic softening. As the deformation rate has increased from 0.01 to 10 s-1, uniform fracture morphologies have gradually transitioned to serrated fracturing. That is, the strain rate affects the fracture mechanism, and thus, the mechanical properties are affected. It has been emphasized that changes in the number of voids or cracks in the microstructure increase with a rising strain rate or decreasing tensile temperature. It has been stated that intergranular fracture occurs at high tensile temperatures and low deformation rates, while intragranular fracture occurs at low tensile temperatures and high deformation rates. Kami et al. [29] examined the effects of strain rate on the mechanical properties of AA5021 and commercially pure aluminum (A1070). It has been shown that the AA5021 alloy exhibits negative strain rate sensitivity within a certain strain rate range but displays positive strain rate sensitivity at high strain rates. It has been stated that the primary factor is due to the effect of Mg atoms locking the dislocations. Ma et al. [30] investigated the variation of mechanical properties at various strain rates in the 5A02-O aluminum alloy. They have shown that significant increases in yield and tensile strength occur at high strain rates. It has been stated that a higher strain rate leads to a higher dislocation density. Bobbili et al. [31] conducted tensile tests on the AA7017 alloy at various strain rates and temperatures. It has been observed that strength increases with increasing strain rate. Chen et al. [32] studied the mechanical behavior of AA6xxx and AA7xxx aluminum alloys across a wide range of strain rates. They have conducted standard tensile tests at low and medium strain rates and split-Hopkinson tests at high strain rates. It has been found that AA6xxx series alloys do not show a significant change in strain rate, but AA7xxx series alloys exhibit a moderate level of rate sensitivity. They have also shown that there is no significant difference in rate sensitivity among different rolling directions in their studies. Wang et al. [33] investigated the effects of strain rate on the mechanical properties and microstructure of the Al-Mg-Si-Cu alloy. It has been stated that increasing the strain rate enhances the alloy's strength but has a limited effect on the microstructure. Aydın et al. [34] studied the impact of strain rate and rolling direction on the tensile properties of dual-phase steels used in the automotive industry. They have shown that both strain rate and rolling direction has a significant impact on the material's tensile properties. Additionally, they have emphasized that the strain rate has a more significant effect on the tensile properties than the rolling direction in both steels. In another study by Aydın et al. [35], has been shown that the effect of strain rate on strength is more pronounced in the AA6082-T6 alloy than in the AA1035-H14 alloy. They have highlighted the significant effects of rolling direction and strain rate on the tensile properties of aluminum alloys.

This investigation focuses on the AA2024-T3 alloy, which is known for its durability and corrosion resistance, making it ideal for high-demand applications [36, 37]. The aim of this research is to investigate the impact of rolling directions and varying strain rates on the tensile properties of the AA2024-T3 alloy. While it is well-established that mechanical properties are direction-dependent due to rolling, this study provides a novel analysis of the combined effects of rolling direction and varying strain rates on the tensile properties of the AA2024-T3 alloy. Unlike previous studies that typically focus on either rolling direction or strain rate independently, our research integrates both factors to provide a comprehensive understanding of their interaction and its impact on the material's performance. The results indicate that both the direction of rolling and the applied strain rates significantly affect the mechanical behavior of the alloy.

2. Material and Method

The AA2024 aluminum alloy has a chemical composition characterized by aluminum itself along with copper, manganese, magnesium, and other elements (Table 1). This composition equips AA2024 with properties such as high strength and good corrosion resistance, making it a preferred material in the aerospace sector. In our study, material manufactured in the form of sheet metal and subjected to T3 tempering has been used. The T3 designation represents the mechanical properties obtained after solution heat treatment followed by cooling and natural aging (aging at room temperature). This heat treatment provides the alloy with strength, corrosion, fatigue, and crack resistance.

Test specimens have been cut in air atmosphere using a laser cutting machine according to the ASTM-E8 standard [38]. Specimens with the dimensions specified in **▶Figure 1** have been prepared in two different orientations relative to the rolling process direction (RD and TD to the rolling direction, **▶Figure 2**). With this method, the effect of the rolling direction on the material has been examined in detail. The prepared samples have been subjected to tensile tests at room temperature using a Shimadzu Autograph 100kN brand tensile test machine. The experiments have been repeated three times to ensure the reliability of the results.

In the tensile testing machine, the lower jaw of the device is fixed, while the upper jaw is movable. As shown in **▶Figure 3**, for each tensile specimen, a total measurement area of 50 mm has been marked, comprising 25 mm above and below the center of the specimen's vertical axis. This marked area has been set as the focus point to be clearly visible by the video camera. The

Table 1. Chemical composition of the alloy.

Material	Fe	Si	Cu	Cr	Mn	Mg	Zn	Zr+Ti
AA2024	0.5	0.5	3.8-4.9	0.1	0.3-0.9	1.2-1.8	0.25	0.15

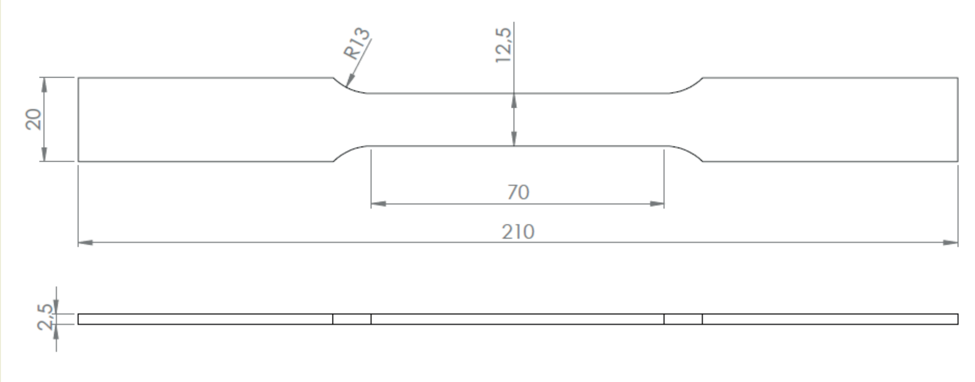

Figure 1. Dimensions of the tensile test specimen (mm).

determination of elongation has been conducted using a video-type extensometer. This method allows for the precise recording of deformations experienced by the samples during tension.

3. Results and Discussion

According to the experimental tests performed, these two factors have affected the mechanical behaviors of the alloy. **▶Figure 4** shows the effect of the rolling direction at a strain rate of 5 mm/min. Specimens parallel to the rolling direction have exhibited higher strength compared to those TD to the rolling direction. This situation is attributed to the material's internal structural characteristics and the orientation of the crystal structure during the rolling process. It is thought that samples parallel to the rolling direction show higher strength due to the alignment of the crystal structure and dislocations. Situations where dislocation movements occur more easily affect the mechanical properties of the material.

Tensile tests conducted at different strain rates (5, 25, and 125 mm/min) are presented in **▶Figure 5**. Specimens prepared in the rolling direction have different strength values compared to those prepared in the transverse direction (TD). This difference in strength values shows that the material has anisotropic properties, meaning its properties vary depending on the direction. This situation demonstrates that the internal structure and crystal orientation of aluminum alloys affect their mechanical properties. During the rolling process, the orientation of crystal structures within the material aligns with the direction of the applied force.

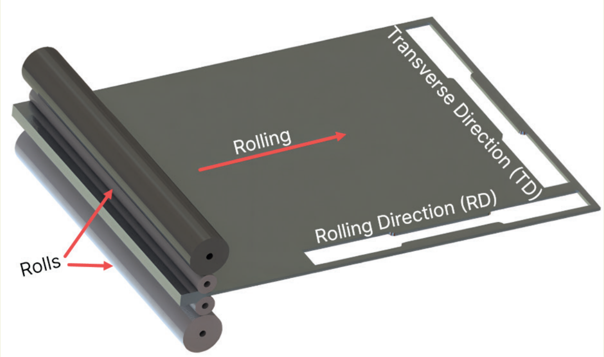

Figure 2. Preparation of samples in different directions on a laser cutting machine.

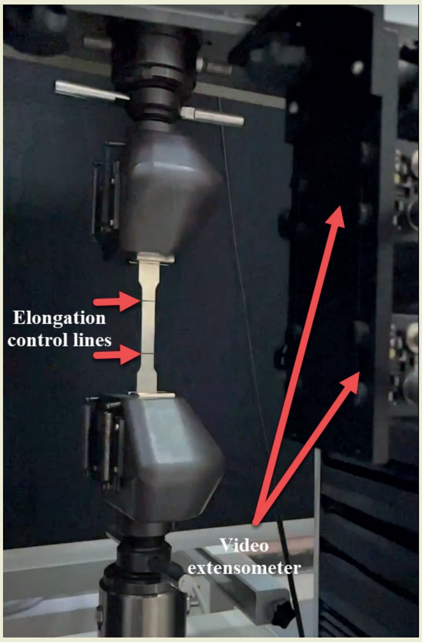

Figure 3. Tensile test setup.

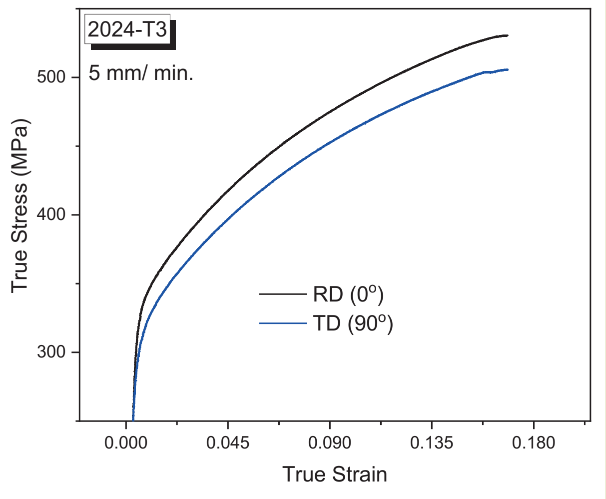

Figure 4. The effect of rolling direction.

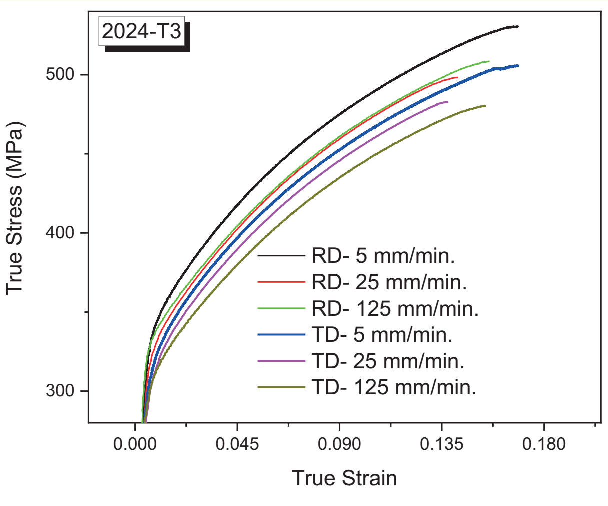

Figure 5. The effect of rolling direction and different strain rates.

This illustrates the significant role of the rolling process on the mechanical properties of the material.

The change in strength as a result of rolling is related to grain orientation. Rolling alters the crystal structure of the material, leading to an alignment of grains in the rolling direction. This alignment affects the movement of dislocations, which are known to move more easily along certain crystallographic planes and directions. According to Goli and Jamaati [16], during the rolling process, the grains become elongated and aligned along the rolling direction, which facilitates dislocation movement in that direction. Similarly, Aghabalaeivahid and Shalvandi [18] noted that the anisotropic behavior of the AA2024-T3 alloy can be attributed to the orientation of grains and dislocations resulting from rolling. This grain orientation reduces the barriers for dislocation movement along the rolling direction, thereby increasing the material's strength in that direction. These mechanisms are well-documented in the literature and support the findings of our study.

▶**Figure 6** shows the stress-strain curve of specimens at different strain rates (5, 25, and 125 mm/min). It is observed that the alloy exhibits a non-linear behavior with respect to strain rate. The highest strength has been obtained at a strain rate of 5 mm/min. On the other hand, the lowest strength has been obtained at a strain rate of 25 mm/min. This phenomenon can be explained by the effect of strain rate on the material's microstructural arrangement and dislocation movements. Low strain rates provide sufficient time for dislocations to move and rearrange within the material's internal structure, leading to higher strength values. However, the material may struggle to adapt to these microstructural arrangements at certain speed ranges. This situation results in a decrease in the strength. Although an increase in strain rate is generally known to increase strength, these results demonstrate that this relationship is not always linear. These observations emphasize that strain rate has a significant effect on the mechanical properties of the material and that the relationship between strength and strain rate is complex.

▶**Figure 7** presents the stress-strain curves of specimens prepared in the TD at different strain rates (5, 25, and 125 mm/min). According to the data obtained, there is a negative linear relationship between strain rate and stress. The highest strength has been achieved at a strain rate of 5 mm/min, while the lowest strength has been observed at 125 mm/min. This negative linear relationship observed in specimens prepared in the TD can be due to the material having a more homogeneous microstructure in this orientation. As a result, the material exhibits more predictable behavior against increasing strain rates.

The results obtained experimentally are in agreement with findings reported in the literature. Due to the anisotropic properties of the AA2024 alloy, it has been observed that the yield/tensile strengths differ [39]. It has been determined that the highest yield and tensile strength in the AA2024-T4 alloy are exhibited in the rolling direction [40]. Our study has shown through tensile tests conducted in the rolling direction and at different strain rates that there is a non-linear relationship between strain rate and stress. Moreover, in experiments where the material has been stretched in the rolling direction, elongation and stress have been found to be higher compared to specimens prepared in the TD.

It is known that the effect of strain rate causes different types of fracture (intergranular or transgranular fracture) to occur in the material, which in turn affects the strength [28]. Furthermore, it is understood that an increase in strain rate, by locking dislocations in the internal structure of the atoms, provides an increase in

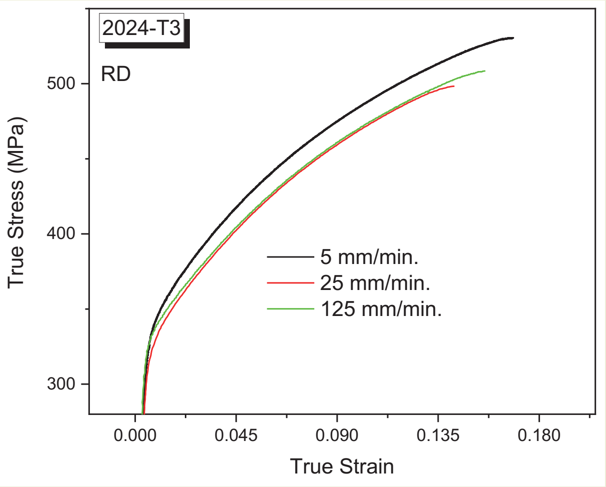

Figure 6. Stress-strain curves for specimens prepared in the rolling direction at different strain rates.

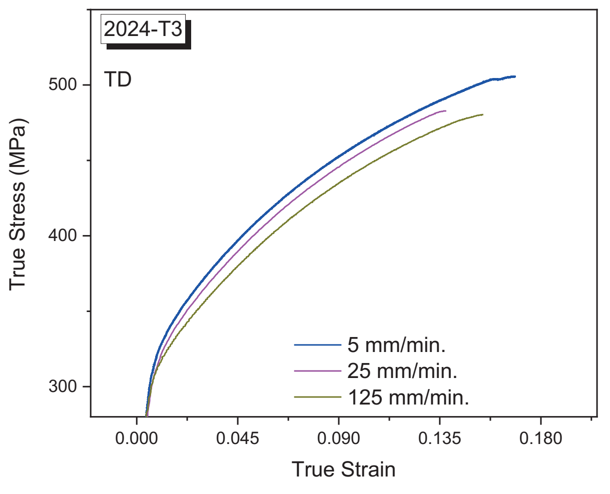

Figure 7. Stress-strain curves for specimens prepared in the TD at different strain rates.

strength. High strain rates have the effect of increasing dislocation density, resulting in increased strength [29, 30]. In experiments conducted at 400 °C on the AA2024 alloy, an increase in strain rate has been observed to increase yield/tensile strength [41]. In the AA2014-T6 alloy, experiments conducted at room temperature have shown that an increase in strain rate also have increased yield and tensile strength [42]. Similarly, the same results have been obtained at different temperatures.

4. Conclusion

In this study, the variations in the mechanical properties of the AA2024-T3 aluminum alloy have been examined in relation to the variations in rolling direction and strain rate parameters. The tensile tests conducted at various strain rates (5, 25, and 125 mm/min) and rolling directions (parallel and perpendicular to the rolling direction) have revealed several key findings:

- *Effect of Rolling Direction*: The tensile strength and elongation of the AA2024-T3 alloy are significantly influenced by the rolling direction. Samples tested as parallel to the rolling direction (RD) have exhibited higher tensile strength and elongation compared to those tested perpendicular to the rolling direction (TD). For instance, at a strain rate of 5 mm/min, the tensile strength in RD samples is 530.72 MPa with an elongation of 0.168, while in TD samples, it is 505.76 MPa with the same elongation of 0.168.

- *Effect of Strain Rate:* The strain rate also has a complex effect on the tensile properties of the alloy. The highest tensile strength has been observed at the lowest strain rate of 5 mm/min, with RD samples showing 530.72 MPa and TD samples showing 505.76 MPa. At a strain rate of 25 mm/min, the tensile strength in RD samples is 498.31 MPa and in TD samples is 482.91 MPa. At 125 mm/min, the tensile strength is 508.52 MPa in RD and 480.36 MPa in TD.

- *Interaction of Factors*: The combined effects of rolling direction and strain rate on the mechanical properties highlight the importance of considering both parameters in the design and manufacturing processes of AA2024-T3 alloy components. The study provides a comprehensive understanding of how these factors interact and influence the material's performance, which can lead to improved application-specific properties.

Overall, the findings of this research highlight the need to optimize rolling direction and strain rate during the manufacturing of AA2024-T3 alloy to achieve the desired mechanical properties. These insights contribute to a better understanding of the anisotropic behavior of the alloy and its implications for industrial applications, particularly in the aerospace sector.

Research Ethics

Ethical approval is not required.

Author Contributions

The author(s) accept full responsibility for the content of this article and have approved its submission.

Competing Interests

The author(s) declare that there are no competing interests.

Research Funding

Not reported.

Data Availability

Not applicable.

References

[1] Liu, D., Liu, Z., & Wang, E. (2014). Effect of rolling reduction on microstructure, texture, mechanical properties and mechanical anisotropy of AZ31 magnesium alloys. *Materials Science and Engineering: A, 612*(1), 208-213. https://doi.org/10.1016/j.msea.2014.06.034

[2] Wang, J., Jin, P., Li, X., Wei, F., Shi, B., Ding, X., & Zhang, M. (2020). Effect of rolling with different amounts of deformation on microstructure and mechanical properties of the Mg–1Al–4Y alloy. *Materials Characterization, 161*, 110149. https://doi.org/10.1016/j.matchar.2020.110149

[3] Ma, Y., Du, Z., Cui, X., Cheng, J., Liu, G., Gong, T., Liu, H., Wang, X., & Chen, Y. (2018). Effect of cold rolling process on microstructure and mechanical properties of high strength β titanium alloy thin sheets. *Progress in Natural Science: Materials International, 28*(6), 711-717. https://doi.org/10.1016/j.pnsc.2018.10.004

[4] Kacar, I., Öztürk, F., Toros, S., & Kılıç, S. (2020). Prediction of strain limits via the Marciniak-Kuczynski model and a novel semi-empirical forming limit diagram model for dual-phase DP600 advanced high strength steel. *Strojniski Vestnik/Journal of Mechanical Engineering, 66*(10), 602-612. https://doi.org/10.5545/sv-jme.2020.6755

[5] Kilic, S., Ozturk, F., & Toros, S. (2020). Analysis of yield criteria and flow curves on FLC for TWIP900 steel. *Experimental Techniques, 44*(5), 597-612. https://doi.org/10.1007/s40799-020-00382-9

[6] Khalifeh, A., Banaraki, A. D., Manesh, H. D., & Banaraki, M. D. (2018). Investigating of the tensile mechanical properties of structural steels at high strain rates. *Materials Science and Engineering: A, 712*(1), 232-239. https://doi.org/10.1016/j.msea.2017.11.025

[7] Davies, R., & Magee, C. (1975). The effect of strain-rate upon the tensile deformation of materials. *Journal of Materials Processing Technology, 1*(1). https://doi.org/10.1115/1.3443275

[8] Kılıç, S., & Demirdöğen, M. F. (2022). Investigation of the effect of temperature and strain rate on mechanical properties. *International*

Journal of Engineering Research & Development (IJERAD), 14(2). https://doi.org/10.29137/umagd.987547

[9] Kilic, S. (2019). Experimental and numerical investigation of the effect of different temperature and deformation speeds on mechanical properties and springback behaviour in Al-Zn-Mg-Cu alloy. *Mechanics, 25*(5), 406-412. https://doi.org/10.5755/j01.mech.25.5.22689

[10] Ozturk, F., Toros, S., Bas, M. H., & Kilic, S. (2008). Evaluation of tensile properties of high strength steels at warm temperatures and various strain rates. *Steel Research International, 79*(2), 295.

[11] Rout, M. (2020). Texture-tensile properties correlation of 304 austenitic stainless steel rolled with the change in rolling direction. *Materials Research Express, 7*(1), 016563. https://doi.org/10.1088/2053-1591/ab677c

[12] Vegi, N., & Ragothaman, B. (2023). Effect of rolling direction and gauge length on the mechanical properties of S460MC high strength low alloy steel. *SAE Technical Paper.*

[13] Medjahed, A., Moula, H., Zegaoui, A., Derradji, M., Henniche, A., Wu, R., Hou, L., Zhang, J., & Zhang, M. (2018). Influence of the rolling direction on the microstructure, mechanical, anisotropy and gamma rays shielding properties of an Al-Cu-Li-Mg-X alloy. *Materials Science and Engineering: A, 732*(1), 129-137. https://doi.org/10.1016/j.msea.2018.06.074

[14] Ma, Q. L., Wang, D. C., Liu, H. M., & Lu, H. M. (2009). Effect of temper rolling on tensile properties of low-Si Al-killed sheet steel. *Journal of Iron and Steel Research International, 16*(3), 64-67. https://doi.org/10.1016/S1006-706X(09)60045-5

[15] Kim, D. G., Son, H. T., Kim, D. W., Kim, Y. H., & Lee, K. M. (2011). Effect of cross-roll angle on microstructures and mechanical properties during cross-roll rolling in AZ31 alloys. *Materials Transactions, 52*(12), 2274-2277. https://doi.org/10.2320/matertrans.M2011260

[16] Goli, F., & Jamaati, R. (2019). Effect of strain path during cold rolling on the microstructure, texture, and mechanical properties of AA2024 aluminum alloy. *Materials Research Express, 6*(6), 066514. https://doi.org/10.1088/2053-1591/ab0a1f

[17] Pang, Y., Chen, B. K., & Liu, W. (2019). An investigation of plastic behaviour in cold-rolled aluminium alloy AA2024-T3 using laser speckle imaging sensor. *The International Journal of Advanced Manufacturing Technology, 103*(1), 2707-2724. https://doi.org/10.1007/s00170-019-03717-y

[18] Aghabalaeivahid, A., & Shalvandi, M. (2021). Microstructure-based crystal plasticity modeling of AA2024-T3 aluminum alloy defined as the α-Al, θ-Al2Cu, and S-Al2CuMg phases based on real metallographic image. *Materials Research Express, 8*(10), 106521. https://doi.org/10.1088/2053-1591/ac2eac

[19] Anijdan, S. M., Sadeghi-Nezhad, D., Lee, H., Shin, W., Park, N., Nayyeri, M., Jafarian, H., & Eivani, A. (2021). TEM study of S'hardening precipitates in the cold rolled and aged AA2024 aluminum alloy: Influence on the microstructural evolution, tensile properties & electrical conductivity. *Journal of Materials Research and Technology, 13*, 798-807. https://doi.org/10.1016/j.jmrt.2021.05.003

[20] Sadeghi-Nezhad, D., Anijdan, S. M., Lee, H., Shin, W., Park, N., Nayyeri, M., & Jafarian, H. (2020). The effect of cold rolling, double aging and overaging processes on the tensile property and precipitation of AA2024 alloy. *Journal of Materials Research and Technology, 9*(6), 15475-15485. https://doi.org/10.1016/j.jmrt.2020.11.005

[21] De Freitas, E., Ferracini Jr, E., & Ferrante, M. (2004). Microstructure and rheology of an AA2024 aluminium alloy in the semi-solid state, and mechanical properties of a back-extruded part. *Journal of Materials Processing Technology, 146*(2), 241-249. https://doi.org/10.1016/j.jmatprotec.2003.11.007

[22] Khan, R. (2013). Anisotropic deformation behavior of Al2024T351 aluminum alloy. *The Journal of Engineering Research [TJER], 10*(1), 80-87. https://doi.org/10.24200/tjer.vol10iss1pp80-87

[23] Najib, L. M., Alisibramulisi, A., Amin, N. M., Bakar, I. A. A., & Hasim, S. (2015). The effect of rolling direction to the tensile properties of AA5083 specimen. In *CIEC 2014: Proceedings of the International Civil and Infrastructure Engineering Conference 2014* (pp. 779-787).

[24] Bo, W., Chen, X. H., Pan, F. S., Mao, J. J., & Yong, F. (2015). Effects of cold rolling and heat treatment on microstructure and mechanical properties of AA 5052 aluminum alloy. *Transactions of Nonferrous Metals Society of China, 25*(8), 2481-2489. https://doi.org/10.1016/S1003-6326(15)63866-3

[25] Hao, Z., Fu, X., Men, X., & Zhou, B. (2018). Study on tensile and fracture properties of 7050-T7451 aluminum alloy based on material forming texture characteristics. *Materials Research Express, 6*(3), 036502. https://doi.org/10.1088/2053-1591/aaf304

[26] Hajlaoui, K., Stoica, M., LeMoulec, A., Charlot, F., & Yavari, A. (2008). Strain rate effect on deformation of Zr-based metallic glass: In-situ tensile deformation in SEM analysis. *Rev. Adv. Mater. Sci, 18*(1), 23-26.

[27] Gómez-del Río, T., Salazar, A., & Rodríguez, J. (2012). Effect of strain rate and temperature on tensile properties of ethylene–propylene block copolymers. *Materials & Design, 42*, 301-307. https://doi.org/10.1016/j.matdes.2012.05.042

[28] Wen, D., Wang, J., Wang, K., Xiong, Y., Huang, L., Zheng, Z., & Li, J. (2019). Hot tensile deformation and fracture behaviors of a typical ultrahigh strength steel. *Vacuum, 169*, 108863. https://doi.org/10.1016/j.vacuum.2019.108863

[29] Kami, T., Yamada, H., & Ogasawara, N. (2018). Dynamic behaviour of Al-Mg aluminum alloy at a wide range of strain rates. *EPJ Web of Conferences, 02028.*

[30] Ma, H., Huang, L., Tian, Y., & Li, J. (2014). Effects of strain rate on dynamic mechanical behavior and microstructure evolution of 5A02-O aluminum alloy. *Materials Science and Engineering: A, 606*(1), 233-239. https://doi.org/10.1016/j.msea.2014.03.081

[31] Bobbili, R., Madhu, V., & Gogia, A. K. (2016). Tensile behaviour of aluminium 7017 alloy at various temperatures and strain rates. *Journal of Materials Research and Technology, 5*(2), 190-197. https://doi.org/10.1016/j.jmrt.2015.12.002

[32] Chen, Y., Clausen, A., Hopperstad, O., & Langseth, M. (2009). Stress–strain behaviour of aluminium alloys at a wide range of strain rates. *International Journal of Solids and Structures, 46*(21), 3825-3835. https://doi.org/10.1016/j.ijsolstr.2009.07.013

[33] Wang, X. F., Shi, T. Y., Wang, H. B., Zhou, S. Z., Peng, W. F., & Wang, Y. G. (2020). Effects of strain rate on mechanical properties, microstructure and texture of Al-Mg—Si—Cu alloy under tensile loading. *Transactions of Nonferrous Metals Society of China, 30*(1), 27-40. https://doi.org/10.1016/S1003-6326(19)65177-0

[34] Tuncel, O., Aydin, H., Karpuz, M., & Aydin, Ö. (2019). The effect of rolling direction and strain rate on the tensile properties of DP450 and DP800 steels used in the automotive industry. *Balıkesir Üniversitesi Fen Bilimleri Enstitüsü Dergisi, 21*(1), 323-335. https://doi.org/10.25092/baunfbed.547191

[35] Aydın, H., Tunçel, O., Yiğit, K., Balamur, F., Çavuşoğlu, O., & Düzgün, O. (2017). The effect of rolling direction and strain rate on the tensile properties of AA6082-T6 and AA1035-H14 aluminum alloys. *Uludağ Üniversitesi Mühendislik Fakültesi Dergisi, 22*(3), 81-96. https://doi.org/10.17482/uumfd.297265

[36] Hughes, A. E., Parvizi, R., & Forsyth, M. (2015). Microstructure and corrosion of AA2024. *Corrosion Reviews, 33*(1-2), 1-30. https://doi.org/10.1515/corrrev-2014-0039

[37] Miramontes, J. C., Gaona Tiburcio, C., García Mata, E., Esneider Alcála, M. Á., Maldonado-Bandala, E., Lara-Banda, M., Nieves-Mendoza, D., Olguín-Coca, J., Zambrano-Robledo, P., López-León, L. D., & Almeraya Calderón, F. (2022). Corrosion resistance of aluminum alloy AA2024 with hard anodizing in sulfuric acid-free solution. *Materials, 15*(18), 6401. https://doi.org/10.3390/ma15186401

[38] ASTM. (2016). *ASTM E8/E8M-16a: Standard test methods for tension testing of metallic materials.* West Conshohocken, PA, USA: ASTM International.

[39] Shamchi, S. P., Queirós de Melo, F. J. M., Tavares, P. J., & Moreira, P. M. G. P. (2019). Thermomechanical characterization of Alclad AA2024-T3 aluminum alloy using split Hopkinson tension bar. *Mechanics of Materials, 139*, 103198. https://doi.org/10.1016/j.mechmat.2019.103198

[40] Park, C. M., Jung, J., Yu, B. C., & Park, Y. H. (2019). Anisotropy of the wear and mechanical properties of extruded aluminum alloy rods (AA2024-T4). *Metals and Materials International, 25*(1), 71-82. htt-

ps://doi.org/10.1007/s12540-018-0164-x

[41] Ebrahimi, G. R., Zarei-Hanzaki, A., Haghshenas, M., & Arabshahi, H. (2008). The effect of heat treatment on hot deformation behaviour of Al 2024. *Journal of Materials Processing Technology, 206*(1), 25-29. https://doi.org/10.1016/j.jmatprotec.2007.11.261

[42] Pandouria, A. K., Yadav, K., & Tiwari, V. (2023). Compressive and tensile behavior of AA2014-T6 under different strain rates and different temperatures. *Structures, 49*, 12-25. https://doi.org/10.1016/j.istruc.2023.01.084

EUROPEAN
MECHANICAL
SCIENCE

Research Article

e-ISSN: 2587-1110

The synthesis and characterization of alkaline niobate-based ceramic composites containing L-lysine Hydrochloride

Henry Ekene Mgbemere[1], Viktoriya Semeykina[2], Chiedozie Valentine Oluigbo[3*]

[1] Department of Metallurgical and Materials Engineering, University of Lagos, Akoka Lagos Nigeria
[2] Institute of Advanced Ceramics, Hamburg University of Technology, Denickestrasse 15, 21073, Hamburg, Germany.
[3] Department of Welding and Fabrication Engineering Technology, Federal Polytechnic Ilaro, Ogun State, Nigeria.

Orcid: H.E. Mgbemere (0000-0003-3887-7628), V. Semeykina (0000-0001-8175-3351), C. V. Oluigbo (0000-0002-8900-2883)

Abstract: Some lead-free piezoelectric ceramics are known to have high dielectric and piezoelectric properties but are limited by their brittle nature. A few amino acids have recently been reported to exhibit rather low dielectric and piezoelectric properties but have the advantage of being biocompatible and flexible. It would therefore be interesting to form a composite that will combine the inherent advantage of high dielectric properties from the ceramics and flexibility from the biomolecule. In this research, the properties of lead-free $(K_{0.45}Na_{0.51}Li_{0.04})(Nb_{0.85}Ta_{0.1}Sb_{0.05})O_3$ (KNNLST) ceramics and L-lysine hydrochloride (L-LHCl) have been combined to produce dielectric composites. The samples were produced by mixing the constituents from 0 wt.% to 100 wt.%, pelletising and heat-treating them. Bulk density, X-ray diffraction, scanning electron microscopy, and dielectric characterisation were techniques used to determine the density, phases, morphology, and dielectric properties of the produced composites. The results show an increasing bulk density value from 1.2 g/cm^3 for L-LHCl to 4.67 g/cm^3 for the KNNLST ceramics. The morphology of the composite shows very tiny grains when small amounts of the ceramics were introduced. The L-LHCl transforms from an amorphous phase to a crystalline phase having the orthorhombic-tetragonal structure with the introduction of the KNNLST ceramics. The dielectric constant values increased with increasing KNNLST ceramics content from 10 @1 kHz to 200 for the composite with 80 wt%. KNNLST content. The dielectric loss values decreased for L-LHCl from 0.9 @1 kHz to 0.2 @1kHz. The electrical conductivity values increased with increasing KNNLST ceramics content. The results show that the composites produced from these constituents may be suitable for dielectric applications.

Keywords: L-lysine hydrochloride, KNN ceramics, Composites, Synthesis, Dielectrics

1. Introduction

Poly L-lysine hydrochloride is a synthetic water-soluble polypeptide with properties similar to other lysine molecules. The crystal structure of amino acids is classified based on the system proposed by Gerbitz [1], where the hydrogen bonding arrangement of the head groups is used. The structure of the lysine molecule has been investigated with X-ray diffraction [2]. Amino acids are often used as ceramic templates, modifiers, and regulators. L-lysine monomer has a high affinity for water under normal atmospheric conditions [3]. It has a monoclinic symmetry with $P2_1$ space group and lattice parameters a = 9.54 Å, b = 5.14 Å, c = 17.06 Å, β = 97.78° (V= 828.9 Å^3). L-lysine monohydrochloride dihydrate (L-LMHCl) is grown using different techniques for non-linear optical applications [4]. Deionised water and its mixture with ethanol have been used to grow L-lysine monohydrochloride dihydrate (L-LMHCl) with lattice parameters: a = 5.8840 Å, b = 13.3359 Å, c = 7.5014 Å, and α = 89.92°, β = 97.63°, γ = 90.01° and

*Corresponding author:
Email: olu7wonders@yahoo.com

Cite this article as:
Mgbemere, H., Semeykina, V., Oluigbo, C. (2024). The synthesis and characterization of alkaline niobate-based ceramic composites containing L-lysine Hydrochloride. *European Mechanical Science, 8*(3): 153-159. https://doi.org/10.26701/ems.1497079

History dates:
Received: 06.06.2024, ***Revision Request***: 05.07.2024, ***Last Revision Received***: 11.07.2024, ***Accepted***: 11.07.2024

V = 583.404 Å^3 for non-linear optical applications [5]. L-lysine hydrochloride and nano-crystallites of amorphous L-arginine hydrochloride substituted hydroxyapatite composite for dental applications have been investigated [6]. Using alkaline and acidic media, the effect of $CaCO_3$ substituted-hydroxyapatite, L-lysine, and L-arginine has been investigated [7]. Bonding was observed on the side chain of L-lysine HCl, while the hydroxyl groups of hydroxyapatites created an anionic form of L-lysine when the pH was ≤ 5. Composites from Potassium dihydrogen phosphate (KDP) crystals and L-lysine were grown, and the dielectric constant and loss values of the pure KDP crystals were better than those of the composite [8].

With different solvents, the structure of Poly-L-lysine has been studied [9]. Amino acids have recently been reported to exhibit dielectric and piezoelectric responses [10], which are, however, low, with a dielectric constant value of about 10 and piezoelectric constant values between 0.02 and 100 pC/N [11]. Ceramics like Lead zirconate titanate (PZT), $K_xNa_{1-x}(NbO_3)$ (KNN), and Barium titanate (BT) possess relatively high electrical responses. Their values are usually in orders of magnitude higher than those of amino acids. The challenge with piezoelectric ceramics generally is that they are usually very rigid and fail catastrophically in service most times. There have also been efforts to eliminate the use of lead-based piezoelectric ceramics because of their toxicity. KNN-based ceramics have been researched severally in the last couple of years, and they have been reported to exhibit relatively high dielectric and piezoelectric properties [12,13]. Composites typically act as a bridge to lessen the effect of monolithic materials like ceramics and amino acids in fabricating devices like sensors and actuators for electromechanical applications. Ceramics and amino acids tend to modulate the response of the resulting composite. The type, arrangement, crystal structure, and stress/strain application are some of the factors that determine the magnitude of these interactions. In this research, L-LHCl has been mixed with KNNLST ceramics to form a wide range of dielectric composites. The research aims to investigate how the beneficial properties of both L-LHCl and KNNLST ceramics can be combined to properties suitable for producing dielectric devices.

2. Materials and Method

2.1. Ceramics preparation

To prepare the KNNLST ceramics, raw powders of the following ceramics were used as procured: Na_2CO_3, Li_2CO_3, K_2CO_3, (99+%), Nb_2O_5, Ta_2O_5 (99.9%) (Chempur Feinchemikalien und Forschungs GmbH, Karlsruhe, Germany), and Sb_2O_3 (99.9%) (Alfa Aesar GmbH Kandel, Germany). The correct quantities of the individual powders were measured. The powders were then milled using an attritor mill operating at 500 rpm for 2 h, where zirconia balls (3 mm diameter) and ethanol were the milling media. After milling, the ethanol was separated from the powder using a solvent extractor, while the powder was calcined using a tube furnace. The furnace parameters are 3 °C/min heating rate to 850 °C, for 4 h holding time and 10 °C/min cooling rate. The powder was milled again using the same parameters to ensure small particle sizes.

2.2. Composite preparation

The composite was produced by weighing the required quantity of L-LHCl and then dissolving it in 10 ml of deionised water. The following compositions of the composite in weight percentage were made: 0, 20, 40, 50, 60, 80, and 100. The L-LHCl was then placed in a magnetic stirrer, and the temperature was gradually increased until it stabilised at 70 °C and maintained for 90 min to allow for complete dissolution. The ceramic powders are then slowly introduced to the solution and continuously stirred at 70 °C for 90 min until a slurry is formed. Ethanol was added to the solution to enable re-precipitation of the ceramic powder, and a centrifuge was used to decant the solvent from the composite solution. The resulting cake was allowed to dry. The powder was pressed using a uniaxial press operating at 10 kN for 30 s and a cold isostatic press at 500 MPa for 2 min. The samples were heat-treated at 150 °C for 48 h. Bloating of the sample was observed on the L-lysine hydrochloride.

2.3. Composite characterisation

The bulk density values of the samples were determined geometrically by measuring the dimensions and the mass. A minimum of 5 samples for each composition was used to determine the density value. The scanning electron microscope images were acquired using field emission scanning electron microscopy (SEM, Zeiss Supra VP 55, Jena, Germany). The samples were coated with silver paints at the sides to reduce the incidence of sample charging during the measurement. Enough vacuum was generated inside the sample chamber before the measurements were initiated. The images were acquired using the Secondary electron detection mode.

The phases in the samples were determined with an X-ray diffractometer (Bruker D8 Discover, USA) operating with Cu$k\alpha$ anode (λ = 1.5406 Å) at a voltage of 40 kV and 40 mA. The measurement was made from 10° to 60° using Grazing Incidence diffraction mode (GID) with a source fixed angle of 5°, a scanning speed of 3 s with an increment of 0.01°. The samples for electrical characterisation were coated with silver paints on both sides and poled in silicon oil at room temperature with electric fields between 1 – 2 kV/mm for 5 min, depending on the composition. The dielectric characterisation was carried out to determine the dielectric constant, dielectric loss, and conductivity by attaching metallic wires to both sides of the Ag-coated sample. The measurement was done at room temperature with an LCR meter (HP 4284, USA). Polarisation hysteresis measurements were attempted with a Sawyer-Tower circuit, but the samples' charging was too high to obtain a suitable measurement.

3. Results and Discussion

3.1. Density

The bulk density values of the L-LHCl-KNNLST composite are shown in **▶Figure 1**. The density of L-LHCl is 1.2049±0.01 g/cm^3 and is 6% less than the density of 1.28 g/cm^3 [14]. As the content of ceramics increases, the density of the composite also increases gradually. The L-LHCl-KNNLST composites tend to be bloated through gas formation during fast heat treatment (especially L-LHCl 80-KNNLST-20), and so needed to be progressively heat-treated from 100 °C to 150 °C, and it affected the obtained density values. The density is enormously increased from 2.05±0.08 g/cm^3 for 60 wt.% to 3.415±0.077 g/cm^3 for 80 wt.%. This value represents 73 % of the density of the ceramics, which was calculated to be 4.67±0.07g/cm^3.

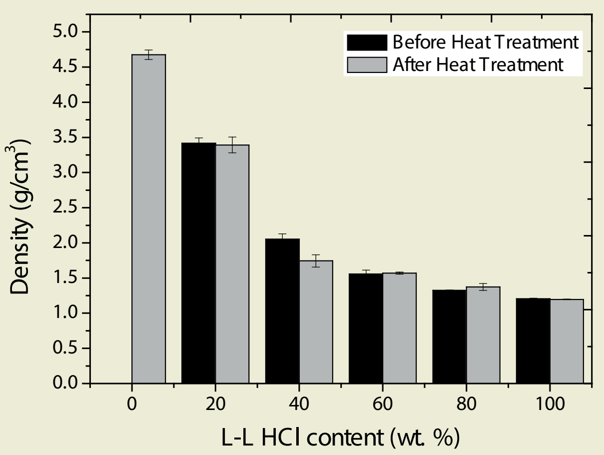

Figure 1. Bulk density values for L-lysine hydrochloride-KNNLST composite measured at room temperature.

3.2. Scanning Electron Microscopy

The scanning electron microscopy images for the L-lysine HCl-KNNLST composite are shown in **▶Figure 2**. For the pure L-LHCl, a film is observed on the surface of the micrograph. A few tiny graphs could also be observed but there are little of no grain boundaries observed, corresponding to the obtained X-ray diffraction pattern. Microcracks and a few rod-like grains can be observed on the sample's surface, which is dense, containing few pores, and relatively rough. It is believed that the heat-treatment process led to some form of polymerization. The SEM images of L-lysine HCl mixed with water and ethanol have been reported to create bubbles [5]. Using Atomic Force Microscopy, Lysine HCl has been reported to have aggregation properties [15]. The introduction of 20 wt.% of KNNLST led to the formation of a crystalline phase. A lot of sub-micron-sized grains could be observed with few amorphous phases. Some grains exhibit the quasi-cubic morphology associated with KNN-based ceramics with few rod-like grains. The sample is relatively dense with uniformly distributed crystallites but contains little porosity. When the ceramics content increased to 40 wt.%, many cracks were observed, possibly due to differences in the expansion/contraction coefficient between the ceramic and the amino acid. The sample is crystalline with grains of different sizes and shapes. Most grains are in the sub-micron size range, and rod-like grains could be observed this time. There is good homogeneity in the distribution of the grains with densely packed grains and few porosities. Increasing the content of the ceramic to 60 wt.% increases the crystallinity of the sample with bi-modal grain size distribution. Some grains are in the sub-micron size range, while others are above 5 μm. The large grains appear to be somehow porous, with some signs of dissociation to form tiny grains. Cracks could also be observed on the surface. When the KNNLST content is 80 wt.%, the microstructure in the composite is remarkably different, showing clear crystallinity. The grains are plate-like with thickness in the nanometer size range, while the diameter of the grains is above 2 μm. There is homogeneity in the distribution of the grains in the composite. The composite is also relatively dense, with little porosity in the microstructure. A new microstructure different from those of L-LHCl and KNNLST was formed.

3.3. X-ray Diffraction

The X-ray diffraction patterns for the L-lysine HCl-KNNLST composite are shown in **▶Figure 3**. The diffraction pattern for L-LHCl shows an amorphous structure with many broad, interconnected peaks. Lysine as an amino acid is crystalline [9,16], but the introduction of HCl led to the structure becoming almost amorphous. The broad peaks are observed throughout the whole range of the measurement, from 20° to 60°. The introduction of KNNLST ceramics led to a crystalline diffraction pattern. Sharp diffraction peaks with high intensities could be observed at 23°, 27° and 50°, respectively. Increasing the KNNLST content to 50 wt.% resulted in the coexistence of the KNNLST and L-LHCl patterns. When the quantity of KNNLST ceramics increased to 80 wt.%, the diffraction pattern was contributed mainly by the KNNLST ceramics. When only the KNNLST ceramics were present, the two-phase orthorhombic-tetragonal pattern associated with modified KNN ceramics was observed.

3.4. Dielectric properties

The dielectric properties graph for the L-LHCl-KNN-LST composite is shown in ▶**Figure 4**. As the content of KNNLST ceramics increases, the dielectric constant values also increase, possibly due to high polarization in the ceramics. As the frequency of measurement increases, the dielectric constant values are found to decrease. This is because, at lower frequencies, all the polarization mechanisms are present. Still, as the frequency increases, the natural frequency of bound charge is no longer equal to the frequency of the electric field. The irregularities usually observed at low frequencies are primarily due to electrode polarization [17]. L-LHCl has a dielectric constant value of 12 at 20 Hz, gradually decreasing to 7 at 1 MHz [5], introducing 20 wt.% KNNLST ceramics led to a slight decrease in the dielectric constant value from 14 at 20 Hz to 7 at 1 MHz. The dielectric constant values for 40 and 50 wt.% of KNNLST ceramics did not change significantly as the same trend was followed. A significant differ-

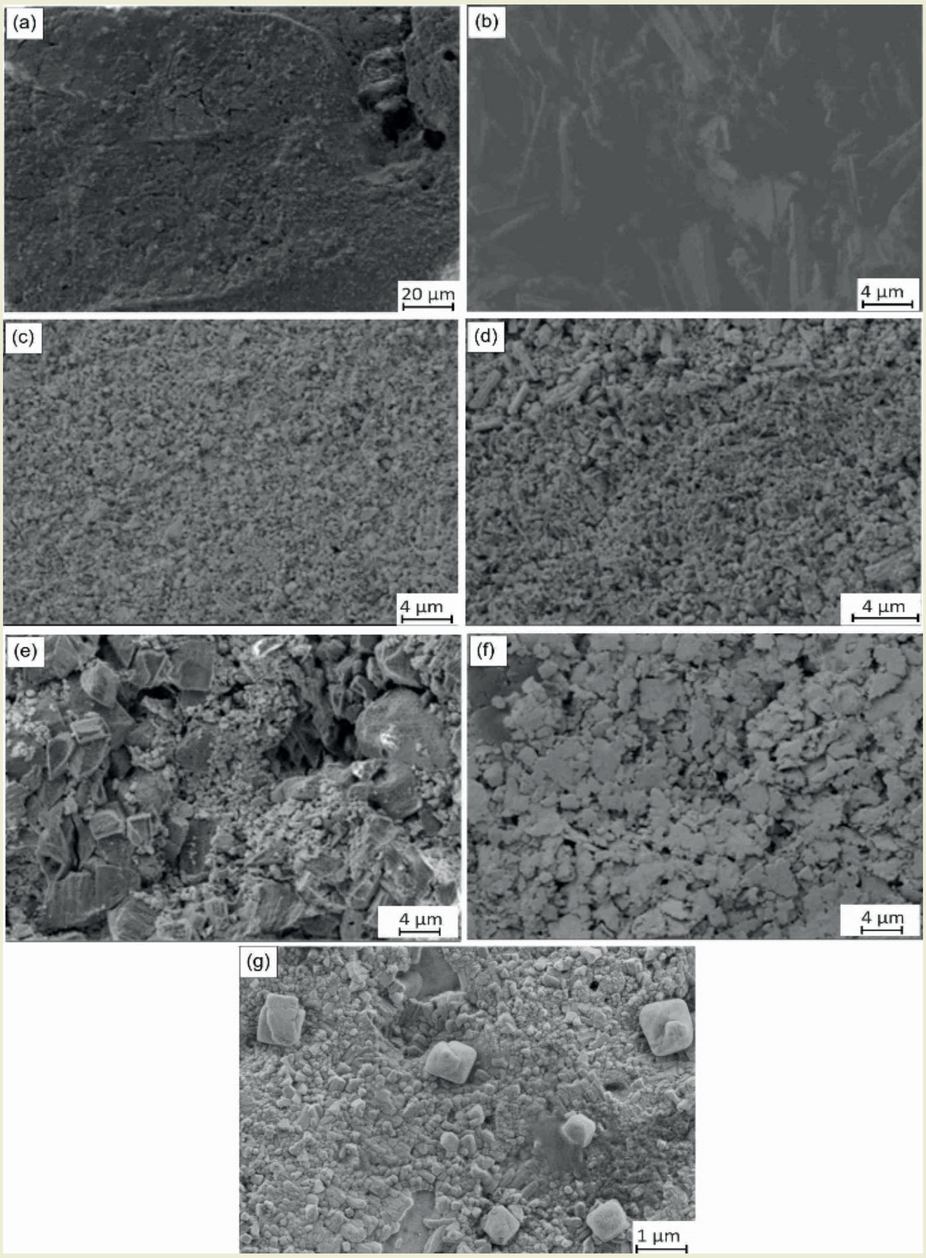

Figure 2. Scanning Electron Microscopy images for (a) L-LHCl (b) L-LHCl with water solution (c) L-LHCl 80-KNNLST 20 (d) L-LHCl 60-KNNLST 40 (e) L-LHCl 40-KNNLST 60 (f) L-LHCl 20-KNNLST 80 and (g) KNNLST ceramics.

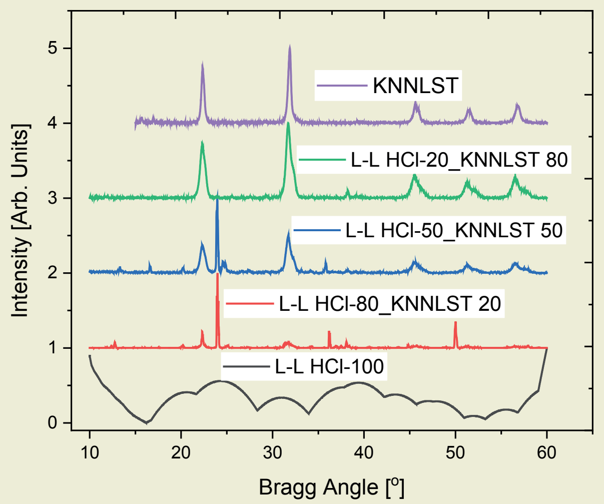

Figure 3. X-ray diffraction patterns for L-lysine HCl-KNNLST composite. The measurements were carried out at room temperature.

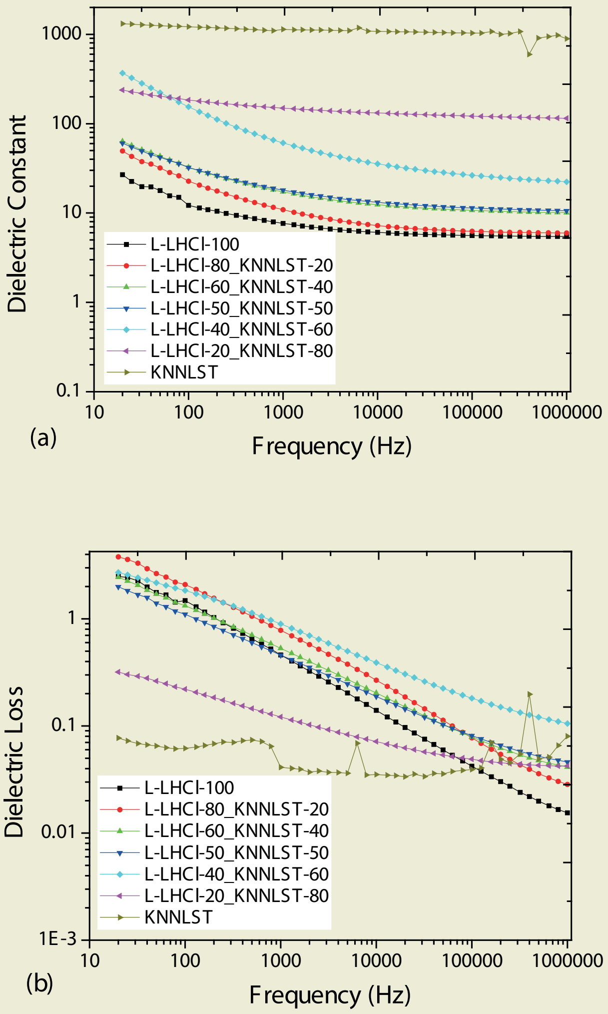

Figure 4. Log-log plots of (a) the dielectric constant and (b) the dielectric loss values for L-LHCl-KNNLST composites. The measurements were measured at room temperature.

ence was observed for 60 wt.% of KNNLST ceramics, where the dielectric constant at 20 Hz was 380 at 20 Hz and gradually reduced to 49 at 1 MHz. The composite containing 80 wt.% of KNNLST ceramics has the most stable dielectric constant value over the entire frequency range measured with a value of ~150. The dielectric constant value for the KNNLST ceramics is also stable, with a value of 1240 at 20 Hz, which gradually reduced to 934 at 1 MHz.

The dielectric loss values for the L-LHCl-KNNLST composite are shown in ▶**Figure 4b**. The dielectric loss values decreased with increasing frequency because, at low frequencies, dipole oscillation is present. Still, all the polarization mechanisms are absent at high frequencies, reducing the energy for dipole oscillation. The L-LHCl has a relatively high dielectric constant value of 3 at 20 Hz, steadily decreasing to 0.3 at 1 MHz. The dielectric loss values for the composite with ceramics content between 20 and 60 wt.% are similar to that of the amino acid—the composite containing 80 wt.% of KNNLST ceramic is more stable as the loss values varied between 0.3 and 0.08 from 20 Hz to 1 MHz. The dielectric loss value for KNNLST ceramics is stable over the frequency range measured between 0.05 and 0.1. The instability in the dielectric loss values is believed to result from resonance in the sample during the measurement.

3.5. AC Conductivity

The log-log plot of conductivity as a function of the measurement frequency is shown in ▶**Figure 5**. As the frequency for all the composites increased, the conductivity value increased. L-LHCl has the lowest conductivity value of all the samples measured. Its conductivity value at 20 Hz is 8 $*10^{-8}$ S/m and grows to 5 $*$ 10^{-6} S/m at 1 MHz. As the content of the KNNLST ceramics

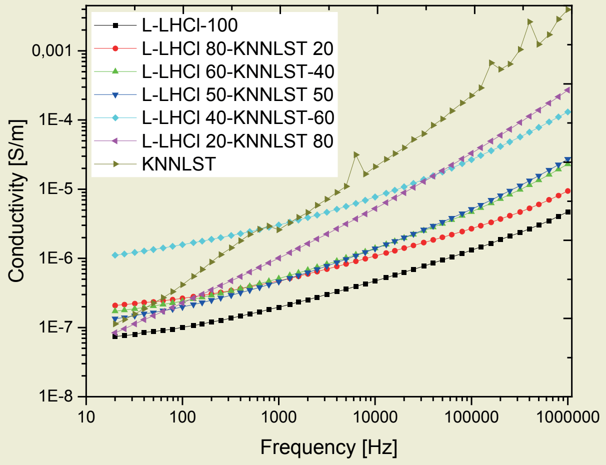

Figure 5. A log-log graph of conductivity as a function of frequency for L-LHCl-KNNLST composite.

in the composite increases, the conductivity values also increase. The conductivity value for KNNLST ceramics shows that at 20 Hz, the conductivity value is similar to that of other samples. Still, as the frequency rises to more than 1 kHz, the conductivity value increases more than any other sample. This is because there are more structural imperfections in ceramics, leading to the creation of more pathways for electrons to move.

4. Conclusion

The study examined the creation of a composite for dielectric devices by mixing L-Lysine HCl with KNNLST ceramics. The morphology of the L-LHCl was affected by the introduction of water as a solvent. The addition of ceramics resulted in the formation of new nanosized grains, and at high ceramics content, flake-like grains were obtained. The phases in the composites changed from amorphous for L-lysine HCl to two-phase tetragonal-orthorhombic for KNNLST ceramics. Increasing ceramics content increases the composite's dielectric constant value. The dielectric properties follow the same trend, decreasing with increasing frequency, while conductivity values increase with increasing frequency.

Acknowledgment

The research leading to this manuscript was carried out while the first author was a visiting researcher at the Institute of Advanced Ceramics, Hamburg, Germany. The authors are grateful to Prof. G. A. Schneider for the opportunity to carry out the work.

Research Ethics

Ethical approval is not required.

Author contributions

Henry Ekene Mgbemere: Conceptualization, Formal analysis, Investigation, Writing original draft. **Viktoriya Semeykina:** Conceptualisation, Experiment and Formal analysis. **Chiedozie Valentine Oluigbo:** Formal analysis, Writing final draft, Review and Editing.

Conflicts of interest

The authors declare no conflicts of interest.

Research Funding

Not reported.

Data Availability

Not applicable.

References

[1] Gerbitz, V.-D. (1980). Gerbitz: Pankreatische B-Zellen-Peptide Pankreatische B-Zellen-Peptide: Kinetik und Konzentration von Proinsulin, Insulin und C-Peptid in Plasma und Urin, Probleme der Meßmethoden, klinische Aussage und Literaturübersicht. *Journal of Clinical Chemistry and Clinical Biochemistry, 18*, 313-320.

[2] Shmueli, U., & Traub, W. (1965). An X-ray diffraction study of poly-L-lysine hydrochloride. *Journal of Molecular Biology, 12*(1), 205–214. https://doi.org/10.1016/S0022-2836(65)80294-7

[3] Williams, P. A., Hughes, C. E., & Harris, K. D. M. (2015). L-lysine: Exploiting powder x-ray diffraction to complete the set of crystal structures of the 20 directly encoded proteinogenic amino acids. *Angewandte Chemie International Edition, 54*(13), 3973–3977. https://doi.org/10.1002/anie.201411520

[4] Ramesh Babu, R., Vijayan, N., Gopalakrishnan, R., & Ramasamy, P. (2006). Growth and characterization of L-lysine monohydrochloride dihydrate (L-LMHCl) single crystal. *Crystal Research and Technology, 41*(4), 405–410. https://doi.org/10.1002/crat.200510594

[5] Ramesh Babu, R., Sethuraman, K., Vijayan, N., Bhagavannarayana, G., Gopalakrishnan, R., & Ramasamy, P. (2006). Etching and dielectric studies on L-lysine monohydrochloride dihydrate single crystal. *Crystal Research and Technology, 41*(9), 906–910. https://doi.org/10.1002/crat.200510693

[6] Goloshchapov, D., Kashkarov, V., Nikitkov, K., & Seredin, P. (2021). Investigation of the effect of nanocrystalline calcium carbonate-substituted hydroxyapatite and L-lysine and L-arginine surface interactions on the molecular properties of dental biomimetic composites. *Biomimetics, 6*(4). https://doi.org/10.3390/biomimetics6040070

[7] Goloshchapov, D., Kashkarov, V., Nikitkov, K., Bartenev, V., Ippolitov, I., Ippolitov, Y., & Seredin, P. (2020). Study of the impact of amino acids hydrochloride forms on the formation of biomimetic composites in the presence of nanocrystalline hydroxyapatite. *Journal of Physics: Conference Series, 1697*(1). https://doi.org/10.1088/1742-6596/1697/1/012040

[8] Kanagathara, N., & Anbalagan, G. (2012). Growth, optical and dielectric studies on pure and L-lysine doped KDP crystals. *International Journal of Optics, 2012*. https://doi.org/10.1155/2012/826763

[9] Mirtič, A., & Grdadolnik, J. (2013). The structure of poly-l-lysine in different solvents. *Biophysical Chemistry, 175–176*, 47–53. https://doi.org/10.1016/J.BPC.2013.02.004

[10] Guerin, S., Stapleton, A., Chovan, D., Mouras, R., Gleeson, M., McKeown, C., Noor, M. R., Silien, C., Rhen, F. M. F., Kholkin, A. L., Liu, N., Soulimane, T., Tofail, S. A. M., & Thompson, D. (2018). Control of piezoelectricity in amino acids by supramolecular packing. *Nature Materials, 17*(2), 180–186. https://doi.org/10.1038/NMAT5045

[11] Guerin, S., Tofail, S. A. M., & Thompson, D. (2019). Organic piezoelectric materials: milestones and potential. *NPG Asia Materials, 11*(1). https://doi.org/10.1038/s41427-019-0110-5

[12] Mgbemere, H. E., Hinterstein, M., & Schneider, G. A. (2011). Electrical and structural characterization of (K x Na 1-x)NbO 3 ceramics modified with Li and Ta. *Journal of Applied Crystallography, 44*(5), 1080–1089. https://doi.org/10.1107/S0021889811027701

[13] Saito, Y., Takao, H., Tani, T., Nonoyama, T., Takatori, K., Homma, T., Nagaya, T., & Nakamura, M. (2004). Lead-free piezoceramics. *Nature, 432*, 84–87. https://doi.org/10.1038/nature03028

[14] ChemicalBook. (n.d.). Retrieved March 16, 2024, from https://www.chemicalbook.com/

[15] Koshti, B., Kshtriya, V., Singh, R., Walia, S., Bhatia, D., Joshi, K. B., & Gour, N. (2021). Unusual aggregates formed by the self-assembly of proline, hydroxyproline, and lysine. *ACS Chemical Neuroscience, 12*(17), 3237–3249. https://doi.org/10.1021/acschemneuro.1c00427

[16] Padden Jr., F. J., Keith, H. D., & Giannoni, G. (1969). Single crystals of poly-L-lysine. *Journal of Polymer Science, Part A-2: Polymer Physics, 7*(10), 1675–1682.

[17] Durmus, Z., Kavas, H., Toprak, M. S., Baykal, A., Altinçekiç, T. G., Aslan, A., Bozkurt, A., & Coşgun, S. (2009). L-lysine coated iron oxide nanoparticles: Synthesis, structural and conductivity characterization. *Journal of Alloys and Compounds, 484*(1–2), 371–376. https://doi.org/10.1016/j.jallcom.2009.04.103

EUROPEAN MECHANICAL SCIENCE

Research Article

e-ISSN: 2587-1110

Mutual examination of corrosion and wear resistance of sandblasting and etching surface treatments applied to AISI 316L stainless steel

Muhammet Taha Acar[1]

Erzincan Binali Yıldırım University, Faculty of Engineering, Department of Mechanical Engineering, Erzincan, Türkiye

Orcid: M. T. Acar (0000-0002-8367-9623)

Abstract: Since AISI 316L stainless steel has excellent mechanical qualities and resistance to corrosion, it is widely used in many different industries. Surface treatments like etching and sandblasting are frequently used to improve the surface properties for certain uses. It is still difficult to comprehend how these treatments affect the material's resistance to corrosion and wear, though. In this work, we methodically examine how sandblasting and etching affect AISI 316L stainless steel's resistance to corrosion and wear. We assess the morphological, chemical, and performance changes brought about by these treatments using X-ray diffraction, scanning electron microscopy, microhardness testing, and tribological analysis. Our findings show that the surface morphology and chemistry are dramatically changed by both treatments, which has an impact on the corrosion and wear behavior of the material. The best wear resistance was obtained from the sandblasted sample (0.64×10^{-3} mm^3/Nm) and the best corrosion resistance was obtained from the untreated sample. The optimization of surface treatment techniques for stainless steel alloys in many industrial applications is facilitated by these findings.

Keywords: 316L, Etching, Blasting, Wettability, Wear, Corrosion.

1. Introduction

Many industrial applications, such as aerospace components and biomedical implants, use AISI 316L stainless steel as a foundation material [1]. Its exceptional mechanical properties and corrosion resistance are well known. Because of its remarkable corrosion resistance and biocompatibility, AISI 316L stainless steel is a highly favored alloy among its numerous grades [2].

The surface integrity of AISI 316L stainless steel is critical to the effectiveness of material in critical applications since the material's performance can be hampered by exposure to corrosive chemicals and mechanical stresses [3]. Numerous surface treatment methods have been created to enhance surface characteristics; these methods are intended to support specific attributes like corrosion resistance, wear resistance, or visual attractiveness [4].

Sandblasting and etching surface treatments have attracted the greatest attention among these methods and have the potential to enhance surface characteristics since they can alter the chemistry and topography of the surface [5]. While sandblasting creates a rough texture by abrading the surface with high-speed abrasive particles, etching, which involves the chemical disintegration of surface layers, alters the surface morphology and composition [6].

It is difficult to fully understand how etching and shot blasting affect the corrosion and wear resistance of AISI

---

*Corresponding author:
Email: taha.acar@erzincan.edu.tr

Cite this article as:
Acar, M.T. (2024). Mutual examination of corrosion and wear resistance of sandblasting and etching surface treatments applied to AISI 316L stainless steel. *European Mechanical Science, 8*(3): 160-166. https://doi.org/10.26701/ems.1470604

History dates:
Received: 18.04.2024, ***Revision Request***: 04.06.2024, ***Last Revision Received***: 07.06.2024, ***Accepted***: 12.07.2024

316L stainless steel, despite their widespread use[7]. It is critical to close this information gap in order to enhance surface treatment protocols and material selection in a range of industrial applications [8].

When the literature was examined, it was seen that acid etching and sandblasting processes had previously been applied to the 316L material and that wear, corrosion and surface wettability had not been mutually examined. It is thought that this gap in the literature will be filled with this study.

This study methodically looked at the corrosion and wear resistance provided by surface treatments such as sandblasting and etching applied to AISI 316L stainless steel. The purpose of this work is to clarify the intricate relationships between surface morphology, chemistry, and performance properties by combining sandblasting and etching surface treatments, thereby offering crucial information on the design and optimization of surface treatment protocols for stainless steel alloys. Each sample was evaluated using scanning electron microscopy (SEM), X-ray diffraction (XRD), and microhardness testing. The electrochemical and wear properties of the samples were then examined using pin-on-disk tribotester and electrochemical impedance spectroscopy (EIS), respectively.

2. Experimental details

Austenitic stainless-steel samples (AISI 316L) with a diameter of 10 mm and a thickness of 3 mm were used for this research. Alumina powder was used to polish AISI 316L samples after they had been ground using SiC sandpapers (80-1000 mesh). It was then cleaned with ethanol and dried.

Subsequently, the AISI 316L samples underwent surface treatments, including etching and sandblasting, as depicted in ▶**Figure 1**. The sample AISI 316L that was etched was created according to a different study, which involved etching it in diluted hydrofluoric acid and then controlling its oxidation in hydrogen peroxide [9]. As stated in a different work, 700 µm Al_2O_3 was used to prepare the blasted AISI 316L sample[10].

The phase of 316L samples was determined on a 2θ scale spanning 20° to 100° using an XRD-GNR-Explorer X-Ray diffraction apparatus in conjunction with a Cu-K (= 1.54059) source operating at 40 kV and 30 mA. All phases were distinguished by comparing them to the International Diffraction Data Center (ICDD) standard cards. The top was photographed using the FEI QUANTA 250 Scanning Electron Microscope. The contact angles of the samples were determined by means of a contact angle measurement system (Attension Theta Lite C204A, Biolin Scientific, Sweden). 5 mL volumes of distilled water drops were used for contact angle measurements. Five different measurements were made for each sample and average values were used. Experiments were carried out at room temperature. Distilled water was dropped onto the sample surface from a height of 3 cm. All contact angle measurements were performed under the same conditions [11]. Using a Buehler Micromet device, Vickers microhardness measurements were carried out by loading for 10 s at a force of 10 g and averaging data from 5 distinct locations as applied in the previous study [12].

To find out the tribological characteristics of 316L that has been pack sandblasted, etched, and untreated, Turkyus PODT and RWT reciprocating tribotester were utilized. As per the ASTM G133-02 standard, the wear tests were conducted using a 6 mm diameter Al_2O_3 (alumina) ball and 316L under friction circumstances in dry sliding settings, at a room temperature of approximately 22 °C and a relative humidity of roughly 50% [13]. The wear test settings were set to 1 N of load, 8 mm/s of wear track length, and 141 m of sliding distance as for ASTM G133-02.

316L samples that had been sandblasted, etched, and untreated were subjected to electrochemical corrosion testing. The samples underwent two repetitions of the potentiodynamic polarization and open circuit potential (OCP) tests for each parameter assessed with the Gamry Reference 3000 potentiostat/galvanostat/ZRA [14].

3. Results and discussion

▶**Figure 2** shows the X-ray diffraction (XRD) patterns of substrate 316L. It can be seen that the substrate left

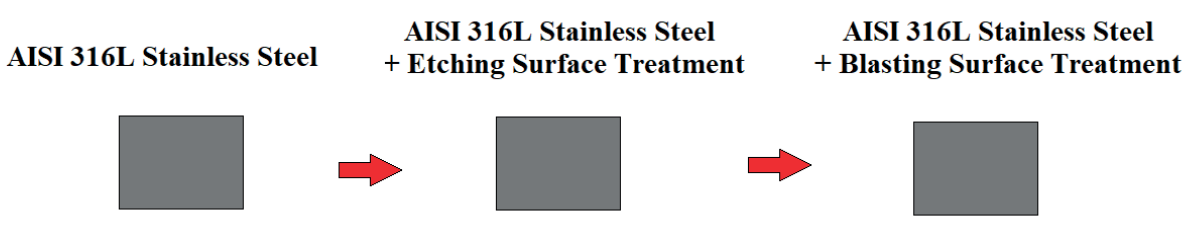

Figure 1. Schematic representation of surface treatments applied to AISI 316L samples

https://doi.org/10.26701/ems.1470604

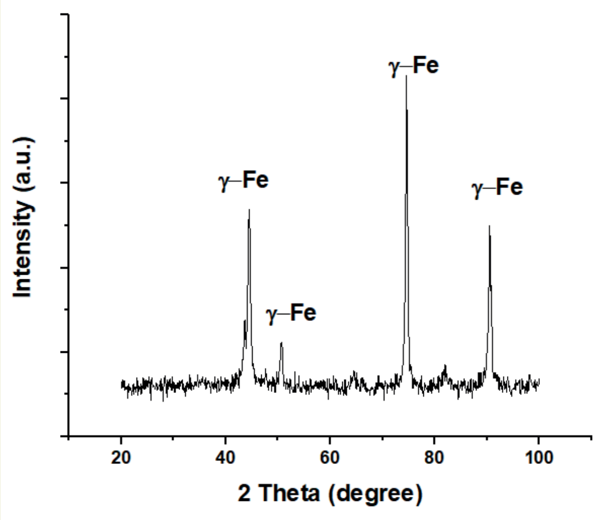

Figure 2. XRD patterns of substrate 316L

untreated consists entirely of austenite structure [15].

▶**Figure 3** shows SEM pictures of etched, sandblasted, and untreated 316L surfaces. As anticipated, the untreated surface merely shows the scratches that were created on it following the application of polishing. Surface roughness increased following the etching procedure in comparison to the untreated surface [16]. It is evident that the 316L surface is severely damaged by the sand grains sprayed on it, resulting in a rougher structure than the untreated surface [17]. Thus, following the application of both surface treatments, it is evident from the SEM pictures that the surface morphology has changed.

▶**Figure 4** presents contact angle measurements of 316L surfaces that have been etched, sandblasted, and left untreated. It is well known that a hydrophilic or hy-

Table 1. Results of tests performed on all samples for wettability, hardness, corrosion, and wear.

	E_{corr} (mV)	i_{corr} (x10^{-6}A/cm^2)	Contact Angle (°)	Hardness (HV$_{0.1}$)	Wear rate (x10^{-3} mm^3/Nm)
Blasted	-150	15.45	65	470-500	0.64
Etched	-140	15.40	30	290-310	0.86
Untreated	-160	15.50	53	280-300	0.84

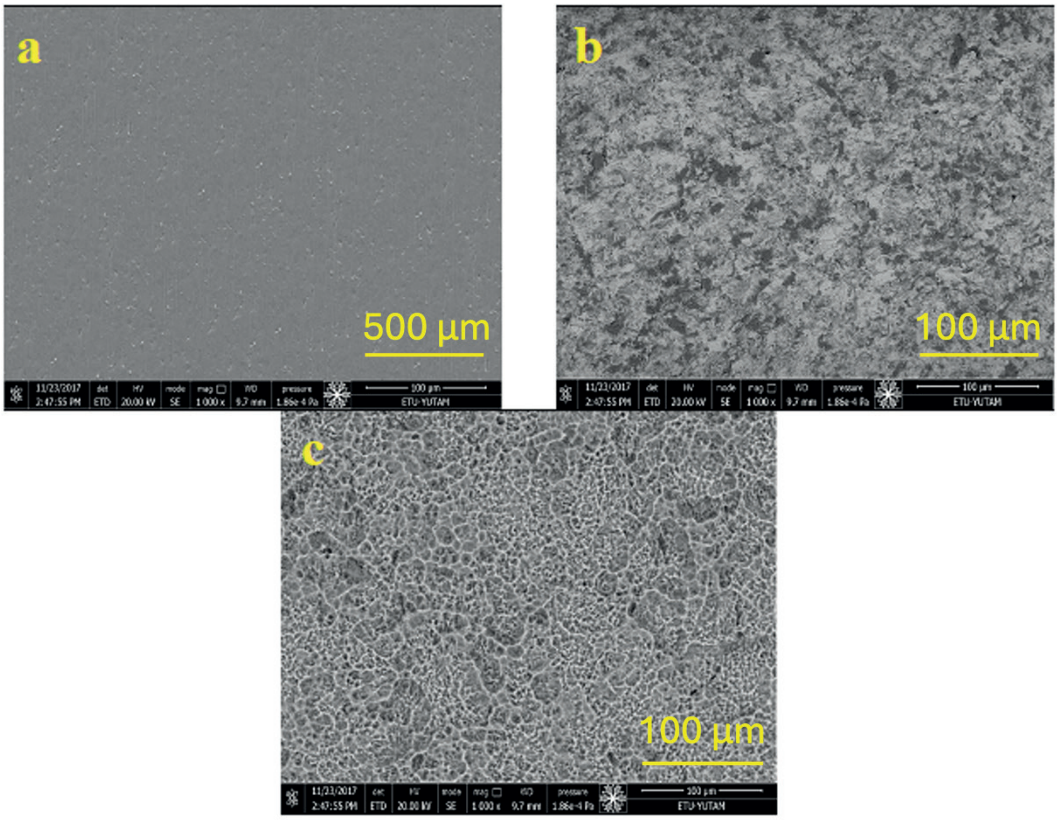

Figure 3. SEM images of (a) substrate, (b) etched, and (c) blasted 316L samples.

drophobic characteristics of surface can be determined by the contact angle values that are derived from the surface [18]. It is known that contact angles less than 90° are hydrophilic, while those greater than 90° are hydrophobic [19]. Hydrophilicity was observed on the untreated surface, with a contact angle of roughly 53°. At a contact angle of 30°, the etched surface exhibited more hydrophilicity than the untreated surface. According to published research, the increase in hydroxyl groups on the surface of etched samples is primarily responsible for their enhanced wettability when compared to untreated samples [20]. At a contact angle of 65°, a hydrophobic surface was achieved on the blasted surface. Prior research in the literature has indicated that the contact angle increases in tandem with surface roughness [21].

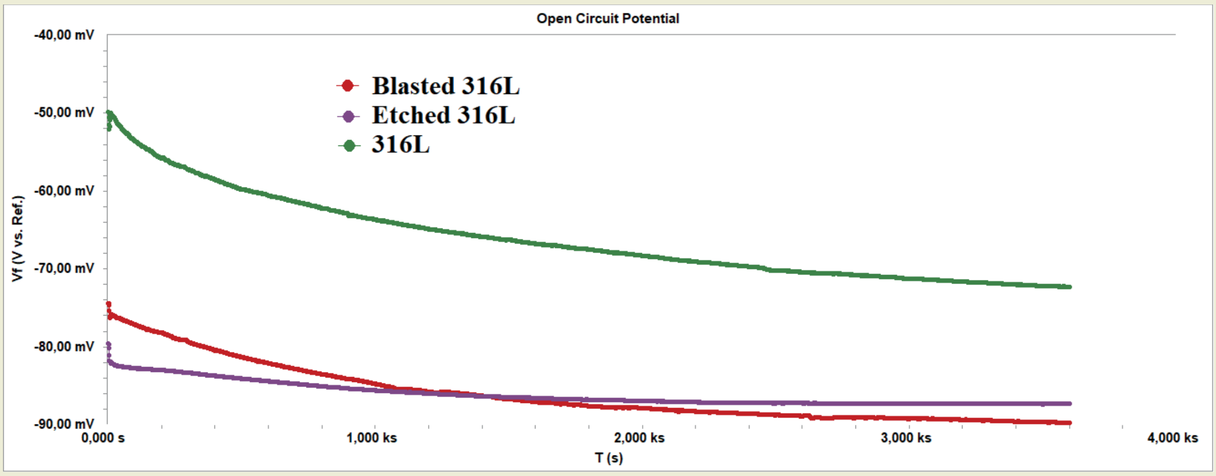

Figure 5. OCP of untreated, etched, and blasted 316L samples.

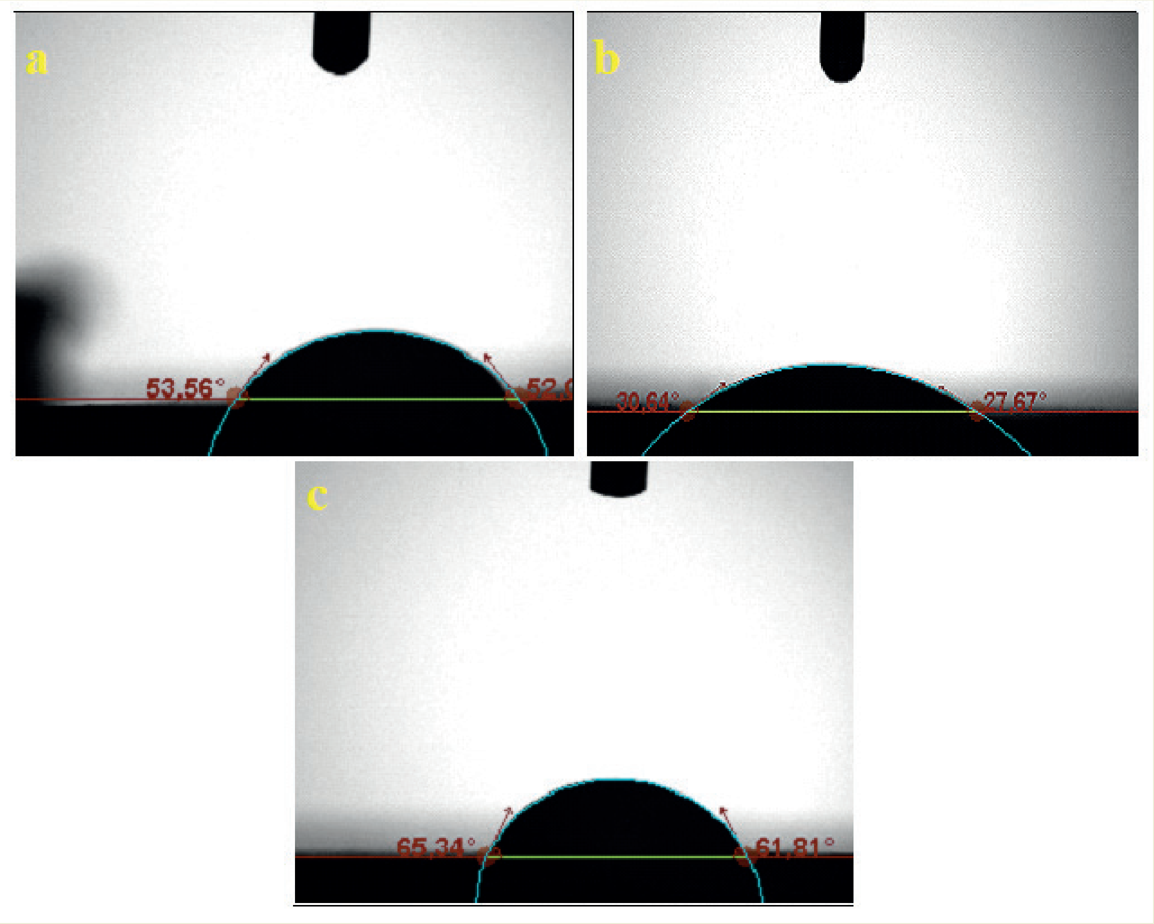

Figure 4. Contact angles of (a) substrate, (b) etched, and (c) blasted 316L samples.

The open circuit potential (OCP) data of 316L samples that were etched, blasted, and untreated are displayed in **▶Figure 5**. Untreated, etched, and blasted samples show comparable OCP curves this trend is common for passive metals [22]. The trend of 316L sample suggests that corrosion cannot happen until voltage is provided [23]. In contrast to the untreated sample, it is evident that the OCP values of the blasted and etched samples moved negatively. This suggests that following the application of surface treatments, the corrosion resistance of surface has decreased.

▶Figure 6 displays the potentiodynamic polarization data that were acquired from electrochemical tests conducted on untreated, etched, and blasted samples in SBF solution. **▶Table 1** presents the data on corrosion potential (Ecorr) and corrosion current density (Icorr) derived from the polarization curves. The corrosion current density (Icorr = 15.5 × 10^{-6}A/cm^2) and corrosion potential (Ecorr = − 160 mV) are highest and lowest, respectively, in the untreated sample. In contrast, the etched sample exhibits the lowest corrosion Icorr (15.4×10^{-6}A/cm^2) and the highest positive Ecorr (− 140 mV) when compared to the etched and blasted sample. Higher Ecorr and lower Icorr values indicate better corrosion resistance [24]. Every potentiodynamic curve

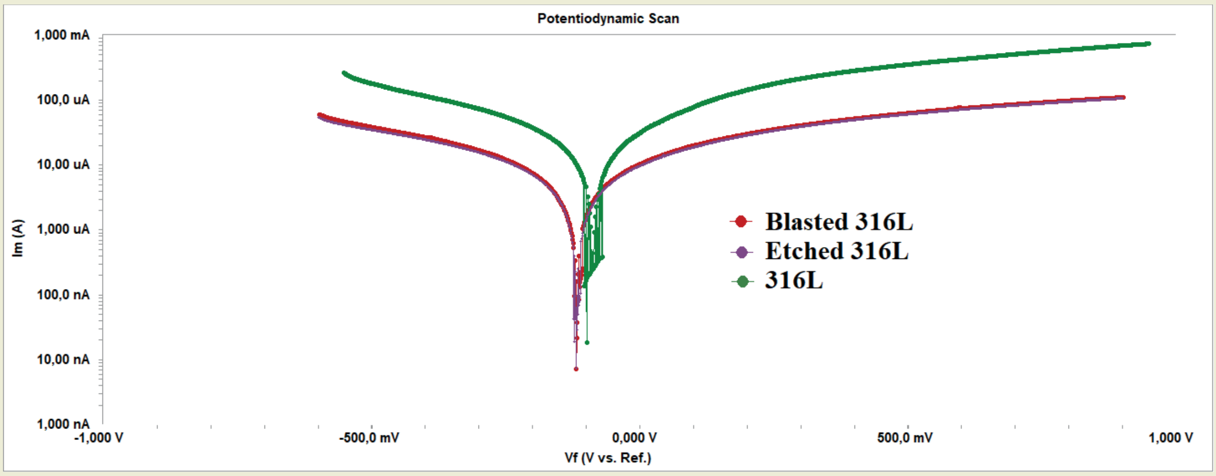

Figure 6. Potentiodynamic polarization curves of untreated, etched, and blasted 316L samples.

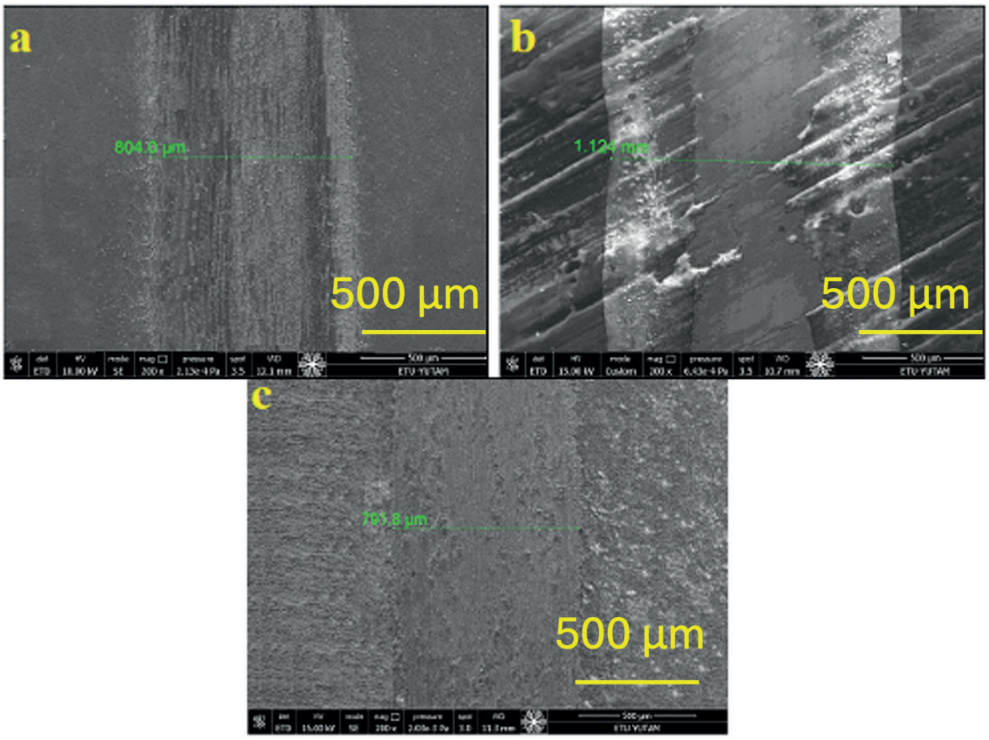

Figure 7. SEM wear trace images of (a) substrate, (b) etched, and (c) blasted 316L samples.

of samples has a 316L-typical form. The etched sample and the blasted sample both stabilize at the lowest potential. As can be observed from the OCP values, the stabilization of the etched and blasted sample at a lower potential than the untreated sample suggests that the 316L surface is damaged as a result of the applied surface treatments [25].

It was clear from looking at ▶**Figure 7** and the wear rate statistics in ▶**Table 1** that the etched sample with the lowest wear resistance was the one with a wear rate of 0.86×10^{-3} mm^3/Nm. After the etched sample, untreated and blasted samples were placed in that order. The blast sample with the highest wear resistance value was the one with the shortest wear trace and lowest wear rate (0.64×10^{-3} mm^3/Nm). It is commonly recognized that an ability of materials to withstand wear is significantly influenced by its surface hardness [26]. Archard's law states that a higher surface hardness actively increases wear resistance by reducing the contact between the coating system and the wear ball [27].

4. Conclusion

Our comprehensive research investigated the effects of sandblasting and etching surface treatments on the corrosion and wear resistance of AISI 316L stainless steel, revealing significant changes in surface properties following these treatments, which notably affected the material's performance in industrial environments. Both sandblasting and etching altered the surface morphology and chemistry, leading to changes in corrosion behavior. Despite the observed increase in surface roughness and hydrophilicity after etching, the corrosion resistance of the material decreased, as evidenced by negative shifts in the open circuit potential. Similarly, while sandblasting provided a rougher surface and higher hydrophobicity, it also compromised the corrosion resistance of the material. Moreover, our tribological investigation revealed significant differences in wear resistance between untreated samples. The etched surface exhibited the lowest wear resistance despite its increased roughness, while the sandblasted surface showed the highest wear resistance, supported by a lower wear rate and smaller wear scar, consistent with Archard's law, which emphasizes the critical role of surface hardness in determining wear resistance. These findings are of practical importance, providing valuable information for optimizing surface treatment protocols in the selection and application of 316L in various industrial contexts.

Research Ethics

Ethical approval not required.

Author Contributions

The author(s) accept full responsibility for the content of this article and have approved its submission.

Competing Interests

The author(s) declare that there are no competing interests.

Research Funding

Not reported.

Data Availability

Not applicable.

Peer-review

Externally peer-reviewed.

References

[1] A.S.M. International, & Narayan, R. J. (2012). *Materials for medical devices*. ASM International. https://dl.asminternational.org/handbooks/edited-volume/56/chapter/667361/Medical-Implant-Materials

[2] Ali, S., Abdul Rani, A. M., Altaf, K., Hussain, P., Prakash, C., Hastuty, S., Rao, T. V. V. L. N., Aliyu, A. A., & Subramaniam, K. (2019). Investigation of alloy composition and sintering parameters on the corrosion resistance and microhardness of 316L stainless steel alloy. In B. Gapiński, M. Szostak, & V. Ivanov (Eds.), *Advances in Manufacturing II* (pp. 532–541). Springer International Publishing. https://doi.org/10.1007/978-3-030-16943-5_45

[3] Ren, Z., & Ernst, F. (2020). Stress–corrosion cracking of AISI 316L stainless steel in seawater environments: Effect of surface machining. *Metals, 10*(1324). https://doi.org/10.3390/met10101324

[4] Acar, M. T. (2023). Investigation of the effects of Sr and Mn doping on corrosion tribocorrosion and cyclic voltammetry performances of TiO2 nanotubes. *European Mechanical Science, 7*, 138–145. https://doi.org/10.26701/ems.1265161

[5] Acar, M. T. (2023). Investigation of surface wettability, corrosion and tribocorrosion behavior of machined, etched, blasted and anodized Cp-Ti samples. *MRS Communications, 13*, 587–593. https://doi.org/10.1557/s43579-023-00387-6

[6] Liu, J., Xue, Y., Dong, X., Fan, Y., Hao, H., & Wang, X. (2023). Review of the surface treatment process for the adhesive matrix of composite materials. *International Journal of Adhesion and Adhesives, 126*, 103446. https://doi.org/10.1016/j.ijadhadh.2023.103446

[7] Menezes, M. R., Godoy, C., Buono, V. T. L., Schvartzman, M. M., & Wilson, J. A.-B. (2017). Effect of shot peening and treatment temperature on wear and corrosion resistance of sequentially plasma treated AISI 316L steel. *Surface and Coatings Technology, 309*, 651–662. https://doi.org/10.1016/j.surfcoat.2016.10.066

[8] Vafadar, A., Guzzomi, F., Rassau, A., & Hayward, K. (2021). Advances in metal additive manufacturing: A review of common processes, industrial applications, and current challenges. *Applied Sciences, 11*(1213). https://doi.org/10.3390/app11031213

[9] Ferraris, S., Vitale, A., Bertone, E., Guastella, S., Cassinelli, C., Pan, J., & Spriano, S. (2016). Multifunctional commercially pure titanium

for the improvement of bone integration: Multiscale topography, wettability, corrosion resistance and biological functionalization. *Materials Science and Engineering: C, 60*, 384–393. https://doi.org/10.1016/j.msec.2015.11.040

[10] Rakngarm, A., & Mutoh, Y. (2009). Characterization and fatigue damage of plasma sprayed HAp top coat with Ti and HAp/Ti bond coat layers on commercially pure titanium substrate. *Journal of the Mechanical Behavior of Biomedical Materials, 2*, 444–453. https://doi.org/10.1016/j.jmbbm.2008.12.007

[11] Akpinar, I. A. (2024). The effect of chemical etching and nanostructure additive epoxy coating technique on adhesion strength in aluminum joints bonded with nanostructure additive adhesive. *International Journal of Adhesion and Adhesives, 129*, 103584. https://doi.org/10.1016/j.ijadhadh.2023.103584

[12] Acar, M. T., Kovacı, H., & Çelik, A. (2021). Enhancement of the tribological performance and surface wettability of Ti6Al4V biomedical alloy with boric/sulfuric acid anodic film. *Surface Topography: Metrology and Properties, 9*(035024). https://doi.org/10.1088/2051-672x/ac011e

[13] Acar, M. T. (2024). Analyzing the corrosion and tribocorrosion performances of monolayer TiO2 and bilayer TiO2-SiO2 coatings at different SBF temperatures. *Physica Scripta, 99*(025910). https://doi.org/10.1088/1402-4896/aa5677

[14] Acar, M. T., Çomaklı, O., Yazıcı, M., Arslan, M. E., Yetim, A. F., & Çelik, A. (2024). The effect of doping different amounts of boron on the corrosion resistance and biocompatibility of TiO2 nanotubes synthesized on SLM Ti6Al4V samples. *Surfaces and Interfaces*, 104472. https://doi.org/10.1016/j.surfin.2023.104472

[15] Çakır, M. A., & Köseoğlu, B. (2023). Investigation of the structural, tribological, and electrochemical properties of nitrided and boronized AISI 316L stainless steel. *Transactions of the Indian Institute of Metals, 76*, 1517–1533. https://doi.org/10.1007/s12666-023-02624-w

[16] Strasser, T., Preis, V., Behr, M., & Rosentritt, M. (2018). Roughness, surface energy, and superficial damages of CAD/CAM materials after surface treatment. *Clinical Oral Investigations, 22*, 2787–2797. https://doi.org/10.1007/s00784-018-2364-2

[17] Sun, J., Wang, W., Liu, Z., Li, B., Xing, K., & Yang, Z. (2020). Study on selective laser melting 316L stainless steel parts with superhydrophobic surface. *Applied Surface Science, 533*, 147445. https://doi.org/10.1016/j.apsusc.2020.147445

[18] Hebbar, R. S., Isloor, A. M., & Ismail, A. F. (2017). Contact angle measurements. In *Membrane Characterization* 219–255. Elsevier. https://doi.org/10.1016/B978-0-444-63776-5.00012-7

[19] Patankar, N. A. (2003). On the modeling of hydrophobic contact angles on rough surfaces. *Langmuir, 19*, 1249–1253. https://doi.org/10.1021/la026612+

[20] Huang, Y., Sarkar, D. K., & Chen, X. G. (2015). Superhydrophobic aluminum alloy surfaces prepared by chemical etching process and their corrosion resistance properties. *Applied Surface Science, 356*, 1012–1024. https://doi.org/10.1016/j.apsusc.2015.08.168

[21] Meiron, T. S., Marmur, A., & Saguy, I. S. (2004). Contact angle measurement on rough surfaces. *Journal of Colloid and Interface Science, 274*, 637–644. https://doi.org/10.1016/j.jcis.2004.03.026

[22] Fazel, M., Salimijazi, H. R., & Golozar, M. A. (2015). A comparison of corrosion, tribocorrosion and electrochemical impedance properties of pure Ti and Ti6Al4V alloy treated by micro-arc oxidation process. *Applied Surface Science, 324*, 751–756. https://doi.org/10.1016/j.apsusc.2014.11.118

[23] Zou, J. X., Zhang, K. M., Hao, S. Z., Dong, C., & Grosdidier, T. (2010). Mechanisms of hardening, wear and corrosion improvement of 316 L stainless steel by low energy high current pulsed electron beam surface treatment. *Thin Solid Films, 519*, 1404–1415. https://doi.org/10.1016/j.tsf.2010.07.031

[24] Noor, E. A., & Al-Moubaraki, A. H. (2008). Corrosion behavior of mild steel in hydrochloric acid solutions. *International Journal of Electrochemical Science, 3*, 806–818.

[25] Mu, J., Sun, T., Leung, C. L. A., Oliveira, J. P., Wu, Y., Wang, H., & Wang, H. (2023). Application of electrochemical polishing in surface treatment of additively manufactured structures: A review. *Progress in Materials Science*, 101109. https://doi.org/10.1016/j.pmatsci.2023.101109

[26] Burwell, J. T. Jr. (1957). Survey of possible wear mechanisms. *Wear, 1*, 119–141. https://doi.org/10.1016/0043-1648(57)90046-8

[27] Tkadletz, M., Schalk, N., Daniel, R., Keckes, J., Czettl, C., & Mitterer, C. (2016). Advanced characterization methods for wear resistant hard coatings: A review on recent progress. *Surface and Coatings Technology, 285*, 31–46. https://doi.org/10.1016/j.surfcoat.2015.11.004

EUROPEAN MECHANICAL SCIENCE

Research Article

e-ISSN: 2587-1110

Mechanical analysis of al/foam composite sandwich panels under elastic and elastoplastic states

Sait Özmen Eruslu[1*]

[1]Çorlu Faculty of Engineering, Department of Mechanical Engineering, Tekirdağ Namık Kemal University, Çorlu, Türkiye

Orcid: S.O.Eruslu (0000-0003-2942-378X)

Abstract: This study performs mechanical analysis for Al/Foam composite sandwich panels under 3-point bending using numerically and experimentally. The flexural rigidity, elastic deflections, and normal, shear stresses are obtained by analytical calculations of the Timoshenko beam equation and compared finite element (FE) models for 3-point bending loading conditions. The FE models are constructed using 2D single-layer shell and 3D solid discrete-layer models. The validity of FE models at the analysis is evaluated for Al/PVC Foam sandwich composites for the elastic state. The experimental bending results of Al/XPS Foam sandwich composites are compared with numerical models at elastic and elastoplastic states. The elastic results indicate that the out-of-plane deflection results agree well across numerical and analytical models. Normal stresses at the core are higher in 3D discrete-layer solid models compared to laminated shell theory-based models for thick plates, due to the more accurate characteristics of the discrete-layer solid models. The Timoshenko beam theory-based analytical bending results show a good correlation with the results from laminated shell theory-based finite element method (FEM) analyses. Elastoplastic FEM analysis indicates that discrete-layer-based 3D solid FEM models effectively predict local effects dependent on indentation failure.

Keywords: Sandwich Panels, Timoshenko Beam Theory, Composite Laminate Modeling, Discrete-layer Modeling, Elastic and Elastoplastic Finite Element Analysis (FEA).

1. Introduction

A sandwich structure is a special class of composite structure commonly used in engineering and manufacturing. It consists of two outer layers, called face sheets, and a core material sandwiched between them. This design offers a combination of lightweight construction and high stiffness, making it ideal for various applications across different industries [1]

The core material is positioned between the facesheets and is crucial in determining the structural properties. It is chosen based on the desired characteristics of the sandwich structure, such as weight reduction, stiffness, insulation, or impact resistance. Common core materials include foams, honeycomb structures, and balsa wood [2]

Aluminum polymeric foam sandwich structures combine aluminum facesheets with a polymeric foam core to create lightweight composite materials. These sandwich structures offer a unique combination of properties that make them valuable in various engineering and manufacturing applications. Aluminum facesheets are combined with a foam core to create a lightweight structure, which is critical for applications where weight reduction is required. Aluminum enhances the strength of the structure, ensuring it can withstand mechanical loads and stresses. [3].

*Corresponding author:
Email: oeruslu@nku.edu.tr

Cite this article as:
Eruslu, S. Ö. (2024). Mechanical analysis of al/foam composite sandwich panels under elastic and elastoplastic states. *European Mechanical Science, 8*(3): 167-178. https://doi.org/10.26701/ems.1491014

History dates:
Received: 27.05.2024, ***Revision Request***: 22.06.2020, ***Last Revision Received***: 19.07.2020, ***Accepted***: 19.07.2024

Over the last half-century, various theories have been developed to accurately and effectively analyze composite structures. These include the equivalent single-layer theory, layerwise theory, zig-zag theory, and 3D elastic methods, among others [4].

Equivalent single-layer theories, such as classical laminated plate theory and first-order shear deformation theory, effectively predict the global responses of thin laminated composite plates and shells. However, they struggle to accurately capture the behavior of thick laminated composites, particularly regarding local responses such as the distribution of ply-level stresses. This limitation stems primarily from the continuous assumption of in-plane displacements inherent in these theories [5].

Numerous studies in the literature have employed the equivalent single-layer approach, incorporating 2D finite element (FE) shell models, to conduct comprehensive investigations of laminated composites and sandwich plates in both elastic and elastoplastic regions [6-8].

Shear deformations are important for sandwich panels where the core is relatively thick compared to the facesheets. The Timoshenko beam theory, also known as the first shear deformation theory, considers the effect of shear deformation in addition to classical bending. In theories like the first-order shear deformation theory, where transverse shear strains are assumed to be constant through the thickness direction, shear correction factors are required.

The accuracy of solutions obtained from the first-order shear deformation theory heavily depends on the ability to predict more precise shear correction factors [5].

A FE formulation of the classical linear first-order shear deformation theory for layered shells can be found in Reddy's book [9]. Pagano's pioneering work on the three-dimensional layerwise elasticity solution provides a robust framework for analyzing interlaminar stress fields in multilayered composite plates under mechanical loading conditions [10]. Simple equivalent single-layer theories often fail to accurately characterize the three-dimensional stress field at the ply level, making them unsuitable for simulating damage in laminated composites [11]. Reddy introduced a generalized laminate plate theory that incorporates discrete-layer transverse shear and transverse normal effects, effectively reducing the 3D elasticity theory of plates into a 2D laminate theory [12].

The Layerwise Theory characterizes laminated composites by treating them as an assembly of individual layers. Alternatively, it employs one-dimensional interpolation functions to model the displacement and stress fields along the thickness direction. This approach enables a detailed representation of the behavior of each layer within the composite structure, capturing the complexities of interlaminar interactions and allowing for accurate analysis of laminate performance [11]. The discrete-layer-based layerwise method typically offers more precise predictions of stresses and deformations within the sandwich panel by explicitly modeling the composite's layering and facilitating detailed stress analysis in each layer. It is a valuable tool for analyzing sandwich panels, especially when dealing with composite materials with complex layering and when detailed information about interlaminar stresses and failures is required. It allows for a comprehensive understanding of the structural behavior of these composite structures. [13].

Discrete-layer implemented FE shell modeling is a common approach for modeling laminated composites both in linear and nonlinear cases, as demonstrated by Mawenya and Davies [14] and Reddy [15]. When modeling sandwich panels, it is crucial to consider various failure modes, such as delamination between layers, core shear, indentation, and local buckling, depending on the application and loading conditions. [16-18]

The interaction between the facesheets and the core material is crucial in determining failure modes. A comprehensive FEA study should consider these interactions and provide insights into the structural performance and safety of the sandwich panel under various loading conditions. For detailed analysis of sandwich panels, especially for critical engineering applications, finite element analysis (FEA) is often employed to account for both bending and shear deformation. FEA allows for accurate modeling of complex geometries and material properties and can consider discrete deformation modes simultaneously [19].

The 3D displacement-based finite element method (FEM) can provide precise displacement and stress field solutions, but it demands substantial computational resources [11-12]

3D FEM discrete-layer models can capture local failure and debonding characteristics. These models permit the definition of interface damage. Abrate and coworkers investigated the cohesive zone delamination of interface layers using a 3D FEM discrete-layer model [20]. Höwer and coworkers studied the effects of fiber bridging on the delamination of the face sheet and core of honeycomb sandwich panels using a FE model [21].

In this study elastic properties of Al/foam sandwich panels are obtained by simple mechanics of materials approach and compared with commercial FEA code Ansys results namely 2D single-layer Shell and 3D discrete-layer solid modeling approaches. Shear terms are considered both in analytical and numerical calculations. The FEA 2D Shell model is based on the laminated shell theory namely the Mindlin plate shell approach. Shell elements have been shown to yield accurate results for thin-walled composite plates when considering the first-order shear deformation theory [22]. The effectiveness of 3D solid single-layer and discrete-layer FEM models in the nonlinear zone is established and compared with experimental test results.

2. Materials Method

2.1. Sandwich Beams Bending Equations

In Timoshenko's theory for sandwich beams, deflection is typically calculated using beam bending theory. Timoshenko's theory accounts for shear deformations in addition to bending, providing a more accurate prediction of deflection compared to the Euler-Bernoulli beam theory, which neglects shear effects [23].

The displacement field in Timoshenko beam sandwich beam theory

$$u(x,z) = u_0\,(x) - z\,\emptyset_x \tag{1}$$

$$w\,(x) = w_0(x) \tag{2}$$

The strain fields is defined as follow

$$\varepsilon_x = \frac{du_0}{dx} + \frac{d\emptyset_x}{dx} \tag{3}$$

$$\gamma_{xz} = \frac{dw_0}{dx} + \frac{dU}{dz} \tag{4}$$

Here $u(x,z)$ is the axial displacement across the thickness, ε_x and γ_{xz} are the axial and shear strain of the composite, u_0 , w_0 is the axial and transverse displacement of the midplane, $\emptyset_x$ is the rotation of the cross section according to the x axis.

The governing equations bending for a Timoshenko sandwich beam with transverse uniform external load q(x), which include the effects of bending and shear deformation, can be formulated as follows

$$\frac{dN}{dx} = 0 \tag{5}$$

$$\frac{dQ}{dx} + q(x) = 0 \tag{6}$$

$$\frac{dM}{dx} - Q_x = 0 \tag{7}$$

The stress resultants namely axial force, moment and shear forces can be written as follows [24]

$$N_x = A\,\frac{du_0}{dx} + B\frac{d\emptyset}{dx} \tag{8}$$

$$M_x = B\frac{du_0}{dx} + D\,\frac{d\emptyset}{dx} \tag{9}$$

$$Q_x = k_s G_c A_c\,(\frac{dw}{dx} + \emptyset_x) \tag{10}$$

Here A,B and D are the extensional, coupling and bending stiffness respectively, k_s is the shear correction factor,G_c is the shear modulus of the core, A_c is the cross - sectional area of the core. The governing differential equations can be obtained by combining stress resultants.

The following assumptions are used in formulations of symmetric laminated beam theory [24]

$M_{yy} = M_{xy} = Q_y = \emptyset_y = 0$, w_0 *and* $\emptyset_x$ are the functions of x and $q(x) = F_0$ is defined as transverse point load.

The out-of-plane deflections are considered in the analysis A and B stiffness are zero in the absence of plane forces at symmetric laminate beam theory. The three-point bending problem with transverse point load, the moment, and shear resultants are given as follows by these assumptions.

$$M(x) = D\,\frac{d\emptyset}{dx} = \frac{F_0 x}{2} \tag{11}$$

$$Q(x) = k_s G_c A_c\,\left(\frac{dw}{dx} + \emptyset_x)\right) = \frac{dM}{dx} = \frac{F_0}{2} \tag{12}$$

The stress resultants are solved according to the simply supported boundary conditions below and integration constants are found.

$$x = 0,\;\; w(0) = u(0) = 0,\;\; x = L\,, w(L) = 0\,,\;\; \emptyset_x\left(\frac{a}{2}\right) = 0$$

The $\emptyset_x$ *and* w_x values are obtained respectively with boundary conditions, maximum transverse deflection is occurs at the x=a/2 is given in the following formula.

$$w_{max} = \frac{PL^3}{48D} + \frac{PL}{4K\;G_c A_c} = \frac{PL^3}{48(EI)_{eq}} + \frac{PL}{4\,(AG)_{eq}} \tag{13}$$

Here $D = (EI)_{eq}$, $G_c A_c = (AG)_{eq}$ is the equivalent elastic and shear rigidity, and K is a shear correction factor.

The equivalent elastic properties of the sandwich composite are obtained using the parallel axis theorem below [25]

$$(EI)_{eq} = \frac{E_f b\,t^3}{6} + \frac{E_c^*\,b\,c^3}{12} + \frac{E_f b t d^2}{2} \approx \frac{E_f b\,c^2}{2} \tag{14}$$

Sandwich composites typically consist of two facesheets bonded to a lightweight core material. Here E_f, E_c^* are the face material and core materials' elastic modulus, respectively.

https://doi.org/10.26701/ems.1491014

t is the facesheet thickness, L is the face sheet span length, b is the facesheet width, c is the core thickness, and d is the total beam thickness seen in Figure 1.

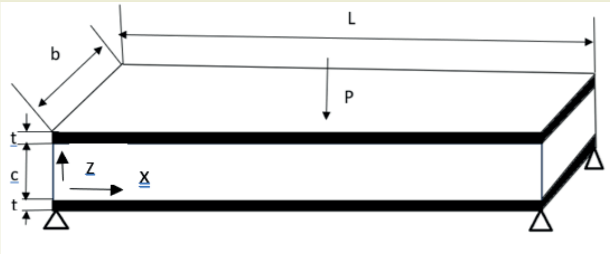

Figure 1. Sandwich beam in three-point bending with central transverse load

The equivalent shear rigidity is given below.

$$(AG)_{eq} = \frac{bd^2G_c}{c} \tag{15}$$

This equation assumes that the facesheets contribute negligibly to the overall shear stiffness compared to the core material. When a sandwich beam is subjected to bending, it experiences bending and shear deformation. This deformation results in both normal and shear stresses within the beam. The studies indicate that the core experiences negligible normal stresses, while its main function is to withstand shear loads [26]. The maximum normal stresses at the core and facesheets and shear stresses at the core of a sandwich beam are typically calculated using appropriate stress formulas derived from both bending and shear deformation theories [25].

$$\sigma_c(z) = \frac{M_z E_c^*}{(EI)_{eq}} = \frac{PL}{4btc}\,\frac{E_c^*}{E_f} \tag{16}$$

$$\sigma_f(z) = \frac{M_z E_f}{(EI)_{eq}} = \frac{PL}{4btc} \tag{17}$$

$$\tau_c(z) = \frac{P}{2(EI)_{eq}}\left[\frac{E_f td}{2}\right] \approx \frac{P}{2bc} \tag{18}$$

2.2. Finite Element (FE) Modeling of Sandwich Composites

In this study, numerical modeling of Al/foam sandwich composites is conducted using shell laminated single-layer modeling and solid discrete-layer approaches. The validity of these models under elastic conditions is discussed, and numerical examples are provided for Al/PVC Foam sandwich composites. The solid discrete-layer model and solid laminated single-layer models are also compared with experimental results for Al/XPS Foam sandwich composites under three-point bending.

Laminated Shell Model

Layer-based shell and solid elements are a known approach used in FEA to simulate the behavior of sandwich structures [27]. The shell layer-based models simplify the complex three-dimensional geometry of the sandwich structure into two-dimensional shell elements with an equivalent single-layer theory approach.

Shell modeling balances computational efficiency and accuracy, making it a widely used approach for analyzing sandwich composites in engineering applications. This study utilizes the Mindlin shell theory in the numerical model. The mechanical properties of Al / PVC Foam sandwich composites are given in Table 1 [28]. The three-point bending dimensions in the analysis are determined according to the ASTM C393 standards.

The shell model and simply supported boundary conditions are given in Figure 2.

The two-dimensional quadratic type element Shell281

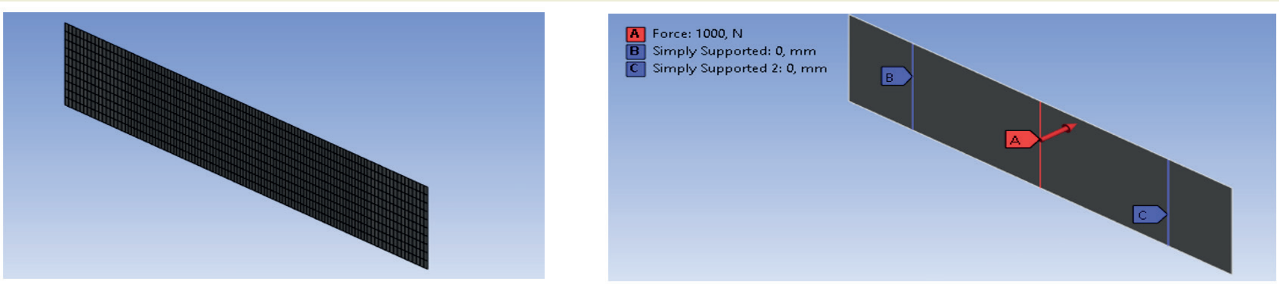

(a)

(b)

Figure 2. The shell laminated single-layer model **a**) Mesh **b**) Boundary conditions

Table 1. The Mechanical Properties of Al/ PVC Foam Sandwich Composites

PVC Foam Elastic Modulus [MPa]	PVC Foam Shear Modulus [MPa]	PVC Foam Density [kg/m^3]	PVC Foam Thickness [mm]	Al Sheet Elastic Modulus [MPa]	Al Sheet Density [kg/m^3]	Al Sheet Thickness [mm]
104	30	80	15	70000	2710	1.5

uses 1120 elements in the shell FE model, considering convergence seen in Figure 3. The midspan load is 1000N considering elastic loading conditions. Beam width (c) is 75mm and beam span length (L) is 200mm in the analysis.

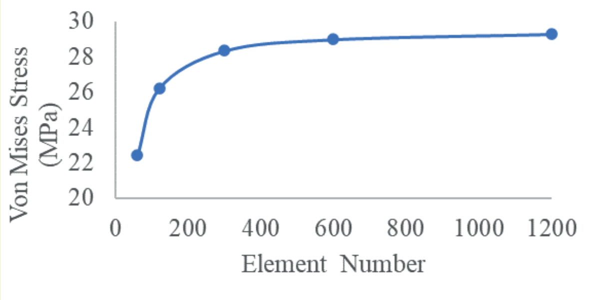

Figure 3. The convergence study at the shell model

Discrete-Layer Sandwich Composite Model

Discrete-Layer sandwich model is a composite structural analysis that accounts for the individual layers within a sandwich structure, considering their specific material properties and orientations. In the solid discrete-layer finite element model, the three-dimensional quadratic type element Solid186 is utilized, incorporating 7200 elements. This model considers both convergence and computational time factors. The hex-dominant multizone mesh and node merging command are employed at the interface between facesheets and the core to ensure continuity of load transfer. The FE solid model and boundary conditions are depicted in Figure 4.

2.3. Three-Point Bending Test of Al/XPS Foam Sandwich Panels

To assess the effectiveness of the discrete-layer model in the plastic region, experimental three-point bending results, specifically load-deflection data, for Al/XPS Foam sandwich composites are compared. The dimensions for the three-point bending test are obtained for three specimens according to ASTM C393 standards. The experimental setup and deflection scenes are depicted in Figure 5. The beam geometry, face, and core material properties are given in Table 2. The XPS mechanical properties are obtained from compression tests from the literature [29].

Here ($E_{f,}$ E_c) is the elastic modulus of the Aluminum sheet and XPS foam core respectively, (σ_{fy}, σ_{ft}) is the yield and tensile strength of Aluminum sheet respectively, ($\varepsilon_{f,ult,}\varepsilon_{c,ult}$) is the ultimate strain at break of facesheet and core material respectively, $\sigma_{c,c}$ is the compressive strength of XPS foam, (ρ_f ,ρ_c) are the density of the facesheet and foam core respectively.

In this research, the mechanical properties of XPS Foam are determined through the results of compression tests. A multilinear kinematic hardening model is employed to obtain accurate material behavior data for XPS foam compression stress-strain curves, and the multilinear isotropic hardening material model is used for the modeling of Al 1050, as seen in Figure 6 below.

Table 2. Al/XPS sandwich beam geometry and face/ core material properties

Beam Geometry [mm]				Face Material Al 1050					Core Material XPS Foam			
b	c	t	L	E_f [GPa]	σ_{fy} [MPa]	σ_{ft} [MPa]	$\varepsilon_{f,ult}$	ρ_f $[\frac{kg}{m^3}]$	E_c [MPa]	$\sigma_{c,c}$ [MPa]	$\varepsilon_{c,ult}$	ρ_c $[\frac{kg}{m^3}]$
75	19.5	2	200	70	45	120	0.35	2710	7	0.150	0.25	28

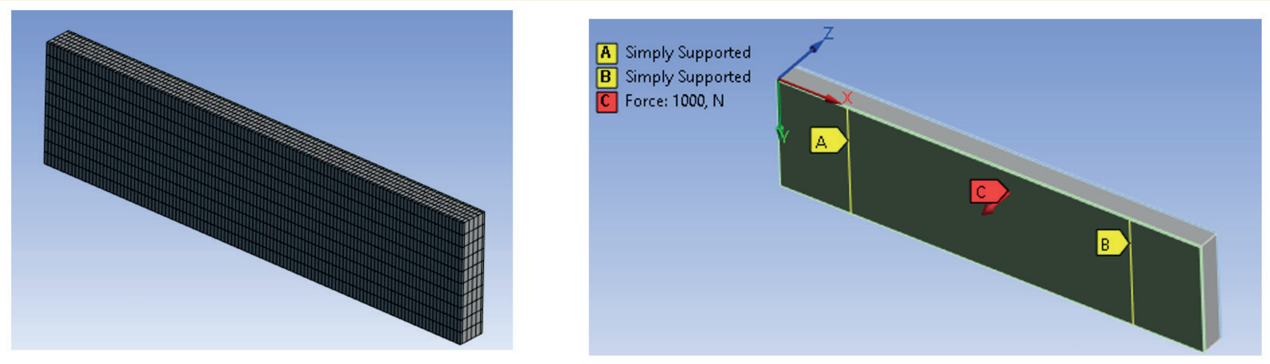

Figure 4. The discrete-layer model a) Mesh b) Boundary conditions

3. Results and Discussion

3.1. Laminated Shell Model Results

This section presents the results of the laminated shell model derived from the 2D shell model for Al/PVC Foam sandwich composites subjected to three-point bending. These results are compared with those from the Timoshenko sandwich beam model.

The shell layer-based single-layer theory approach has been shown to provide results that correlate well with the Timoshenko beam theory for bending isotropic and functionally graded beams [30]. This correlation is also

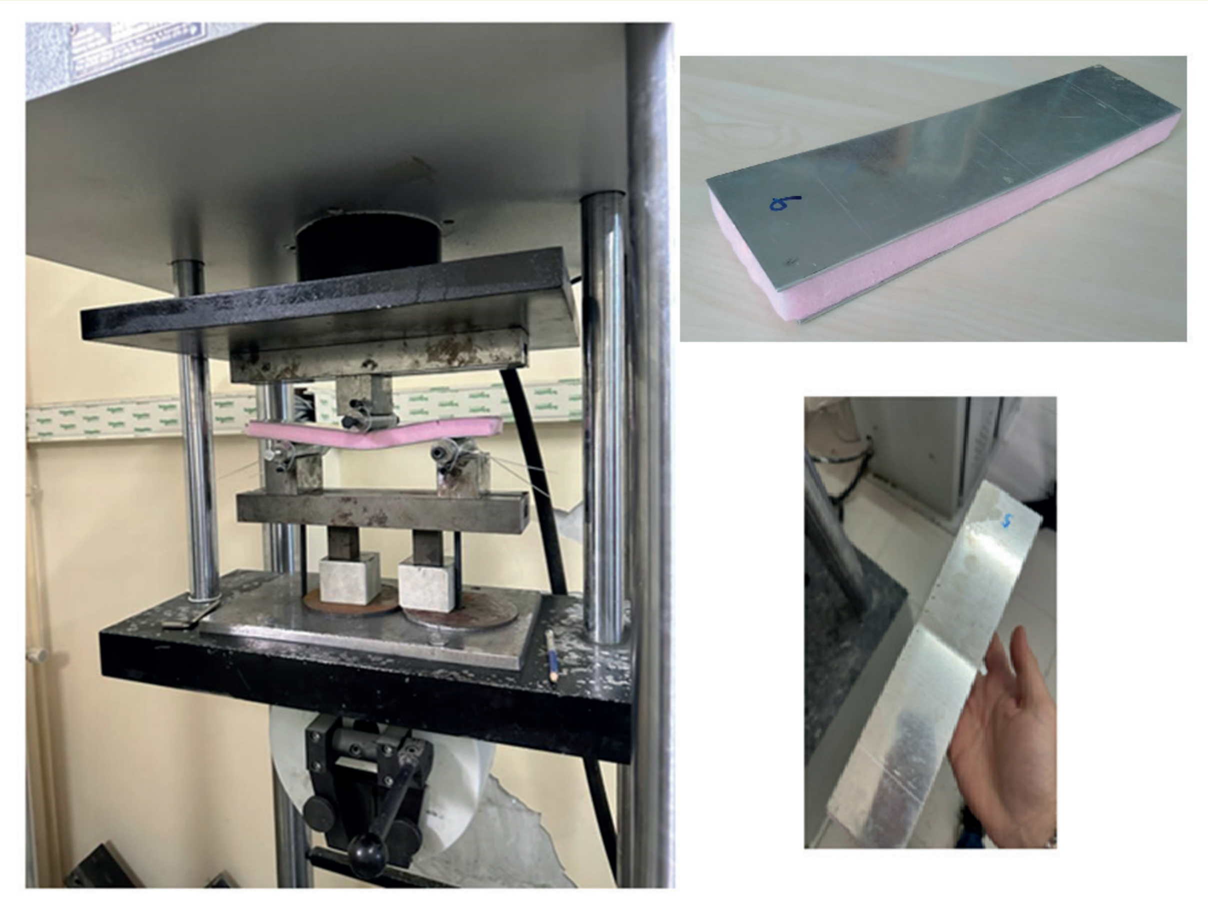

Figure 5. Three-point bending test setup and samples

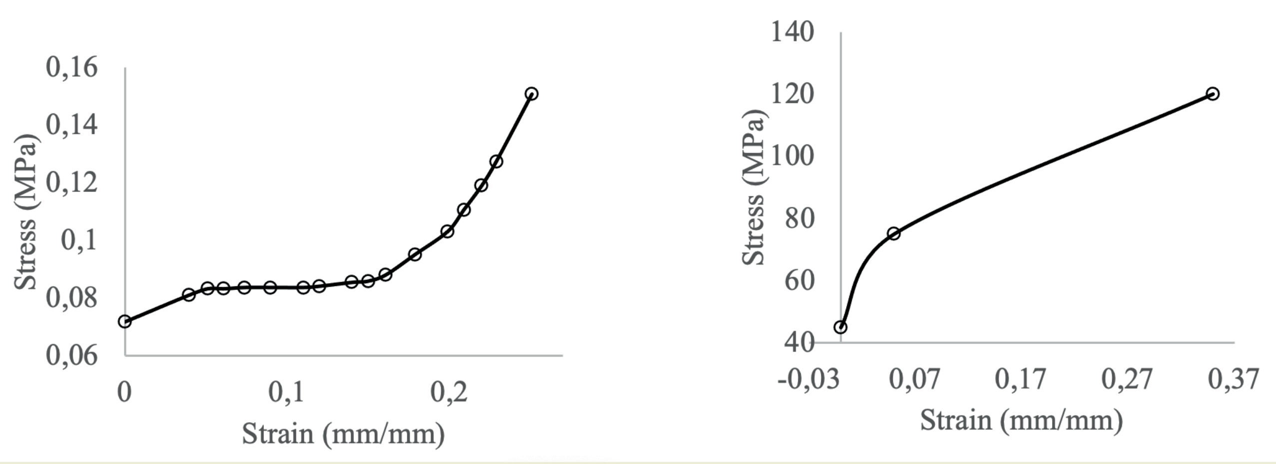

(a) (b)

Figure 6. Materials models definitions at fem analysis **a)** Multilinear kinematic hardening model of XPS foam **b)** Multilinear isotropic hardening model of aluminum

demonstrated in Kholkin's study on the 3-point bending characteristics of laminated composite beams [31].

The normal stress results are shown in Figure 7 below.

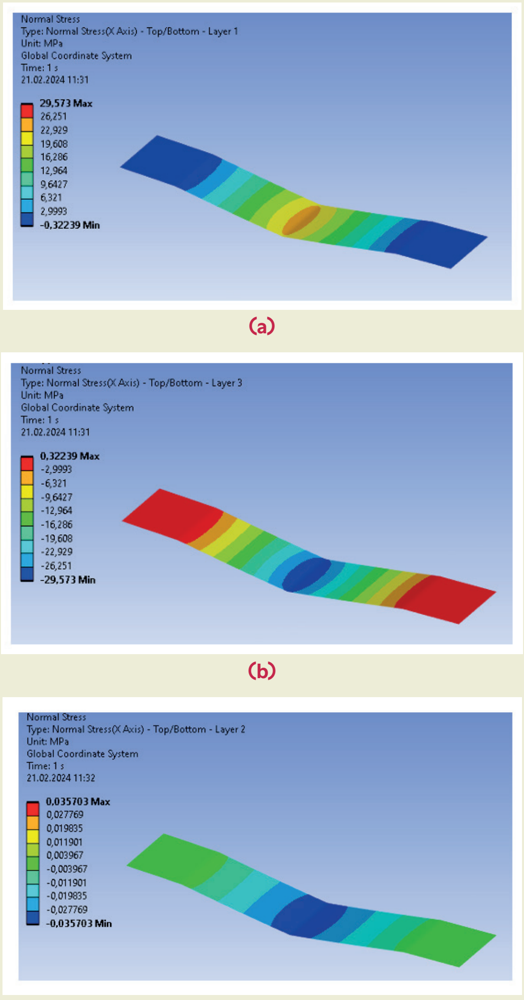

(a)

(b)

(c)

Figure 7. Normal stresses shell model a) Outer face sheet b) Inner facesheet c) Core

The normal stress results indicate that the core experiences compressive stress at the top and tensile stress at the bottom surface. The facesheets also experience maximum normal stresses during bending. The outer facesheet on the tension side experiences maximum tensile stress, while the inner facesheet on the compression side experiences maximum compressive stress.

Shear stresses are typically highest at the interface between the facesheets and the core material. Shear stresses in the core usually peak near the neutral axis as seen in Figure 8 below.

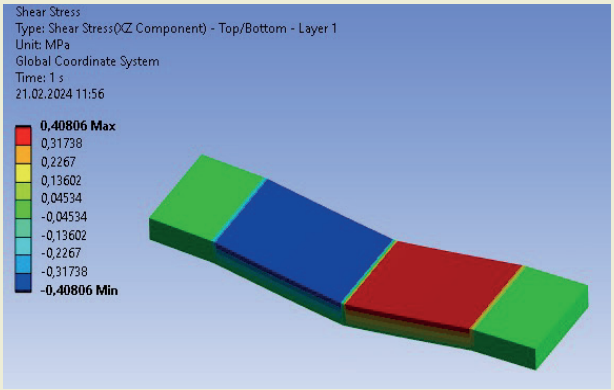

Figure 8. Shear stresses of the core at the shell model

The analytical results obtained from the Timoschenko sandwich beam model are compared with a laminated beam sandwich composite using a 2D Shell FE model, as seen in

Table 3. In Table 3 analytical and shell model results are denoted by subscripts "A" and "SH" respectively. The facesheet and core are denoted by "F" and "C" respectively. The maximum deflection, bending, and shear stresses are denoted by symbols δ, σ and τ respectively.

3.2. Discrete-layer Sandwich Composite Model Results

The results of the discrete-layer solid model obtained for Al/PVC Foam sandwich composites under three-point bending are presented. These results are compared with those from the laminated shell model. The normal and shear stress results are shown in Figure 9-10 below. It is seen from the figures that the stress zones in the discrete-layer solid model correlate with those in the shell model, whereas the local load-affected zone is more pronounced in the discrete-layer model.

The numerical results obtained from the discrete-layer model is compared with the Shell model at the following Table 4. In the table, SOL" denotes solid model results.

A good correlation is observed in the deflection and normal/shear stress results of the core material within the elastic region. However, underestimated results are

Table 3. The shell model results versus analytical results.

δ_A [mm]	$\sigma_{A,F}$ [MPa]	$\sigma_{A,C}$ [MPa]	$\tau_{A,C}$ [MPa]	δ_{SH} [mm]	$\sigma_{SH,F}$ [MPa]	$\sigma_{SH,C}$ [MPa]	$\tau_{SH,C}$ [MPa]
1.073	29.62	0.044	0.444	1.072	29.57	0.035	0.408

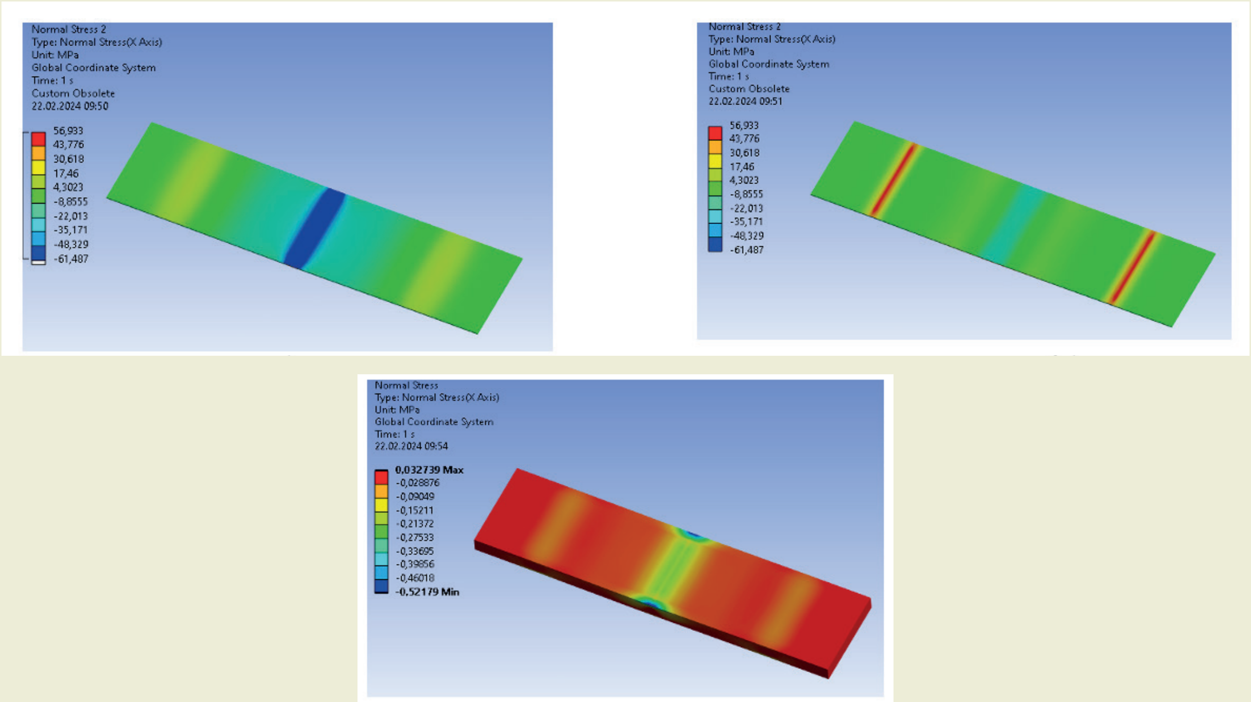

Figure 9. Normal stresses of discrete-layer model a) Outer facesheet b) Inner face sheet c) Core

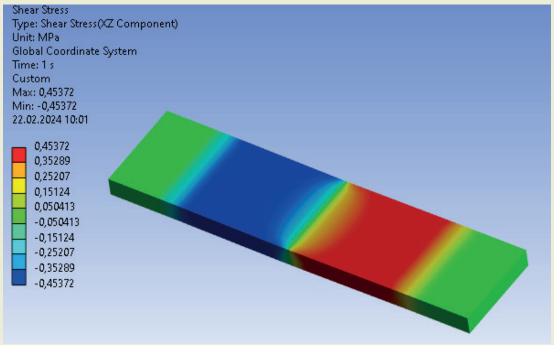

Figure 10. Maximum shear stresses at the core at discrete-layer model

noted for the facesheet stresses, which are particularly crucial for the failure analysis of sandwich composites.

It is evaluated that the discrete-layer model offers more precise predictions of stresses and deformations within the sandwich panel due to its explicit modeling of the composite's layering, enabling detailed stress analysis within each layer. The effectiveness of the discrete-layer model in elastoplastic states is studied in the following section to make predictions regarding the failure analysis of sandwich panels.

3.3. Effectiveness of Discrete-layer Model at Elastoplastic Region

Discrete-layer models are particularly suitable for capturing nonlinear deformations in sandwich composite structures, including plastic deformation, in contrast to laminated shell models. These models offer a more detailed representation of the composite's behavior by accounting for variations in material properties and deformations through the thickness of each layer. Radhakrishnan and coworkers show that the discrete-layer solid FEM model provides results that correlate well with 3-point bending experimental results of Al sandwich composites for different support span-to-thickness ratios and width-to-thickness ratios [32]. The experimental three-point bending results, specifically load-deflection data, for Al/XPS Foam sandwich composites are compared with the discrete-layer model in Figure 11.

Table 4. The discrete-layer solid model results versus laminated shell single-layer model results.

δ_{SOL} [mm]	$\sigma_{SOL,F}$ [MPa]	$\sigma_{SOL,C}$ [MPa]	$\tau_{SOL,C}$ [MPa]	δ_{SH} [mm]	$\sigma_{SH,F}$ [MPa]	$\sigma_{SH,C}$ [MPa]	$\tau_{SH,C}$ [MPa]
1.049	56.93	0.032	0.45	1.072	29.57	0.035	0.408

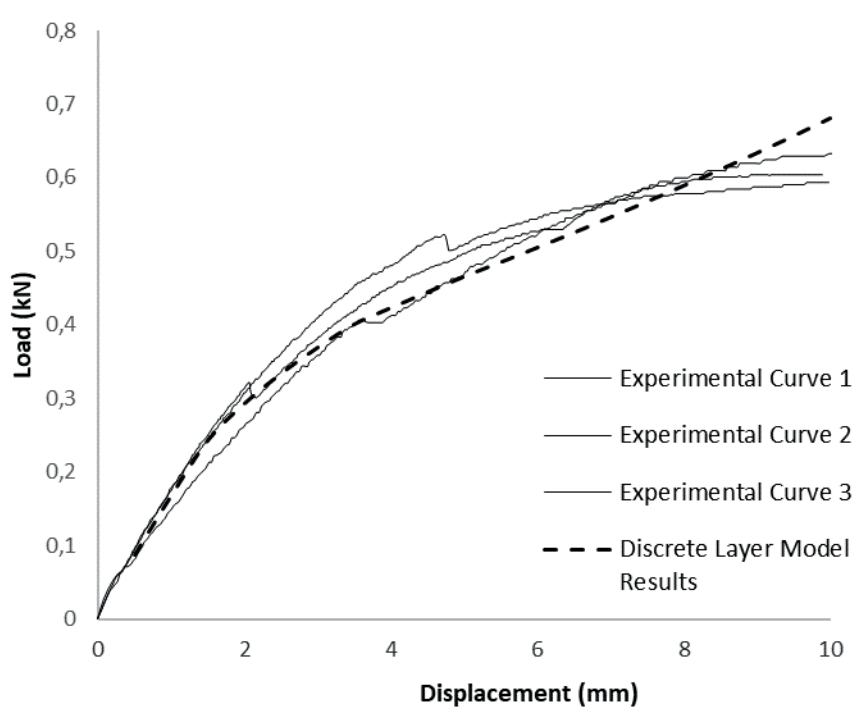

Figure 11. Load- deflection curves of Al/Xps foam sandwich panels under transverse load

The failure study focuses on facesheet yield and indentation. This study can extended by counting other failure types such as core shear and debonding failures, particularly with higher core layer thickness ratios.

The load-deflection results indicate that the discrete-layer model predicts well in the elastic region, and approximate results are obtained in the elastoplastic regions. However, it is observed that the ultimate failure is not well predicted, which highlights the limitations of the multilinear kinematic hardening model and the poor bonding at sheet-core interfaces observed in experiments.

Uzay and coworkers [18], as well as Alshahrani and coworkers [33], noted in their numerical and experimental studies that under 3-point bending loading conditions, the predominant failure modes of foam core-based composite sandwich panels can be summarized as a tensile failure, local indentation, upper skin debonding at the impact point of the indenter, and delamination through the thickness of the sandwich composites. Similar correlated results are observed in our study.

The types of failures observed in the experiments are summarized in Figure 12 below.

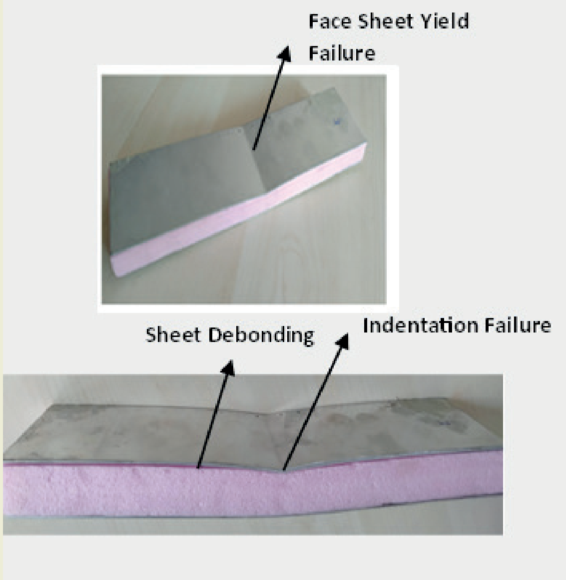

Figure 12. Failure zones occurred during the three-point bending test of the Al/XPS sandwich plate

A modification is made to a discrete-layer model to analyze the effects of indentation by adding supports, potentially roller supports, particularly in the plastic region seen in the following figures. The results of the discrete-layer model are compared with those of the laminated solid composite single-layer model in Figure 13.

The figures indicate that the face yield zone is larger for discrete-layer models than for laminated composite models. Additionally, discrete-layer models more accurately predict local strains. Both discrete-layer and

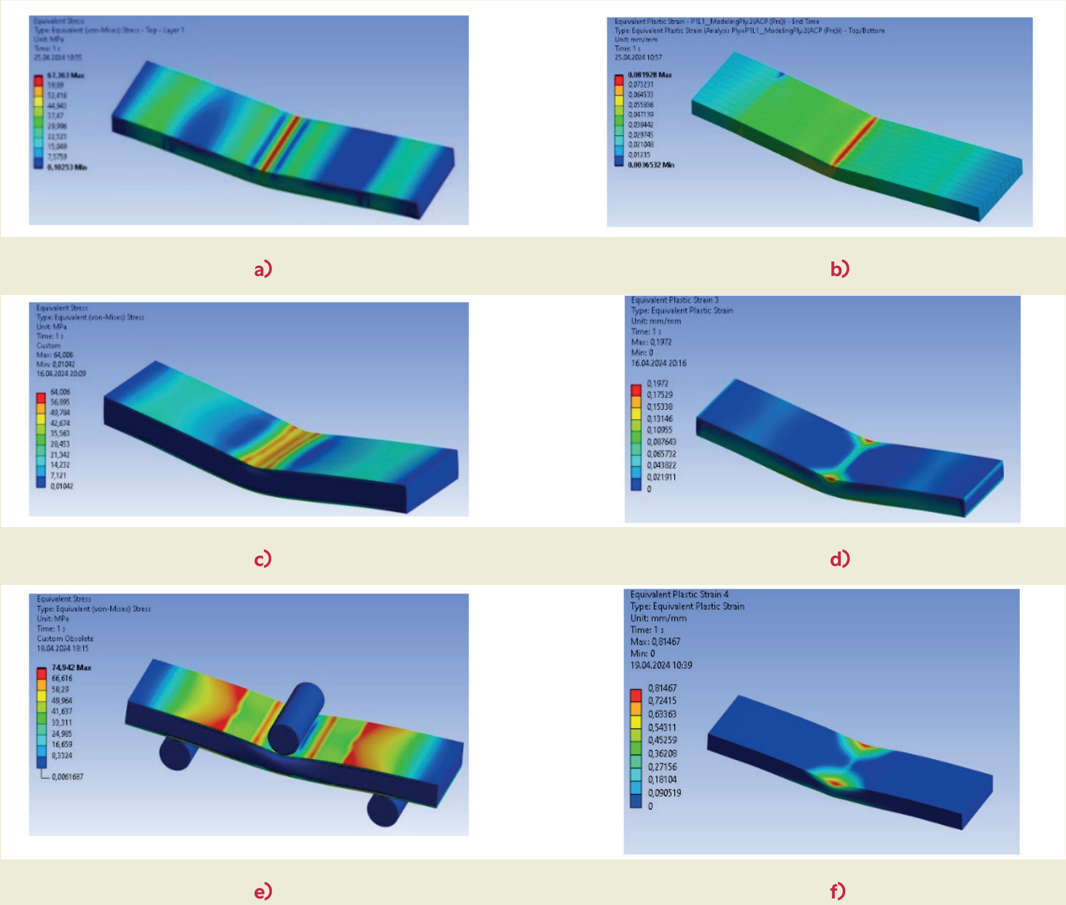

Figure 13. Three-point bending results a) Laminated model von Mises stresses b) Laminated model core plastic strains c) Discrete-layer model 1 Von Mises stresses d) Discrete-layer model 1 core plastic strains e) Discrete-layer model 2 Von Mises stresses f) Discrete-layer model 2 core plastic strains

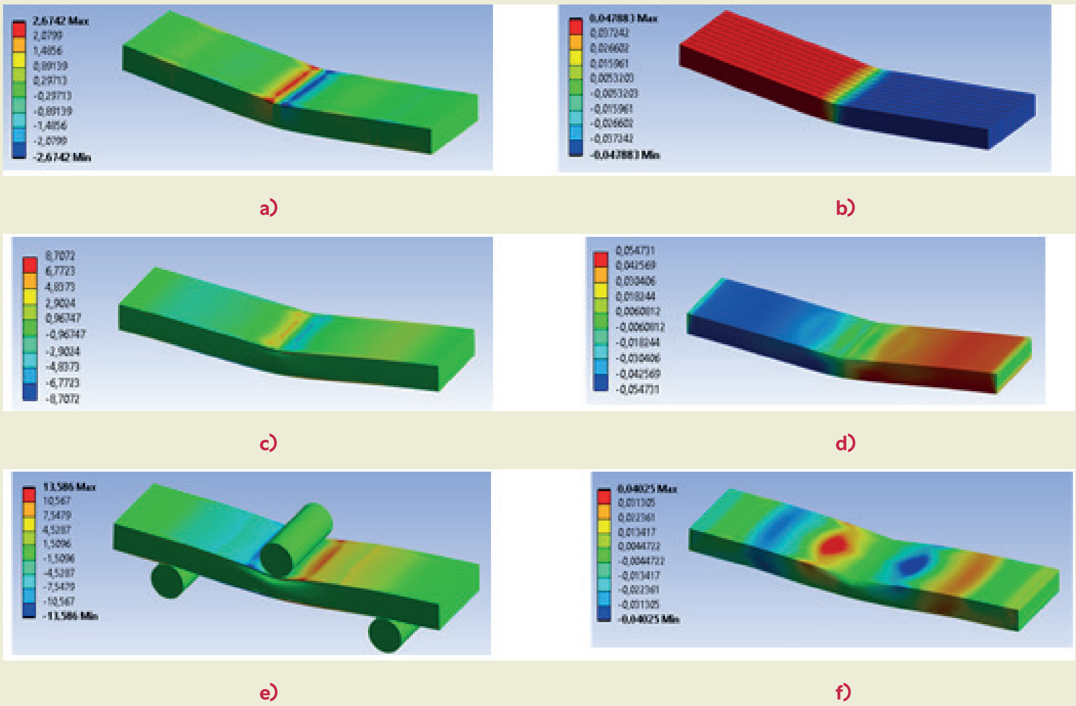

Figure 14. Three-point bending results a) Laminated model shear stresses at face sheet b. Laminated model shear stresses at core c. Discrete-layer model 1 shear stresses at face sheet d. Discrete-layer model 1 shear stresses at core e. Discrete-layer model 2 shear stresses at face sheet f. Discrete-layer model 2 shear stresses at the core

composite models predict the face yield failure. The local strains effective in the larger face yield zone and indentation failure are predicted more accurately by the discrete-layer models. The sheet debonding failure at the core and sheet interface is another issue observed at experiments due to the interlaminar shear stresses and poor bonding of epoxy. The shear stress results obtained from the discrete-layer models and the laminated composite model are compared in Figure 14.

Shear stresses are critical in the failure of sandwich panels, with core shearing failure occurring when the shear stress in the core reaches the yield strength of the core material. Face debonding and indentation occur when the loading is extremely localized [34]. In our study, the discrete-layer solid FEM model results, seen in Figures 13 and 14, correlated with experimental results, indicate that the face yield affected plastic strain and shear stress zones in the core are localized. This localization is the reason for the indentation and debonding at the interface. The indentation failure is more accurately predicted by adding roller supports.

4. Conclusions

In this study, the effectiveness of the shell-based laminated single-layer composite model versus the discrete-layer solid FE model is focused on Al/foam sandwich composites. The sandwich beam three-point bending calculations derived using the Timoschenko sandwich beam model are compared with results from shell-based and discrete-layer solid FE models in the elastic region. The results indicate that the shell-based FE model results agree well with Timoshenko's sandwich beam theory. The normal and shear stress effective zones correlate in both shell-based and discrete-layer solid FE models. However, the face sheet stresses, crucial for face sheet failure analysis, are higher in the discrete-layer solid model. The studies in the literature note that discrete-layer solid models typically offer more detailed information, especially in capturing nonlinear behavior and stress distributions within individual layers of the sandwich composite.

The effectiveness of the discrete-layer model in the nonlinear zone is verified through experimental study. The possible failure modes according to the load span to thickness ratio are face sheet yield and interface delamination. The analysis results obtained from the discrete-layer model align closely with calculations and experimental results. The stress intensity-based local strains, crucial for understanding indentation failure, typically exhibit higher values in discrete-layer models than in laminated composite models. This localized strain can lead to indentation or deformation at the interface between the core and face sheets, compromising the structural integrity of the sandwich panel.

Research Ethics

Ethical approval not required.

Author Contributions

The author(s) accept full responsibility for the content of this article and have approved its submission.

Competing Interests

The author(s) declare that there are no competing interests.

Research Funding

Not reported.

Data Availability

Not applicable.

Peer-review

Externally peer-reviewed.

References

[1] Kaw, A. K. (2006). *Mechanics of composite materials* (2nd ed.). Taylor and Francis.

[2] Gay, D., Hoa, S. V., & Tsai, S. W. (2003). *Composite materials: Design and applications*. CRC Press.

[3] Tunca, E., & Kafalı, H. (2021). Compression and three-point bending analyses of aerospace sandwich composites produced with polymeric core materials using Ansys. *European Journal of Science and Technology, 31*(1), 553–561. https://doi.org/10.31590/ejosat.1012658

[4] Liew, K. M., Pan, Z. Z., & Zhang, L. W. (2019). An overview of layerwise theories for composite laminates and structures: Development, numerical implementation, and application. *Composite Structures, 216*, 240–259. https://doi.org/10.1016/j.compstruct.2019.02.074

[5] Matsunaga, H. (2004). A comparison between 2-D single-layer and 3-D layerwise theories for computing interlaminar stresses of laminated composite and sandwich plates subjected to thermal loadings. *Composite Structures, 64*, 161–177. https://doi.org/10.1016/j.compstruct.2003.08.001

[6] Rao, K. P. (1978). A rectangular laminated anisotropic shallow thin shell finite element. *Computer Methods in Applied Mechanics and Engineering, 15*(1), 13–33. https://doi.org/10.1016/0045-7825(78)90003-8

[7] Saigal, S., Kapania, R. K., & Yang, T. Y. (1986). Geometrically nonlinear finite element analysis of imperfect laminated shells. *Journal of Composite Materials, 20*(2), 197–214. https://doi.org/10.1177/002199838602000206

[8] Kreja, I. (2011). A literature review on computational models for laminated composite and sandwich panels. *Central European Journal of Engineering, 1*(1), 59–80. https://doi.org/10.2478/s13531-011-0005-x

[9] Reddy, J. N. (2002). *Energy principles and variational methods in applied mechanics*. John Wiley and Sons.

[10] Pagano, N. J. (1970). Exact solutions for rectangular bidirectional composites and sandwich plates. *Journal of Composite Materials, 4*(1), 20–34. https://doi.org/10.1177/002199837000400103

[11] Li, D. (2021). Layerwise theories of laminated composite structures and their applications: A review. *Archives of Computational Methods in Engineering, 28*, 577–600. https://doi.org/10.1007/s11831-019-09392-2

[12] Reddy, J. N. (1987). A generalization of two-dimensional theories of laminated composite plates. *Communications in Applied Numerical Methods, 3*, 173–180. https://doi.org/10.1002/cnm.1630030303

[13] Yang, C., Chen, J., & Zhao, S. (2013). The interlaminar stress of laminated composite under uniform axial deformation. *Modeling and Numerical Simulation of Material Science, 3*(2), 49–60. https://doi.org/10.4236/mnsms.2013.32007

[14] Mawenya, A. S., & Davies, J. D. (1974). Finite element bending analysis of multilayer plates. *International Journal for Numerical Methods in Engineering, 8*, 215–225. https://doi.org/10.1002/nme.1620080203

[15] Reddy, J. N. (1989). On refined computational models of composite laminates. *International Journal for Numerical Methods in Engineering, 27*, 361–382. https://doi.org/10.1002/nme.1620270210

[16] Ashby, M. F., Evans, A. G., Fleck, N. A., Gibson, L. J., Hutchinson, J. W., & Wadley, H. N. G. (2000). *Metal foams: A design guide*. Butterworth Heinemann.

[17] Daniel, I. M., Gdoutos, E. E., Wang, K. A., & Abot, J. L. (2002). Failure modes of composite sandwich beams. *International Journal of Damage Mechanics, 11*(4), 309–334. https://doi.org/10.1106/105678902027247

[18] Uzay, Ç., & Geren, N. (2020). Failure analysis of low-density polymer foam core sandwich structures under three-point bending loading. *Çukurova University Journal of the Faculty of Engineering and Architecture, 35*(1), 49–58. https://doi.org/10.21605/cukurovaummfd.764547

[19] Staal, R. A. (2006). Failure of sandwich honeycomb panels in bending (PhD thesis). The University of Auckland, New Zealand.

[20] Abrate, S., Ferrero, J. F., & Navarro, P. (2015). Cohesive zone models and impact damage predictions for composite structures. *Meccanica, 50*, 2587–2620. https://doi.org/10.1007/s11012-015-0221-1

[21] Höwer, D., Lerch, B. A., Bednarcyk, B. A., Pineda, E. J., Reese, S., & Simon, J. W. (2018). Cohesive zone modeling for mode I facesheet to core delamination of sandwich panels accounting for fiber bridging. *Composite Structures, 183*, 568–581. https://doi.org/10.1016/j.compstruct.2017.07.005

[22] Eruslu, S. O., & Aydogdu, M. (2009). Vibration analysis of inclusion reinforced composite square plates under various boundary conditions. *Journal of Reinforced Plastics and Composites, 28*, 995–1012. https://doi.org/10.1177/07316844070877

[23] Karamanlı, A. (2018). Flexure analysis of laminated composite and sandwich beams using Timoshenko beam theory. *Journal of Polytechnic, 21*(3), 633–643. https://doi.org/10.2339/politeknik.386958

[24] Reddy, J. N. (2004). *Mechanics of laminated composite plates and shells: Theory and analysis* (2nd ed.). CRC Press.

[25] McCormack, T. M. (1999). Failure of structural sandwich beams with metallic foam cores (MSc thesis). Massachusetts Institute of Technology, United States of America.

[26] Studzinski, R., Pozorski, Z., & Garstecki, A. (2009). Optimal design of sandwich panels with a soft core. *Journal of Theoretical and Applied Mechanics, 47*(3), 685–699.

[27] Manet, V. (1998). The use of ANSYS to calculate the behavior of sandwich structures. *Composites Science and Technology, 58*(12), 1899–1905. https://doi.org/10.1016/S0266-3538(98)00010-4

[28] Kaboglu, C., Yu, L., Mohagheghian, I., Blackman, B. R. K., Kinloch, A. J., & Dear, J. P. (2018). Effects of the core density on the quasi-static flexural and ballistic performance of fiber-composite skin/foam core sandwich structures. *Journal of Material Science, 58*, 16393–16414. https://doi.org/10.1007/s10853-018-2799-x

[29] Çınar, K. (2018). Evaluation of sandwich panels with composite tube-reinforced foam core under bending and flatwise compression. *Journal of Sandwich Structures and Materials, 22*(2), 480–493. https://doi.org/10.1177/1099636218798161

[30] Eruslu, S. Ö. (2018). The effect of particle type and distribution on bending analysis of glass particle reinforced composite beams. *CRPASE: Transactions of Mechanical Engineering, 6*, 1–5.

[31] Kholkin, A. (2012). Numerical simulation of damage and failure of laminated 3-point bending specimens (PhD thesis). Vienna University of Technology, Austria.

[32] Radhakrishnan, G., Breaz, D., Al Hattali, A. H. M. S., Al Yahyai, A. M. N., Al Riyami, A. M. N. O., Al Hadhrami, A. M. D., & Karthikayen, K. R. (2023). Influence of aspect ratio on the flexural and buckling behavior of an aluminum sandwich composite: A numerical and experimental approach. *Materials, 16*(19), 1–11. https://doi.org/10.3390/ma16196544

[33] Alshahrani, A., & Ahmed, A. (2022). Study on flexural behavior of glass fiber reinforced plastic sandwich composites using liquid thermoplastic resin. *Polymers, 14*(19), 1–20. https://doi.org/10.3390/polym14194045

[34] Wang, B., Shi, Y., Zhou, C., & Li, T. (2016). Failure mechanism of PMI foam core sandwich beam in bending. *International Journal of Simulation and Multidisciplinary Design Optimization, 6*, A8:1–11. https://doi.org/10.1051/smdo/2015008

EUROPEAN MECHANICAL SCIENCE

Research Article

e-ISSN: 2587-1110

Solution scheme development of the nonhomogeneous heat conduction equation in cylindrical coordinates with Neumann boundary conditions by finite difference method

Melih Yıldız[1*]

[1]Iğdır University, Faculty of Engineering, Department of Mechanical Engineering/ Türkiye

Orcid: M. Yıldız (0000-0002-6904-9131)

Abstract: Partial differential heat conduction equations are typically used to determine temperature distribution within any solid domain. The difficulty and complexity of the solution of the equation depend on differential equation characteristics, boundary conditions, coordinate systems, and the number of dependent variables. In the current study, the numerical solution schemes were developed by the Explicit Finite Difference and the Implicit Method- the Crank-Nicolson techniques for the partial differential heat conduction equation including heat generation term described as one-dimensional, time-dependent with the Neumann boundary conditions. The solution schemes were, then, applied to the battery problem including highly varying heat generation. Besides, the solution of the problem was performed by using Matlab pdepe solver to verify the developed schemes. Results suggest that the Crank-Nicolson scheme is unconditionally stable, whereas the explicit scheme is only stable when the Courant-Friedrichs-Lewy condition requirement is less than 0.3404. Comparing the developed schemes to the results obtained from the pdepe solver, the schemes are as reliable as the pdepe solver with certain grid structures. Besides, the developed numerical schemes allow for shorter computational times than the pdepe solver at the same grid structures when considering CPU times.

Keywords: Heat conduction, heat generation, Neumann boundary condition, Crank-Nicolson, pdepe solver.

1. Introduction

Determining the temperature distribution within a solid medium is crucial for various engineering and scientific applications, ranging from the design of efficient heating or cooling systems to predicting material behavior under thermal stress [1]. The partial differential equations (PDEs) of heat conduction represent the mathematical model of the heat conduction phenomena of physical problems defined in the solid domain. Therefore, it serves as a fundamental tool in analyzing such problems and, in turn, offers an insight into how heat propagates over time and spatial direction. However, the analytic solution of the PDEs is possible for the simple problems [2], and/or it requires a quite difficult solution process with different methods [3-5]. In many real problems, solving the PDEs analytically can be challenging due to complex geometries, the number of dependent variables, boundary conditions, etc. In this regard, numerical approaches employing finite difference (FDM) [6], finite element (FEM) [7], and finite volume methods (FVM) [8] offer the approximate solution of the PDEs.

The three methods aim to discretize and solve the PDEs but the discretization methods differ from each other

---

*Corresponding author:
Email: melih.yildiz@igdir.edu.tr

Cite this article as:
Yıldız, M. (2024). Solution scheme development of the nonhomogeneous heat conduction equation in cylindrical coordinates with neumann boundary condition by finite difference method. *European Mechanical Science, 8*(3): 179-190. https://doi.org/10.26701/ems.1469706

History dates:
Received: 17.04.2024, *Revision Request*: 01.07.2024, *Last Revision Received*: 11.07.2024, *Accepted*: 23.07.2024

in these methods. The FDM approximates the PDEs by using a local Taylor expansion while the integral forms of the PDEs are used in the FEM and the FVM. Besides, the FDM uses generally a square grid structure to discretize the PDEs while the FEM and FVM offer to discretize the PDEs defined in more complex geometries [9]. Therefore, the FDM is frequently applied to issues involving regular geometry and is rather easy to apply. There are two main strategies used in numerical methods for solving PDEs: explicit and implicit schemes. The explicit approach updates the unknown function at each grid point by considering known values at each time step and/or grid point, which results in simple algebraic equations. Alternatively, the implicit method uses the values of the unknown function at each grid point for both the current and prior time steps and/or grid points. Thus, the implicit method is computationally more expensive than explicit methods. However, the implicit method offers typically unconditionally stable solutions while the explicit method has a stability restriction. Fine grid structures are needed to overcome the stability issue in the explicit technique, which raises computational costs for particularly stiff problems. In addition to two methods, the Crank-Nicolson method, known as implicit method [10], averages the explicit and implicit methods. As the Crank-Nicolson approach is second-order accurate in time, the solution is more accurate and stable [11].

In many research, the FDM was used for solving the partial differential heat conduction equations. Mojumder et al. [12] analyzed a one-dimensional transient heat conduction equation with Dirichlet boundary conditions in a cartesian coordinate system by using the explicit FDM and the Crank-Nicolson method. They reported that the Crank Nicolson method is unconditionally stable while the explicit scheme is only stable in a certain range of the Courant-Friedrichs-Lewy (CFL) condition criteria. Similarly, using both the explicit and implicit FDM method, Suarez-Carreno and Rosales-Romero [13] examined the one-dimensional transient heat conduction equation with Dirichlet boundary conditions in a cartesian coordinate system. They stated that the accuracy of the methods relies on the time step and grid size, and that the Crank-Nicolson technique is unconditionally stable. Whole et al.[14] implemented the explicit finite difference method for a two-dimensional steady-state heat conduction problem with Dirichlet boundary conditions in cartesian coordinates. They presented that the solutions obtained from the finite difference method have low errors comparing to the analytical solutions. Rieth et al.[15] presented the implicit FDM schemes for the generalized heat conduction equation in one spatial dimension for a shifted field approach. They compared the results with those obtained by the finite element method. They reported that the Crank-Nicolson type implicit scheme resulted in the most accurate. Han and Dai [16] presented the finite difference schemes by combining the Crank-Nicolson method and Richardson extrapolation which are unconditionally stable and provide better accurate solutions for the heat conduction equation with Neumann and Dirichlet boundary conditions in a one-dimensional domain. In the same manner, Yosaf et al.[17] carried out the solving of one-dimensional heat equations with Dirichlet and Neumann boundary conditions by developing a higher-order compact finite difference method. Dai [18] presented an extensive study on the heat conduction equation with Neumann boundary conditions for cartesian, cylindrical, and spherical coordinates by the finite difference schemes combining Crank-Nicolson or higher-order methods. They reported that the developed schemes are unconditionally stable and have high-fidelity solutions.

The literature survey shows that most of the studies using the FDM methods have focused on solving the homogeneous partial differential heat conduction equation, meaning without source term. Besides, the schemes in these studies have been presented mostly in cartesian coordinates. The current study aimed to develop finite difference schemes for the heat conduction problem including highly varying heat generating in cylindrical solid domains like batteries, nuclear fuel rods, etc. Therefore, the explicit finite difference and the Crank-Nicolson finite difference schemes were developed for the non-homogeneous partial differential heat conduction equation with the Neumann boundary conditions. The non-homogenous partial differential equation was also solved by the Matlab built-in function pdepe solver used in many studies [19- 21] to validate the developed schemes with a test problem defined by the determination of temperature distribution through a battery discharge period. Thus, the relative errors of the developed schemes were determined by comparing the results with those obtained from the pdepe solver. Besides, the stability criteria of these schemes were evaluated testing CFL conditions.

2. Model Equations and Finite Difference Scheme Development

Considering the one-dimensional heat conduction in the cylindrical coordinates with initial and Neumann boundary conditions which are axial symmetric boundary at r=0 and the convection heat transfer at r=R in an ambient temperature of T_∞, the governing partial differential heat conduction equation is as follows;

$$\frac{1}{r}\frac{\partial}{\partial r}\left(r\frac{\partial T}{\partial r}\right)+\frac{1}{k}s(r,t)=\frac{1}{\alpha}\frac{\partial T}{\partial t}$$

$$0 < r \le R, 0 < t \le t_s\, , \qquad (1.a)$$

or,

$$\frac{\partial^2 T}{\partial r^2}+\frac{1}{r}\frac{\partial T}{\partial r}+\frac{1}{k}s(r,t)=\frac{1}{\alpha}\frac{\partial T}{\partial t}$$

$$0<r\le R, 0<t\le t_s\,, \qquad (1.b)$$

where, k and α are the thermal conductivity and thermal diffusivity, respectively. s denotes the heat generation or source term.

When examining Equation 1b, it has an indeterminate form 0/0 ratio at r =0 due to the second term (1/r ΔT/Δr). By employing L'Hospital's rule as in Equation 2, Equation 1.b at r =0 becomes Equation 3.

$$\left(\frac{1}{r}\frac{\partial T}{\partial r}\right)_{r=0}=\frac{(\frac{\partial}{\partial r})(\frac{\partial T}{\partial r})}{(\frac{\partial}{\partial r})(r)}=\left.\frac{\partial^2 T}{\partial r^2}\right|_{r=0} \qquad (2)$$

$$2\frac{\partial^2 T}{\partial r^2}+\frac{1}{k}s(r,t)=\frac{1}{\alpha}\frac{\partial T}{\partial t} \qquad r=0, 0<t\le t_s\,, \quad (3)$$

The initial and boundary conditions are given below.

$$T(r,0)=T_\infty, \qquad r\,\epsilon\,[0,R], \qquad (4)$$

$$\frac{\partial T(0,t)}{\partial r}=0, \qquad t\in[0,t_s] \qquad (5.a)$$

$$\frac{\partial T(R,t)}{\partial r}=-\frac{h}{k}[T(R,t)-T_\infty], \qquad t\in[0,t_s] \quad (5.b)$$

Equation 5.a is due to the axial symmetric boundary at r=0, and Equation 5.b implies the convective heat transfer at r=R.

It is now examined the numerical solution schemes development, based on the finite difference method-Explicit method and the Crank Nicolson Implicit method. Let *m* and *k* be the number of nodes on a grid structure for the spatial and time variables, respectively. Thus, the grid steps and the grid structure, Ω as shown in **▶Figure 1**, are defined as follows.

$$\Delta r=\frac{R}{m}\,, \quad \Delta t=\frac{t_s}{k} \qquad (6.a)$$

and,

$$\Omega=\{(r_i,t_\tau):\ r_i=i\Delta r, t_\tau=\tau\Delta t, i=0,1,\dots,m, \tau=0,1,\dots,k\} \qquad (6.b)$$

2.1. Explicit Method

The governing equations require approximations for the first and second derivate in space, and the first derivate in time. By using the first-order forward finite-difference and the second-order centered finite-divided differences formula, the first and second derivate terms are discretized as follows.

The second order centered finite- difference formula:

$$\frac{\partial^2 T}{\partial r^2}\cong\frac{T_{i+1}^{\tau}-2T_i^{\tau}+T_{i-1}^{\tau}}{(\Delta r)^2} \qquad (7)$$

The firs order forward finite- difference formula:

$$\frac{\partial T}{\partial r}\cong\frac{T_{i+1}^{\tau}-T_i^{\tau}}{\Delta r} \qquad (8.a)$$

and,

$$\frac{\partial T}{\partial t}\cong\frac{T_i^{\tau+1}-T_i^{\tau}}{\Delta t} \qquad (8.b)$$

By substituting Eq.7, and Eq.8.a,b into Eq.1.b and Eq.3, the resulting explicit finite-difference approximations become as below.

For Eq.1.b:

$$\frac{T_{i+1}^{\tau}-2T_i^{\tau}+T_{i-1}^{\tau}}{(\Delta r)^2}+\frac{1}{i.\Delta r}\frac{T_{i+1}^{\tau}-T_i^{\tau}}{\Delta r}+\frac{1}{k}s_i^t$$
$$=\frac{1}{\alpha}\frac{T_i^{\tau+1}-T_i^{\tau}}{\Delta t} \qquad for\ \ i>0\ \ (r\neq 0) \qquad (9)$$

For Eq.3:

$$2\frac{T_{i+1}^{\tau}-2T_i^{\tau}+T_{i-1}^{\tau}}{(\Delta r)^2}++\frac{1}{k}s_i^t=\frac{1}{\alpha}\frac{T_i^{\tau+1}-T_i^{\tau}}{\Delta t}$$
$$for\ \ i=0 \quad (r=0) \qquad (10)$$

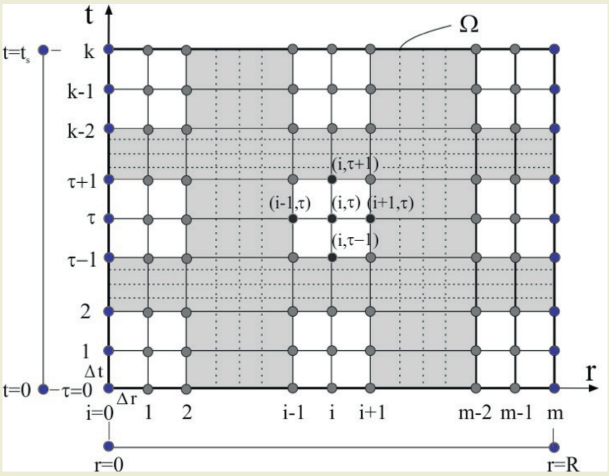

Figure 1. The schematic grid structure for the finite difference discretization

https://doi.org/10.26701/ems.1469706

By arranging Eq.9 and Eq.10,

$$T_i^{\tau+1} = KT_{i-1}^{\tau} + \left[1 - K\left(2 + \frac{1}{i}\right)\right]T_i^{\tau} + K\left(1 + \frac{1}{i}\right)T_{i+1}^{\tau} + \alpha\Delta t G_i^{\tau}\ , \quad for\ 0 < i < m\ \ (r \neq 0) \tag{11}$$

and,

$$T_i^{\tau+1} = 2KT_{i-1}^{\tau} + (1 - 4K)T_i^{\tau} + 2KT_{i+1}^{\tau} + \alpha\Delta t G_i^{\tau}\ ,\ \ for\ \ i = 0\ \ (\ r = 0) \tag{12}$$

where,

$$K = \frac{\alpha\Delta t}{(\Delta r)^2}\ , and\ \ G_i^{\tau} = \frac{1}{k}\ s_i^{\tau} \tag{13}$$

Additionally, the nodes *i-1* and *i+1* are fictitious nodes meaning a fictitious temperature for the defining nodes corresponding to *r=0* and *r=R*. Therefore, by applying a second-order central difference formula to the boundary conditions, the fictitious temperatures are eliminated as follows.

$$\left.\frac{T_{i+1}^{\tau} - T_{i-1}^{\tau}}{2\Delta r}\right|_{r=0} = 0, \quad giving;\ \ T_{i+1}^{\tau} = T_{i-1}^{\tau} \tag{14}$$

$$\left.\frac{T_{i+1}^{\tau} - T_{i-1}^{\tau}}{2\Delta r}\right|_{r=R} = -\frac{h}{k}\,(T_i^{\tau} - T_{\infty}),$$

$$giving;\ \ T_{i+1}^{\tau} = T_{i-1}^{\tau} - \frac{2\Delta rh}{k}T_i^{\tau} + \frac{2\Delta rh}{k}T_{\infty} \tag{15}$$

By introducing Eq.14 into 12, and Eq.15 into 11, the finite difference equations for boundary nodes are obtained as

$$T_i^{\tau+1} = (1 - 4K)T_i^{\tau} + 4KT_{i+1}^{\tau} + \alpha\Delta t G_i^{\tau}\ , \quad for\ \ i = 0\ \ (r = 0) \tag{16}$$

and,

$$T_i^{\tau+1} = K\left(2 + \frac{1}{i}\right)T_{i-1}^{\tau} + \left[1 - K\left(2 + \frac{1}{i}\right) - KH\left(1 + \frac{1}{i}\right)\right]T_i^{\tau} + KH\left(1 + \frac{1}{i}\right)T_{\infty} + \alpha\Delta t G_i^{\tau} \quad for\ \ i = m\ (\ r = R) \tag{17}$$

where, H=2Δrh/k.

Ultimately, the governing equation defined by Eq.1a or 1b with the initial and boundary conditions is solved by the obtained explicit finite difference approximations which are Eq.16 (for boundary node at *r = 0*), Eq.11 (for interior nodes), and Eq.17 (for boundary node at *r =R*). The numerical scheme provides an equation system including *m* algebraic equations for τ number with Δ*t* interval. The equation system is given in the matrix form as follows.

$$\begin{Bmatrix} T_0 \\ T_1 \\ T_2 \\ . \\ . \\ . \\ T_{m-1} \\ T_m \end{Bmatrix}^{\tau+1} = \begin{bmatrix} 1-4K & 4K & \square & \square & \square & \square & \square \\ K & \beta_{1,i} & \beta_{2,i} & \square & \square & \square & \square \\ \square & K & \beta_{1,i} & \beta_{2,i} & \square & \square & \square \\ \square & \square & . & . & . & \square & \square \\ \square & \square & \square & . & . & . & \square \\ \square & \square & \square & \square & K & \beta_{1,i} & \beta_{2,i} \\ \square & \square & \square & \square & \square & \beta_{3,i} & \beta_{4,i} \end{bmatrix} \begin{Bmatrix} T_0 \\ T_1 \\ T_2 \\ . \\ . \\ . \\ T_{m-1} \\ T_m \end{Bmatrix}^{\tau} + \begin{Bmatrix} \alpha\Delta t G_0 \\ \alpha\Delta t G_1 \\ \alpha\Delta t G_2 \\ . \\ . \\ . \\ \alpha\Delta t G_{m-1} \\ \alpha\Delta t G_m + KH(1 + \frac{1}{m}) \end{Bmatrix}^{\tau} \tag{18}$$

where,

$$\beta_{1,i} = 1 - K\left(2 + \frac{1}{i}\right), \beta_{2,i} = K\left(1 + \frac{1}{i}\right),\ \ \beta_{3,i} = K\left(2 + \frac{1}{i}\right),\ \ \beta_{4,i} = 1 - K\left(2 + \frac{1}{i}\right) - KH\left(1 + \frac{1}{i}\right)$$

Thus, Eq.18 is solved up to a given time by starting the initial condition values.

2.2. The Crank Nicolson Method

The explicit finite difference approximations can result in a problem with stability. To overcome the problem, the implicit finite-difference methods are an alternative way that is somewhat more complicated than the explicit method. The simple implicit method is unconditionally stable but limits the use of large-time steps for reasonable accuracy [10]. In this regard, the Crank-Nicolson method presents an implicit scheme that is second-order accurate in both spatial and time. Therefore, it gives a high level of accuracy with a coarser grid in the time. In the current study, the first and second derivate terms were discretized by the Crank-Nicolson method as follows.

$$\frac{\partial^2 T}{\partial r^2} \cong \frac{1}{2}\left[\frac{T_{i+1}^{\tau} - 2T_i^{\tau} + T_{i-1}^{\tau}}{(\Delta r)^2} + \frac{T_{i+1}^{\tau+1} - 2T_i^{\tau+1} + T_{i-1}^{\tau+1}}{(\Delta r)^2}\right] \quad (19)$$

$$\frac{\partial T}{\partial r} \cong \frac{1}{2}\left[\frac{T_{i+1}^{\tau} - T_i^{\tau}}{\Delta r} + \frac{T_{i+1}^{\tau+1} - T_i^{\tau+1}}{\Delta r}\right] \quad (20)$$

$$\frac{\partial T}{\partial t} \cong \frac{T_i^{\tau+1} - T_i^{\tau}}{\Delta t} \quad (21)$$

,and

$$G_i^{\tau+1/2} = \frac{G_i^{\tau+1} + G_i^{\tau}}{2} \quad (22)$$

By substituting Eq.19, Eq.20, Eq.21, and Eq.22 into Eq.1.b and Eq.3, the resulting Crank-Nicolson approximations become as below.

$$\begin{aligned} -\theta T_{i-1}^{\tau+1} + \left[1 + \theta\left(\frac{1}{i} + 2\right)\right] T_i^{\tau+1} - \theta\left(1 + \frac{1}{i}\right) T_{i+1}^{\tau+1} \\ = \theta T_{i-1}^{\tau} + \left[1 - \theta\left(\frac{1}{i} + 2\right)\right] T_i^{\tau} + \theta\left(1 + \frac{1}{i}\right) T_{i+1}^{\tau} \\ + \alpha \Delta t G_i^{\tau+1/2} \\ for\ 0 < i < m\ (r \neq 0) \end{aligned} \quad (23)$$

,and

$$\begin{aligned} K T_{i-1}^{\tau} + (1 - 2K) T_i^{\tau} + K T_{i+1}^{\tau} + \alpha \Delta t G_i^{\tau} \\ = -K T_{i-1}^{\tau+1} + (1 + 2K) T_i^{\tau+1} - K T_{i+1}^{\tau+1} \\ for\ \ i = 0\ \ (\ r = 0) \end{aligned} \quad (24)$$

where, $\theta = K/2 = \alpha\Delta t \,/\, 2(\Delta r)^2$.

By applying boundary conditions to Eq. 23 for the node at $r=R$ (for $i=m$), and to Eq.24 for the node at $r=0$ (for $i=0$), the following finite-difference equations are obtained.

$$\begin{aligned} -\theta(2 + \frac{1}{i}) T_{i-1}^{\tau+1} + \left[1 + \theta(\frac{1}{i} + H\left(1 + \frac{1}{i}\right) + 2)\right] T_i^{\tau+1} \\ = \theta(2 + \frac{1}{i}) T_{i-1}^{\tau} + \left[1 - \theta(\frac{1}{i} + H\left(1 + \frac{1}{i}\right) + 2)\right] T_i^{\tau} \\ + 2\theta H\left(1 + \frac{1}{i}\right) T_{\infty} + \alpha \Delta t G_i^{\tau+1/2} \quad for\ i = m \end{aligned} \quad (25)$$

$$\begin{aligned} (1 + 2K) T_i^{\tau+1} - 2K T_{i+1}^{\tau+1} \\ = (1 - 2K) T_i^{\tau} + 2K T_{i+1}^{\tau} + \alpha \Delta t G_i^{\tau+\frac{1}{2}}\ , \\ for\ i = 0 \end{aligned} \quad (26)$$

Thus, by employing the finite difference equations, Eq. 23, 25, and 26, the equation system in the matrix form is written as,

$$\begin{bmatrix} 1+2K & -2K & \square & \square & \square & \square & \square \\ -\theta & \lambda_{l1,i} & \lambda_{l2,i} & \square & \square & \square & \square \\ \square & -\theta & \lambda_{l1,i} & \lambda_{l2,i} & \square & \square & \square \\ \square & \square & . & . & . & \square & \square \\ \square & \square & \square & . & . & . & \square \\ \square & \square & \square & \square & -\theta & \lambda_{l1,i} & \lambda_{l2,i} \\ \square & \square & \square & \square & \square & \lambda_{l3,i} & \lambda_{l4,i} \end{bmatrix} \left\{ \begin{matrix} T_0 \\ T_1 \\ T_2 \\ . \\ . \\ . \\ T_{m-1} \\ T_m \end{matrix} \right\}^{\tau+1} =$$

$$\begin{bmatrix} 1-2K & 2K & \square & \square & \square & \square & \square \\ \theta & \lambda_{r1,i} & -\lambda_{l2,i} & \square & \square & \square & \square \\ \square & \theta & \lambda_{r1,i} & -\lambda_{l2,i} & \square & \square & \square \\ \square & \square & . & . & . & \square & \square \\ \square & \square & \square & . & . & . & \square \\ \square & \square & \square & \square & \theta & \lambda_{r1,i} & -\lambda_{l2,i} \\ \square & \square & \square & \square & \square & -\lambda_{l3,i} & \lambda_{r4,i} \end{bmatrix} \left\{ \begin{matrix} T_0 \\ T_1 \\ T_2 \\ . \\ . \\ . \\ T_{m-1} \\ T_m \end{matrix} \right\}^{\tau}$$

$$+ \left\{ \begin{matrix} \alpha\Delta t G_0 \\ \alpha\Delta t G_1 \\ \alpha\Delta t G_2 \\ . \\ . \\ . \\ \alpha\Delta t G_{m-1} \\ \alpha\Delta t G_m + 2\theta H\left(1 + \frac{1}{m}\right) T_{\infty} \end{matrix} \right\}^{\tau+1/2} \quad (27)$$

where,

$$\lambda_{l1,i} = 1 + \theta\left(2 + \frac{1}{i}\right), \quad \lambda_{r1,i} = 1 - \theta\left(2 + \frac{1}{i}\right)$$

$$\lambda_{l2,i} = -\theta\left(1 + \frac{1}{i}\right), \quad \lambda_{l3,i} = -\theta\left(2 + \frac{1}{i}\right),$$

$$\lambda_{l4,i} = 1 + \theta\left(\frac{1}{i} + H\left(1 + \frac{1}{i}\right) + 2\right),$$

$$\lambda_{r4,i} = 1 - \theta(\frac{1}{i} + H\left(1 + \frac{1}{i}\right) + 2)$$

By defining the coefficient matrixes and the vectors in the right and left side hand of Eq.27 as [L], [R], {T}, and {Nh}, the equation can be written as follows.

$$[L]\{T\}^{\tau+1} = [R]\{T\}^{\tau} + \{Nh\}^{\tau+1/2} \tag{28}$$

By multiplying both sides of the equation by the inverse of matrix L, Eq.28 becomes in the form as follows,

$$\{T\}^{\tau+1} = [L]^{-1}[R]\{T\}^{\tau} + [L]^{-1}\{Nh\}^{\tau+1/2} \tag{29}$$

As in the explicit method, Eq.29 is solved by starting with initial values for a given time.

3. The pdepe Solver Model

The model equation was also solved using the Matlab built-in function *pdepe* which solves initial-boundary elliptic and parabolic partial differential equation (PDEs), systems in one spatial variable and time. In the pdepe solver, the approximate solution is obtained by integrating the ordinary differential equations (ODEs) in a certain time, emerging with spatial discretization [22].

The general form of the equation in *pdepe* solver is defined as follows [23].

$$c\left(x,t,u,\frac{\partial u}{\partial x}\right)\frac{\partial u}{\partial t} = x^{-m}\frac{\partial}{\partial x}\left(x^{m} f\left(x,t,u,\frac{\partial u}{\partial x}\right)\right) + s\left(x,t,u,\frac{\partial u}{\partial t}\right) \tag{30}$$

When considering the general form for m=1, it resembles Equation 1. a. The variables, u, x correspond to T and r in Equation 1.a. Thus, the functions *c, f,* and *s* are defined as

$$c = \frac{1}{\alpha}\,, \qquad f = \frac{\partial u}{\partial x}\ , and \qquad s = G(x,t) \tag{31}$$

To implement the *pdepe* solver, the initial and boundary conditions are defined in sub-functions with the form as follows.

Initial condition:

$$u(x,0) = u0 = T_{\infty} \tag{32}$$

The *pdepe* solver satisfies the boundary conditions as following equation form.

$$p(x,t,u) + q(x,t)f\left(x,t,u,\frac{\partial u}{\partial x}\right) = 0 \tag{33}$$

Recalling boundary conditions given in Eq.5.a ,b, the *p* and *q* were defined as follows.

$$\begin{aligned} &pl = 0, && ql = 1,\ \ left\ side\ (at\ \ r = 0\ ) \\ &pr = \frac{h}{k}.(ur - T_{\infty}), && qr = 1\ , right\ side\ (at\ \ r = R) \end{aligned} \tag{34}$$

4. Implementation

The developed numerical schemes were applied to a physical model of a cylindrical battery cell to determine time-dependent temperature variation in the radial direction of the cell. The geometric and thermophysical properties are given in ▶**Table 1**. To define the heat source during the discharge period of the cell, the volumetric heat generation was regarded as a time-dependent polynomial function derived from the study performed by Hwang et al.[24]. The equation was obtained at 1C discharging rate meaning that the total simulation time is 3600 s.

$$\begin{aligned} s(t) &= 59116.31 + 58.03t - 0.138t^{2} \\ &+ 1.102\ 10^{-4}t^{3} - 3.75110^{-8}t^{4} \\ &+ 4.683\ 10^{-12}t^{5} \end{aligned} \tag{35}$$

The function values defined by *G* in Eq.13 and Eq.31 were, thus, attained by dividing the *k* value.

To implement the developed solving schemes and the *pdepe* solver for the problem, it was assumed that the initial temperature, T_0 is equal to T_∞ which is the ambient temperature of 25 °C. Furthermore, the convective heat transfer coefficient between the battery surface and the ambient is regarded as 10 W/m^{2}K [25].

Table 1. The battery cell specifications [24, 26]

Properties	**Value**
Radius	9 mm
Density(ρ)	2939 kg/m^3
Conductivity (k)	1.6 W/mK
Specific heat (cp)	2400 j/kg.K
Thermal diffusivity (m^2/s)	2.268 10^{-7} m^2/s

The developed numerical schemes were coded in Matlab and tested with the model defined above. The CFL condition was first investigated for a stable solution of the explicit method. The results were compared in stable conditions with those obtained by the pdepe solver known as the unconditionally stable and high accuracy numerical approach. Moreover, the computational performances of three solution schemes were evaluated in the same grid structures in terms of CPU time.

5. Results

In this section, the stability of the developed schemes, and the results of the numerical schemes implemented for the battery problem in stable condition are presented by comparing them to those obtained from the pdepe solver.

5.1. Stability Evaluation of the Developed Numerical Schemes

Stability in numerical schemes is crucial for obtaining accurate and reliable solutions to mathematical problems. A stable numerical scheme enables accurate and reliable results over time. Otherwise, the numerical scheme amplifies errors or produces wildly fluctuating solutions in unstable conditions. Many techniques have been developed for stability analysis such as von Neumann stability analysis [27], and Courant–Friedrichs–Lewy (CFL) condition [28]. The CFL condition for the numerical schemes of a typical one-dimensional heat conduction equation states that the time step and thermal diffusivity divided by the square of the spatial step size must be less than a certain value for stability [10]. Therefore, the K value given in Eq.13 becomes the criteria for stability investigation.

Figure 2 shows the instability of the explicit scheme for two K values obtained by changing the time step (Δt). As seen in **▶Figure 1a**, the instability at K=0.3714 with Δt=1.64 has a maximum amplitude of fluctuation with an order of 10^{35} and it grows early time stage of the total simulation period. **▶Figure 1b** illustrates that the instability partially alleviates due to decreasing the K value, as the stability both grows later time stage and has lower maximum fluctuation than those of K=0.3714.

To reveal the effect of Δr and Δt together on the instability of the explicit scheme, the solution of the explicit scheme with Δr = 1.1e-3 and Δt=2.06 was tested. Thus, the K value was kept at 0.3689 around the values of the cases in **▶Figure 2**. As seen in **▶Figure 3**, although the time step increases the instability of the solution doesn't result in higher order fluctuation than the case in **▶Figure 2a** due to increasing also the spatial step size.

To determine the CFL condition for the stability of the developed explicit scheme, several trials were tested, ultimately, the stable solution of the explicit scheme was provided in the case of K ≤0.3404 as shown in **▶Figure 4**. Besides, although the solution at K=0.3599 resembles a stable solution it is an inconsistent solution due to the constant temperature values for each a certain time interval.

The thermal diffusivity α also influences the stability. **▶Figure 5** shows the thermal diffusivity effect on the stability. If α becomes 2.55 e-7 m^2/s instead of 2.27e-7 m^2/s, the explicit numerical scheme results in an unstable solution due to increasing K value as seen in **▶Figure 5**. The solution illustrated in **▶Figure 5** proves the CFL condition depends on the *K* value. Consequently, if the CFL condition is not satisfied, an unstable numerical solution leads to non-physical phenomena like oscillations or divergent solutions. The stability criterion of the developed explicit scheme is determined as $0 < K \leq 0.3404$.

Figure 7 verifies the finite difference scheme based on the Crank-Nicolson method to be unconditionally stable as stated in the study [29]. As can be seen in **▶Figure 6** for three different K values by changing the time step, the Crank Nicolson scheme gives stable solutions

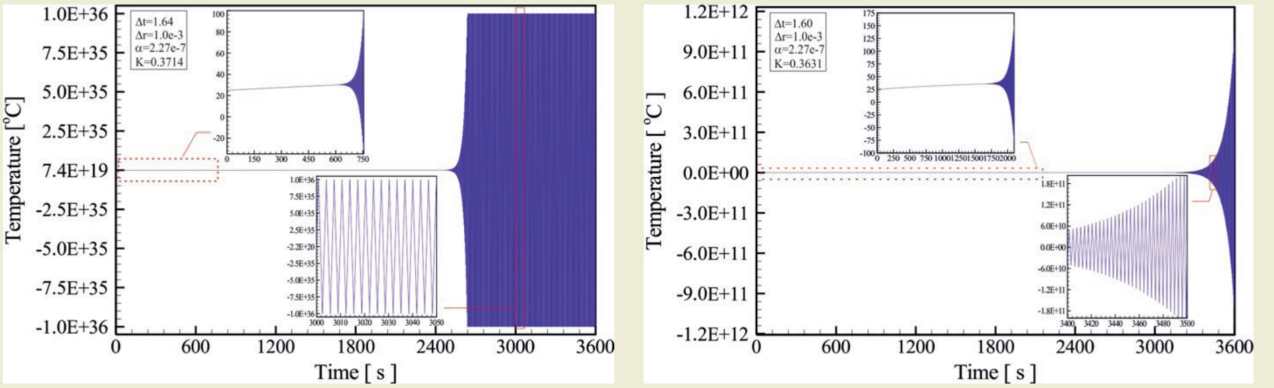

(a) **(b)**

Figure 2. Unstable solution in explicit scheme at spatial domain r= 9 mm **(a)** *K*=0.3714, **(b)** *K*= 0.3631

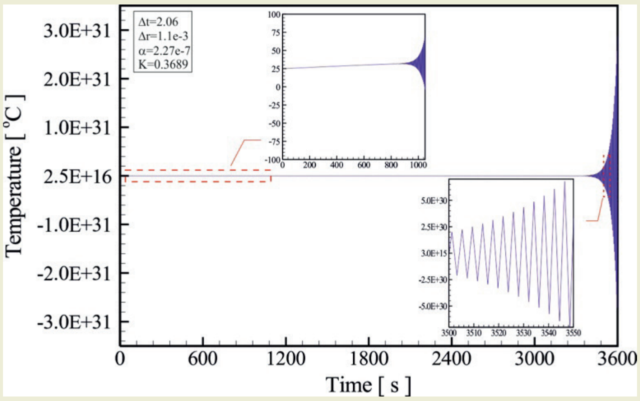

Figure 3. Unstable solution in the explicit scheme for □r=1.1e-3 m and □t=2.06 s at r=9 mm

Table 2. The temperature values obtained from the Crank-Nicolson scheme at t=3600 s for different K values by changing time steps

Time step [s]	Δt=1.0 (K=0.2269)	Δt=4.5 (K=1.0022)	Δt=225 (K=51.0380)
Temperature [°C]	45.9574	45.9575	46.0850

in each case even if the K value is quite greater than the stability criterion of 0.3404 of the explicit scheme. Unsurprisingly, the change in the time step influences the results. It should be also noted that smaller time step allows the more accurate results due to definition of derivate [30]. ▶**Table 2** presents the temperature values at 3600 s and r=9 mm for the Crank Nicolson scheme. The differences in the temperature values relative to Δt=1.0 s are 0.0001 °C and 0.1276 °C for Δt= 4.5 s and 225 s, respectively.

5.2. Comparison of the Numerical Solutions:

The finite difference schemes' results were compared to those obtained from the pdepe solver with the same grid structures in stable conditions. ▶**Figure 7** shows the time-dependent temperature variations at r=9 mm obtained from the numerical methods with the two grid structures. As seen in the Figure, the results of the two schemes developed are nearly identical. Moreover, the results of the schemes approach those of the pdepe solver when the grid structure gets fine size. ▶**Figure 8** also illustrates the absolute error of both the schemes developed relative to the results of the pdepe solver. The absolute error changes in time due to including highly

Table 3. Comparison of temperature values at different radial positions and times (Δr=0.5e-3 m, Δt=0.25 s)

	Temperature [°C]									
	ES	CN	pdepe	$\lvert\Delta T_{ES}\rvert$	$\lvert\Delta T_{CN}\rvert$	ES	CN	pdepe	$\lvert\Delta T_{ES}\rvert$	$\lvert\Delta T_{CN}\rvert$
Time [s]	r=4 mm					r=8 mm				
900	32.1442	32.1439	32.0865	0.0576	0.0574	32.0289	32.0287	31.9731	0.0558	0.0555
1800	36.5474	36.5470	36.5028	0.0446	0.0442	36.3589	36.3585	36.3165	0.0424	0.0420
3600	46.2708	46.2719	46.2761	0.0052	0.0042	45.9261	45.9272	45.9340	0.0078	0.0068

ES: Explicit scheme, CN: Crank Nicolson scheme
$\lvert\Delta T_{ES}\rvert = \lvert T_{pdepe} - T_{ES}\rvert$, $\lvert\Delta T_{CN}\rvert = \lvert T_{pdepe} - T_{CN}\rvert$

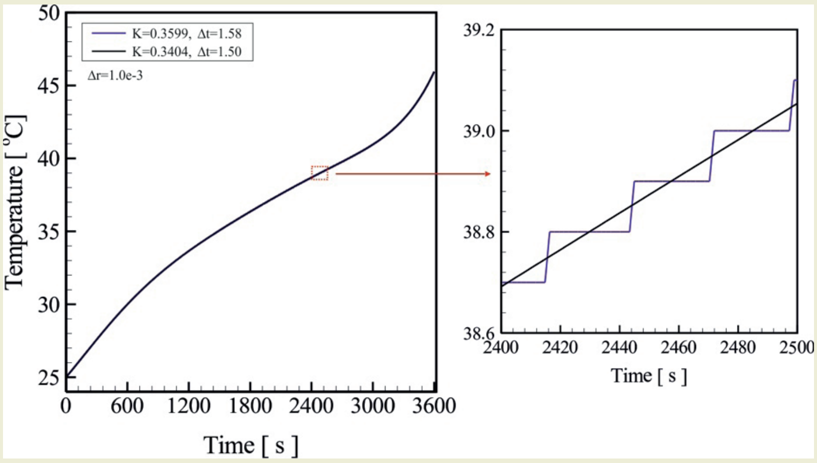

Figure 4. Stable and inconsistence solutions of the developed explicit scheme at r = 9 mm

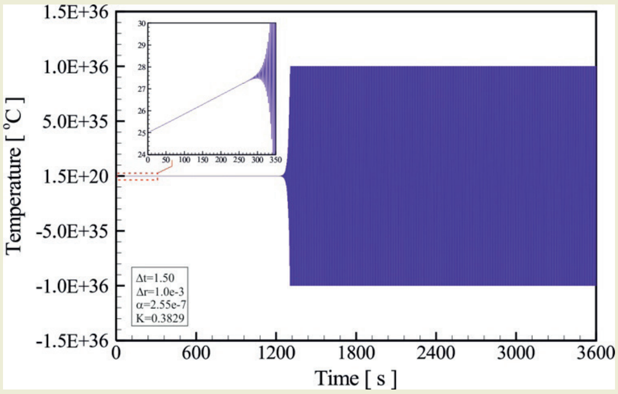

Figure 5. Unstable solution in the explicit scheme with α=2.55e-7

varying time-dependent heat generation terms as given in Eq.35. Thus, the maximum absolute error is about 0.2117 ^{o}C, corresponding to a maximum relative error of 0.43 %, at the grid structure with $\Delta t=1.0$ s and $\Delta r=1.0e-3$ m. In the grid structure of $\Delta t=0.25$ s and $\Delta r=0.5e-3$ m , it is about 0.0859 ^{o}C, corresponding to a maximum relative error of 0.21 %.

Figure 9 shows the results in the radial direction at different times, the difference temperature values between both the explicit and Crank Nicolson schemes are on the order of 10^{-4}. On the other hand, the temperature differences between the developed schemes and the pdepe solver change with time and are on the order of 10^{-2} and 10^{-3}. Similarly, **▶Figure 10** illustrates these results given in **▶Figure 9** in contour plots of the solutions of the defined time-dependent model equation in the radial direction. As shown in the plots in **▶Figure 10**, the differences in temperature distributions are quietly low and they are nearly identical for three numerical solutions at t= 3600 s. Some numerical solutions and absolute errors, relative to the pdepe, are given in **▶Table 3** for different times. The results suggest that the schemes developed are as reliable as the pdepe solver.

To evaluate the computational performance of the ex-

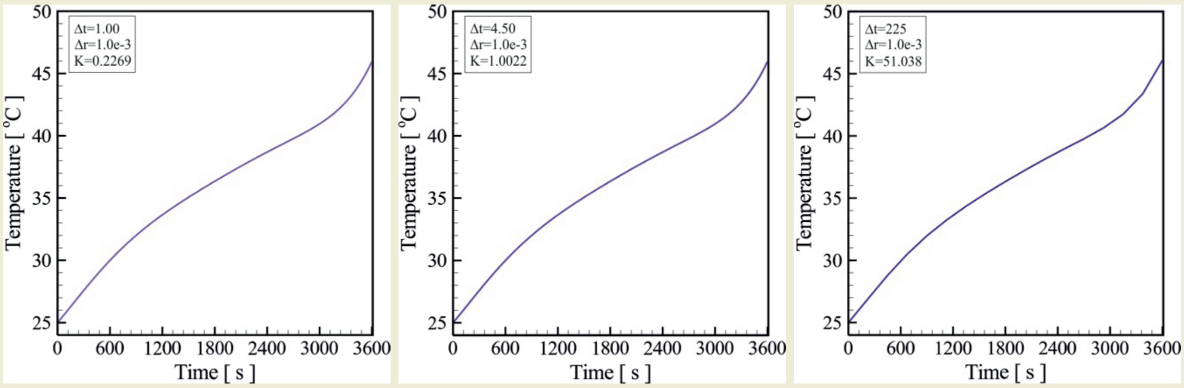

Figure 6. The Crank-Nicolson scheme solutions for different K values at r=9.0 mm

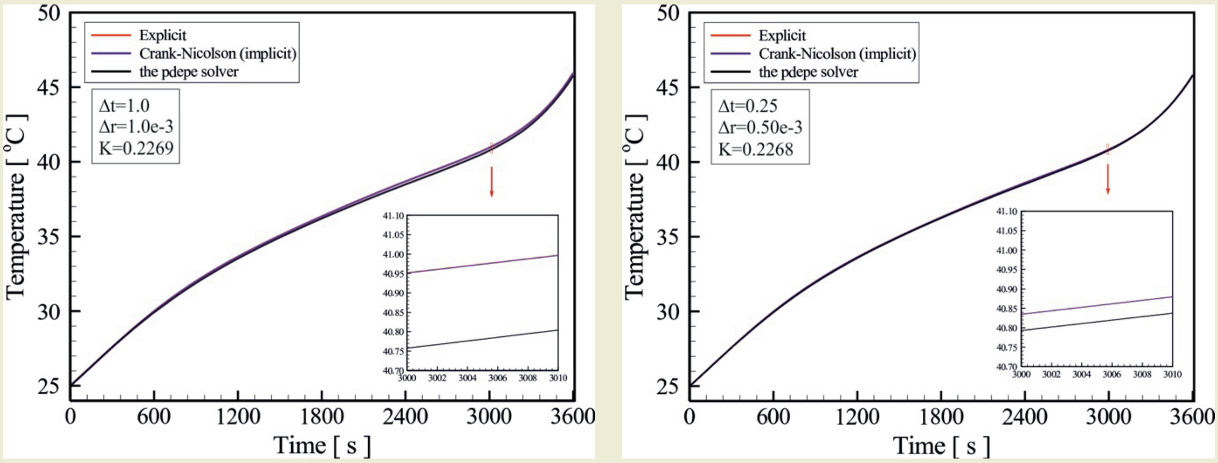

Figure 7. Comparison of the numerical solutions at r=9 mm

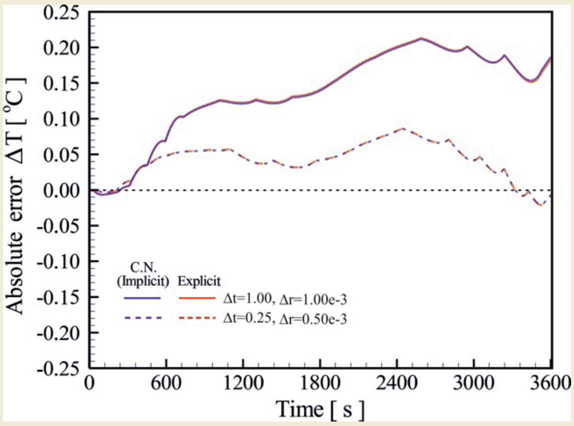

Figure 8. The absolute errors of the explicit and Crank-Nicolson schemes relative to the ***pdepe*** solver at r=9 mm

plicit and Crank-Nicolson FDM schemes in terms of computing time, the CPU times of the developed numerical schemes were compared to those of the pdepe solver in the same grid structures. All computational analyses were performed on a PC with a 2.00 GHz Intel (R) Core ™ i7-2630 CPU and 8 GB RAM. **▶Table 3** presents the CPU times of the numerical schemes.

As shown in **▶Table 4**, the developed explicit and Crank-Nicolson schemes consume fewer CPU times than those of the pdepe solver, as in the reference [31]. Besides, the explicit scheme has the least CPU times for

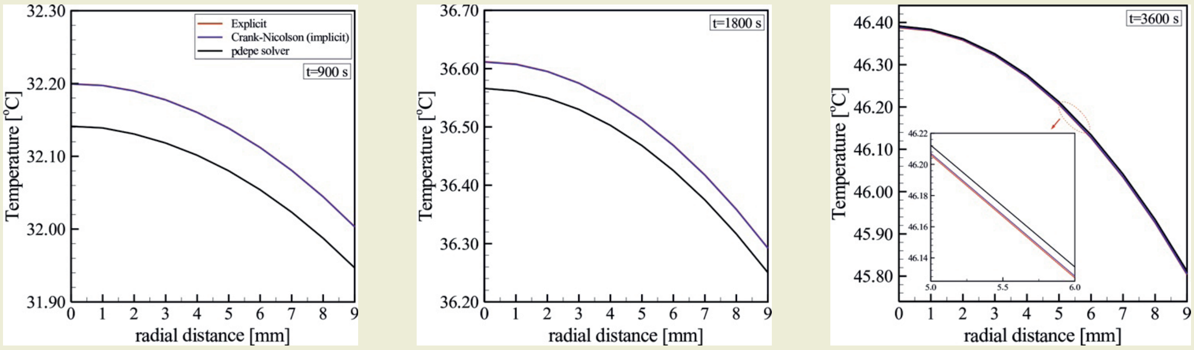

Figure 9. Comparison of the numerical solutions in radial direction at different times（Δr=0.5e-3 m, Δt=0.25 s）

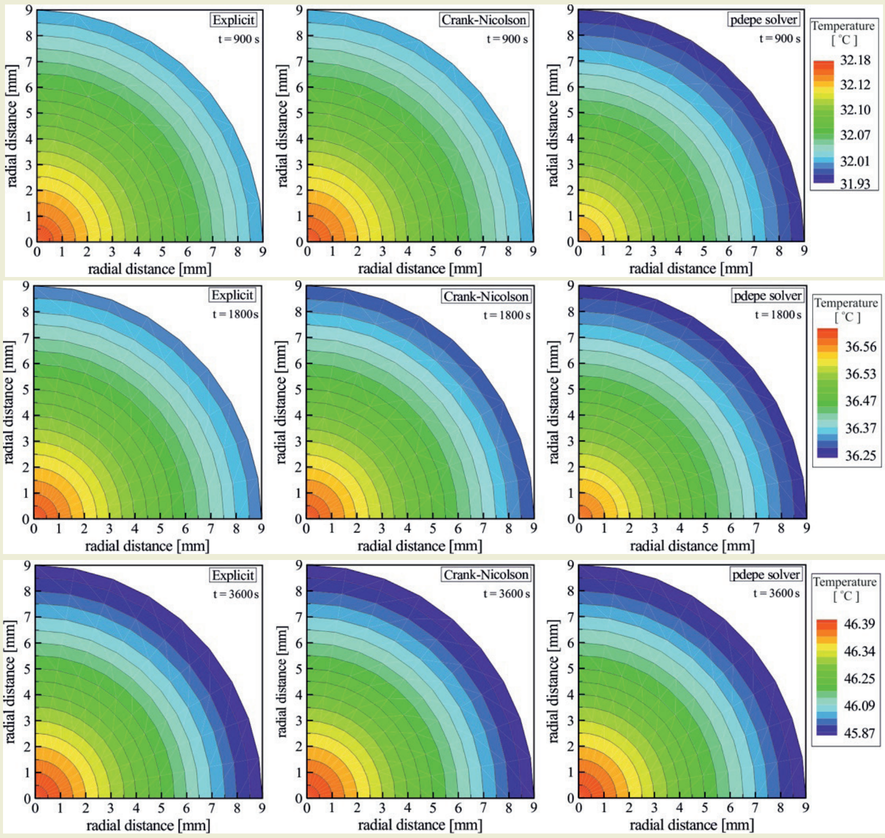

Figure 10. Temperature distribution, Δr=0.5e-3 m, Δt=0.25 s

Table 4. CPU time of the schemes developed and pdepe solver

	Grid structure	Explicit FDM	Crank-Nicolson FDM	Pdepe solver
CPU time [s]	Δr=1e-3, Δt=1.0	0.0342	0.0513	0.5133
	Δr=5e-4, Δt=0.25	0.0693	0.2015	0.8308
	Δr=2.65e-4, Δt=0.1	0.2064	0.9490	1.4283

each grid structure in stable conditions due to its solving scheme consisting of the simpler algebraic equation system.

6. Conclusions

In this research, the explicit and Crank-Nicolson FDM schemes were successfully developed for solving one-dimensional heat conduction equations including heat generation source terms with Neumann boundary conditions in cylindrical coordinates. The numerical schemes were, then, applied to solving the cylindrical battery problem including highly varying heat generation in time. The problem was also solved by the pdepe solver, a Matlab built-in function to verify the numerical schemes. Considering the results, the following main conclusion can be stated.

- The stability requirement for the developed explicit scheme was found to be the condition of $0 \leq K \leq 0.3404$. It is also shown that the developed Crank Nicolson FDM scheme is unconditionally stable with several trials of K values.
- The explicit and Crank Nicolson schemes give nearly identical results with the order of 10^{-4} differences. Comparing the developed schemes to the pdepe solver known as having high accuracy, the maximum relative errors to the pdepe solver results is about 0.21 % with the grid structure of Δt=0.25 s and Δr=0.5 mm.
- The developed schemes enable lower computational time than the pdepe solver when considering CPU time at the same grid structures.

As a general result, the developed schemes are as reliable as the pdepe solver. The numerical schemes can be applied to one-dimensional transient heat conduction problems with/without heat generation source terms, and Neumann boundary conditions in cylindrical coordinates.

Research Ethics

Ethical approval not required.

Author Contributions

The author(s) accept full responsibility for the content of this article and have approved its submission.

Competing Interests

The author(s) declare that there are no competing interests.

Research Funding

Not reported.

Data Availability

Not applicable.

Peer-review

Externally peer-reviewed.

7. References

[1] Çengel, Y. A. (2007). *Heat and mass transfer: A practical approach* (3rd ed.). McGraw-Hill Education.

[2] Götschel, S., & Weiser, M. (2019). Compression challenges in large scale partial differential equation solvers. *Algorithms, 12*(9), 197.

[3] Zada, L., Nawaz, R., Nisar, K. S., Tahir, M., Yavuz, M., Kaabar, M. K. A., & Martinez, F. (2021). New approximate-analytical solutions to partial differential equations via auxiliary function method. *Partial Differential Equations in Applied Mathematics, 4,* 100045.

[4] Chiang, K.-T., Kung, K.-Y., & Srivastava, H. M. (2009). Analytic transient solutions of a cylindrical heat equation with a heat source. *Applied Mathematics and Computation, 215,* 2877–2885.

[5] Cooper, J. (1998). Boundary value problems for heat equations. In *Introduction to partial differential equations with Matlab* (pp. 131–156). Birkhauser. https://doi.org/10.1007/978-1-4612-1754-1_4

[6] Hanafi, L., Mardlijah, M., Utomo, D. B., & Amiruddin, A. (2021). Study numerical scheme of finite difference for solution partial differential equation of parabolic type to heat conduction problem. *Journal of Physics: Conference Series, 1821,* 012032. https://doi.org/10.1088/1742-6596/1821/1/012032

[7] Taler, J., & Oclon, P. (2014). Finite element method in steady-state and transient heat conduction. In *Encyclopedia of thermal stresses* (pp. 1594–1600). Springer. https://doi.org/10.1007/978-94-007-2739-7_897

[8] Li, W., Yu, B., Wang, X., Wang, P., & Sun, S. (2012). A finite volume method for cylindrical heat conduction problems based on local analytical solution. *International Journal of Heat and Mass Transfer, 55,* 5570–5582.

[9] Peiro, J., & Sherwin, S. (2005). Finite difference, finite element and finite volume methods for partial differential equations. In *Handbook of materials modeling* (pp. 2417–2431). Springer. https://doi.org/10.1007/978-1-4020-3286-8_127

[10] Chapra, S. C., & Canale, R. P. (2015). *Numerical methods for engineers* (7th ed.). McGraw-Hill Education.

[11] Huang, P., Feng, X., & Liu, D. (2013). A stabilized finite element method for the time-dependent Stokes equations based on Crank-Nicolson scheme. *Applied Mathematical Modelling, 37,* 1910–1919.

[12] Mojumder, M., Haque, M., & Alam, M. (2023). Efficient finite difference methods for the numerical analysis of one-dimensional heat equation. *Journal of Applied Mathematics and Physics, 11,* 3099–3123. https://doi.org/10.4236/jamp.2023.1110204

[13] Suarez-Carreno, F., & Rosales-Romero, L. (2021). Convergency and stability of explicit and implicit schemes in the simulation of the heat equation. *Applied Sciences, 11,* 4468. https://doi.org/10.3390/app11104468

[14] Han, F., & Dai, W. (2013). New higher-order compact finite difference schemes for 1D heat conduction equations. *Applied Mathematical Modelling, 37,* 7940–7952.

[15] Whole, A., Lobo, M., & Ginting, K. B. (2021). The application of finite difference method on 2-D heat conductivity problem. *Journal of Physics: Conference Series, 2017,* 012009.

[16] Rieth, A., Kovacs, R., & Fülöp, T. (2018). Implicit numerical schemes for generalized heat conduction equation. *International Journal of Heat and Mass Transfer, 126,* 1177–1182.

[17] Yosaf, A., Rehman, S. U., Ahmad, F., Ullah, M. Z., & Alshomrani, A. S. (2016). Eighth-order compact finite difference scheme for 1D heat conduction equation. *Advances in Numerical Analysis,* 2016, Article ID 8376061, 12 pages. https://doi.org/10.1155/2016/8376061

[18] Dai, W. (2010). A new accurate finite difference scheme for Neumann (insulated) boundary condition of heat conduction. *International Journal of Thermal Science, 49,* 571–579.

[19] Kumar, D., Kumar, V., & Singh, V. P. (2010). Mathematical modeling of brown stock washing problems and their numerical solution using Matlab. *Computers & Chemical Engineering, 34,* 9–16.

[20] Li, Y.-X., Mishra, S. R., Pattnaik, P. K., Baag, S., Li, Y.-M., Khan, M. I., Khan, N. B., Alaoui, M. K., & Khan, S. U. (2022). Numerical treatment of time dependent magnetohydrodynamic nanofluid flow of mass and heat transport subject to chemical reaction and heat source. *Alexandria Engineering Journal, 61,* 2484–2491.

[21] Courtier, N. E., Richardson, G., & Foster, J. M. (2018). A fast and robust numerical scheme for solving models of charge carrier transport and ion vacancy motion in perovskite solar cells. *Applied Mathematical Modelling, 68,* 329–348.

[22] Yudianto, D., & Yuebo, X. (2010). A comparison of some numerical method in solving 1-D steady-state advection dispersion reaction equation. *Civil Engineering and Environmental Systems, 27*(2), 155–172.

[23] MathWorks. (n.d.). Partial differential equations. *MathWorks.* Retrieved February 8, 2024, from https://www.mathworks.com/help/matlab/math/partial-differential-equations.html

[24] Hwang, F. S., Confrey, T., Scully, S., Callaghan, D., Nolan, C., Kent, N., & Flannery, B. (2020). Modeling of heat generation in an 18650 lithium-ion battery cell under varying discharge rates. In *5th Thermal and Fluids Engineering Conference* (pp. 333–341). New Orleans, LA, USA.

[25] Wang, Z., Ma, J., & Zhang, L. (2017). Finite element thermal model and simulation for a cylindrical Li-ion battery. *IEEE Access, 5,* 15372–15379.

[26] Gümüşsu, E., Ekici, Ö., & Köksal, M. (2017). 3D CFD modeling and experimental testing of thermal behavior of Li-ion battery. *Applied Thermal Engineering, 120,* 484–495.

[27] Rostamy, D., & Abdollahi, N. (2019). Stability analysis for some numerical schemes of partial differential equation with extra measurements. *Hacettepe Journal of Mathematics & Statistics, 48*(5), 1324–1335.

[28] Trivellato, F., & Castelli, M. R. (2014). On the Courant-Friedrichs-Lewy criterion of rotating grids in 2D vertical-axis wind turbine analysis. *Renewable Energy, 62,* 53–62.

[29] Liu, W., & Wu, B. (2022). Unconditional stability and optimal error estimates of a Crank-Nicolson Legendre-Galerkin method for the two-dimensional second-order wave equation. *Numerical Algorithms, 90,* 137–158. https://doi.org/10.1007/s11075-021-01182-x

[30] Majchrzak, E., & Mochnacki, B. (2017). Implicit scheme of the finite difference method for 1D dual-phase lag equation. *Journal of Applied Mathematics and Computational Mechanics, 16*(3), 37–46.

[31] Khalifa, I. (2020). Comparing numerical methods for solving the Fisher equation (Master's thesis, Lappeenranta-Lahti University of Technology LUT, Finland).

EUROPEAN
MECHANICAL
SCIENCE

Research Article

e-ISSN: 2587-1110

Investigation of monolayer anodized TiO_2 film and bilayer spin coated graphene film on corrosion and tribocorrosion properties of Ti45Nb alloy

Muhammet Taha Acar [1*]

[1]Erzincan Binali Yıldırım University, Faculty of Engineering, Department of Mechanical Engineering, Erzincan, Türkiye

Orcid: M. T. Acar (0000-0002-8367-9623)

Abstract: This study investigates the structural, corrosion, and tribocorrosion properties of Ti45Nb alloy coated with monolayer and bilayer films. Ti45Nb samples were ultrasonically degreased, anodized in a H_2SO_4 and H_3PO_4 solution, and coated with graphene oxide (GO) films via spin coating and subsequent annealing. The anodized samples exhibited anatase and rutile phases, while GO films displayed characteristic Raman shifts indicating graphite oxidation. Corrosion tests in simulated body fluid (SBF) revealed enhanced corrosion resistance in bilayer samples, evidenced by a lower corrosion current density (2.28×10^{-6} A/cm^2) and a higher corrosion potential (10 mV) compared to monolayer and untreated samples. Electrochemical impedance spectroscopy (EIS) indicated superior charge transfer resistance (9.72 Ωcm^2) for bilayer coatings. Tribocorrosion tests demonstrated reduced wear rates and coefficient of friction (COF) in bilayer films, attributed to increased surface hardness and load-carrying capacity. The findings suggest that the bilayer coating significantly enhances the corrosion and tribocorrosion resistance of Ti45Nb, making it a promising material for biomedical applications.

Keywords: Graphene, Thin film, Tribology, Corrosion, TiO_2, Ti45Nb.

1. Introduction

The excellent strength qualities and low specific gravity of titanium and its alloys make them desirable materials for use in several applications [1][2]. Though they vary based on climatic conditions and regions of usage, titanium and its alloys are susceptible to wear and corrosion over time, much like other metals, which results in substantial economic losses [3]. Because of this, a great deal of research has been done on protective coatings that shield metals and alloys from wear and corrosion [4][5]. Titanium and its alloys are particularly well-suited for usage in biomedical applications because of their biocompatibility. Therefore, the development of a cost-effective and biocompatible surface coating has been the main focus of efforts in recent years to improve the resistance to wear and corrosion of titanium and its alloys [6][7].

In comparison to other titanium alloys, Ti45Nb possesses a lower Young's modulus and greater corrosion resistance, rendering it a popular choice for biomedical applications [8]. Numerous experiments have been conducted to improve the wear and corrosion resistance with the surface coating, despite the high corrosion resistance of Ti45Nb material [9]. Because it has been discovered that these qualities become insufficient when simultaneously exposed to wear, corrosion and an acidic environment [10]. In addition, due to their poor tribological performance, residues can accumulate and grow in human tissues and also dissolve in blood. Some health problems, such as inflammation and carcinogenic responses, may occur due to these consequences, and bone loss that may result from this is among the possible possibilities [11].

Oxide-based coatings are commonly utilized to improve

---

*Corresponding author:
Email: taha.acar@erzincan.edu.tr

Cite this article as:
Acar, M. (2024). Investigation of monolayer anodized TiO2 film and bilayer spin coated graphene film on corrosion and tribocorrosion properties of Ti45Nb alloy. *European Mechanical Science, 8*(3): 191-198. https://doi.org/10.26701/ems.1485412

History dates:
Received: 16.05.2024, *Revision Request*: 07.06.2024, *Last Revision Received*: 09.07.2024, *Accepted*: 12.07.2024

the corrosion, tribocorrosion, and wear resistance of Ti45Nb material, as seen in the literature [12]. A review of the literature reveals that many experiments on oxide-based protective coatings use the TiO_2 structure. Because it is known that TiO_2, in addition to having a biocompatible structure, also increases wear resistance and corrosion resistance [13][14]. As a result, it has been noted that a variety of surface treatments, including anodic oxidation, chemical vapor deposition, physical vapor deposition, and sol-gel coating, can produce TiO_2 structure on titanium surfaces [15].

However, monolayer coatings have been replaced by bilayer coatings. Because it is known from experimental research that bilayer coatings have more benefits than monolayer coatings. It has been noted that bilayer coatings exhibit more toughness than nonolayer coatings, that increasing the hardness increases wear resistance, and that the structures in between the layers act as a protective barrier against corrosion [16][17]. Çomaklı et al. [11] created multilayer films with TiO_2-SiO_2 structures on β-type Ti45Nb alloy substrates. As a result, they highlighted that the values of multilayer film-coated substrates were higher than those of untreated substrates in terms of wear resistance, corrosion resistance, and surface hardness. Wei et al. [18] investigated the surface hardness of multilayer structures and found that for samples with multilayer coatings, the maximum hardness was reached approximately 3 times greater than that of the substrate material.

As a result of the analysis of the studies, it was observed that the wear and corrosion resistance of titanium alloys increased with double-layer structures. In order to further increase the wear and corrosion resistance, it is thought that the use of graphene-based structures together with the TiO_2 structure will increase the corrosion and wear resistance of titanium materials to the desired level. In previous studies using graphene-based structures, it was stated that wear and corrosion resistance increased. Chen et al. [19] emphasized that graphene nanolayers well dispersed improved the anti-corrosion performance and wear resistance properties.

In this research, graphene is coated on TiO_2 using a spin coating process, and TiO_2 anodic layer is formed on Ti45Nb by anodization method, which is commonly employed mainly in biomedical applications since it encourages bone formation on titanium surfaces. Examining the corrosion and tribocorrosion characteristics of monolayer TiO_2 and bilayer TiO_2-graphene coatings on Ti45Nb is the aim of this study. The structural characterization of the samples was performed using X-ray diffraction (XRD), Raman spectroscopy, and scanning electron microscopy (SEM) techniques. By using potentiodynamic polarization and open circuit potential (OCP) approaches, electrochemical characteristics were examined and their tribocorrosion characteristics in simulated body fluid (SBF) were investigated and contrasted.

2. Methodology

2.1. Sample preparation

In this study, Ti45Nb samples with their chemical composition as provided in **▶Table 1** were utilized [20]. Ti45Nb samples with dimensions of 1.5*1.5 cm^2 and 3 mm in thickness were ultrasonically degreased in acetone and ethanol for 20 minutes, respectively, then dried after being cleaned one more with an ultrasonic cleaner and distilled water.

Table 1. The chemical composition of Ti45Nb (wt%).

Substrate	Ti	Nb (max)	Others
Ti45Nb	54.69	45.11	0.2

2.2. Experimentation

The electrolytes were utilized to make the anodization solution H_2SO_4 = 0.75 molar and H_3PO_4 = 0.5 molar as described in our previous study [21][22]. Before anodization, the Ti45Nb sample was immersed in HNO_3 for a minute. It was then rinsed with distilled water and dried. A graphite rod served as the negative electrode and a Ti45Nb sample as the positive electrode. During

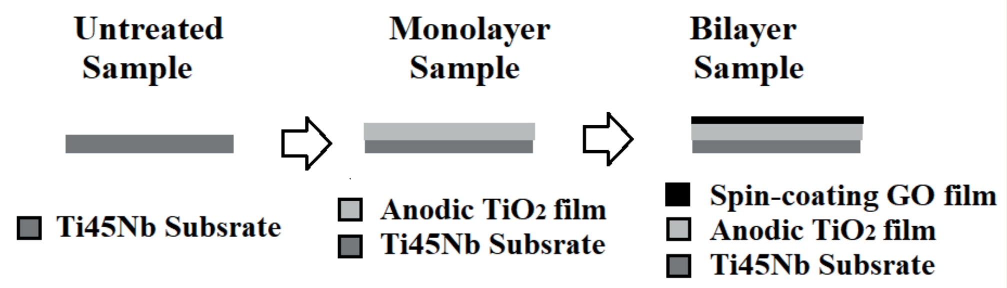

Figure 1. Schematic diagram of the coating processes of the monolayer TiO_2 and bilayer TiO_2-GO films on Ti45Nb samples with anodization and spin-coating methods.

the anodization process, the distance between them was fixed at 30 mm. The anodic layer was formed in the prepared solution by applying a voltage of 200 V to the samples and letting them anodize for 20 minutes at room temperature. After that, the sample was dried and rinsed with distilled water. As shown Fig.1 to make the graphene oxide films (GO), the graphite oxide flakes were dissolved in deionized water at a concentration of 10 mg/ml. The solution was sonicated for thirty minutes, and then it was swirled for two hours. The solution was then spin-coated onto the substrate for 30 seconds at 3500 rpm to form GO film. GO films were then annealed for 30 minutes at 500°C in an argon atmosphere to produce conductive graphene films [23]. All coatings were repeated 3 times to check their reproducibility.

Using a Cu-K (=1.54059) source operated at 40 kV and 30 mA, an XRD-GNR-Explorer X-Ray diffraction apparatus was used to determine the phase of Ti45Nb samples on a 2θ scale spanning from 10° to 80°. By comparing them to the International Diffraction Data Center (ICDD) standard cards, all phases were identified. Using a WITec alpha 300 R instrument with a 532 nm wavelength and 0.3 mWatt of power, the Raman studies were conducted. Using the FEI QUANTA 250 Scanning Electron Microscope, pictures of the top and cross-section were captured. Vickers microhardness measurements were performed using a Buehler Micromet device with an average obtained from five distinct spots and a loading duration of 10 s under a 10 g load.

All experimental parameters used in corrosion and tribocorrosion experiments and the chemical composition of the SBF liquid in which the experiments were carried out are given in our previous study [22].

The GAMRY series G750TM (Gamry Instruments, Warminster, USA) with potentiodynamic polarization was used for the electrochemical investigations. Using a heater, the SBF temperature was set and maintained during the tribocorrosion and corrosion tests. The samples of Ti45Nb underwent corrosion resistance testing at 37 ± 0.5 °C. The three-electrode method was applied in the electrochemical experiments [24]. The reference electrode was Ag/AgCl, and the counter electrode was graphite. The prior study provided the basic test parameters for electrochemical analyses.

At 50% relative humidity, tribocorrosion tests were conducted using the Turkyus PODWT&RWT reciprocating tribotester and electrochemical monitoring apparatus. After potential equilibration, tribocorrosion rubbing experiments were carried out in open-circuit potential settings. The pin was an Al_2O_3 ball with a 6 mm diameter, and 1 N of normal force was applied as for ASTM G133-02. The stroke had a length of 8 mm and a frequency of 1 Hz of reciprocation. A Bruker Contour GT-K1 3D surface profilometer was used to investigate the wear depth. In order to verify the test results, all corrosion and tribocorrosion experiments were repeated 3 times.

3. Results and discussion

3.1. Structural characterization

Fig. 2-a illustrates the XRD patterns for the untreated, monolayer, and bilayer samples. The XRD patterns revealed the presence of β-Ti peaks in the Ti45Nb substrate. It was observed that the monolayer TiO_2 film formed on the substrate during the anodization process consisted of both anatase and rutile phases. Previous investigations, based on XRD data, demonstrated the compatibility of rutile and anatase structures [21]. The presence of GO structures in the XRD spectrum of the bilayer film was confirmed by a broad peak in the range of approximately 24°-25° on Ti45Nb [25].

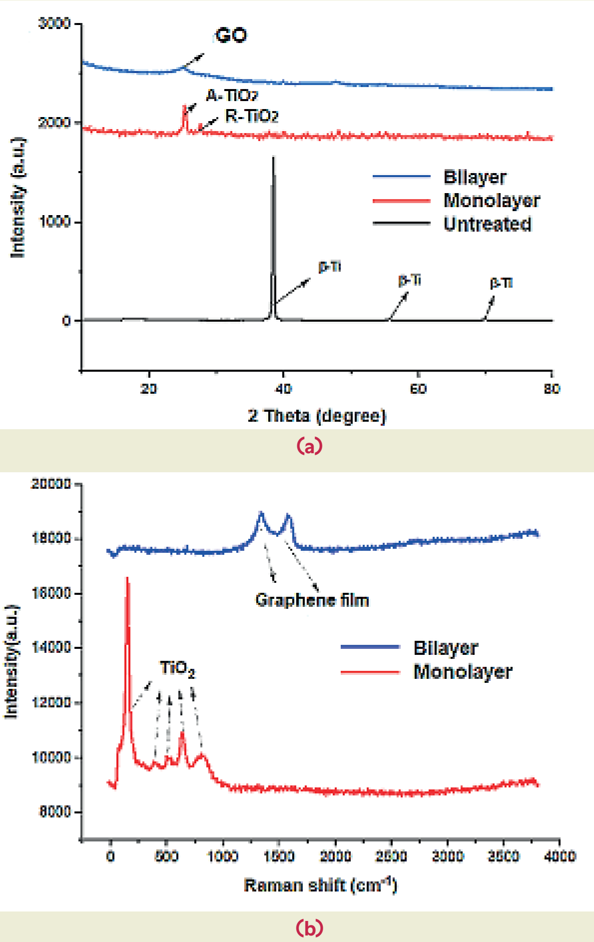

Figyre 2. **(a)** XRD graphs, **(b)** Raman spectra of untreated, monolayer, and bilayer Ti45Nb samples

►**Figure 2-b** displays the Raman spectra of the monolayer and bilayer samples. It can be demonstrated that Raman spectra of the anatase crystal phase exhibit five distinct bands. The maximums were approximately

https://doi.org/10.26701/ems.1485412

144, 196, 391, 514, and 634 cm^{-1}, and they matched the active modes Eg(1), Eg(2), B1g, A1g, and Eg(3) respectively. Because the Raman spectra only show the bulk material and not the pores in the structures formed in the anodic films, where the rutile phase is concentrated near the open pores, they only show the anatase phase. All anodized Ti45Nb samples have the anatase phase as the primary phase, according to Raman spectra. ►**Figure 2**-b GO Raman spectra show the shift in GO structure brought on by graphite oxidation, with the G (sp^2) band corresponding to structures. Conversely, oxidation results in uneven, amorphous structures in the D (sp^3) band. The GO G-band and D-band are visible at 1595 cm^{-1}and 1360 cm^{-1}, respectively. In graphite, the G-band is present in all sp2 carbon systems due to the stretching of the C-C bond. Structural flaws resulting from epoxy and hydroxyl group attachment to the GO basal plane give rise to the D-band [26].

Figure 3 presents cross-sectional view images of the bilayer sample and top-view SEM images of the untreated, monolayer, and bilayer samples. The sample exhibits small open pores on its surface following anodization. The formation of micropores is consistent with prior

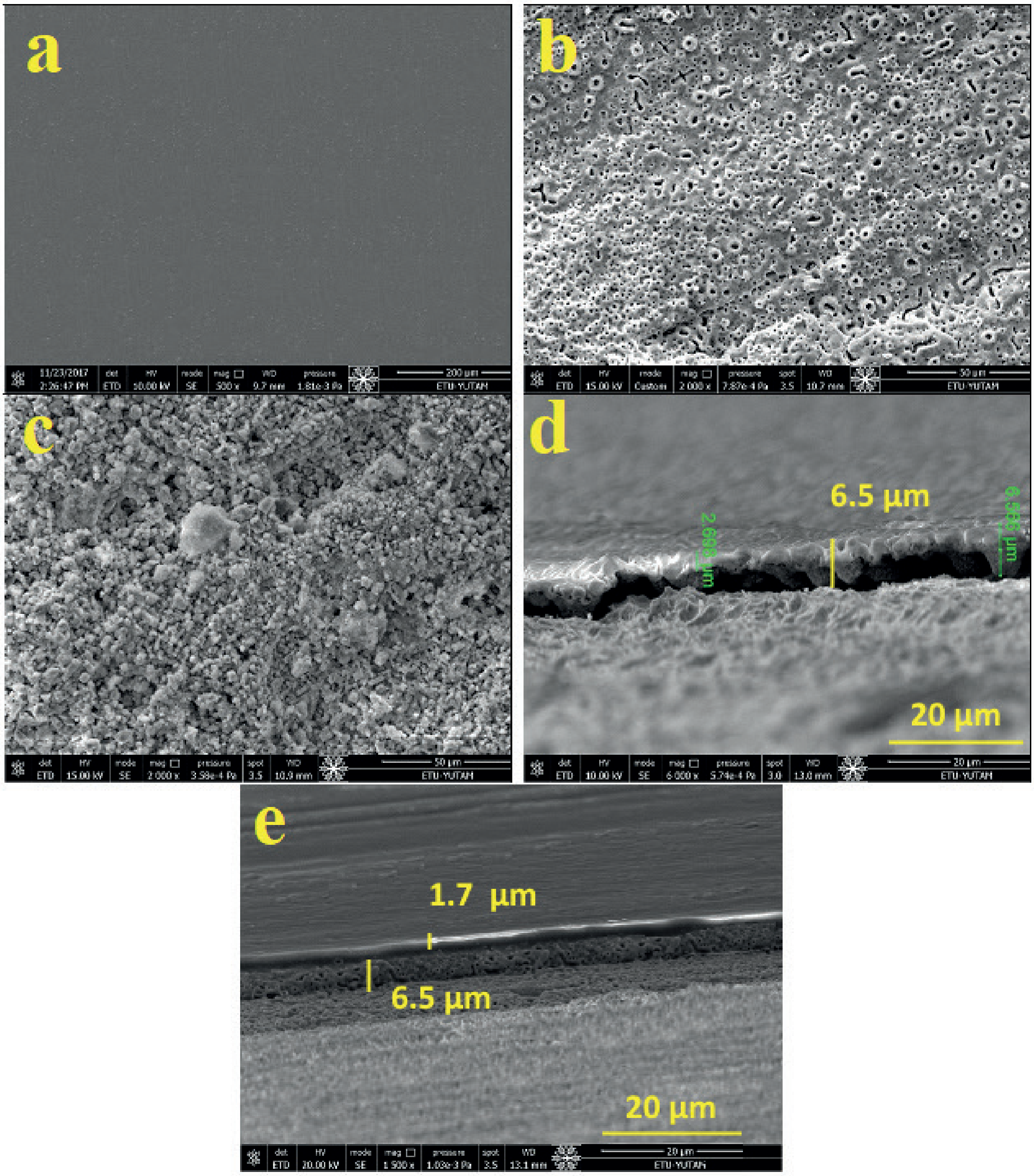

Figure 3. SEM images of **(a)** untreated, **(b)** monolayer, and **(c)** bilayer Ti45Nb samples **(d)** cross-section SEM image of monolayer sample and **(e)** cross-section SEM image of bilayer sample

studies [21]. It is evident from the SEM image that there are additional nanopores formed due to the presence of oxygen. Nanopores are generated during the anodizing process when oxygen bubbles form as a result of the oxidation reaction [27]. The SEM image of the graphene structure fabricated on TiO_2 using the spin coating technique reveals a change in surface morphology. It is hypothesized that the action of centrifugal force induces dense clustering of graphene structures around open pores. Analysis of the cross-section SEM image indicated a thickness of 1.7 µm for the graphene film, while the TiO_2 anodic layer measured 6.5 µm.

3.2. Corrosion experiment

The potentiodynamic polarization curves for untreated, monolayer, and bilayer materials in SBF solution are depicted in ▶**Figure 4-a**. These curves were obtained through electrochemical testing. ▶**Table 2** presents the

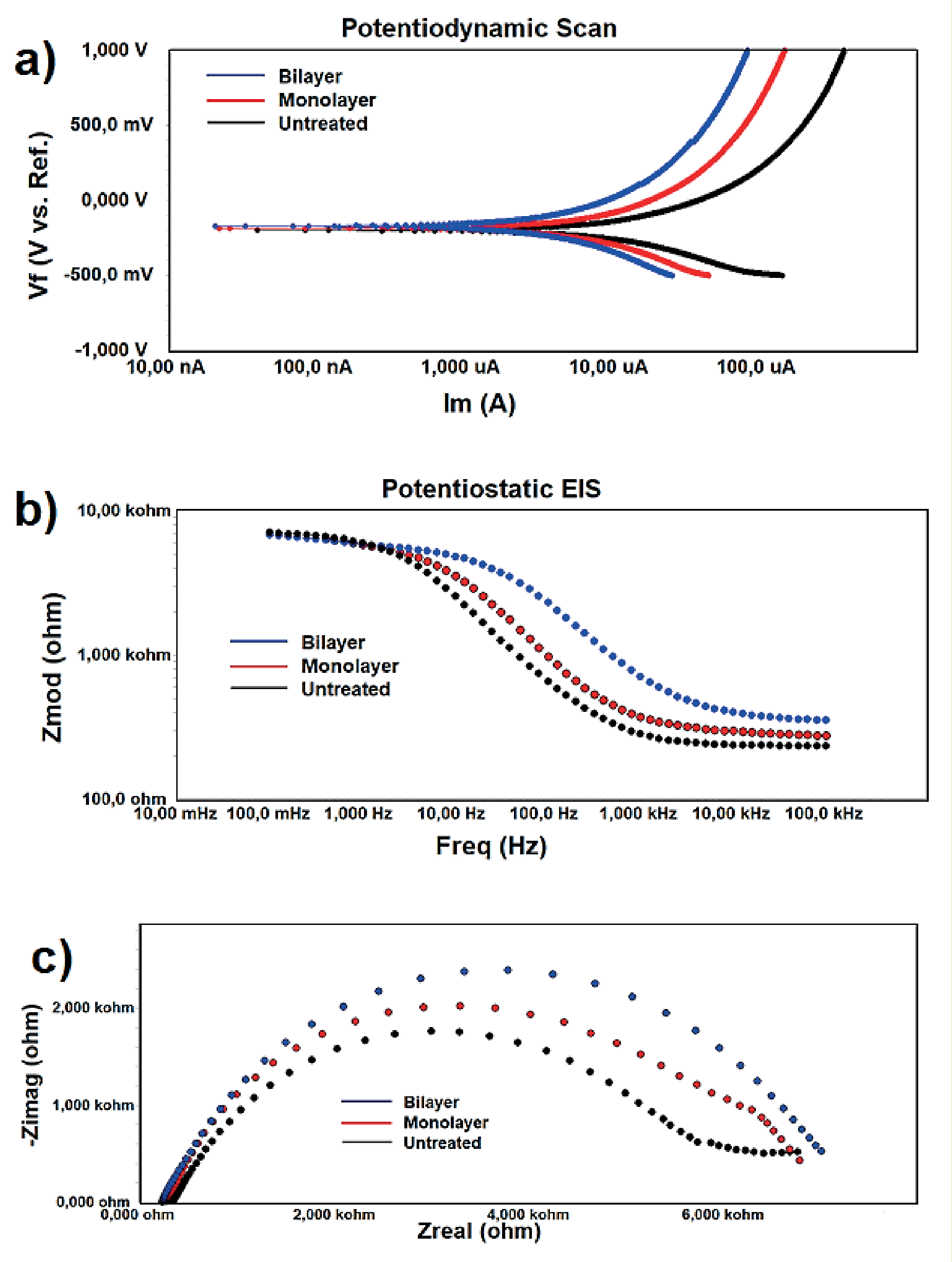

Figure 4. **(a)** Potentiodynamic polarization curves, **(b)** Bode, and **(c)** Nyquist plots of untreated, monolayer, and bilayer Ti45Nb samples

corrosion potential (Ecorr) and corrosion current density (Icorr) values derived from the polarization curves. Lower Icorr values and higher Ecorr values indicate greater corrosion resistance [28]. When compared to untreated samples, both monolayer and bilayer samples demonstrate higher corrosion current density and lower corrosion potential. In contrast, the bilayer sample exhibits lower corrosion Icorr ($2.28 x10^{-6}$ A/cm^2) and greater positive Ecorr (10 mV) values than the monolayer sample. The bilayer sample exhibits the best corrosion resistance due to its greater film thickness, which creates an interface acting as a barrier, thereby preventing contact between the SBF liquid and the Ti45Nb substrate [29].

The Bode and Nyquist plots are presented in **▶Figure 4-b** and **▶Figure 4-c**, respectively. The results of the simulated EIS are shown in **▶Table 2**. The charge transfer resistance (Rct) is a critical parameter for assessing a electrochemistry of samples. It represents the rate of corrosion between the coating and the substrate [30]. Due to the thinner oxide layer on untreated Ti45Nb compared to anodized samples, the Rct is lower. Additionally, the presence of anatase and rutile oxide enhances the performance of anodized samples as insulators with lower capacitance. When the corrosion resistance of the bilayer film (9.72 Ωcm^2) is compared with the corrosion resistance of the monolayer film (6.56 Ωcm^2), it has been discovered that the corrosion resistance of the bilayer film is higher. It has been established that in this case, the interlayer spacing and film thickness play significant roles in corrosion resistance [31]. As a result, the bilayer coating displayed maximum corrosion resistance, making it more challenging for SBF to reach the substrate.

3.3. Tribocorrosion experiment

The open circuit potential (OCP) graphs of the untreated, monolayer, and bilayer Ti45Nb samples are depicted in Fig. 5-a. Initially, during the rubbing process, the OCP curve of the untreated sample exhibited the largest reduction compared to the other samples once the system reached equilibrium. This reduction in OCP values (-650mV) for the untreated Ti45Nb sample was attributed to damage caused to the natural oxide film by the surface treatment. OCP values of -150 mV and -40 mV were observed for the monolayer and bilayer samples, respectively. It was observed that after the onset of the friction process, the OCP values of the monolayer sample decreased at a slower rate compared to those of the untreated sample. As expected, the rubbing action on the bilayer film resulted in the highest average OCP values.

The average COF for the untreated sample ranged between 0.35 and 0.45. Average COF values ranging from 0.26 to 0.36 were obtained in the monolayer film. Additionally, the lowest average COF values were obtained from the bilayer film, ranging from 0.17 to 0.22. The higher COF values observed in the untreated sample are associated with the breakdown of the oxide layer on pure titanium alloys due to wear and corrosion, resulting in residues that cause abrasive wear [32].

As seen in **▶Figure 5-b** and **▶Figure 5-c** the untreated sample has the highest wear rate ($0.72 x10^{-3}$ mm^3/Nm), whereas the bilayer sample has the lowest wear rate ($0.12 x10^{-3}$ mm^3/Nm). In addition to the formation of an interface between the bilayer films serving as a protective barrier against corrosion, their higher load-carrying capacity has increased the tribocorrosion resistance of the bilayer film. The presence of the interface was found to enhance the load-carrying capacity of bilayer coatings compared to monolayer films in previous studies [11]. The bilayer surfaces prevent dislocation and reduce the system's plastic deformation, thereby increasing its hardness. According to Archard's rule, higher surface hardness reduces the contact between the wear ball and the films, resulting in the minimum wear rate being achieved in the bilayer film with maximum hardness [33].

Consequently, the influence of increasing layer thickness and obtained surface hardness on corrosion and tribocorrosion resistance is evident when Fig. 3-c and **▶Table 2** are compared. However, the advantages gained in the bilayer film have a greater impact here. According to the literature, the interlayer in the bilayer coating enhanced resistance to corrosion and tribocorrosion by lowering internal tensions, allowing displacement movement, and exhibiting a barrier effect against corrosion [34].

4. Conclusions

In this study, the corrosion and tribocorrosion resistance of Ti45Nb samples coated with graphene oxide (GO) films were systematically investigated.

Table 2. Results of tests performed on all samples for film thickness, hardness, corrosion, and tribocorrosion.

	E_{corr} (mV)	i_{corr} (x10–^{6}A/cm^2)	Rct (Ωcm^2)	Film thickness (μm)	Hardness ($HV_{0.1}$)	COF	Wear rate (x10^{-3} mm^3/Nm)
Bilayer	10	2.28	9.72	6.5+1.7	1270	0.17-0.22	0.14
Monolayer	-163	40.24	6.56	6.5	765	0.26-0.36	0.58
Untreated	-285	72.86	3.84	-	378	0.35-0.45	0.72

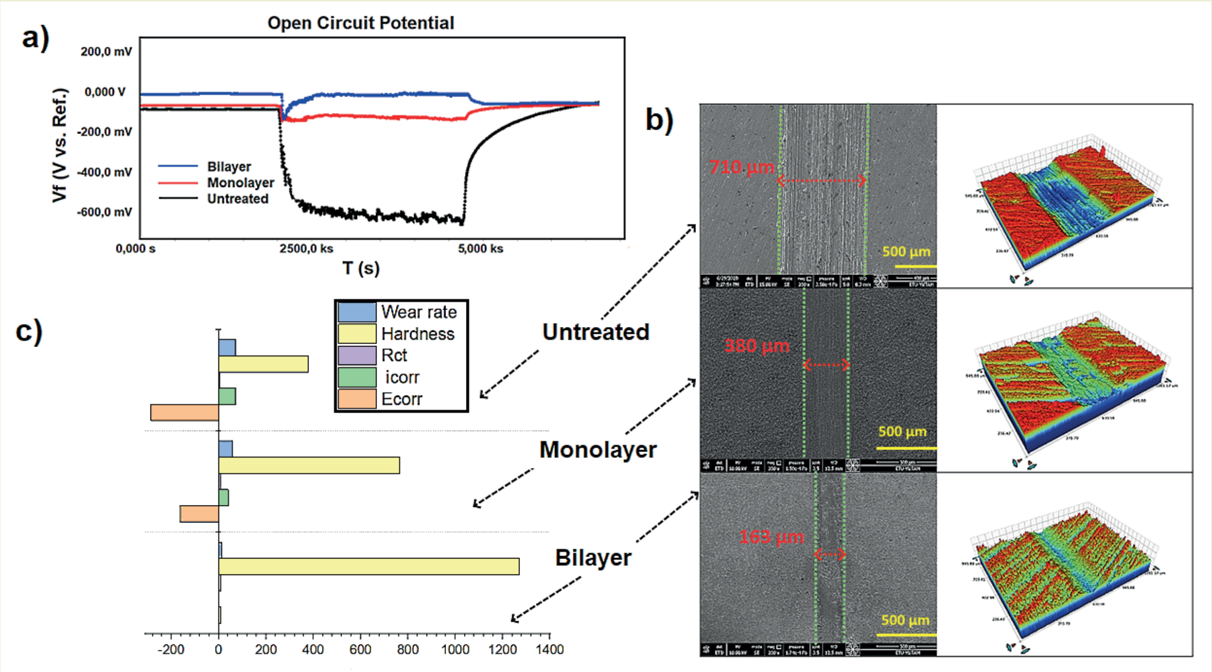

Figure 5. (a) Open circuit potential, **(b)** 3D profilometer and SEM images **(c)** graphical presentation of the all data of untreated, monolayer, and bilayer Ti45Nb samples

- The results demonstrated that the bilayer GO films exhibited superior corrosion resistance compared to monolayer films and untreated samples. This enhanced performance is attributed to the increased film thickness and the presence of an interfacial layer, which acts as an effective barrier against simulated body fluid (SBF) penetration.

- The XRD and Raman spectroscopy analyses confirmed the formation of anatase and rutile phases in the anodized TiO_2 layer and the successful incorporation of GO structures in the bilayer films.

- The electrochemical tests revealed that the bilayer samples exhibited the lowest corrosion current density (Icorr) and the most positive corrosion potential (Ecorr), indicating their excellent corrosion resistance.

- The tribocorrosion experiments further validated these findings, with the bilayer samples showing the highest open circuit potential (OCP) and the lowest coefficient of friction (COF) and wear rate. The significant reduction in wear rate and improved tribocorrosion resistance are due to the enhanced load-carrying capacity and hardness provided by the bilayer films.

These results contribute to the growing body of knowledge on the use of graphene-based coatings in enhancing the performance of biomedical implants, paving the way for further innovations in the field of biomaterials engineering.

Research Ethics

Ethical approval not required.

Author Contributions

All authors contributed to the study conception and design. Material preparation, data collection and analysis were performed by [M. Taha ACAR].

Conflicts of interests

The authors declare that they have no known competing financial interests or personal relationships that could have appeared to influence the work reported in this paper.

Research Funding

Not reported.

Data availability

Data supporting this study are included within the article.

Peer-review

Externally peer-reviewed.

References

[1] Boyer, R. R. (1996). An overview on the use of titanium in the aerospace industry. *Materials Science and Engineering: A, 213*, 103–114.

[2] Acar, M. T. (2023). Investigation of surface wettability, corrosion and tribocorrosion behavior of machined, etched, blasted and anodized Cp-Ti samples. *MRS Communications, 13*, 587–593. https://doi.org/10.1557/s43579-023-00387-6

[3] Geetha, M., Singh, A. K., Asokamani, R., & Gogia, A. K. (2009). Ti based biomaterials, the ultimate choice for orthopaedic implants–a review. *Progress in Materials Science, 54*, 397–425.

[4] Hoque, M. A., Yao, C.-W., Lian, I., Zhou, J., Jao, M., & Huang, Y.-C. (2022). Enhancement of corrosion resistance of a hot-dip galvanized steel by superhydrophobic top coating. *MRS Communications, 12*, 415–421.

[5] Guo, C., Kang, T., Wu, S., Ying, M., Liu, W. M., & Chen, F. (2021). Microstructure, mechanical, and corrosion resistance of copper nickel alloy fabricated by wire-arc additive manufacturing. *MRS Communications, 11*, 910–916.

[6] Bandyopadhyay, A., Bose, S., & Narayan, R. (2022). Translation of 3D printed materials for medical applications. *MRS Bulletin, 47*, 39–48.

[7] Rathnakumar, S., Bhaskar, S., Badiya, P. K., Sivaramakrishnan, V., Srinivasan, V., & Ramamurthy, S. S. (2023). Electrospun PVA nanofibers doped with titania nanoparticles in plasmon-coupled fluorescence studies: An eco-friendly and cost-effective transition from 2D nano thin films to 1D nanofibers. *MRS Communications, 13*, 290–298.

[8] Comakli, O. (2020). Influence of CrN, TiAlN monolayers and TiAlN/CrN multilayer ceramic films on structural, mechanical and tribological behavior of β-type Ti45Nb alloys. *Ceramics International, 46*, 8185–8191.

[9] Çomaklı, O. (2021). Improved structural, mechanical, corrosion and tribocorrosion properties of Ti45Nb alloys by TiN, TiAlN monolayers, and TiAlN/TiN multilayer ceramic films. *Ceramics International, 47*, 4149–4156.

[10] Laketić, S., Rakin, M., Momčilović, M., Ciganović, J., Veljović, D., & Cvijović-Alagić, I. (2021). Influence of laser irradiation parameters on the ultrafine-grained Ti45Nb alloy surface characteristics. *Surface and Coatings Technology, 418*, 127255.

[11] Çomaklı, O., Yazıcı, M., Demir, M., Yetim, A. F., & Çelik, A. (2023). Effect of bilayer numbers on structural, mechanical, tribological and corrosion properties of TiO2–SiO2 multilayer film-coated β-type Ti45Nb alloys. *Ceramics International, 49*, 3007–3015.

[12] Zorn, G., Lesman, A., & Gotman, I. (2006). Oxide formation on low modulus Ti45Nb alloy by anodic versus thermal oxidation. *Surface and Coatings Technology, 201*, 612–618.

[13] Yin, J., Chu, Y., & Tan, L. (2023). Cu/N co-doped TiO2 nanopowder with high antibacterial activity under visible light. *MRS Communications*. https://doi.org/10.1557/s43579-023-00377-8

[14] Krishna, D. S. R., & Sun, Y. (2005). Thermally oxidised rutile-TiO2 coating on stainless steel for tribological properties and corrosion resistance enhancement. *Applied Surface Science, 252*, 1107–1116.

[15] Kulkarni, M., Mazare, A., Schmuki, P., Iglič, A., & Seifalian, A. (2014). Biomaterial surface modification of titanium and titanium alloys for medical applications. Nanomedicine, *111*, 111.

[16] PalDey, S., & Deevi, S. C. (2003). Single layer and multilayer wear resistant coatings of (Ti, Al) N: A review. *Materials Science and Engineering: A, 342*, 58–79.

[17] Ding, Z., Zhou, Q., Wang, Y., Ding, Z., Tang, Y., & He, Q. (2021). Microstructure and properties of monolayer, bilayer and multilayer Ta2O5-based coatings on biomedical Ti-6Al-4V alloy by magnetron sputtering. *Ceramics International, 47*, 1133–1144.

[18] Wei, Y., & Gong, C. (2011). Effects of pulsed bias duty ratio on microstructure and mechanical properties of TiN/TiAlN multilayer coatings. *Applied Surface Science, 257*, 7881–7886.

[19] Chen, W., Yang, Y., Zhao, Q., Liu, X., & Fu, Y.-Q. (2022). Nanoscale mechanics of metal-coated graphene nanocomposite powders. *Materials Today Communications, 33*, 104731.

[20] Acar, M. T., Kovacı, H., & Çelik, A. (2022). Comparison of the structural properties, surface wettability and corrosion resistance of TiO2 nanotubes fabricated on Cp-Ti, Ti6Al4V and Ti45Nb. *Materials Today Communications, 33*, 104396.

[21] Acar, M. T., Kovacı, H., & Çelik, A. (2022). Improving the wettability and corrosion behavior of Cp-Ti by applying anodization surface treatment with the addition of boric acid, graphene oxide and hydroxyapatite. *Materials Today Communications, 31*, 103683. https://doi.org/10.1016/j.mtcomm.2022.103683

[22] Acar, M. T. (2024). Analyzing the corrosion and tribocorrosion performances of monolayer TiO2 and bilayer TiO2-SiO2 coatings at different SBF temperatures. *Physica Scripta, 99*, 025910.

[23] Umar, M. I. A., Yap, C. C., Awang, R., Salleh, M. M., & Yahaya, M. (2014). The effect of spin-coated polyethylene glycol on the electrical and optical properties of graphene film. *Applied Surface Science, 313*, 883–887.

[24] Salasi, M., Stachowiak, G. B., & Stachowiak, G. W. (2011). Three-body tribocorrosion of high-chromium cast irons in neutral and alkaline environments. *Wear, 271*, 1385–1396. https://doi.org/10.1016/j.wear.2011.01.066

[25] Wang, Y., Wang, S., Wu, Y., Wang, Z., Zhang, H., Cao, Z., He, J., Li, W., Yang, Z., & Zheng, L. (2021). A α-Fe2O3/rGO magnetic photocatalyst: Enhanced photocatalytic performance regulated by magnetic field. *Journal of Alloys and Compounds, 851*, 156733.

[26] Oktay, A., Yilmazer, H., Przekora, A., Yilmazer, Y., Wojcik, M., Dikici, B., & Ustundag, C. B. (2023). Corrosion response and biocompatibility of graphene oxide (GO) serotonin (Ser) coatings on Ti6Al7Nb and Ti29Nb13Ta4.6Zr (TNTZ) alloys fabricated by electrophoretic deposition (EPD). *Materials Today Communications, 34*, 105236.

[27] Li, X., Li, C., Gong, T., Su, J., Zhang, W., Song, Y., & Zhu, X. (2021). Comparative study on the anodizing process of Ti and Zr and oxide morphology. *Ceramics International, 47*, 23332–23337.

[28] Mansfeld, F., Liu, G., Xiao, H., Tsai, C. H., & Little, B. J. (1994). The corrosion behavior of copper alloys, stainless steels and titanium in seawater. *Corrosion Science, 36*, 2063–2095.

[29] Marcus, P., Maurice, V., & Strehblow, H.-H. (2008). Localized corrosion (pitting): A model of passivity breakdown including the role of the oxide layer nanostructure. *Corrosion Science, 50*, 2698–2704.

[30] Dehri, I., & Erbil, M. (2000). The effect of relative humidity on the atmospheric corrosion of defective organic coating materials: An EIS study with a new approach. *Corrosion Science, 42*, 969–978.

[31] Volovitch, P., Vu, T. N., Allély, C., Aal, A. A., & Ogle, K. (2011). Understanding corrosion via corrosion product characterization: II. Role of alloying elements in improving the corrosion resistance of Zn-Al-Mg coatings on steel. *Corrosion Science, 53*, 2437–2445.

[32] Khan, M. A., Williams, R. L., & Williams, D. F. (1999). Conjoint corrosion and wear in titanium alloys. Biomaterials, *20*, 765–772.

[33] Acar, M. T., Kovacı, H., & Çelik, A. (2022). Investigation of corrosion and tribocorrosion behavior of boron doped and graphene oxide doped TiO2 nanotubes produced on Cp-Ti. *Materials Today Communications, 32*, 104182.

[34] Çomaklı, O. (2021). Improved structural, mechanical, corrosion and tribocorrosion properties of Ti45Nb alloys by TiN, TiAlN monolayers, and TiAlN/TiN multilayer ceramic films. *Ceramics International, 47*, 4149–4156.

EUROPEAN MECHANICAL SCIENCE

Review Article

e-ISSN: 2587-1110

A critical review of composite filaments for fused deposition modeling: Material properties, applications, and future directions

Arslan Kaptan[1*], **Fuat Kartal**[2]

[1]Sivas Cumhuriyet University, Sivas Technical Sciences Vocational School, Motor Vehicles and Transportation Technologies Department, Türkiye
[2]Kastamonu University, Engineering and Architecture Faculty, Mechanical Engineering Department, Türkiye

Orcid: A. Kaptan (0000-0002-2431-9329), F. Kartal (0000-0002-2567-9705)

Abstract: This review paper provides a comprehensive analysis of recent advancements in the development and application of composite filaments for fused deposition modeling (FDM) 3D printing technology. Focusing on the integration of various materials such as nano-fillers, fibers, and bio-based polymers into polylactic acid (PLA) and other thermoplastics, this study delves into how these composites enhance mechanical, thermal and functional properties of the printed objects. We critically assess studies that investigate the impact of raster orientation, filler content, and material composition on tensile, bending, and impact strength, as well as on the thermal stability and degradation behavior of composite filaments. The review highlights key findings from the literature, including the optimization of filament formulations to achieve superior mechanical performance, improved thermal resistance, and specific functional characteristics suitable for a wide range of applications from biomedical to structural components. Moreover, this paper discusses the challenges associated with composite filament production, including material compatibility, dispersion of nano-fillers, and the need for printer hardware adjustments. Future directions for research in the field are identified, emphasizing the potential for new material combinations, sustainability considerations, and the development of filaments designed for specific industrial applications. An effective way to better meet designers' expectations for qualified materials is composite filaments. This review focuses on how these elements can be applied to improve both product design and functionality. A guide is presented in choosing composite filaments that can meet the features expected from the designed product.

Keywords: 3D printing, composite filaments, fused deposition modeling, material properties, additive manufacturing.

1. Introduction

The advent of three dimensional (3D) printing, or additive manufacturing (AM), has revolutionized the way we conceive, design, and manufacture objects across a myriad of industries, from aerospace and automotive to biomedical and consumer goods. At the heart of this transformation lies fused deposition modeling (FDM), one of the most accessible and widely used 3D printing technologies. FDM's popularity is largely attributed to its simplicity, cost-effectiveness, and the vast array of materials it can process. However, the quest for materials that offer enhanced properties suitable for more demanding applications has led to significant research and development efforts, particularly in the realm of composite filaments. Composite filaments for FDM combine a base material, typically a thermoplastic such as polylactic acid (PLA) or acrylonitrile butadiene styrene (ABS), with reinforcing materials like carbon fibers, glass fibers, metals, or ceramics. These composites

---

[*]*Corresponding author:*
Email: akaptan@cumhuriyet.edu.tr

Cite this article as:
Kaptan, A., Kartal, F. (2024). A critical review of composite filaments for fused deposition modeling: Material properties, applications, and future directions. *European Mechanical Science, 8*(3): 199-209. https://doi.org/10.26701/ems.1451829

History dates:
Received: 14.03.2024, ***Revision Request***: 21.04.2024, ***Last Revision Received***: 24.05.2024, ***Accepted***: 25.05.2024

aim to overcome the limitations of conventional filaments by improving mechanical strength, thermal stability, electrical conductivity and other functional properties. The integration of nano-fillers such as graphene, carbon nanotubes (CNTs), and nano-silica (SiO_2) has also been explored to enhance filament performance further. With improved material properties, FDM 3D printing can transcend its traditional prototyping role, moving towards the production of functional parts that meet the rigorous requirements of industrial applications. The fabrication of personalized objects, previously unachievable with standard filaments, has become possible through the development of composite filaments. This review aims to provide a comprehensive overview of the current state of composite filaments for FDM 3D printing. It will explore the various types of materials used in composite filaments, examining how the incorporation of different fillers affects the physical, mechanical and thermal properties of the printed objects. The impact of printing parameters such as raster orientation and filler density on the performance of composite filaments will also be discussed. The complex relationship between material composition, processing conditions and final properties of 3D printed objects will be highlighted. Furthermore, the review will address the challenges associated with the production and use of composite filaments, including issues related to material compatibility, uniform dispersion of fillers, and the need for specialized printing settings or equipment modifications. Despite these challenges, the potential of composite filaments to push the boundaries of FDM 3D printing is undeniable. In addition to summarizing key findings from recent studies, this review will identify gaps in the current knowledge and suggest directions for future research. With continuing advances in materials science and AM technologies, development of new composite filaments holds great promise to further enhance the capabilities of FDM 3D printing. Thus, it paves the way for greater adoption in high-performance and special applications.

By delving into the intricate world of composite filaments, this review seeks to shed light on the progress made thus far and the potential that lies ahead. It is intended for researchers, engineers, and practitioners in the field of AM who are interested in the latest material innovations and their implications for the future of 3D printing.

1.1. Literatur surway

In the rapidly evolving field of additive manufacturing, particularly within the domain of FDM, the development and application of composite filaments have garnered significant attention. This increase in interest is largely due to the potential of composite materials to significantly improve the mechanical, thermal and functional properties of 3D printed objects. Thus, the use of FDM technology is being extended beyond prototyping to the manufacturing of end-use parts. The literature surrounding composite filaments is extensive and reflects interdisciplinary research aimed at overcoming the limitations of traditional 3D printing materials. This section provides an overview of the existing body of work on composite filaments for FDM, highlighting key themes, findings, and the methodologies employed by researchers to advance the field. The exploration of composite filaments encompasses a wide range of base materials and reinforcements. Base materials commonly include thermoplastics like PLA, ABS, and polyamide (nylon), which are favored for their ease of printing, availability, and relatively low cost. On the other hand, reinforcement materials are very diverse, including carbon fiber, glass fiber, metal, ceramics and various nanoparticles such as graphene, carbon nanotube and nano-silica. Each of these reinforcements brings specific advantages to the composite filament, such as increased tensile strength, improved thermal resistance, enhanced electrical conductivity, or added biocompatibility, catering to the demands of specialized applications. Significant research has focused on the optimization of filament composition, examining how different ratios of matrix to reinforcement materials affect the final properties of printed objects. Studies often utilize a combination of experimental testing and computational modeling to predict the behavior of composite filaments under various loading conditions and printing parameters. Tensile, compressive and flexural tests are routinely conducted alongside more specialized analyses such as dynamic mechanical analysis (DMA), thermogravimetric analysis (TGA), and differential scanning calorimetry (DSC) to comprehensively evaluate the performance enhancements offered by composite filaments. Another critical area of investigation within the literature is the impact of printing parameters on the properties of objects made from composite filaments. Factors such as nozzle temperature, print speed, layer height, raster angle, and infill density have all been shown to influence the mechanical integrity and surface finish of printed parts. Researchers have systematically varied these parameters to determine optimal printing conditions that maximize the advantages of composite materials. Challenges associated with the use of composite filaments, such as nozzle clogging, uneven material distribution, and the need for printer modifications, are also extensively documented. Solutions to these challenges, including the development of new nozzle designs and the formulation of advanced composite materials with improved flow characteristics, are actively being explored. The literature survey reveals a dynamic and rapidly advancing field, characterized by a constant quest for new material combinations and processing techniques. As this body of work continues to grow, it not only enhances our understanding of composite filament behavior but also pushes the boundaries of what is possible with FDM technology, opening up new horizons for the future of AM. This introduction to the literature survey sets the stage for a detailed examination of specific studies and findings, which collectively illustrate the current state of knowledge in the field of composite filaments for FDM 3D printing. Through this exploration, we aim to capture the breadth of research activities, identify prevailing trends, and underscore the innovative approaches being adopted to address the complex challenges inherent in this area of study.

In this study, the literature review is generally categorized as follows according to the subject areas focused on, although no clear distinctions can be made from each other.

Properties of composite filaments

In a study by Wu et al. (2016), to improve the thermal properties of PLA filament, a composite filament was produced using a PLA and nano-SiO_2 mixture, and the distribution of nano-SiO_2 and the fracture surfaces of the filaments were examined with a scanning electron microscope (SEM). The thermal performances of the composite filament were evaluated using DSC and TGA, showing that as the amount of nano-SiO_2 increased, there was a slight increase in the degree of orientation, friction coefficient, thermal decomposition temperature and glass transition (Tg) temperature. It was mentioned that adding 1% by weight SiO_2 to PLA increased tensile strength, but adding 3% by weight SiO_2 decreased it, demonstrating that nano-SiO_2 dispersed within PLA and could reduce the cohesion between PLA crystals [1].

Daver et al. (2018) showed in the TGA analysis of 3D print samples of mushroom/PLA mixture filaments that pure PLA lost 5% of its mass at 342°C, 10% of its mass at 352°C, 50% of its mass at 378°C, and experienced maximum mass loss at 383°C. They stated that the addition of mushroom to PLA resulted in a 10% mass loss at lower temperatures and a more than 50% mass loss at higher temperatures [2].

Kariz et al. (2018) produced filaments using a 1/9 ratio of wood/PLA, increasing the tensile strength from 55 MPa to 57 MPa, and found that in a 1/1 ratio of wood/PLA mixture, the value dropped to 30 MPa. They determined that adding wood particles up to 10% increased the strength of the filaments, but higher wood ratios decreased it [3].

Haq et al. (2018) observed changes in the mechanical properties of polycaprolactone (PCL/PLA) composite filaments with different molecular weights (400, 6000, and 10,000 g/mol) and mixture ratios (5,10,15 phr) of polyethylene glycol (PEG) in PCL/PLA. They showed that increasing the molecular weight of PEG significantly improved the tensile and impact strength of PCL/PLA and the PCL/PLA/PEG composite increased the tensile strength and elasticity modulus. Increasing the PEG content from 5phr to 15phr decreased the tensile strength and Young's modulus, but increasing molecular weight of PEG from 400 to 10,000 increased the impact resistance of PCL/PLA/PEG composites. They showed that better mechanical properties of PCL/PLA/PEG composites could be achieved by optimizing the PEG content and molecular weight [4].

Kamarudin et al. (2020) found that increasing the ratio of epoxidized jatropha oil (EJO, 1-5%), processed kenaf fiber (TK, 30%), and PLA (65-69%) mixtures decreased the Tg and increased the Tm [5].

Singh et al. (2020) examined the mechanical performance of chitosan-reinforced PLA scaffolds. They determined that the strength of composite samples significantly depends on the chitosan load and density and that the annealing temperature does not affect the mechanical properties. Increasing the chitosan ratio (1%, 1.5%, 2% wt.) in PLA decreased tensile and bending strength but increased compressive strength. Overall, PLA/chitosan composite scaffolds were mechanically effective and suitable for clinical purposes [6].

The study by Jayswal and Adanur (2023) focuses on the production and characterization of composite filaments containing PLA and thermoplastic polyurethane (TPU) for FDM in 3D printing. The article discusses the preparation of PLA/TPU composite filaments via solvent mixing method, examination of their mechanical, thermal and morphological properties, influence of FDM process parameters, and the mechanical behavior of 3D printed samples. According to the findings, the tensile strength and modulus of the filaments decrease as the TPU content increases, while elongation at break increases. Additionally, partial compatibility of polymer components is observed in the composite filament solution [7].

The article by Kantaros et al. (2023) examines advanced composite materials, particularly filaments containing fillers, used in FDM/FFF 3D printing manufacturing processes. It discusses how various reinforcements such as carbon fibers, glass fibers, and nanoparticles are integrated into the polymer matrix of FDM/FFF filaments. The article explains how the filler material layer enhances mechanical, thermal and electrical properties of 3D printed parts compared to pure polymers, expanding the potential application areas for FDM/FFF 3D printed components. Additionally, the article addresses the challenges encountered in using filler-containing filaments in FDM/FFF 3D printing, including filament extrusion stability, nozzle clogging, and interfacial adhesion between the reinforcement and matrix. Lastly, the article showcases examples demonstrating significant advantages of filler-containing filaments over standard FDM/FFF raw materials in various industries such as aerospace, automotive, medical, electronics and tooling. It also explores the possibility of future advancements and integration of innovative reinforcement materials [8].

Advantages of composite filaments

Liu et al. (2018) produced samples by FDM method using SiC/C/PLA mixtures composite filaments. They determined that as the SiC and C ratio in the filaments increases, the thermal conductivity property increases and the shape recovery time also decreases [9].

Chen et al. (2017) stated that the addition of graphene oxide (GO) to thermoplastic polyurethane (TPU)/PLA/GO nanocomposites increased the compressive modulus by 167% and the tensile modulus by 75.5%. On the other hand, it showed high levels of cell viability in cell culture tests. Thus, they point to the conclusion that a small amount of GO is beneficial for cell proliferation [10].

Çanti et al. (2018) successfully produced composite filaments reinforced with different nano/microparticles (SiO2, ZrB2, Al) in ABS at 175-210°C using a twin-screw extruder. Çanti›s characterization results showed that the new composites could be used as filaments in commercial FDM printers without modification. Adding micro/nanoparticles to ABS increased tensile strength by about 16%, and adding microparticles (ZrB2 and Al alloy) increased the type of stress by at least 18% [11].

Li et al. (2018) showed that using cellulose, glass fiber and PLA to make filaments for FDM 3D printers increased the impact resistance of the cellulose and PLA mixture filament by 34-60% and tensile strength by 43-52% compared to PLA filament. They also found that different ratios of cellulose and PLA mixture filament increased the impact toughness by 13-35% and tensile strength by 54-61% higher than pure PLA [12].

Ertane et al. (2018) produced filaments from a mixture of biochar and PLA, which is 100% recyclable from wood, plants, and soil. They observed that increasing amount of biochar slightly hindered the FDM printing process [13].

Caminero et al. (2019) analyzed the mechanical performance, dimensional accuracy, and texture of 3D printed samples of commercially available PLA, PLA3D850, and PLA-Graphene composite filaments. They stated that PLA 3D850 has less thermal shrinkage and better mechanical properties than conventional PLA. They mentioned that this makes it suitable for high accuracy, high resolution and high performance applications [14].

Charoenying et al. (2020) used an FDM 3D printer to design a capsule for controlling the release and gastric retention of domperidone Tablets. They made the capsule's lid hollow with wall thicknesses of 1.2-1.5mm using polyvinyl alcohol filament, and body with 1-2mm openings using PLA filament for drug release. They investigated how the floating time of the capsule and drug release in the stomach would be affected. It found that a capsule lid thickness of less than 1.3 mm increased stomach floating time and that reducing the size of the holes in the capsule body resulted in longer DOM release. X-ray diffraction (XRD) analyzes showed that the capsules remained in the rabbit stomach for more than 10 hours. Thus, it showed that the capsule was suitable for sustained drug delivery in the stomach with its floating and sustained drug release capabilities [15].

Huerta-Cardoso et al. (2020) mixed agave tequila waste fibers (ATF)/PLA at ratios of 20, 40, and 60 (w/v) and produced them using extrusion molding. They analyzed the tensile, bending, impact and water absorption properties of samples produced using press molding, observing the use of ATF as a filler. The reinforcement material in PLA improved mechanical properties, achieving the best results in a 40% (wt/vol) ATF blend, showing a flexural strength of 98.8 MPa and an impact strength of 6.8 kJ/m^2. These values were close to those of commonly used PLA composite polymers [16].

The article by Zhou et al. (2023) focuses on the development and application of conductive polymer composites (CPCs) for FDM. CPCs combine the electrical conductivity of conductive fillers with the excellent properties of polymers. FDM is a technique that produces products by depositing polymers layer by layer based on a digital model. FDM enables the preparation of complex structures and electronic devices with excellent properties using CPCs. This article introduces FDM technology, material requirements, and the conductivity mechanism of CPCs. Various design ideas for CPCs are summarized, and the current development status of different methods is introduced and compared. Finally, some perspectives on the future development of FDM technology and CPCs for FDM are presented [17].

Materials used in FDM 3D printing

Gkartzou et al. (2017) showed in their study on 3D printing with PLA/lignin mixture filaments that as the lignin content in PLA increased, the values of maximum stress and elongation at break decreased, and DSC analysis showed that increasing the lignin ratio from 5% to 20% did not cause significant changes in Tg, melting temperature (Tm) and melting enthalpy values [18].

Yu et al. (2017) observed in TGA analyses of FDM 3D printing work with PLA/graphene/CNTs mixtures that PLA lost about 5% of its mass at 310°C, PLA+6% CNT at 287°C, and PLA+2% graphene at 282°C. They stated that the thermal degradation properties of PLA-based composites changed little compared to pure PLA, and the thermal degradation temperature of the composites was approximately 30°C lower. Based on this, it is suggested that the super thermal conductivity feature of the graphene/CNT phase in PLA accelerates heat diffusion [19].

Ausejo et al. (2018) stated that mixtures of thermoplastic PLA and polyhydroxyalkanoate (PHA) could be used in biocompatible 3D printing applications. The 3D printed material using a PLA / PHA mixture showed suitable mechanical properties, thermal stabilities, and cell viability for tissue engineering applications. Biological tests on 3D print samples showed no toxicity against cell growth and demonstrated good biocompatibility with HEK293 cells [20].

Mansour et al. (2018) found that adding carbon fiber to polyethylene terephthalate glycol (PETG) material at a 1/4 ratio decreased the damping capacity of the resulting product [21].

Corcione et al. (2019) used pure PLA and spray-dried hydroxyapatite (sdHA)/PLA filaments for FDM 3D printing. They found that the presence of sdHA did not affect the decomposition temperature of PLA, with thermograms showing almost no change after 270°C [22].

Kumar et al. (2020) conducted a study on biapplications using PLA, biocompatible polyamide (PA6), and TiO2 mixtures alongside pure PLA filaments in the same 3D print samples. SEM and energy-dispersive X-ray spectroscopy (EDS) analyses showed that internal solidification gaps formed at the joining parts of the PLA layer with PA6/TiO2, negatively affecting the samples' bending strength [23].

Nevado et al. (2020) produced a polymer/ceramic mixture of PLA and biphasic calcium phosphates (BCPs) at a diameter of 1.7 mm using single screw extrusion, finding the filaments slightly brittle but suitable for FDM printers. BCPs were obtained by combustion synthesis, and the filaments were made considering a mixture of 15% BCP and 85% PLA by weight. Biological tests showed that the ceramic and polymer mixture filaments were not toxic to Detroit cells, Saos-2, and U937 macrophages, did not affect their proliferation, and allowed for cell anchorage in adhesion analyses. They observed sufficient compatibility between the material and osteoblasts in terms of viability, proliferation, and adhesion. However, they noted that other types of testing should also be considered to recommend such filaments for bone tissue engineering applications in 3D printing [24].

The study by Del Pilar Fabra Rivera et al. (2023) focuses on the production of PLA composites using FDM and examines their mechanical, thermal and morphological properties. The article describes how PLA composites with different layer thicknesses, infill densities, and infill patterns are printed using FDM. The printed samples undergo tensile, bending, impact, and hardness tests, while their thermal stability is evaluated through TGA. Additionally, the fracture surfaces of the samples are observed using SEM. The results indicate that the mechanical and thermal properties of PLA composites vary depending on FDM process parameters. Furthermore, the fracture mechanisms of PLA composites are correlated with the morphology of the fracture surfaces [25].

The study by Palaniappan et al. (2023) focuses on the development and application of CPCs for FDM. CPCs combine the electrical conductivity of conductive fillers with the excellent properties of polymers. FDM is a technique that produces products by depositing polymers layer by layer based on a digital model. FDM enables the preparation of complex structures and electronic devices with excellent properties using CPCs. This article first introduces FDM technology, material requirements, and the conductivity mechanism of CPCs. It then summarizes various design ideas for CPCs and introduces the current development status of different methods, comparing them. Finally, it presents some opinions on the future development of FDM technology and CPCs for FDM [26].

Effect of printing parameters

Letcher and Waytashek (2014) evaluated studies on the production of composite filaments for use in 3D printers. They tested the orientation effects on part strength by performing tensile tests at 0, 45 and 90° raster orientation angles on 3D printed samples made with PLA filament. They found the highest tensile strength at 45° raster orientation condition with 64 MPa, the highest bending strength at 102 MPa with 0° raster orientation, and the worst fatigue test values at 90° raster orientation [27].

Naveed (2020) examined the defects in 3D printed samples produced with PLA at raster orientation angles of 0°, 30°, 45°, 60° and 90° using SEM analysis of microstructure images. They noted that samples printed at 0, 30°, and 60° showed solidification gaps between two rasters on the outer surfaces. Ultimately, this indicates that the rasters were not connected properly during printing, causing gaps on the inner layer surfaces. Samples printed at 60° had longer average gap lengths (1.2 mm), while those at 45° had shorter gaps [28].

Vinay et al. (2024) investigates the impact of processing parameters on the adhesion strength of metal-polymer composites produced through FDM. Employing a design of experiments approach, the authors optimize parameters including nozzle temperature, bed temperature, layer height, and extrusion speed. Adhesion strength is assessed through peel and lap shear tests, while microstructure and interfacial bonding are analyzed via SEM and energy dispersive spectroscopy. Results indicate that adhesion strength increases with higher nozzle and bed temperatures, but decreases with increased layer height and extrusion speed. Optimal parameters are identified as 230°C nozzle temperature, 70°C bed temperature, 0.2 mm layer height and 30 mm/s extrusion speed. Authors conclude that processing variables significantly affect adhesion strength, suggesting FDM as a viable method for enhancing adhesion properties in metal-polymer composites [29].

Singh et al. (2024) investigated increasing the mechanical properties of composites prepared by adding multi-walled carbon nanotubes (MWCNT) at different rates (1%, 2%, and 3% by weight) to the ABS matrix. In the study, it was observed that MWCNTs were homogeneously distributed in the ABS matrix and their effects on mechanical properties were examined. The addition of MWCNT resulted in significant improvements in tensile strength and thermal properties compared to pure ABS. In particular, composites containing 3%

MWCNT showed an increase in tensile strength of up to 60% compared to pure ABS. Research results have revealed that MWCNTs are evenly distributed within the ABS matrix and these composites have superior mechanical properties, especially for use in the automotive and aerospace industries [30].

The study by Kargar and Ghasemi-Ghalebahman (2023) investigates the production of carbon fiber-reinforced PLA composites using FDM and examines their fatigue life and tensile strength. The article presents experimental studies where the infill density (50% and 75%) and raster angle (0, 45, and 90°) were varied to determine the optimal process parameters for enhancing the mechanical properties of FDM-produced parts. Experimental results indicate that increasing the infill density and decreasing the raster angle enhance the tensile strength, but the fatigue behavior is more complex and dependent on the infill density. Additionally, the effects of 100% infill density, raster width and nozzle diameter on mechanical properties are also investigated [31].

Table 1. Synthesizing some research efforts on PLA and its composites

References	Material Composition	Key Findings	Implications
Letcher and Waytashek (2014)	PLA	Highest tensile strength at 45° raster orientation (64 MPa), highest bending strength at 0° (102 MPa), worst fatigue at 90°.	Orientation affects part strength significantly, providing guidelines for optimizing print settings for specific mechanical properties.
Wu G. et al. (2016)	PLA and nano-SiO_2 mixture	Addition of 1% SiO_2 increased tensile strength; 3% SiO_2 decreased it. Improved thermal properties with nano-SiO_2.	Nano-fillers can enhance or degrade mechanical properties, highlighting the need for balance in composite filament formulations.
Liu W. et al. (2018)	SiC/C/PLA mixtures	Increased thermal conductivity and reduced shape recovery time with increased SiC and C ratios.	Demonstrates the potential for FDM materials with improved thermal management capabilities.
Gkartzou et al. (2017)	PLA/lignin mixture	Increasing lignin content decreased maximum stress and elongation at break; little change in Tg, Tm, and melting enthalpy.	Suggests a trade-off between biodegradability and mechanical performance with lignin as a filler.
Yu et al. (2017)	PLA/graphene/CNT mixtures	Slight decrease in thermal degradation temperature with additives, indicating accelerated heat diffusion.	Highlights the potential for advanced thermal management in PLA composites with graphene/CNT.
Chen et al. (2017)	TPU/PLA/GO nanocomposites	Increased compression and tensile modulus, excellent cell viability, indicating GO's benefit for cell proliferation.	GO's addition to composites can enhance mechanical properties and biocompatibility for medical applications.
Daver et al. (2018)	Mushroom/PLA mixture	Addition of mushroom affected thermal degradation, with a significant mass loss at higher temperatures.	Indicates potential for biodegradable composites with altered thermal properties.
Çanti et al. (2018)	ABS with nano/microparticles (MWCNTs, SiO2, ZrB2, Al)	Increased tensile strength with micro/nanoparticle addition, showing promise for enhanced FDM filament properties.	Suggests that adding micro/nanoparticles can significantly improve the mechanical strength of ABS composites.
Kariz et al. (2018)	Wood/PLA mixtures	Wood particles up to 10% increased strength; higher ratios decreased it.	Highlights the potential for wood particle reinforcement in PLA but notes the limitations of filler content.
Li et al. (2018)	Cellulose, glass fiber, and PLA	Increased impact resistance and tensile strength with cellulose and PLA mixture compared to pure PLA.	Demonstrates the effectiveness of cellulose and glass fibers in enhancing mechanical properties of PLA filaments.
Ausejo et al. (2018)	PLA/PHA mixtures	Suitable mechanical properties, thermal stabilities, and cell viability for tissue engineering applications.	Indicates potential for PLA/PHA mixtures in biocompatible 3D printing applications.
Vinay et al. (2024)	Metal-polymer composites	Optimized nozzle and bed temperatures improve adhesion strength; processing variables significantly affect metal-polymer composite properties.	Points to the importance of processing parameters in achieving strong adhesion in metal-polymer composites.
Zhou, X., et al. (2023)	Conductive polymer composites (CPCs)	Introduction to CPCs for FDM, focusing on electrical conductivity and complex structure capabilities.	Suggests a growing field of FDM applications in electronics and complex structures with conductive properties.
Palaniappan et al. (2023)	Conductive polymer composites (CPCs)	Discusses FDM technology, CPC design ideas, and future development perspectives.	Reinforces the potential and challenges of developing CPCs for advanced FDM applications.
Jayswal and Adanur (2023)	PLA/TPU composites	Tensile strength and modulus decrease with increased TPU content; increased elongation at break.	Highlights the trade-offs in mechanical properties with TPU content, indicating customization potential for specific applications.

The conclusion here is that the mechanical, physical, and chemical properties of the filaments planned to be produced significantly depend on the raw material and mixture ratios. Additionally, 3D printing parameters have a significant impact on the mechanical properties of parts produced with FDM 3D printers.

The pie chart (**▶Figure 1**) shows the distribution of material types utilized in the composite filament studies for FDM 3D printing. It highlights the diversity in material use, with PLA-based composites forming a significant portion of the studies, followed closely by other composite materials, biocompatible composites, pure PLA and ABS. This visualization underscores the research community's interest in exploring a wide range of materials to enhance the properties and applications of 3D printed objects.

This line graph (**▶Figure 2**) depicts a hypothetical trend in the improvement of mechanical and thermal properties of composite filaments used in FDM 3D printing over the years 2014 to 2023. The graph illustrates a steady increase in both mechanical and thermal properties, highlighting ongoing advancements in composite filament technology. The markers and lines represent the annual average percentage improvement in these properties, with mechanical properties showing a slightly more pronounced improvement over time compared to thermal properties. This visualization underscores the progressive enhancement in filament quality, driven by research and development in the field, leading to broader and more effective applications of 3D printing technology.

The heatmap (**▶Figure 3**) displays a hypothetical correlation matrix between various properties of composite filaments used in FDM 3D printing. This matrix provides insights into how different properties such as tensile strength, thermal stability, printability, impact resistance, and flexural strength are interrelated. Positive values indicate a direct correlation, where an increase in one property tends to coincide with an increase in another, while negative values suggest an inverse relationship. For instance, a strong positive correlation is observed between flexural strength and impact resistance, indicating that improvements in one could likely lead to enhancements in the other. Conversely, printability shows a negative correlation with both tensile strength and thermal stability, suggesting that materials optimized for ease of printing may compromise on these mechanical or thermal properties.

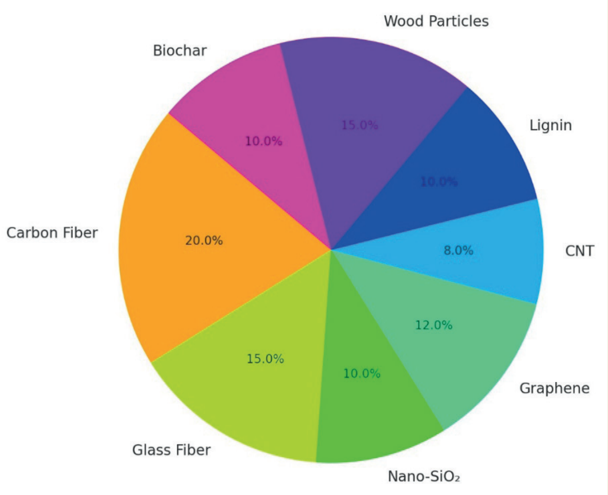

Figure 1. Distribution of material types utilized in the composite filament studies for FDM 3D printing

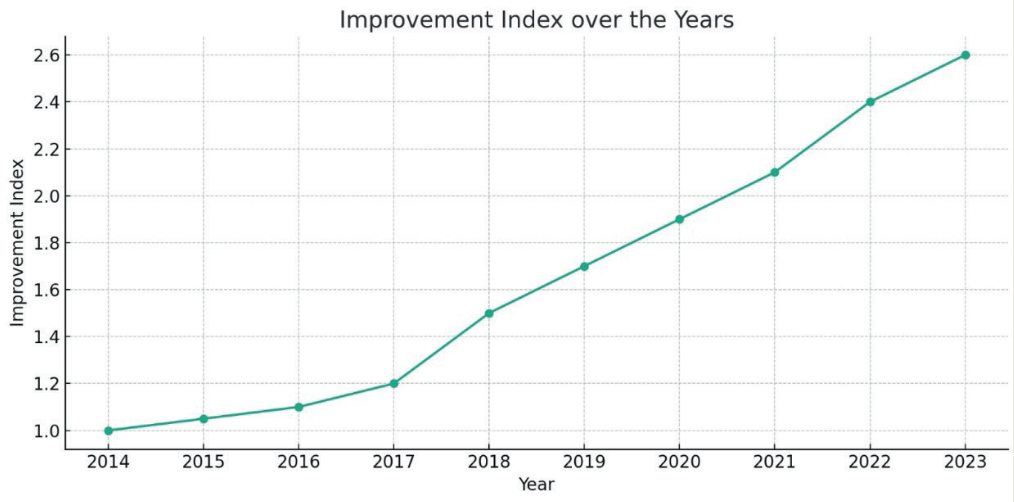

Figure 2. Trend in the improvement of mechanical and thermal properties of composite filaments used in FDM 3D printing over the years 2014 to 2023

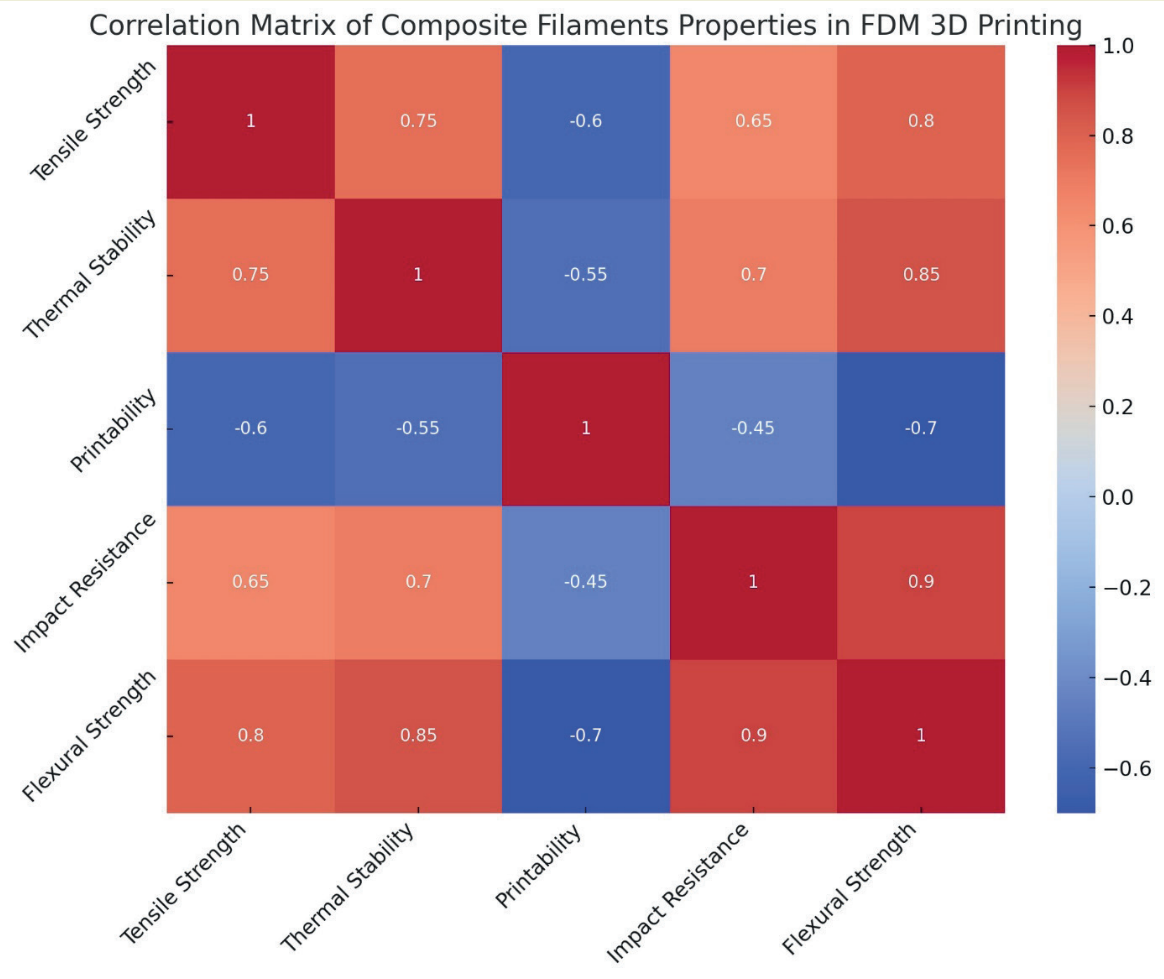

Figure 3. Correlation matrix between various properties of composite filaments used in FDM 3D printing

The stacked bar chart (▶**Figure 4**) illustrates the distribution of various reinforcements used in composite filaments for FDM 3D printing over selected years (2014 - 2023). Each color represents a different type of reinforcement material—carbon fiber, glass fiber, nanoparticles and bio-fillers—with the height of each colored segment indicating the number of studies focusing on that particular reinforcement type in a given year. A general increase in the number of studies across all types of reinforcements over the years, indicating growing interest and research activity in the field of composite filaments. Carbon fiber remains the most popular reinforcement, showing a steady increase in its research focus, reflecting its importance in enhancing mechanical properties. Glass fiber and nanoparticles also show significant growth, underscoring their roles in improving filament performance. Bio-fillers, while representing a smaller portion of the studies, exhibit a rising trend, highlighting a growing interest in sustainable and environmentally friendly reinforcement options. This visualization underscores the dynamic nature of research in composite filaments, with a clear trend towards diversifying and enhancing the properties of materials for 3D printing.

Applied fields

Composite filaments attract a lot of attention in industrial areas where rapid prototyping is required. Some of these are automotive, aviation, medical, computer hardware, etc. can be listed as follows. In addition to the superior properties of the polymer material used in 3D printers, which is an alternative to traditional materials, it also has mechanical strength, heat resistance, etc. It has some weaknesses such as: Researchers point out that one of the effective ways to improve these drawbacks is to obtain composite materials. The results obtained from the research are practically applied to industrial fields. In industries such as automotive, aerospace and biomedical, composite materials have been placed at the center of studies focused on reducing the weight of components, long-lasting designs and recycling.

Composite filaments, made from a mixture of polymers and materials like carbon fibers or ceramics, enhance the properties of objects created with 3D printers. Despite their advantages in mechanical strength and heat resistance, they do have some drawbacks, such as cost and specialized processing requirements.

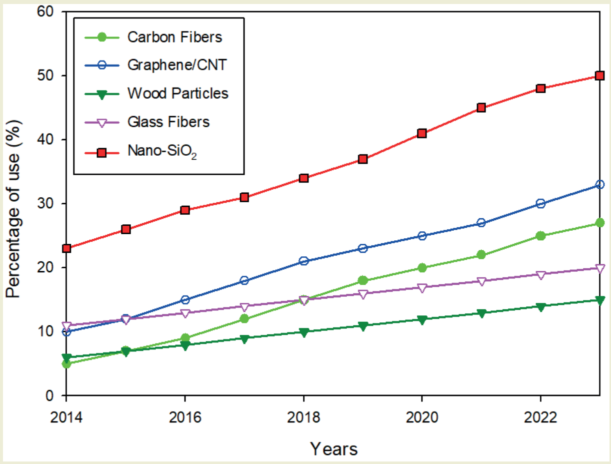

Figure 4. Distribution of various reinforcements used in composite filaments for FDM 3D printing between 2014 and 2023

Researchers have identified that enhancing these filaments with composite materials can mitigate these weaknesses. The practical applications derived from ongoing research are particularly evident in sectors focused on lightweight components, durability and recyclability. In automotive, aerospace and biomedical fields, composite materials are crucial in studies aimed at reducing component weight and enhancing long-term usability and sustainability. This makes composite filaments a focal point in efforts to advance and refine the capabilities of 3D printing technologies in various industrial applications.

2. Discussions

The review of recent studies on the production and evaluation of composite filaments for FDM 3D printing reveals a rapidly advancing field marked by innovative approaches to enhancing filament properties. This discussion synthesizes key insights, addresses challenges, and proposes avenues for future research, aiming to contribute to the development of high-performance, application-specific composite filaments.

Synthesis of Findings: The literature indicates a strong emphasis on improving the mechanical and thermal properties of filaments through the incorporation of various reinforcements, including carbon fibers, glass fibers, nanoparticles, and bio-fillers. Studies such as Letcher and Waytashek (2014) and Wu G. et al. (2016) highlight the significant impact of material composition and print parameters on filament performance [1,2]. Moreover, the introduction of bio-compatible and sustainable materials, as seen in the works of Ausejo et al. (2018) and Ertane et al. (2018), reflects a growing interest in environmental sustainability and medical applications [12,14].

Challenges and Limitations: Despite notable advancements, several challenges remain. The heterogeneity of composite materials often complicates filament production, requiring careful optimization of material ratios and processing conditions to achieve desired properties without compromising printability. Additionally, studies like that of Kumar et al. (2020) point to difficulties in achieving uniform dispersion of reinforcements within the polymer matrix, which can adversely affect the mechanical integrity and consistency of printed objects [19].

Material Innovation: Developing new composite materials that balance strength, flexibility, and thermal stability with ease of printing. Exploration of novel bio-based and biodegradable materials could also contribute to sustainability goals.

Advanced Processing Techniques: Investigating more sophisticated methods for mixing and extruding composite filaments to enhance the uniformity and dispersion of reinforcements. Techniques such as microencapsulation of nanoparticles could offer improved material properties and processing characteristics.

Printer Adaptations: Designing printer modifications or developing new printer technologies tailored to the specific requirements of composite filaments. This includes novel nozzle designs and advanced temperature control mechanisms to accommodate a wider range of materials.

Application-Specific Studies: Expanding research into practical applications of composite filaments, particularly in industries where FDM 3D printing has been underutilized due to material limitations. This includes aerospace, automotive and biomedical sectors, where the demand for customized, high-performance parts is significant.

Exploration of composite filaments for FDM 3D printing represents a vibrant area of research with the potential to significantly expand the capabilities and applications of additive manufacturing. By addressing the current challenges and focusing on the outlined future directions, the field can continue to innovate, paving the way for the development of next-generation materials and printing technologies.

3. Conclusions

This comprehensive review of studies on composite filaments for FDM 3D printing underlines the dynamic and innovative nature of research in this field. The results obtained from this compilation study can be listed as follows:

- Integration of various reinforcements into base thermoplastics has been shown to significantly increase the mechanical, thermal, and functional properties of 3D printed objects. From increased tensile strength and thermal stability to improved biocompatibility and sustainability, composite filaments are pushing the boundaries of what can be achieved with FDM 3D printing.

- Despite these advances, challenges such as material compatibility, uniform reinforcement distribution, and printability remain. However, ongoing research into new material formulations, advanced processing techniques, and printer modifications offers viable solutions.
- Future of composite filaments in FDM 3D printing is bright and there are many opportunities for further research. Key areas include developing new composite materials that offer a balance between performance and printability, investigating sustainable and biodegradable options, and customizing printing technologies to expand the range of usable materials.
- Advances in composite filaments are significantly expanding the capabilities of FDM 3D printing, transforming it from a tool used primarily for prototyping into a viable method for producing functional, high-performance parts. Thus, it not only expands the scope of application of FDM technology, but also contributes to the wider adoption and integration of 3D printing in various industries.

This review brings together significant research in the development of composite filaments, revealing their potential as an alternative material. The study discusses the advanced material properties, industrial applicability and future trends of composite filaments. Future research may focus on improving mechanical strength, increasing manufacturing speed, and improving thermal properties. These developments will directly affect the increase in the usage areas of composite filaments.

Acknowledgments

The authors would like to thank Kastamonu University and the project unit staff for the support of the project numbered KÜBAP-1/2023-18.

Research Ethics

Ethical approval not required.

Author Contributions

There is no conflict of interest. The funders had no role in any phases of the design, analysis, interpretation, writing, or conclusion of the study.

Competing Interests

The authors declare that there is no conflict of interest regarding the publication of this paper.

Research Funding

Not reported.

Data Availability

Not applicable.

Peer-review

Externally peer-reviewed.

References

[1] Wu, G., Liu, S., Jia, H., & Dai, J. (2016). Preparation and properties of heat resistant polylactic acid (PLA)/Nano-SiO2 composite filament. *Journal of Wuhan University of Technology-Mater. Sci. Ed.*, 31(1), 164-171. https://doi.org/10.1007/s11595-016-1347-2

[2] Daver, F., Lee, K. P. M., Brandt, M., & Shanks, R. (2018). Cork-PLA composite filaments for fused deposition modelling. *Composites Science and Technology, 168,* 230-237. https://doi.org/10.1016/j.compscitech.2018.10.008

[3] Kariz, M., Sernek, M., Obucina, M., & Kuzman, M. K. (2018). Effect of wood content in FDM filament on properties of 3D printed parts. *Materials Today Communications, 14,* 135-140. https://doi.org/10.1016/j.mtcomm.2017.12.016

[4] Haq, R. H. A., Bin Marwah, O. M. F., Rahman, M. N. A., Haw, H. F., Abdullah, H., Ahmad, S., & Yunos, M. Z. (2018). Mechanical properties of PCL/PLA/PEG composite blended with different molecular weight (MW) of PEG for Fused Deposition Modelling (FDM) filament wire. *International Journal of Integrated Engineering, 10(5),* 187-192. https://doi.org/10.30880/ijie.2018.10.05.028

[5] Kamarudin, S. H., Abdullah, L. C., Aung, M. M., & Ratnam, C. T. (2020). Thermal and structural analysis of epoxidized jatropha oil and alkaline treated kenaf fiber reinforced poly(Lactic acid) biocomposites. *Polymers, 12(11),* Article 2604. https://doi.org/10.3390/polym12112604

[6] Singh, S., Singh, G., Prakash, C., Ramakrishna, S., Lamberti, L., & Pruncu, C. I. (2020). 3D printed biodegradable composites: An insight into mechanical properties of PLA/chitosan scaffold. *Polymer Testing, 89,* Article 106722. https://doi.org/10.1016/j.polymertesting.2020.106722

[7] Jayswal, A., & Adanur, S. (2023). Characterization of polylactic acid/thermoplastic polyurethane composite filaments manufactured for additive manufacturing with fused deposition modeling. *Journal of Thermoplastic Composite Materials, 36(4),* 1450-1471. https://doi.org/10.1177/08927057211062561

[8] Kantaros, A., Soulis, E., Petrescu, F. I. T., & Ganetsos, T. (2023). Advanced composite materials utilized in FDM/FFF 3D printing manufacturing processes: The case of filled filaments. *Materials, 16(18),* Article 6210. https://doi.org/10.3390/ma16186210

[9] Liu, W., Wu, N., & Pochiraju, K. (2018). Shape recovery characteristics of SiC/C/PLA composite filaments and 3D printed parts. *Composites Part A: Applied Science and Manufacturing, 108,* 1-11. https://doi.org/10.1016/j.compositesa.2018.02.017

[10] Chen, Q., Mangadlao, J. D., Wallat, J., De Leon, A., Pokorski, J. K., & Advincula, R. C. (2017). 3D printing biocompatible polyurethane/poly(-

lactic acid)/graphene oxide nanocomposites: Anisotropic properties. *ACS Applied Materials and Interfaces, 9(4),* 4015-4023. https://doi.org/10.1021/acsami.6b11793

[11] Çanti, E., Aydin, M., & Yildirim, F. (2018). Production and characterization of composite filaments for 3D printing. *Journal of Polytechnic, 21(2),* 397-402. https://doi.org/10.2339/politeknik.389591

[12] Li, X., Ni, Z., Bai, S., & Lou, B. (2018). Preparation and mechanical properties of fiber reinforced PLA for 3D printing materials. *IOP Conference Series: Materials Science and Engineering, 322(2),* Article 022012. https://doi.org/10.1088/1757-899X/322/2/022012

[13] Ertane, E. G., Domer-Reisel, A., Baran, O., Welzel, T., Matner, V., & Svoboda, S. (2018). Processing and wear behaviour of 3D printed PLA reinforced with biogenic carbon. *Advances in Tribology, 2018,* Article 1763182. https://doi.org/10.1155/2018/1763182

[14] Caminero, M. A., Chacon, J. M., Garcia-Plaza, E., Nunez, P. J., Reverte, J. M., & Becar, J. P. (2019). Additive manufacturing of PLA-based composites using fused filament fabrication: Effect of graphene nanoplatelet reinforcement on mechanical properties, dimensional accuracy and texture. *Polymers, 11(5),* Article 799. https://doi.org/10.3390/polym11050799

[15] Charoenying, T., Patrojanasophon, P., Ngawhirunpat, T., Rojanarata, T., Akkaramongkolporn, P., & Opanasopit, P. (2020). Three-dimensional (3D)-printed devices composed of hydrophilic cap and hydrophobic body for improving buoyancy and gastric retention of domperidone tablets. *European Journal of Pharmaceutical Sciences, 155,* Article 105555. https://doi.org/10.1016/j.ejps.2020.105555

[16] Huerta-Cardoso, O., Durazo-Cardenas, I., Longhurst, P., Simms, N. J., & Encinas-Oropesa, A. (2020). Fabrication of agave tequilana bagasse/PLA composite and preliminary mechanical properties assessment. *Industrial Crops and Products, 152,* Article 112523. https://doi.org/10.1016/j.indcrop.2020.112523

[17] Zhou, X., Wu, L., & Wang, J. (2023). Recent developments in conductive polymer composites for fused deposition modeling. *Composites Part A: Applied Science and Manufacturing,* Article 107739. https://doi.org/10.1016/j.compositesa.2023.107739

[18] Gkartzou, E., Koumoulos, E. P., & Charitidis, C. A. (2017). Production and 3D printing processing of bio-based thermoplastic filament. *Manufacturing Review, 4,* Article 20. https://doi.org/10.1051/mfreview/2016020

[19] Yu, W. W., Zhang, J., Wu, J. R., Wang, X. Z., & Deng, Y. H. (2017). Incorporation of graphitic nano-filler and poly(lactic acid) in fused deposition modeling. *Journal of Applied Polymer Science, 134(15),* Article 44703. https://doi.org/10.1002/app.44703

[20] Ausejo, J. G., Rydz, J., Musial, M., Sikorska, W., Sobota, M., Wlodarczyk, J., & Kowalczuk, M. (2018). A comparative study of three-dimensional printing directions: The degradation and toxicological profile of a PLA/PHA blend. *Polymer Degradation and Stability, 152,* 191-207. https://doi.org/10.1016/j.polymdegradstab.2018.04.024

[21] Mansour, M., Tsongas, K., Tzetzis, D., & Antoniadis, A. (2018). Mechanical and dynamic behavior of fused filament fabrication 3D printed polyethylene terephthalate glycol reinforced with carbon fibers. *Polymer-Plastics Technology and Engineering, 57(16),* 1715-1725. https://doi.org/10.1080/03602559.2017.1419490

[22] Corcione, E. C., Gervaso, F., Scalera, F., Padmanabhan, S. K., Madaghiele, M., Montagna, F., & Maffezzoli, A. (2019). Highly loaded hydroxyapatite microsphere/PLA porous scaffolds obtained by fused deposition modelling. *Ceramics International, 45(2),* 2803-2810. https://doi.org/10.1016/j.ceramint.2018.07.297

[23] Kumar, S., Singh, R., Singh, M., Singh, T., & Batish, A. (2020). Multi material 3D printing of PLA PA6/TiO2 polymeric matrix: Flexural, wear and morphological properties. *Journal of Thermoplastic Composite Materials,* 089270572095319. https://doi.org/10.1177/0892705720953193

[24] Nevado, P., Lopera, A., Bezzon, V., Fulla, M. R., Palacio, J., Zaghete, M. A., & Garcia, C. (2020). Preparation and in vitro evaluation of PLA/biphasic calcium phosphate filaments used for fused deposition modelling of scaffolds. *Materials Science and Engineering C, 114,* Article 111013. https://doi.org/10.1016/j.msec.2020.111013

[25] Del Pilar Fabra Rivera, A., de Castro Magalhães, F., & Campos Rubio, J. C. (2023). Experimental characterization of PLA composites printed by fused deposition modelling. *Journal of Composite Materials, 57(5),* 941-954. https://doi.org/10.1177/00219983221146619

[26] Palaniappan, M., Tirlangi, S., Mohamed, M. J. S., Moorthy, R. S., Valeti, S. V., & Boopathi, S. (2023). Fused deposition modelling of polylactic acid (PLA)-based polymer composites: A case study. In *Development, Properties, and Industrial Applications of 3D Printed Polymer Composites* (pp. 66-85). IGI Global. https://doi.org/10.4018/978-1-6684-6009-2.ch005

[27] Letcher, T., & Waytashek, M. (2014). Material property testing of 3D-printed specimen in PLA on an entry-level 3D printer. *ASME International Mechanical Engineering Congress and Exposition, Proceedings (IMECE),* 2A. https://doi.org/10.1115/IMECE2014-39379

[28] Naveed, N. (2020). Investigate the effects of process parameters on material properties and microstructural changes of 3D-printed specimens using fused deposition modelling (FDM). *Materials Technology,* 1-14. https://doi.org/10.1080/10667857.2020.1758475

[29] Vinay, D. L., Keshavamurthy, R., Erannagari, S., Gajakosh, A., Dwivedi, Y. D., Bandhu, D., ... & Saxena, K. K. (2024). Parametric analysis of processing variables for enhanced adhesion in metal-polymer composites fabricated by fused deposition modeling. *Journal of Adhesion Science and Technology, 38(3),* 331-354. https://doi.org/10.1080/01694243.2023.2228496

[30] Singh, P., Singari, R. M., & Mishra, R. S. (2024). Enhanced mechanical properties of MWCNT reinforced ABS nanocomposites fabricated through additive manufacturing process. *Polymers for Advanced Technologies, 35(2),* e6308. https://doi.org/10.1002/pat.6308

[31] Kargar, E., & Ghasemi-Ghalebahman, A. (2023). Experimental investigation on fatigue life and tensile strength of carbon fiber-reinforced PLA composites based on fused deposition modeling. *Scientific Reports, 13(1),* Article 18194. https://doi.org/10.1038/s41598-023-45046-x